THE GEOLOGICAL CONTROLS ON THE HEAVY RARE EARTH ELEMENT ENRICHED ALTERATION ZONE OF AREA 4, LOFDAL, KHORIXAS, NAMIBIA

SUBMITTED BY

EDWARD LOYE

TO THE UNIVERSITY OF EXETER AS A THESIS FOR THE DEGREE OF MASTERS BY RESEARCH (MRes) IN GEOLOGY

June 2014

This thesis is available for Library use on the understanding that it is copyright material and that no quotation from the thesis may be published without proper acknowledgement.

I certify that all material in this thesis which is not my own work has been identified and that no material has previously been submitted and approved for the award of a degree by this or any other University.

(Signature) ……

Supervisors: Dr Scott Swinden, of Swinden Geosciences & Professor Frances Wall, of Camborne School of Mines

SUMMARY

The “heavy” rare earths (HREEs) are the most critical of all REEs, and are attracting much market and exploration attention today since China imposed export quotas in 2011.

The Lofdal Intrusive Complex, Khorixas, Namibia is enriched with heavy rare earth (HREE) mineralisation within the late hydrothermal zones associated with carbonatites, proximate to the complex’s syenite intrusions, and are generally controlled by older basement structures. One of these enriched HREE alteration zones is “Area 4”, now a proven CIM NI 43-101 compliant indicated and inferred resource, and sits at the top for REE basket price in the TMR world index of REE projects. Brecciated fenite zones are repeatedly overprinted, commonly hosting greater HREE mineralisation amongst the “busiest” overprints. The fenitisation and brecciation providing the ground preparation for REE deposition in Area 4 have similarities to the Kangankunde and Chilwa carbonatite complexes in Malawi, where HREE enrichment can be found in proximal brecciated fenite zones.

90% of the HREE deportment in Area 4 is in the mineral xenotime, and is commonly associated with rutile (+/-Nb), apatite, zircon, aeschynite, synchysite, and thorite. Variations of this assemblage reside in carbonate phases (calcite, dolomite, ankerite), albite, phlogopite-biotite, and magnetite/hematite. This study enhances the characterisation of the HREE mineral resource in Area 4 by combining details of drill core textural features, whole-rock major to trace element data analysis (ICP-MS) through the alteration zone and HREE mineralisation, with petrological and geochemical analysis of the major HREE bearing phases. 41 samples, representing a range of xenotime mineralised intercepts, of have been analysed petrologically via microscopy, cathodoluminescence and SEM/EDS; and geochemically via EPMA.

The variability, fractionation, and partitioning between the REE in the Area 4 xenotimes is compared to synthetic analogues, and to other xenotimes of the Lofdal Complex outside of Area 4, and compared to xenotimes from Witwatersrand, South Africa, and from Browns Range, Australia.

REE budget in xenotime can vary in proportion, as well as other element substitution and replacement into either the Y-site (A), or PO4 site (T). Substitutions into the xenotime lattice importantly include Th and U. Tested here is whether variations in ionic radii between the REE in xenotime can provide valuable clues to formational environment, and help to delineate differentiation in paragenses. Gd is in a unique position as it marks the change from unpaired to paired electrons in the filling stages of 4f orbitals, and Gd is shared between the second and the third tetrad. How the GdPO4 polymorph relates across the miscibility gap between LREE phosphate (monazite) and HREE (xenotime) in the Area 4 xenotimes appears temperature dependent. Experimental studies here have shown that in

greater overprinted sections modifying fluids effectively “steal” Gd from xenotime to be lost to the fluid, and to LREE phases such as synchysite. Any xenotime that re-crystallises from these lower temperature fluids has been shown to have a higher HREE content, lower Th, but smaller grain size. Corrosion and re-precipitation of xenotime leads to Th being expelled from hydrothermal fluid leading Th to form its own phase, i.e. the silicate thorite, albeit proximal to xenotime, but importantly not substituting into the xenotime lattice, and that this is also shown to be temperature dependent.

Textural and compositional data indicate hydrothermal modification of earlier REE bearing phases. Suggested REE transporting ligands in carbo-hydrothermal fluids to later modifying hydrothermal fluids are perhaps a combination, and evolution through, HCO_3, PO_4 and HS, for example at >300°C, to Cl complexing ligands at to lower temperature <300°C . Decompression as a result of pregnant solution migrating into open space in fractures, fluid/rock interaction with albite, and especially dolomite, have been shown to be effective factors in depositing xenotime from solution.
The different stages of hydrothermal activity have been shown to have implications on the chemical and physical structure of the xenotime. This variability has economic implications when it comes to targeting ore, and to mineral processing.

Acknowledgements:

I would like to give special thanks to Dr Scott Swinden of Swinden Geoscience Consultants, Halifax Nova Scotia for his continued support, providing assay data and other related resources, throughout the extended project.

Many thanks to Franck Bizouerne, Don Burton and Gerald McConnell of Namibia Rare Earths Inc.

Thanks to Professor Frances Wall for her supervision at Camborne School of Mines.

Thanks to Vicky de Gabo, Ministry of Mines, Namibia, for access and comparison to her studies on the carbonatite dykes of the Lofdal Complex.

Thanks to Professor A. E Williams-Jones of McGill University, Montreal – as well as his post-graduate students Rowan Isabel and Sarah Bodeving, who both are undertaking detailed investigations within the Lofdal property.

Thanks to the onsite geologists and assistants at the Lofdal camp: Chris Anthonissen, Elsabe Cloete, Lindi Fryer, Alan Johnson, Bonnie Katanga, Gideon, Joseph Goveia, Stephen Bruwer, Mervin, and the dog with no name.

Thanks to Sam Broom-Fendley and Dr Jonathan Pickles at CSM for their help with setting up and calibration of the EPMA. Thanks to CSM staff: Sharon Uren and Gavyn Rollinson.

Table of Contents

LIST OF FIGURES 3
Abbreviations 5
1 INTRODUCTION 6
1.1 Aims and objectives 6
1.2 Specific Objectives 6
2 OVERVIEW OF RARE EARTH ELEMENTS 7
2.1 Definition of REEs 7
2.2 Production of REEs 7
2.3 REE applications 8
2.4 The market demand for REEs 11
2.5 Location of REE deposits 13
2.6 REE mineralogy 15
2 GEOLOGY OF THE STUDY AREA 19
3.1 Regional geology 19
3.2 Local geology 22
3.3 Accumulations of REE at Lofdal 25
4 RESOURCE DELINEATION of AREA 4 26
4.1 Introduction 26
4.2 Drilling campaigns, sampling and NI 43-101 compliant resource 26
4.3 General overview of the lithologies of the alteration zone 30
4.3 Mineralisation within the alteration zone 33
5 FIELDWORK 33
5.1 Core logs overview 33
6 ALTERATION ZONE IN DETAIL 39
6.1 Methodology whole-rock analysis 39
6.2 Optical petrography 40
6.2.1 Methodology microscopy 40
6.2.2 Methodology cathodoluminescence microscopy (CL) 40
6.3 Scanning electron microscopy - SEM/EDS 40
6.3.1 Methodology 40
6.4 Hosts for xenotime mineralisation in Area 4 42

6.4.1 Dolomite carbonatite 42
6.4.2 Magnetite bearing dolomitic & calcite carbonatites 45
6.4.3 Stringers in brecciated albitite 47
6.4.4 Ankeritic ferruginous apatite reaction fronts 51
6.4.6 Multi-phase xenotime 53
6.4.4 Biotite-phlogopite association with xenotime 54
6.4.7 Heavily overprinted mineralised sections 55
7 MICROPROBE ANALYSIS – EPMA 59
7.1 Methodology 59
7.1.1 Considerations 59
7.1.2 Microprobe Qa/Qc 62
7.2 Samples for analysis 62
7.3 Results from xenotime analysis 63
8 DISCUSSION 67
8.1 Host rocks for mineralisation – whole-rock analysis 67
8.2 Ground preparation for REE mineralisation in Area 4 71
8.2 The REE mineralisation in Area 4 74
8.2.1 Xenotimes types in Area 4 75
8.2.2 Xenotime REE variability and fractionation 76
8.2.3 The actinides issue - Th and U 88
8.4 Hydrothermal system and mineralising fluids 93
8.5 Blending core studies with analytical observations 104
9 PARAGENETIC SEQUENCE 107
10 CONCLUSIONS 109
11 LIMITATIONS & RECOMMENDATIONS 111
12 REFERENCES 112

LIST OF FIGURES

Figure 2.1 Periodic table of the elements highlighting the lanthanide group	8
Figure 2.2 Rare earth use by application (For 2012) by tonnes	9
Figure 2.3 Dy added to NdFeB magnets to control intergranular structure when operating at high T	10
Figure 2.4 Dy substitution into NdFeB magnets by end use	10
Figure 2.5 Estimated end uses for REEs – US Department of Energy	11
Figure 2.6 Rare earth concentrate production – US Department of Energy	12
Figure 2.7 US Department of Energy, Technology Metal Research 2011	12
Figure 2.8 Rare earth oxide (REO) supply and demand IMCOA 2012	12
Figure 2.9 World distribution of REE	14
Figure 2.10 Xenotime structure	16
Figure 3.1 Geological map of Namibia	20
Figure 3.2 Southern Africa cratons and stratigraphic column	21
Figure 3.3 The Evolution of the Damara Orogeny	22
Figure 3.4a Geology of the Lofdal area	22
Figure 3.4b Geology of the Lofdal area	23
Figure 3.5 Map showing intrusives of the Lofdal Igneous Complex and structural alignments	23
Figure 3.6 HREE concentration results around the Main Intrusion, Lofdal	26
Figure 4.1 Airborne radiometric survey image	26
Figure 4.2 Positions of definition drilling collars	27
Figure 4.3 Cross section of alteration zone in Area 4	28
Figure 4.4 Site of diamond drill-core delineation collars and this report's study area	28
Figure 4.5 Drill section 563E showing continuity of main mineralised zone	29
Figure 4.6 High "basket price" of Area 4, Lofdal as listed on TMR Index Nov 2013	29
Figure 4.7 Partly albitised basement gneiss	31
Figure 4.8 Chondrite normalised plots of wholerock of REE enrichment through the alteration zone	31
Figure 5.1 Site of diamond drill-core delineation collars and this report's study area	34
Figure 5.2 Example of cross-section through deposit at Area 4	34
Figure 5.3 Example of drill Plan for Area 4, Lofdal NRE 2012	35
Figure 5.4 Olympus X-Delta portable XRF, and Radeye	35
Figure 5.5 Dino-Lite Pro portable microscope	36
Figure 5.6 layout of Hole 4081 drill core	38
Figure 5.7 Wholerock data downhole on Hole 4081	39
Figure 6.1 4081 73.50m Thin section of dolomitic carbonatite	42
Figure 6.2 4081 73.50m CL image "sky at night" REE minerals in dolomite	42
Figure 6.3 BSE image close up of 4081 73.50m. Monazite crystals at base of albite grain	43
Figure 6.4 4081 73.50m CL images unusual "pits" and halo structures	43
Figure 6.5 4081 73.50m BSE image close up of "halo" in Figure 6.4.	44
Figure 6.6 4086 118.80m BSE image shows fine grained nature of the REE minerals & thorite	44
Figure 6.7 4013 36.00m x200 Subhedral pale 1mm xenotime aggregate crystals	45
Figure 6.8 4013 35.99m again sporadic subhedral magnetite and xenotime	45
Figure 6.9 4013 35.99m BSE image xenotime, pyrite, and magnetite	45
Figure 6.10 4087 131.50m thin section with CL transect	46
Figure 6.11a 47.44m magnetitic veins cross-cutting dolomitic carbonatite	46
Figure 6.11b 4032 47.56m moving across the section xenotime appears orientated to shear	47
Figure 6.12 4032 47.56m BSE image magnetite with Th-rich xenotime mantled by apatite	47
Figure 6.13 4081 80.60m thin section	48
Figure 6.14 4081 80.60m CL image strongly vein orientated xenotime with opaques	48
Figure 6.15 4081 80.60m BSE image of Figure 6.14	48
Figure 6.16 4081 80.60m BSE image close up of Figure 6.15	49
Figure 6.17 4082 91.86m ferruginous channel-way	49
Figure 6.18 4082 92.20m thin section with CL transect	50
Figure 6.19 4082 92.20m interstitial ankerite and xenotime in heavily fractured albitite	51

Figure 6.20 4031 22.25m thin section with CL transect	51
Figure 6.21 4031-22.25m the ankeritic darker carbonatite hosts xenotime crystals	51
Figure 6.22 4031 22.25m BSE images of xenotime intergrown with apatite at contact	52
Figure 6.23 4086 117.14m thorite mineralisation in an orientated vein	53
Figure 6.24 4013 46.93m thin section showing a brown smear across the brecciated albitite	53
Figure 6.25 4013 46.93m CL image types of xenotime LHS larger crystals	54
Figure 6.26 4013 46.93m BSE image close up of Figure 6.25	54
Figure 6.27 4014 65.95m thin section shear orientated micas carry HREE grade	55
Figure 6.28 4014 65.95m many subhedral xenotimes, and relatively large to 50µm	55
Figure 6.29 4014-66.45m heavily overprinted with xenotime	56
Figure 6.30 4014-66.45m BSE images calcite cutting xenotime	56
Figure 6.31 4015-38.40m BSE image of orientated zoned xenotime crystals	57
Figure 6.32 4032 62.35m thin section with CL transect	58
Figure 6.33 4032 62.35m albitite hosting tiny (<10 µm) xenotimes along grain boundaries	58
Figure 7.1 Typical chondrite normalised patterns of xenotimes across the alteration zone	63
Figure 8.1 comparison of the REE mineralised intercepts of Area 4 Lofdal vs VDC peripheral dykes	67
Figure 8.2 ternary plots Top: Vicky DC dykes vs Bottom: Area 4	68
Figure 8.3 BSE image comparison of Area 4 xenotime and VDC dyke xenotime	69
Figure 8.4 Whole-rock chondrite normalised plots of VDC dykes vs Hole 4081	70
Figure 8.5 sequence of main fluid events in fenite at Chilwa Island, Malawi. Dowman (2014)	74
Figure 8.6 preservation of Dy zoning in xenotime and zircon. Cherniak (2006)	77
Figure 8.7 Comparison of REE diffusion between xenotime and zircon. Cherniak (1997)	78
Figure 8.8 Gd correlates with lighter REs, but Dy to Lu not so well	79
Figure 8.9 Gd generally correlates with heavier REs like Dy, but dependant on type of xenotime	80
Figure 8.10 THREE vs Y apfu 16 oxygens Area 4 xenotimes vs Wall (2008) dyke xenotimes	80
Figure 8.11 comparison of chondrite-normalised plots for xenotimes: Witwatersrand SA vs Lofdal	82
Figure 8.12 Kositcin's model. Log scale binary plots of xenotimes from the Witwatersrand, SA	83
Figure 8.13 Eu vs Dy Lofdal xenotime comparisons to worldwide xenotimes	83
Figure 8.14 Yb vs Gd Lofdal xenotime comparisons to worldwide xenotimes	84
Figure 8.15 Eu vs Gd Lofdal xenotime comparisons to worldwide xenotimes	85
Figure 8.16 Figure 8.16 - xenotime zircon grain from Brown's Range, Australia Cook et al. (2013)	86
Figure 8.17 Th vs Si for a range of Lofdal xenotimes	89
Figure 8.18 Th vs P for a range of Lofdal xenotimes	90
Figure 8.19 Th vs Ca for a range of Lofdal xenotimes	91
Figure 8.19 plot of U/Th against U Kositcin (2003) Wits xenotime vs Area 4 Lofdal xenotimes	91
Figure 8.20 4032 47.56m BSE image magnetite with Th-rich xenotime crowned by apatite	92
Figure 8.21 P site vs Y site apfu 16 oxygens	92
Figure 8.22 Si+Ca+U+Th vs REE+Y apfu 4 oxygens	94
Figure 8.23 *X* monazite/Y T plot of monazite Y limb of the miscibility gap at various pressures	95
Figure 8.24 Vicky Do Cabo's O and C isotope data from Lofdal dykes and plugs	97
Figure 8.25 Y-Ho and Zr-Hf CHARAC behaviour, Bau (1996)	98
Figure 8.26 Zr/Hf versus Y/Ho for Area 4 wholerock data CHARAC range after Bau (1996)	99
Figure 8.27 Hole 4092 189.59m fluorite in high grade intercept	100
Figure 8.28 EDS and CL image of fluorite in Hole 4015 37.30m compared to Do Cabo Type 5 dyke	101
Figure 8.29 Cathodoluminescence spectra of fluorite from VDC type 5 dyke	102
Figure 8.30 Hole 4092 189.80m xenotime associated with pyrite in elevated HREE grade section	106-107
Figure 9.1 suggested model of sequence of REE mineralisation in Area 4	108

LIST OF TABLES

Table 2.1 – List of the REEs partitioned into light, medium, and heavy	8
Table 2.2– List of economically important REE minerals	16
Table 5.1 - Selected holes and from Area 4, Lofdal Namibia	35
Table 5.2 - Specifications of equipment used during core logging	36
Table 5.3 Summary of alteration zone characteristics for 17 holes over 3 adjoining sections	37
Table 6.1 Samples for analysis – codes, location, description, position, analytical techniques	41
Table 7.1 EPMA standard beams conditions and run beam conditions	60
Table 7.2 Nominated thin sections for EPMA standard beams conditions and run beam conditions	61
Table 7.3 Xenotime characteristics over REE enriched intercepts in Area 4	64
Table 7.4 Results from electron microprobe analysis of xenotime composition from Lofdal Area 4	66-67
Table 8.1 Xenotime EPMA analysis data from Brown's Range, Australia for comparison	87
Table 8.2 Experimental results of heating and pressurising huttonite with xenotime.	92

Abbreviations

RE - Rare earth
REE - Rare earth element
REO – Rare earth oxide
LREE – Light rare earth
TREE – Total rare earth elements
TREO – Total rare earth oxide
MREE – Mid rare earth
HREE – Heavy rare earth
Xen – Xenotime
Nb-rutile – Niobium rutile
Bio – Biotite
Phlog – Phlogopite
Synch – Synchysite
Aesch - Aeschynite
Apa – Apatite
Cal – Calcite
Hem – Hematite
Hem – Hematite
Mag – Magnetite
Thor – Thorite
Alb – Albite
Chlo - Chlorite

Fg – fine grained
Vfg – Very fine grained
NRE – Namibia Rare Earths
LHS – Left hand side
RHS – Right hand side
Upr – Upper
Lwr - Lower
PPL – plain polarised light
XPL – Crossed polarised light
CL – Cathodoluminescence
SEM – Scanning electron microscope
EDS – Energy dispersive spectroscopy
EPMA – Electron probe micro-analyser
Vs - Versus

1 INTRODUCTION

1.1 Aims and objectives

Geological observations of Area 4, Lofdal ahead of this study, revealed the presence of complex overprinting relationships between carbonate phases, and multiple alteration events in the basement gneissic rocks, the latter of which typically carries most of the REE mineralisation. It is aim in this study to determine the geological controls of the REE enrichment. Clues to the conditions and generations of fluid that have passed through the system, age and source of REE can be potentially constrained by mineralogical and petrological observation and associated microanalysis. The chief REE mineral is xenotime and constraints on chemical compositional trends in xenotime can provide valuable clues to formational environment and help to delineate differentiation in paragenses. Xenotime has a complex geochemistry with a large number of elements readily substituted into different sites in the crystal structure (as described by Hetherington et al., 2008).

Electron probe microanalysis (EPMA) is used to discern mineral composition and REE partitioning in xenotimes from different mineralised portions of the Area 4 alteration zone, and findings will be coupled herein with in-depth petrological studies of the resource delineation diamond drill core. This will help to answer what are the visual, geochemical and geophysical clues that identify the REE mineralised zones. Is there an alteration halo, for example, associated with the REE mineralisation? If so what does it look like and how widespread is it? Answering the questions will help to evaluate other geologically similar targets both on the Lofdal property, and elsewhere.

1.2 Specific Objectives

- Identify and describe alteration intercepts from 17 drill holes, that intersect the southerly-dipping structure of heavy rare earth (HREE) enriched Area 4, Lofdal
- Select a range of samples from the alteration zone to study REE mineralogy (specifically xenotime), associations and textures via CL, PPL and SEM/EDS that cover the varied character of alteration zone.
- Attempt to marry ICP-MS whole-rock data from Namibia Rare Earths with the mineralogy to better understand the genesis of the Area 4 HREE enrichment, and the economically pertinent phase relationships. Xenotime occurs in a series of parageneses, and it is an objective to constrain the nature of the transporting fluids and depositional environments of the REE minerals.
- Attention will be given to thorium contents, as actinide content in any future mined ore/concentrate has environmental and social implications.

2 OVERVIEW OF RARE EARTH ELEMENTS

2.1 Definition of REEs

According to International Union of Pure and Applied Chemistry (IUPAC) definition, the REEs comprise a total of 17 elements which include yttrium (Y, atomic number 39), scandium (Sc, atomic number 21) and the lanthanide series, consisting of lanthanum (La, 57) through lutetium (Lu, 71) (Figure 2.1). The REEs have been divided into two groups known as light rare earths (LREE) and heavy rare earths (HREE). LREE consist of lanthanum (La), cerium (Ce), praseodymium (Pr), neodymium (Nd), and samarium (Sm). HREE are the remaining lanthanide series which includes europium (Eu), gadolinium (Gd), terbium (Tb), dysprosium (Dy), holmium (Ho), erbium (Er), thulium (Tm), ytterbium (Yb), and lutetium (Lu) – Y is also considered a HREE (Table 2.1). Promethium (Pm, 61) is not included in either division as it neither stable nor long-lived upon formation (Jones et al., 1996).

2.2 Production of REEs

Despite their name the REE are not so "rare" in the earth's crust, and are similar in abundance to nickel or tin, but are rare to be concentrated in enough amounts to be commercially viable deposits. Today, 89% of REEs are mined and processed in China (USGS, 2014). Information regarding China's reserves, production and stockpiles are rarely disclosed by the Chinese authorities. Critically, China restricted the export of rare earth oxides (REO) in 2011 resulting in unprecedented price spike in the rest of the world (ROW). As China has a vertically integrated REE industry, i.e. "mine to magnet", in the near future China may even end up consuming *all* of its production domestically. Considering the aggrandising use and application of REEs by industries around the world it is no surprise that this has led to increased exploration and development of these critical metals to combat the supply restriction. Mountain Pass, California, once a world leader in REE production, closed in 2004 due to unfavourable economics but has now restarted production under the Molycorp (Molycorp, 2014). There has been much speculation around REE exploitation since the Chinese restrictions. Prices spiked to record levels with Dy, for example, up to over US$2500/kg in 2011, but has since settled down to c. US$600/kg level (Prices quoted from May 2014, Argus Metal Pages) – still a good price considering there was no market for Dy a decade before. New sources of REE are being developed at Mountain Pass, USA and Mount Weld, Australia – however both of these deposits are LREE enriched and only contribute a fraction of the demand for HREE after processing. This could signal that LREE could be expected to be in surplus soon, while HREE will remain in deficit for the foreseeable future. HREEs are therefore considered the most critical of all REE, and will be briefly covered in the following sections.

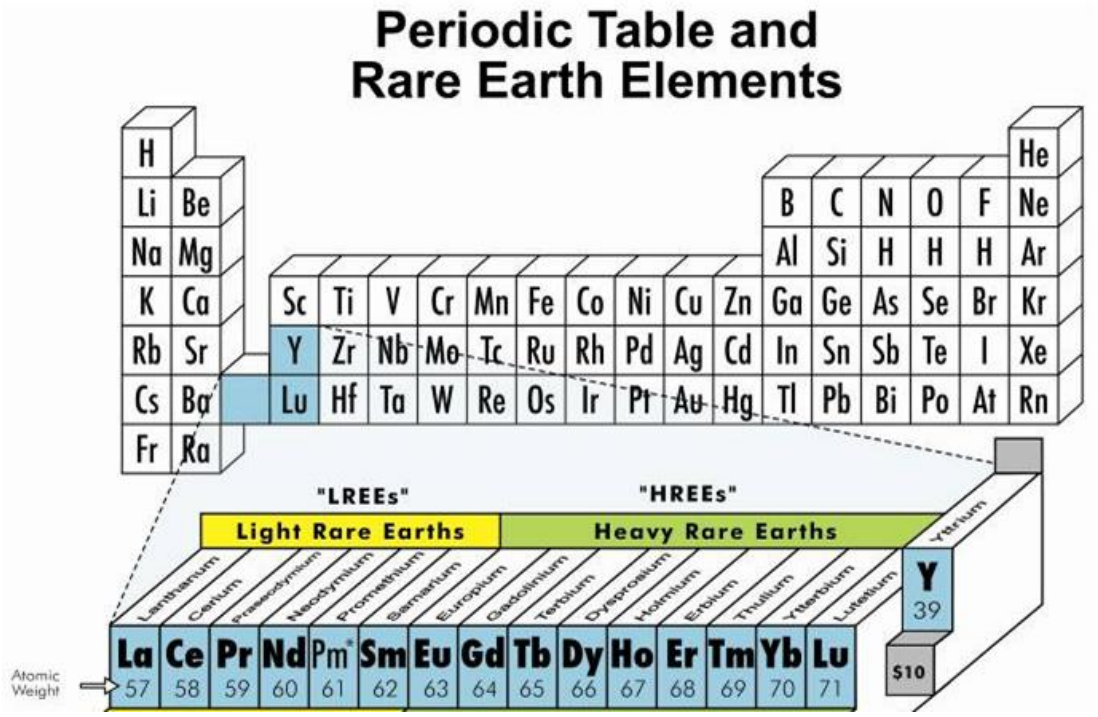

Figure 2.1 –The lanthanides are below Y in the periodic table. Y is classed as an REE because of its similar chemical properties (some workers class Sc as REE) – BGS 2012

Table 2.1 – List of the REEs partitioned into light, medium, and heavy – although today many workers divide between lights (LREEs) and heavies (HREEs). IUPAC definition splits REEs between Sm and Eu – BGS 2012

Element	Type	Symbol	Atomic Weight
Lanthanum	'Light' or 'Ceric'	La	138.92
Cerium		Ce	140.13
Praseodymium		Pr	140.92
Neodymium		Nd	144.27
Samarium	'Medium'	Sm	150.43
Europium		Eu	152.00
Gadolinium		Gd	156.90
Terbium	'Heavy' or 'Yttric'	Tb	159.20
Dysprosium		Dy	162.46
Holmium		Ho	163.50
Erbium		Er	167.20
Thulium		Tm	169.40
Ytterbium		Yb	173.04
Lutetium		Lu	174.99
Yttrium		Y	88.92

2.3 REE applications

LREEs and HREEs have a myriad of uses, most with technological or "enabling" technologies, many of which are burgeoning and rapidly growing "green" applications such as hybrid electric cars and wind

turbines. The highest value sector is that of rare earth permanent magnets (REPMs), the largest growing market segment for REE (Figure 2.2). REPMs are much more powerful than traditional magnets, providing better performance through their smaller size, which has led to miniaturisation, and therefore improved efficiency for many applications. REPMs utilise Nd, Dy, Sm, Pr and Tb – but importantly by utilising alloys of these elements. For example more abundant Nd (a LREE) needs to be utilised alongside less abundant Dy (a HREE) in REPMs in high temperature applications like hybrid car engines, and wind turbines (see figure below) – hence the market concern on Dy supply. It is therefore no surprise that HREE prospects such as Lofdal are attracting attention.

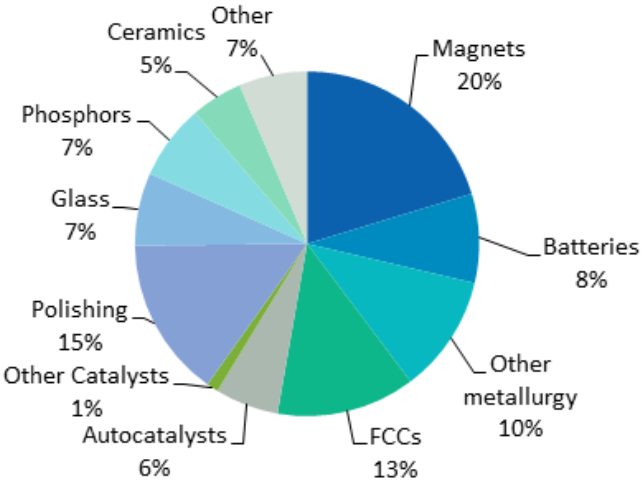

Figure 2.2 Rare Earth Use by application (For 2012) by tonnes. Source: EU Study on critical raw materials (2013) – courtesy of Oakdene Hollins (October 2013).

Dysprosium (Dy) is used with neodymium in magnets that are vital to much modern technology and renewable energy, where Dy is concentrated on the surface of Nd-Fe-B grains. Dysprosium oxide is also used in nuclear reactors to help cool fuel rods to keep the reaction in manageable control. Dy is the problem metal because very few hard-rock sources have ever been put into production outside China (most HREE is won from ion-adsorption clays from SE China). E.g. today electric vehicle (EV) electric motors contain up to 3kg of Nd-Pr, as well as 0.5kg Dy in each vehicle. By 2020 it is forecast that EVs will take up 7% of Nd-Pr and 22.7% of Dy world supply (Oakdene Hollins, 2013).
REE motors in wind turbines contain up to 18 kg of Dy per MW (Oakdene Hollins, 2013). The addition of Dy to NdFeB magnets enables the turbines to operate efficiently at higher temperatures (Figure 2.3). Dy is also an additive to other high temperature applications as demonstrated in Figure 2.4.

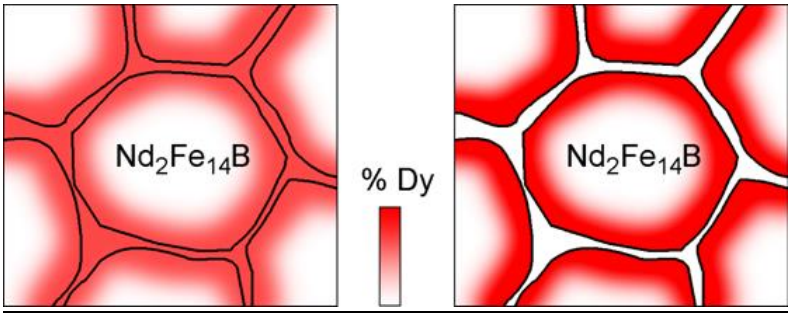

Figure 2.3 Dy is added to REPM to control intergranular structure to counteract problems with eddy currents and resultant overheating (Mann, 2013)

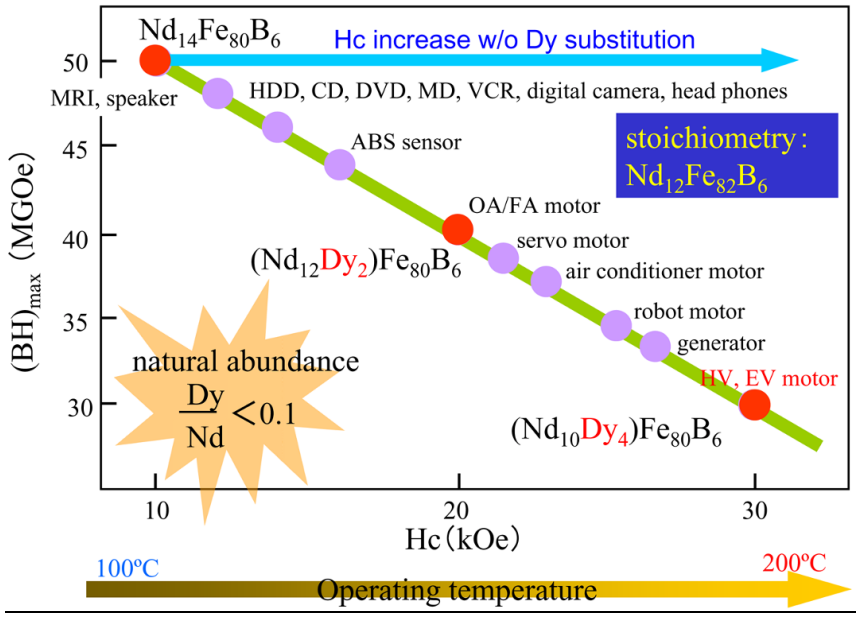

Figure 2.4 Dy substitution into NdFeB magnets (REPMs) by end use (Mann, 2013)

Terbium (Tb) is used in colour television screens as well as solid state hard-drives for computers. Currently, computing speed is limited by conventional hard drives. Solid state hard drives are just now being used by companies such as Apple to dramatically increase computing speed. As production costs are decreased, solid state drives will undoubtedly become the standard. (Oakdene Hollins, 2013).

Europium (Eu) is used in TV screens as well as a doping agent for the plastics used in lasers, and has application for nuclear power, one the priciest REEs ($1000/kg Jan 2014 – USGS).

Yttrium (Y) is used in a variety of application from TV screens to an alloying agent to increase the strength of aluminium and magnesium alloys. It is also used in the polymerization of ethylene vital to the production of plastics. Widespread use as YAG (yttrium garnet) lasers and LED lighting (colouring phosphors). LEDs are seeing increased use in households, and in street lighting slowly eroding the dependence on W-filament bulbs. (Oakdene Hollins, 2013).

2.4 The market demand for REEs

As indicated in the previous section the world needs rare earths to go "green". Usage and market value can be seen in Figure 2.5. However, the US Department of Energy is anticipating a critical shortage of 5 rare earth elements necessary for green technology development and construction. These are Nd, Eu, Tb, Dy and Y – known as the "critical REES" (as plotted in Figure 2.6), and, apart from Nd, are all HREE. Greatest concerns are therefore on the supply of HREE. It is predicted from many quarters, including the EU and US government agencies, that Dy, Tb, Eu, Nd and Y are elements that are facing a critical risk of a supply shortfall until 2015 (Figure 2.7). The criticality of REE is also recognised by the EU and Japan.

Investors are becoming increasingly educated as to the stratification of the REEs in a given deposit, and are beginning to take into account the current and future demand for the *critical* REEs i.e. is a given deposit LREE or HREE enriched. Most REE deposits being readied for production outside of China (i.e. Mountain Pass, Mount Weld) are dominated by LREE. If both Molycorp (MCP:NYSE) and Lynas Corp (LYC:ASX) were in full production by 2015, as their own projections suggest, that would bring approximately 60 thousand tons (Kt) of new TREE production to market. Of that, only about 8 Kt would be Nd, and none of that would be HREEs (IMCOA, 2012). The big issue in REPMs is Dy as it is a vital component alongside Nd, as reviewed above, and demand is only increasing year on year (Figure 2.8).

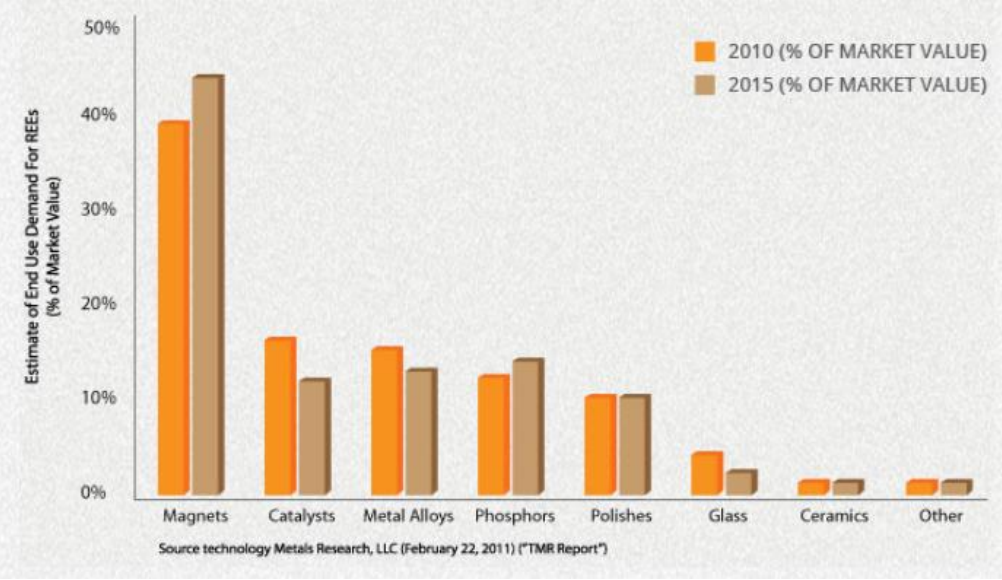

Figure 2.5 Estimated end uses for REEs – US Department of Energy, Technology Metals Research, 2014

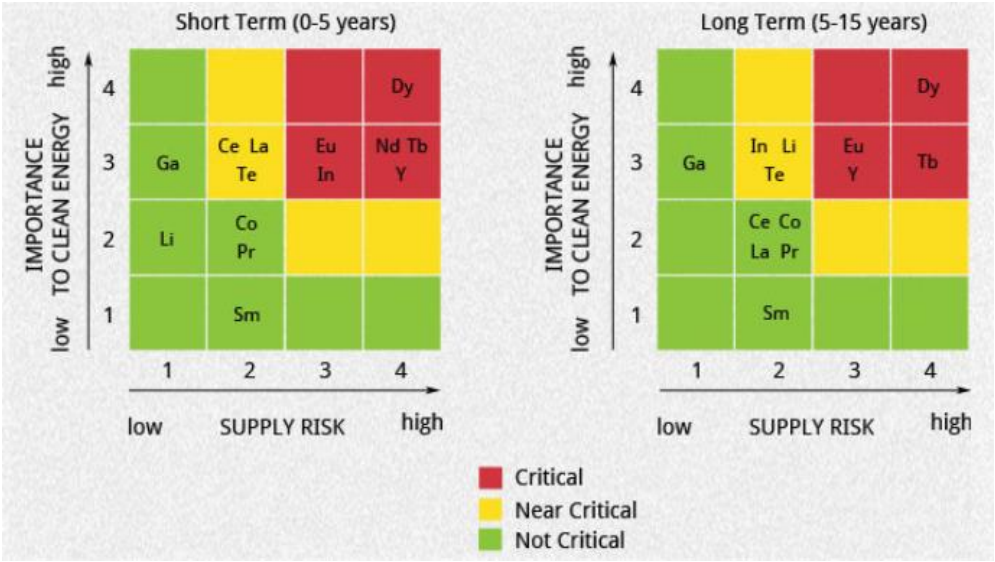

Figure 2.6 – Metal criticality (US Department of Energy, Technology Metal Research LLC 2011)

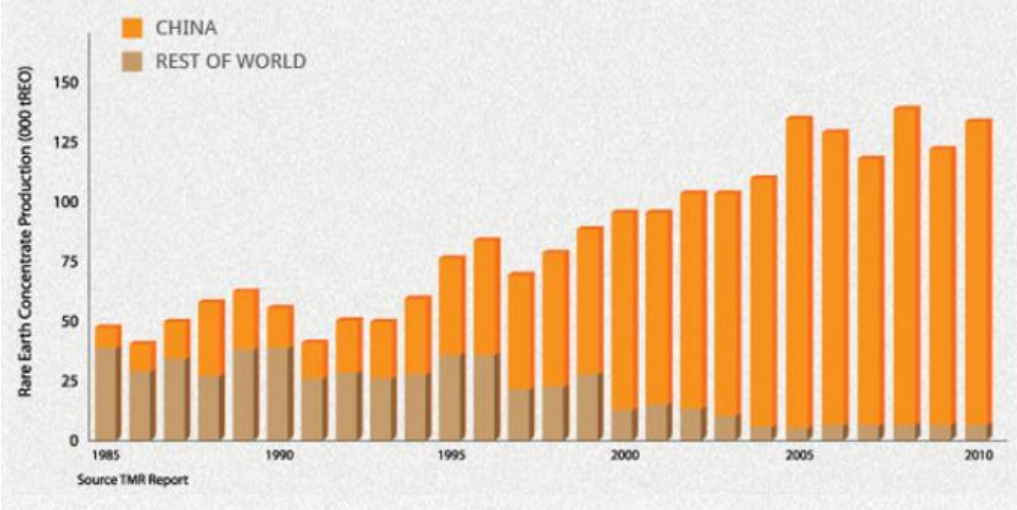

Figure 2.7 Rare earth concentrate production 1985 - 2010 (US Department of Energy, Technology Metals Research, 2014)

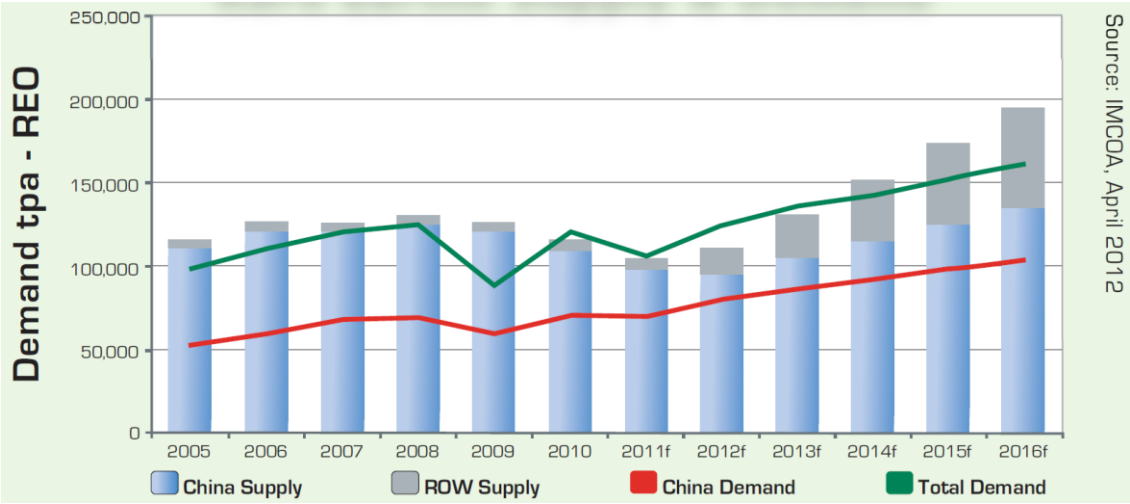

Figure 2.8 - rare earth oxide (REO) supply and demand (IMCOA 2012)

Each potential REE resource is different and therefore the processing routes need to be project specific. Pilot plant studies are an essential element of a "bankable" feasibility study. Many issues need to be accounted for, e.g. REEs are chemically similar so they are difficult to separate, and can't be treated as commodities like classical metals – i.e. they are customer specific. There is usually a long start-up to get a mine operational, and there are limited mining and processing expertise outside China. An important issue is radioactive tailings in the processing of REE ores, notably Th content, and the public perception of the scale of radioactivity which is more scare-mongery than truly quantified risk. Lynas' REE processing plant in Kuantan, Malaysia attracted a lot of protest (BBC, August 2012), but it regarded by the mining industry as the most efficient and cleanest plants of its type in the world, and has been producing RE products since Q1 2013 (Lynas, 2013).

2.5 Location of REE deposits

Although REE accumulations can occur in a variety of terranes from hard-rock anorogenic granites to highly weathered laterites, most REE deposits in the world are intrinsically linked to carbonatites, and they themselves linked to some degree of alkaline intrusive activity (Woolley & Kjarsgaard, 2008). Alkaline intrusives are often enriched in high field strength elements (HFSE) and therefore can host valuable economical concentrations of Th, U, Nb and Zr as well as the REEs. Some carbonatites can be also sources of economic accumulations of P, F and Sr. Based on 527 global occurrences of carbonatite complexes, 90% are stated to have either a magmatic or hydrothermal origin (Woolley & Kjarsgaard, 2008), and dominantly occur in intra-continental settings. Carbonatites are believed to represent either primary magmas derived from partial melting of the mantle, or magmas produced by immiscible separation from, or fractional crystallisation of a primary silicate melt. Lee and Wyllie (1998) and Mitchell and Jambor (1996), state that despite the possibility of primary carbonatite magmas, petrological evidence suggests that carbonatite complexes are most likely derived from alkaline carbonated silicate magmas.

Of the 527 known carbonatite complexes identified by Woolley and Kjarsgaard (2008), 477 (90%) have an igneous association. Of these 477 carbonatite complexes, 84% are magmatic in origin while 16% are identified as of carbohydrothermal in origin. The carbohydrothermal carbonatites are all associated with at least one type of silicate igneous rock, notably nepheline syenites and syenites. Of the magmatic carbonatites, 76% have a diverse range of silicate rock associations. 68 of the 477 carbonatite complexes are associated with phonolite and/or nepheline syenite rocks. It can be inferred that most carbonatite magmas are genetically related to carbonated silicate parental magmas. Lee and Wyllie (1998) used silicate-carbonate-H_2O phase diagrams to show two possible processes of carbonatite formation. They describe a parental carbonated silicate magma following an

evolutionary path of fractional crystallisation, which enriches incompatible carbonate components, and results in a carbonate-rich melt at the silicate-carbonate liquidus boundary. Incompatible REEs can be concentrated in these late carbonaceous fluids. Important REE bearing carbonatite deposits include the huge Bayan Obo deposit in Inner Mongolia (China), the world leader in REE production, and the Sulphide Queen carbonatite of the Mountain Pass district, California.

A diagnostic feature of most carbonatite complexes is the frequent presence of an aureole of metasomatic alteration that develops in the host rocks surrounding carbonatite intrusive bodies. This highly alkaline aureole had led to the description of a rock type called a fenite, a name originating from fenite descriptions at the Fen complex in Norway. Fenitisation refers to the process of alkali metasomatism associated with alkaline silicate and carbonatite magmatism (Le Bas, 2008). The importance of fenitisation at Lofdal will be discussed later.

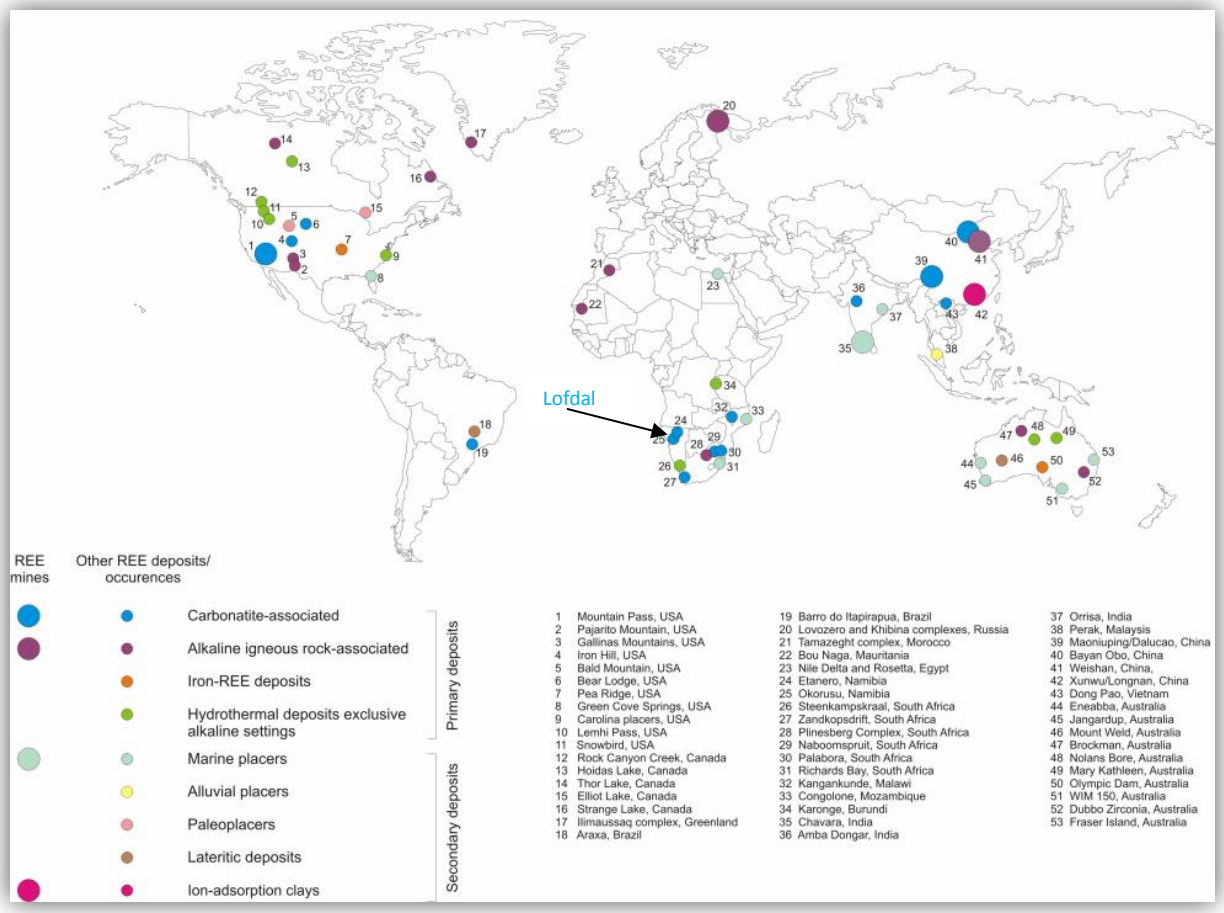

Figure 2.9 – World distribution of notable REE deposits (Walters et al., 2010)

Figure 2.9 displays the world distribution of notable REE deposits, the majority of which are LREE enriched. Much speculation has arisen around many of these prospects since the Chinese quota restrictions, with most not likely to see development for many years.

Examples of HREE prospects outside of China close to production include Bokan Mountain (Ucore Rare Metals Inc., 2014) in Alaska and Norra Karr (Tasman Metals Ltd., 2014) Sweden. These deposits are being developed to produce 3,900 t/a and a little less than 6,000 t/a, respectively. Bokan would produce 120 t and Tasman 350 t of Dy per year at those levels. Mineralogy dictates the LREE:HREE ratio in a given deposit – for example, Lynas' Duncan deposit and the Brown's Range deposit, both in Australia, when put into production, could be a major HREE source as both deposits have xenotime as their major HREE bearing mineral. However, deposits are hampered by processing hurdles of one kind or another– e.g. Norra Karr's REE budget is largely locked within the mineral eudialyte – a REE bearing Zr silicate yet to be proved to be economically extractable. Some REE bearing minerals are in acid-soluble mineral phases, but may be hampered by small grain size, or have an association with deleterious minerals such as thorite. Mineralogy is key to the processing route for any REE deposit, and ultimately its success. The REE can be locked up in a complex Zr-silicate like eudialyte, or the REE distributed between a range of minerals in a given deposit from silicates, to phosphates which would require different processing routes. This leads nicely into the following section, the mineralogy of REE.

2.6 REE mineralogy

Carbonatites are well known to be enriched in a variety of elements (Th, U, Nb, P, F, Sr) including both light and heavy REEs. Fractionation of light REE and heavy REE occurs due to the progressive decrease in ionic radius from light to heavy elements – known as the "lanthanide contraction" (Woolley & Kempe, 1989). However, differing crystal lattice arrangements cause preferential partitioning of LREEs or HREEs into certain minerals. Garnet, for example, strongly favours HREEs; consequently, magmas derived from garnet-bearing sources are relatively depleted in HREEs if garnet was refractory during melting. Thus, specific minerals can be valuable tools for understanding REE concentrations in igneous rocks, and can provide information about magma source region mineralogy. Although both REE groups are enriched in carbonatites, most carbonatite complexes *usually* have high LREE:HREE ratios (Winter, 2001; Bell, 1989). The rare earth minerals of these elements occur in a wide range of mineral types including halides, carbonates, oxide, phosphates, and silicates (Table 2.2). Over 200 minerals have been identified as containing REE, but only a few possess REE in economic recoverable amounts – for example, LREEs from monazite and bastnäsite, and HREE from xenotime, although these will have varying proportions of the lanthanide suite, but are usually biased to LREEs or HREEs respectively.

Table 2.2– List of economically important REE minerals (BGS 2012)

Mineral	Formula	Approximate REO %
Aeschynite-(Ce)	$(Ce,Ca,Fe,Th)(Ti,Nb)_2(O,OH)_6$.	32
Allanite-(Ce)	$(Ce,Ca,Y)_2(Al,Fe^{3+})_3(SiO_4)_3OH$.	38
Apatite	$Ca_5(PO_4)_3(F,Cl,OH)$	19
Bastnäsite-(Ce)	$(Ce,La)(CO_3)F$	75
Brannerite	$(U,Ca,Y,Ce)(Ti,Fe)_2O_6$	9
Britholite-(Ce)	$(Ce,Ca)_5(SiO_4,PO_4)_3(OH,F)$	32
Eudialyte	$Na_4(Ca,Ce)_2(Fe^{2+},Mn,Y)$ $ZrSi_9O_{22}(OH,Cl)_2$(?).	9
Euxenite-(Y)	$(Y,Ca,Ce,U,Th)(Nb,Ta,Ti)_2O_6$	24
Fergusonite-(Ce)	$(Ce,La,Nd)NbO_4$	53
Gadolinite-(Ce)	$(Ce,La,Nd,Y)_2Fe^{2+}Be_2Si_2O_{10}$.	60
Kainosite-(Y)	$Ca_2(Y,Ce)_2Si_4O_{12}CO_3.H_2O$.	38
Loparite	$(Ce,La,Na,Ca,Sr)(Ti,Nb)O_3$	30
Monazite-(Ce)	$(Ce,La,Nd,Th)PO_4$	65
Parisite-(Ce)	$Ca(Ce,La)_2(CO_3)_3F_2$.	61
Xenotime	YPO_4.	61
Yttrocerite	$(Ca,Ce,Y,La)F_3.nH_2O$.	53
Huanghoite-(Ce)	$BaCe(CO_3)_2F$.	39
Cebaite-(Ce)	$Ba_3Ce_2(CO_3)_5F_2$.	32
Florencite-(Ce)	$CeAl_3(PO_4)_2(OH)_6$.	32
Synchysite-(Ce)	$Ca(Ce,LA)(CO_3)_2F$.	51
Samarskite-(Y)	$(Y,Ce,U,Fe^{3+})_3(Nb,Ta,Ti)_5O_{16}$.	24
Knopite	$(CaTi,Ce_2)O_3$	na

REE bearing minerals directly reflect the distribution of REEs during magmatic or carbohydrothermal crystallisation. This in turn elucidates the processes of formation and genetic relationships within surrounding rocks. Area 4 at Lofdal, Namibia is enriched in HREEs, and although a suite of RE minerals is known to occur, xenotime occurs as the chief HREE ore mineral (~90% REE locked in xenotime from metallurgical test work by Mintek, 2013).

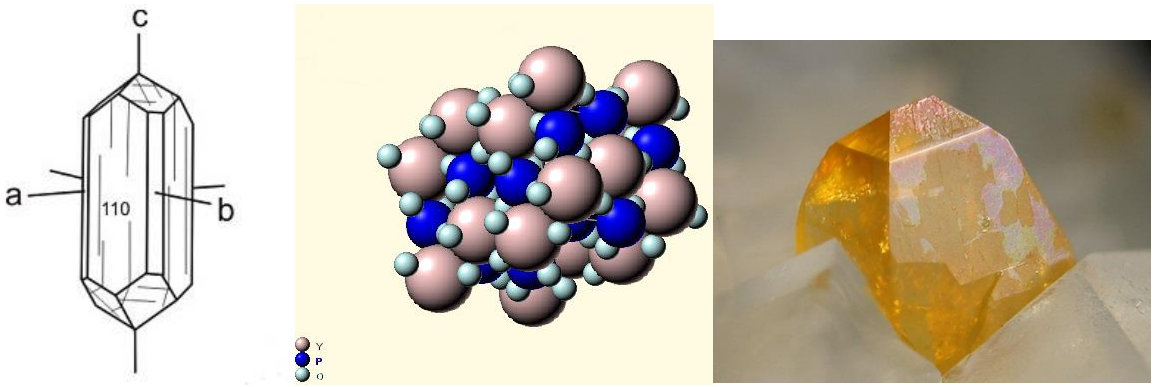

Figure 2.10 Xenotime structure, and crystal from Trimouns, France – www.webmineral.com (1, 2) & www.mindat.org (3) from left to right respectively

Xenotime was discovered in 1832 at Hidra, Norway (the mineral's type locality), and is a tetragonal mineral (space group I41/amd) with a zircon-type structure (Figure 2.10). Specific gravity ranges from 4.4–5.1. Chemically the mineral is characterised by an ideal formula of ATO_4 where A represents yttrium (Y^{3+}) and T a tetrahedrally coordinated atom of phosphorous (P). Yttrium resides in an eight oxygen coordinated polyhedra characterised by two sets of four equivalent bond distances oriented orthogonal to each other forming a dodecahedral cation site (Buck et al., 1999). Because of their similar ionic radii, heavier REE may substitute for Y. Simple isostructural substitution is most favourable with the slightly smaller HREEs (Gd to Lu). Y concentration in xenotime is empirically 60%, but is usually more like 50% with the other 10% made up of mid to heavy lanthanides (Buck et al., 1999). The even-numbered lanthanides (such as Gd, Dy, Er, or Yb) each being present at about the 5% level, and the odd-numbered lanthanides (such as Tb, Ho, Tm, Lu) each being present at about the 1% level within in a *typical* xenotime. Typically dysprosium is usually the most abundant of the even numbered heavies, and holmium is the most abundant of the odd numbered heavies. The lightest lanthanides are generally better represented in xenotime than the heaviest lanthanides are in monazite it is noted, so it is not unusual for xenotime to host variable amounts of minor LREE (Ce-Nd) and MREE (Sm-Gd).

The REE budget in xenotime varies in proportion, but it worth noting that other similarly sized elements substitution into either the A or T sites that *aren't* REE. Constraints on chemical compositional trends in xenotime can provide valuable clues to the formational environment and help delineate differentiation in paragenses. Indeed, xenotime has a complex geochemistry with a large number of elements readily substituted into different sites in the crystal structure (Hetherington et al., 2008).

Of concern and interest, to both ore genesis geoscientists and prospective mining companies alike, is the association of the radioactive actinides elements (namely U and Th) incorporating, and associating with REE bearing minerals, especially monazite, but also, and relevant to this study, with xenotime.

Uranium can occur in xenotime at concentrations ranging from low-ppm level up to several wt.%, forming a solid solution with coffinite ($USiO_4$), via $[Y][PO_4] \leftrightarrow [U][SiO4]$ substitution (Förster, 2006; Hetherington et al., 2008). Xenotime also forms a solid solution with thorite ($ThSiO_4$) via $[Y]\ [PO_4] \leftrightarrow [Th][SiO_4]$ substitution (Förster, 2006; Hetherington et al., 2008). U and Th concentrations have been shown to be significantly lower in hydrothermal xenotime; other types of xenotime generally returning extremely high U and Th (4.22 and 3.50 wt.%) concentrations .

However, while xenotime may contain significant amounts of thorium or uranium, the mineral rarely undergoes metamictisation like titanite and zircon. With its relative high U content and low initial Pb concentration, xenotime is ideal for U–Pb geochronology. F has been shown to enter the T site, as well as Si, at the Pitinga Sn/REE deposit in Amazonia, Brazil to cause unit cell contractions (Pereira, 2012).

The structural relationship between xenotime and zircon is reflected by their occurrence as twinned crystals or intimate overgrowths of one another in pegmatites, evolved granites, but for our attention here, particularly in carbonatites and their metasomatised host rocks as seen at Lofdal (Wall et al., 2008). Recently this association has been also noted from the Browns Range, Northern Territory, Australia (Cook et al., 2013).

3 GEOLOGY OF THE STUDY AREA

The study area of this project is Lofdal 491 farm, 35km northwest of the town of Khorixas in Damaraland, Kunene Region, Namibia and is characterised by a number of discrete alkaline and carbonatite intrusions and associated alteration zones, all harbouring REE mineralisation of variable enrichment.

3.1 Regional geology

The alkaline suites of rocks currently being explored at Lofdal occur in inliers of the Congo Craton within the volcanic and sedimentary rocks of the Damara Orogen (Figure 3.2) in north-central Namibia. There are three exposed inliers known as Kamenjab, Braklaagte, and Welwitschia. The Welwitschia inlier is underlain mainly by the Huab Metamorphic Complex (HMC), which is Mokolian in age (2Ga). It is this unit that was intruded by the Oas Quartz Syenite and what is referred to as the Lofdal Intrusive Complex at about 750 Ma. The HMC was originally described by Frets (1969) and described as being composed predominantly of leucocratic gniesses containing layers of quartzite, mica schist, and amphibolites. On the basis of the age of the intruding Fransfontein granite, which is dated at approximately 1700 Ma, the age of HMC is estimated at between 1.8-2.0 Ga (Frets, 1969) and is thought to have been metamorphosed to amphibolite grade and intensely deformed prior to intrusion of the Fransfontein Granite (FGS). The granite (FGS) is exposed as an intrusion in the northern section of the Welwitschia inlier, and is coarsely-grained consisting of quartz, albite, and microcline with minor biotite, chlorite, magnetite, and other accessories, and can be deemed as the source of deformed granite pegmatite found in gneisses in Area 4. The granite is seen in contact with schistose and foliated gneisses and metasediments of the older HMC.

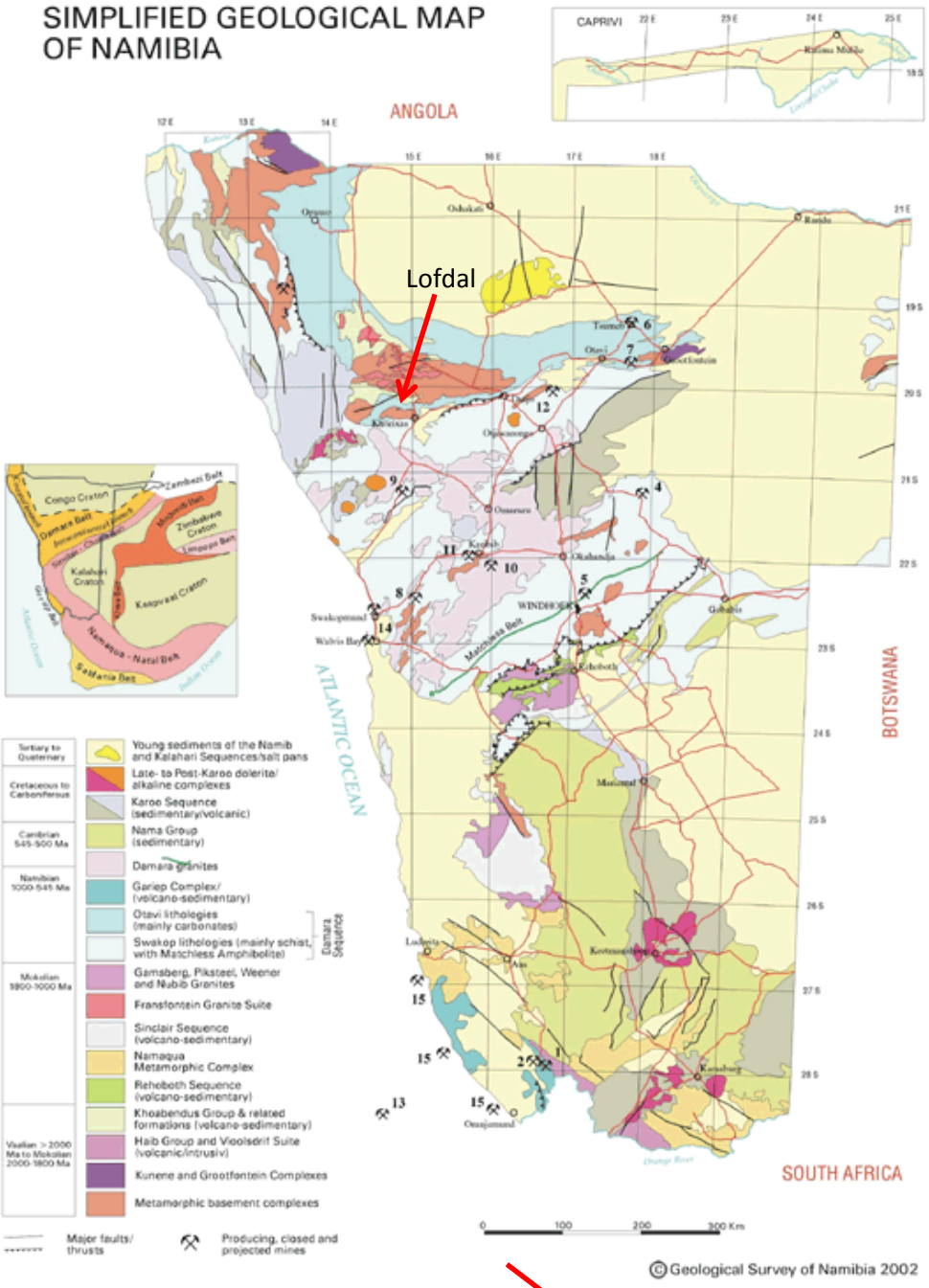

Figure 3.1 – Geological map of Namibia– Courtesy of Geological Survey of Namibia (2002)

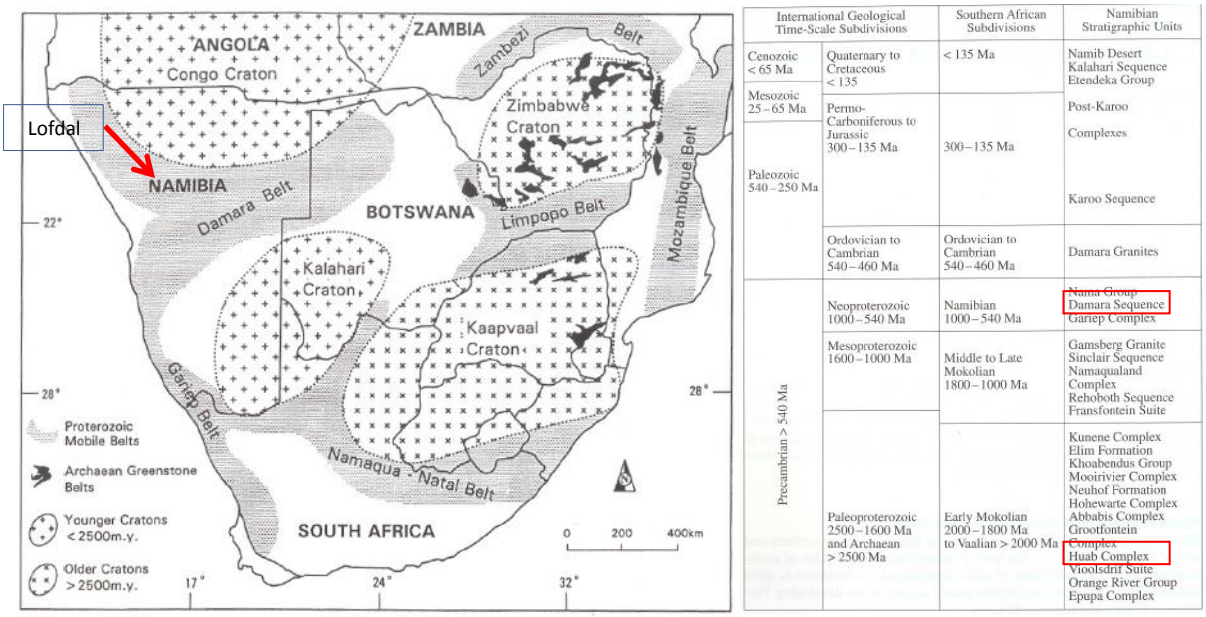

International Geological Time-Scale Subdivisions		Southern African Subdivisions	Namibian Stratigraphic Units
Cenozoic < 65 Ma	Quaternary to Cretaceous < 135	< 135 Ma	Namib Desert Kalahari Sequence Etendeka Group
Mesozoic 25 – 65 Ma	Permo-Carboniferous to Jurassic 300 – 135 Ma	300 – 135 Ma	Post-Karoo Complexes Karoo Sequence
Paleozoic 540 – 250 Ma	Ordovician to Cambrian 540 – 460 Ma	Ordovician to Cambrian 540 – 460 Ma	Damara Granites
Precambrian > 540 Ma	Neoproterozoic 1000 – 540 Ma	Namibian 1000 – 540 Ma	Nama Group Damara Sequence Gariep Complex
	Mesoproterozoic 1600 – 1000 Ma	Middle to Late Mokolian 1800 – 1000 Ma	Gamsberg Granite Sinclair Sequence Namaqualand Complex Rehoboth Sequence Fransfontein Suite
	Paleoproterozoic 2500 – 1600 Ma and Archaean > 2500 Ma	Early Mokolian 2000 – 1800 Ma to Vaalian > 2000 Ma	Kunene Complex Elim Formation Khoabendus Group Mooirivier Complex Neuhof Formation Hohewarte Complex Abbabis Complex Grootfontein Complex Huab Complex Vioolsdrif Suite Orange River Group Epupa Complex

Figure 3.2 – Southern Africa cratons and stratigraphic column - Geological map of Namibia– Geological Survey of Namibia (2002)

Through U/Pb dating methods the FGS was imprecisely dated with two discordia, giving ages of 1871±30Ma and 1730±30Ma (Frets, 1969; Burger et al., 1976) and allowed for the relative dating of the HMC.

The Naauwpoort volcanic sequence rests unconformably on intrusions within the deformed basement gneisses of the HMC (Frets, 1969). The volcanics were extruded during intra-continental rifting, producing K-rich and Na-rich lavas between 820 to 730 Ma (Miller, 2008), an event contemporaneous to the magmatism of the Lofdal Intrusive Complex, as indicated by isotopic evidence aging the complex at c.750 Ma (Do Cabo, 2013). The Damara Orogenic Suite formed during the tectonic sequence involving continental rifting, spreading, passive continental margin formation, mid-ocean ridge formation, oceanic seafloor subduction, and continental collision of the Congo and Kalahari Cratons (see Figure 3.3). The resulting closing of the Damara basin in the late Proterozoic by subduction beneath the Congo Craton led to the metamorphism and deformation of the Damara stratified rocks, as observed from fieldwork of Frets (1969), and Miller (2008). A model of the evolution of the Damaran Orogen is displayed in Figure 3.3.

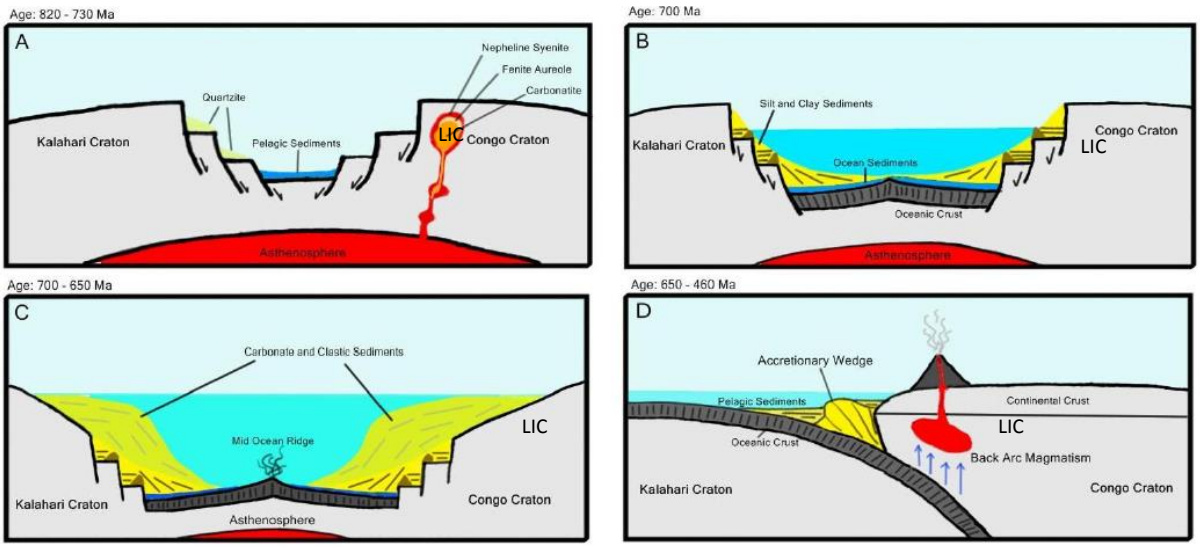

Figure 3.3 – The Evolution of the Damara Orogen. (A) Rifting initiated between the Kalahari and Congo cratons, followed by the deposition of sediments, and intrusions of carbonatitic and alkaline silicate bodies such as the Lofdal Intrusive Complex (LIC). (B) Development of an ocean basin and deposition of shallow marine sediments. (C) Formation of a mid-ocean ridge and eruption of shallow marine basalts. (D) Subduction initiation beneath the Congo craton resulting in closing of the Damaran Ocean basin and Continental collision between the Congo and Kalahari cratons (Image modified after Schneider, 2008).

3.2 Local geology

As outlined in Section 3.1, the Lofdal Intrusive Complex (LIC) is a Pan-African (ca 760 Ma) alkali complex intruding 2Ga metamorphic rocks on southern edge of Congo Craton.

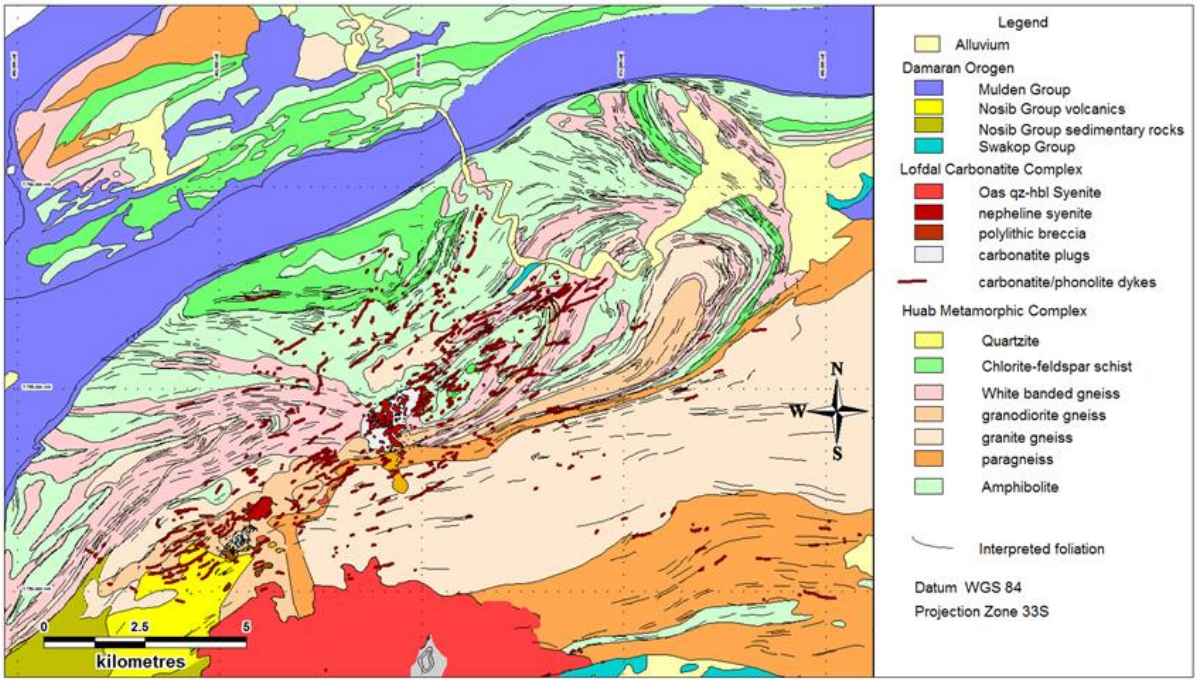

Figure 3.4a - Geology of the Lofdal area, NW Namibia (1:250,000) – (NRE 2012)

The LIC is centred on the Lofdal 491 farm, 35km northwest of the town of Khorixas in Damaraland, Kunene Region, Namibia and is characterised by a number of discrete intrusions of syenite, nepheline syenite, phonolite dykes, diatreme breccias, and carbonatite plugs and dykes (Figure 3.4a

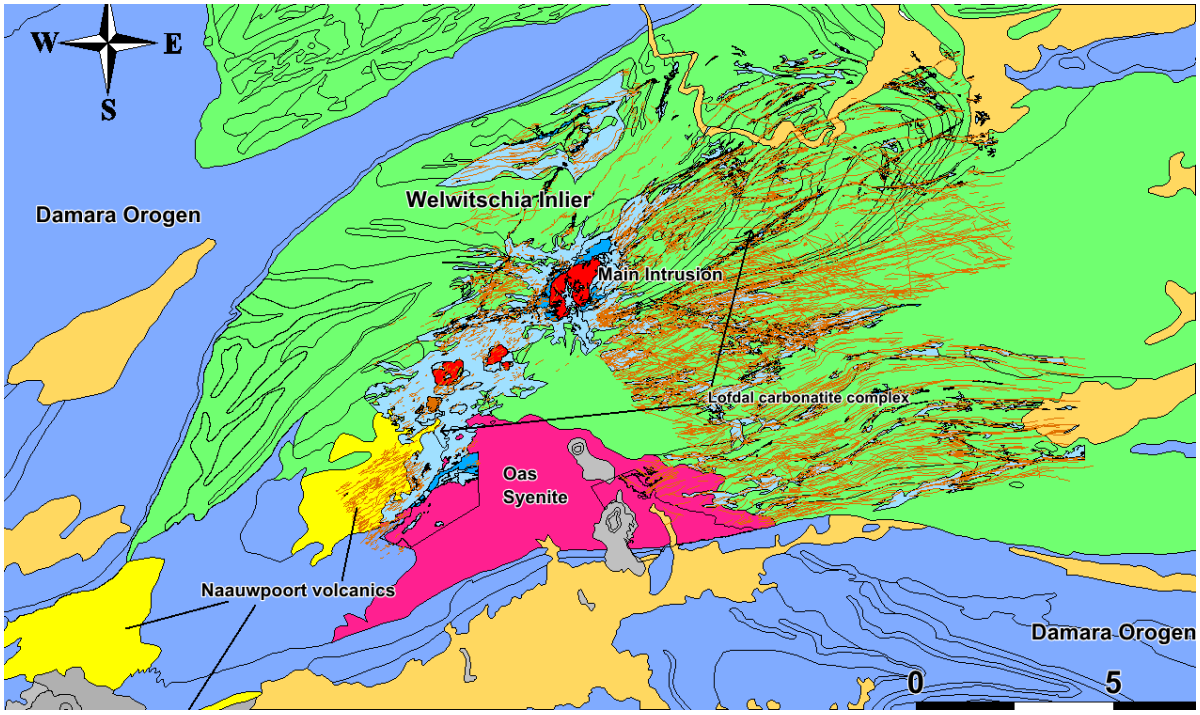

Figure 3.4b - Geology of the Lofdal area, NW Namibia (1:250,000) – (NRE 2014)

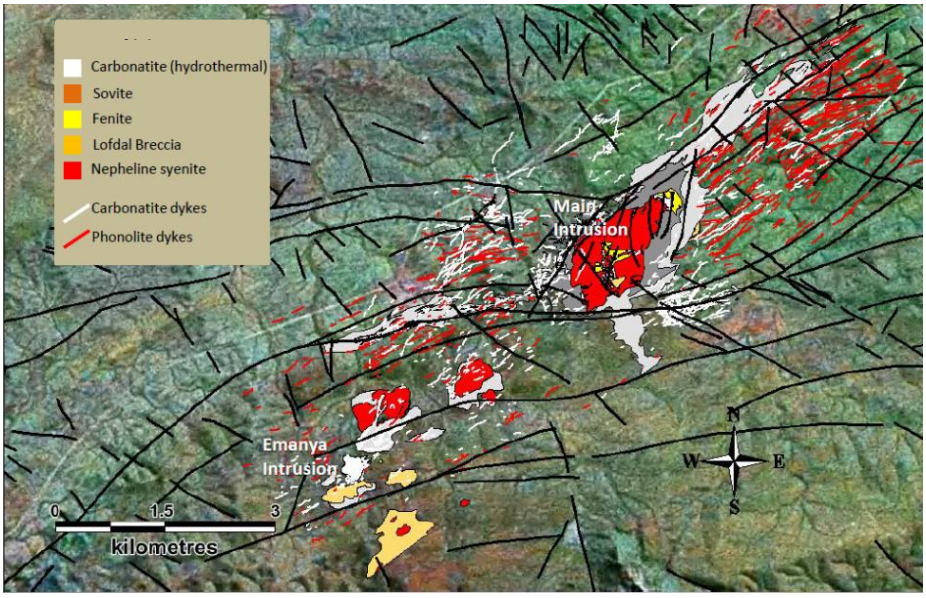

Figure 3.5 Map showing intrusives of the Lofdal Igneous Complex & the addition of structural alignments (NRE 2012)

and b) intruding HMC host rocks. These intrusive units are also related to a widespread area of phonolite and carbonatite dykes (over an area of nearly 200 km^2) (Do Cabo, 2013), and hydrothermal alteration (Swinden and Siegfried, 2012). The Lofdal nepheline syenites occur in a series of genetically and geographically related satellite plugs, with a main 2km^2 plug located in the south-eastern part of the complex (Frets, 1969). These plugs and dykes exploited basement structures hence the NE-SW orientations (Figure 3.5). Later referred to as the Bergville Dyke Swarm (Miller, 2008), the dykes are roughly parallel trending NNE to NE, range from 20 cm to 8 m in width, and cover an area of 20 km by 6 km, including phonolite, trachyte, lamprophyre, and carbonatite. Contact relationships indicate that

the intrusion of several plugs of nepheline syenite and phonolite dykes marked the initial stages of magmatism; this was followed by over-pressuring of the syenitic magmas which led to brecciation of syenites and basement rocks of the HMC (Swinden and Siegfried, 2012). The later stages of magmatism involved the intrusion of two plugs of carbonatite into the nepheline syenite bodies; this was accompanied by carbonatite dykes, which are found adjacent to or overprinting phonolite dykes (Swinden and Siegfried, 2012). The cross-cutting of the siliceous dykes by carbonatite, indicates that the carbonatite dykes are the youngest intrusion in the immediate area (Wall et al., 2008). The Oas Syenite occupies an area of 20 km^2 immediately to the south of the Lofdal project area. It is the largest alkali silicate body associated with the Lofdal Intrusive Complex. The mineralogy of the Oas Syenite was first described by Frets (1969) as being a dominantly coarse-grained, alkali feldspar, sodium plagioclase, hornblende and quartz syenite with apatite and titanite as important accessory minerals. The Oas syenite has been dated at 757 +/-2 Ma (Hoffman et al., 1996), and 758 +/-4 Ma (Jung et al., 2007).

The “Main Intrusion” exposes the top of calcite carbonatite (“sovite”) magma chamber, where it intrudes a pre-existing nepheline syenite plug, as was originally mapped by Frets in 1969. Recent mapping has shown that there are several other satellite intrusions of nepheline syenite within the project area. These intrusions have been dated using U/Pb in magmatic titanite as 754 +/- 8 Ma (Jung et al., 2007). The nepheline syenites at Lofdal have been described by O’Connor (2011). Their typical mineralogy includes coarse-grained or interstitial matrix filling alkali feldspar, sericite, biotite plagioclase, and cancrinite, as a pseudomorph replacing nepheline. Cross cutting relationships indicate that the emplacement of these bodies pre-dated dyking, brecciation, and carbonatite intrusion, thus they represent the earliest component of the alkaline magmatic series (Swinden and Siegfried, 2012). An extensive suite of carbonatite dykes accompanied the intrusion of the Main and Emanya plugs, and exploited the same structures as the earlier phonolites. Importantly the carbonatite dykes are enriched in rare-earth elements (REE), and in some cases unusually high ratios of heavy REE to light REE. Dykes vary in width from 0.5 cm and 5 m, but some are up to 25m wide and extend for several kms.

Previous studies (Kaul, 2010 and Do Cabo, 2013) of the nepheline syenites, phonolites, and carbonatites at the Lofdal intrusive complex have suggested that most of the REE-mineral accumulations are concentrated in late carbonatite dykes and in metasomatised (or fenite) boundary zones. Kaul (2010) identifies a more moderate LREE:HREE ratio in these dykes suggesting that late stage hydrothermal activity may have caused a HREE enrichment; if this is the case then questions surround the mechanisms that preferentially concentrate and deposit the HREE mineralisation.

Notably, carbonatite dykes are widespread, and exhibit considerable variability in geological and geochemical characteristics, generally regarded as late magmatic to hydrothermal as described by Do Cabo (2013). An important factor in hydrothermal alteration of basement fault zones is that they have undergone fenitisation followed by brecciation, and are characteristic of mineralised structures seen in Area 4, outlined in Chapter 4 onwards.

3.3 Accumulations of REE at Lofdal

It has been indicated that early intrusive/hydrothermal carbonatite phases are LREE-rich; late hydrothermal phases are remarkably HREE-enriched, most HREE residing in xenotime (c. 92% of the HREE deportment – NRE, 2013), and this constitutes the principal exploration target at Lofdal. It has been argued that the mineralisation was initially LREE-rich during magmatic and early hydrothermal stages but evolved to unusually HREE-rich mineralization during late hydrothermal stages of the complex's evolution (Do Cabo, 2013). It is also suggested that the Lofdal Igneous Complex was HREE enriched from early on indicated from U-Pb dating of xenotime by Wall, 2008 with ages of 765 ± 16 Ma. There are contrasts at Lofdal, for example the magmatic Emanya Plug is LREE enriched, yet some HREE carbonatite dykes appear both magmatic and hydrothermal in origin. HREE-enrichment or "corridors" are distributed along linear trends that coincide with first and second order basement structures, and that HREE-enrichment is systematically related to structures that have extensive hydrothermal alteration as demonstrated in Figure 3.6.

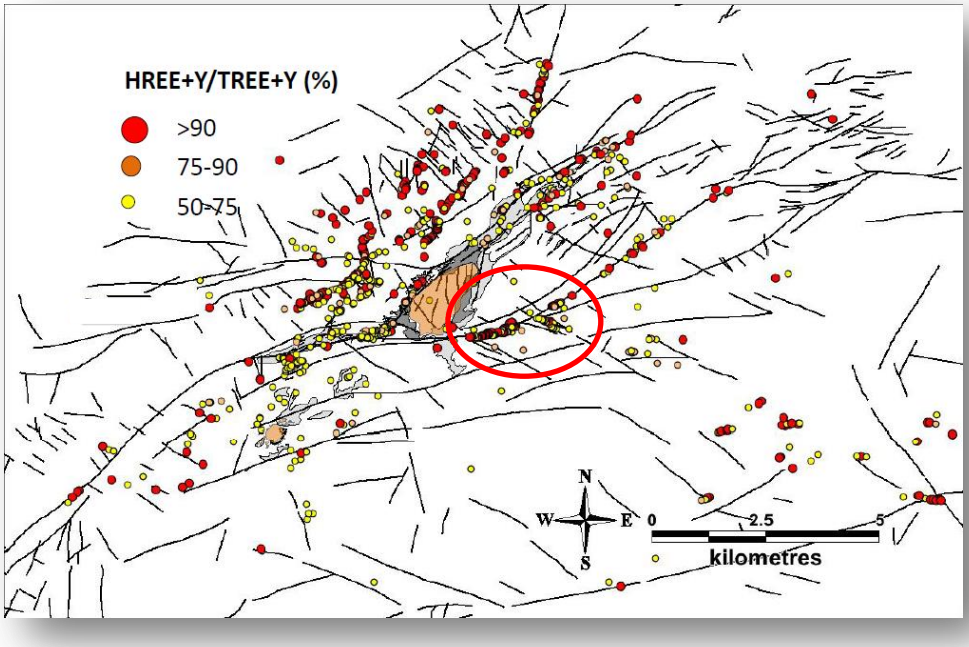

Figure 3.6 – HREE concentration results around the Main Intrusion, Lofdal, Namibia (centre) from surface sampling, Area 4 circled red – NRE 2012

4 RESOURCE DELINEATION of AREA 4

4.1 Introduction

Lithogeochemistry has been the basic exploration technique used at Lofdal and has allowed target definition and identification of priority targets for resource definition by Namibia Rare Earths since 2010. The extent of the Lofdal Igneous Complex is defined by a district-scale Th radiometric anomaly (Figure 4.1). 100 m traverses sampled mainly carbonatite dykes totalling 3700 samples over two sampling campaigns. As of November 2013 Area 4, Lofdal became a CIM NI 43-101 compliant REE resource, details of which are outlined in the following section.

4.2 Drilling campaigns, sampling and NI 43-101 compliant resource

In 2011 an exploration drilling program intersected significant REE mineralisation over a 650m strike length in Area 4. This instigated a mineral resource drilling program to target and delineate the HREE mineralisation. A radiometric anomaly (Th airborne) survey and lithogeochemical sample surveys helped plan the grid for the definition drilling collars (Figure 4.2). The drilling program focused on the first 75 vertical meters of the zone with 10 selected step back holes to 100-150 vertical meters. The total meters drilled for the initial Area 4 resource estimate was 9,520m of NQ diamond core, plus an additional 310m of diamond core available for metallurgical test work. Surface sampling of 13 trenches comprising 870m was also incorporated into the Area 4 resource database.

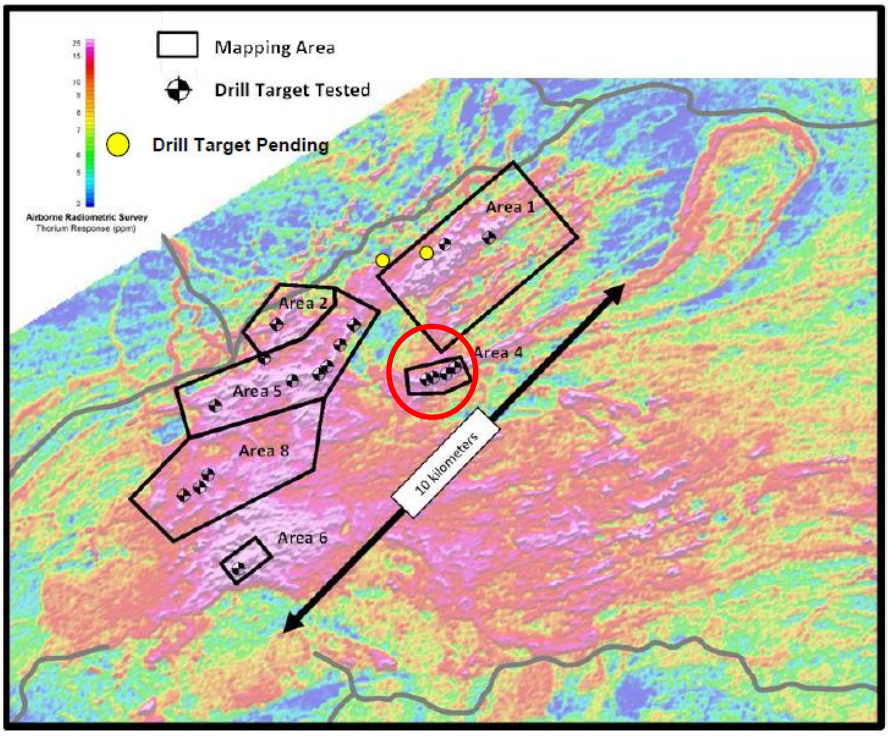

Figure 4.1 Airborne radiometric survey image showing 200km^2 extent of the Lofdal Igneous Complex showing priority drill targets tested in 2011, and the location of Area 4 (NRE 2012)

38 holes where sunk to test the carbonatite-bearing fault zone in Area 4. All the holes were drilled at an azimuth of 345 degrees and inclined between -55 and -75 degrees. Intercept widths are reported as down the hole widths and are not necessarily true widths. Interpreted dips of the mineralised zones vary from 45 to 80 degrees and all holes were drilled at -55 degrees.

The structure was previously identified as a major sinistral basement fault, and drilling confirmed that this zone is indeed a significant fault zone – blocky ground, abundant broken core, fault gouge, core is highly oxidized to significant depths. The zone is easily identified in core by alteration (strong albitisation, carbonatisation). The zone locally contains significant sulphides (mainly pyrite) disseminated and in veins, as well as local white dolomite, purple fluorite and magnetite. Assays returned good values over significant widths with exceptional HREE enrichment. The drill results confirmed that the zone exhibits exceptional HREE enrichment of 70 to 95% over drill widths of 3 to 28 meters with average grades of between 0.2 to 1.4% total rare earth oxides (TREO). Within this zone there are higher grade intervals over drill widths of 0.35 to 7.0 meters with average grades of 1.0 to 6.2% TREO with up to 98% heavy rare earth enrichment.

Alteration zones in Area 4 are characterized by intense albitisation, with widespread crackle brecciation and carbonatisation (carbonate infusion) – locally cut by intense shear zones, late HREE enriched fluids perhaps utilising these shear induced pathways. The alteration zone appears to follow a regional southerly-dipping structure.

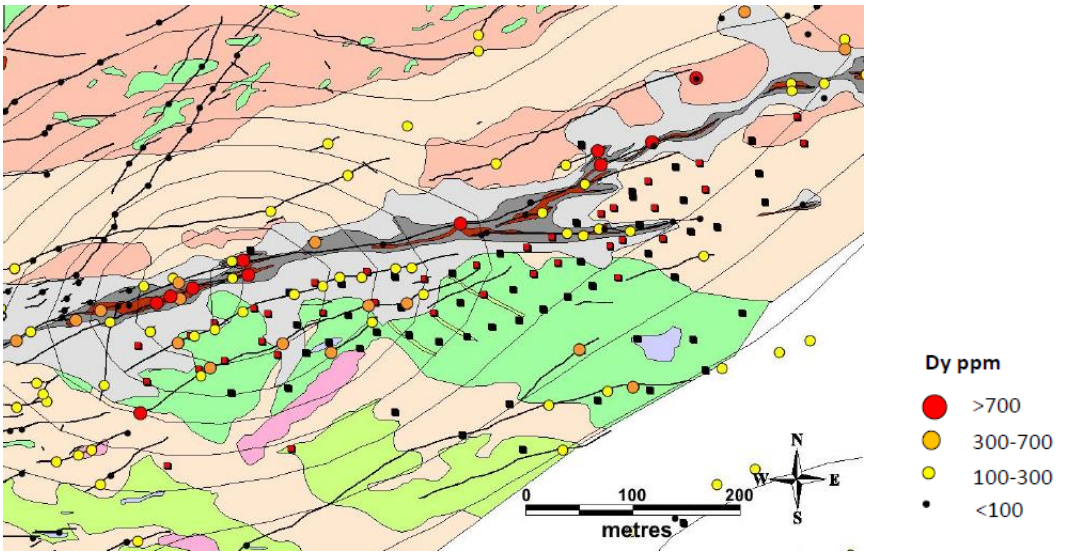

Figure 4.2 – Positions of definition drilling collars shown by red and black squares, Area 4 Lofdal (NRE 2012)

Typically in many holes it has been seen that the hangingwall zone is dominated by carbonatite, with the main zone of the HREE mineralisation dominated by albite, a rock herein referred to as “albitite”, and the highest grades (red colour bars in Figure 4.3) associated with complex overprinting alteration.

Importantly the alteration zone is wider than mineralized zone (Figure 4.3). The mineralized alteration tends to have distinct colour anomaly in drill core – but not always. This report focuses upon the holes outlined in the grid in Figure 4.4.

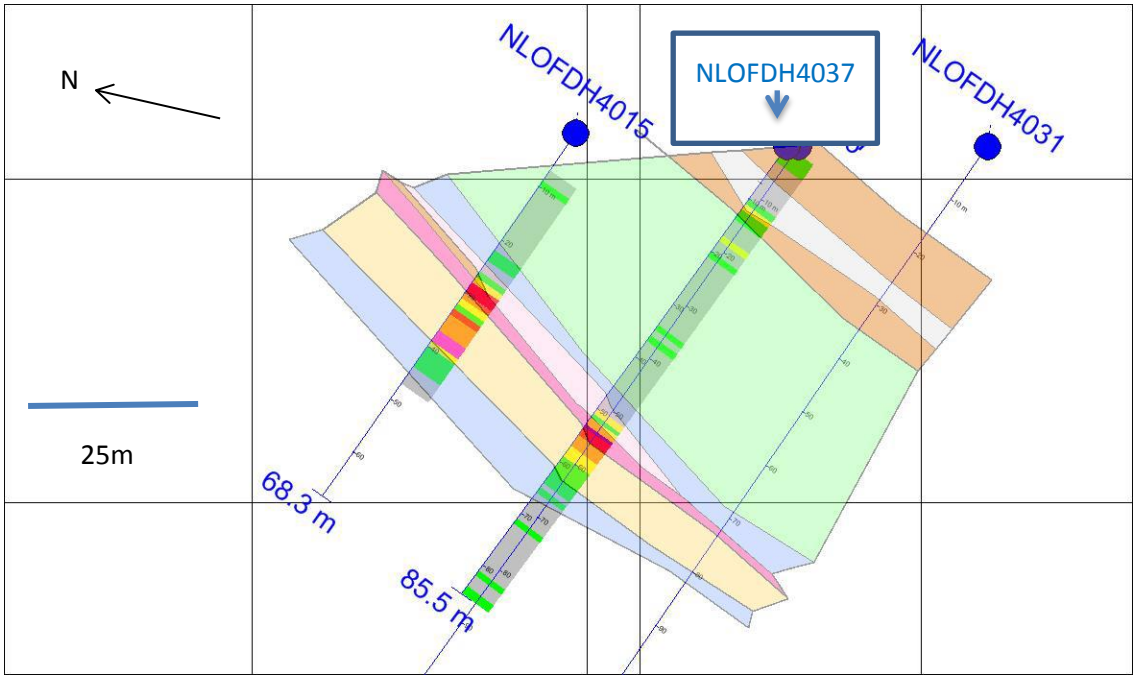

Figure 4.3 – Simplified cross section of alteration zone in Area 4 across 563 E(NB these holes are reviewed in this report in detail in Appendix 1) - HW Zone highly carbonatised (brown), basement (green), main zone pink/tan albitite, altered basement (grey) – NRE 2012.

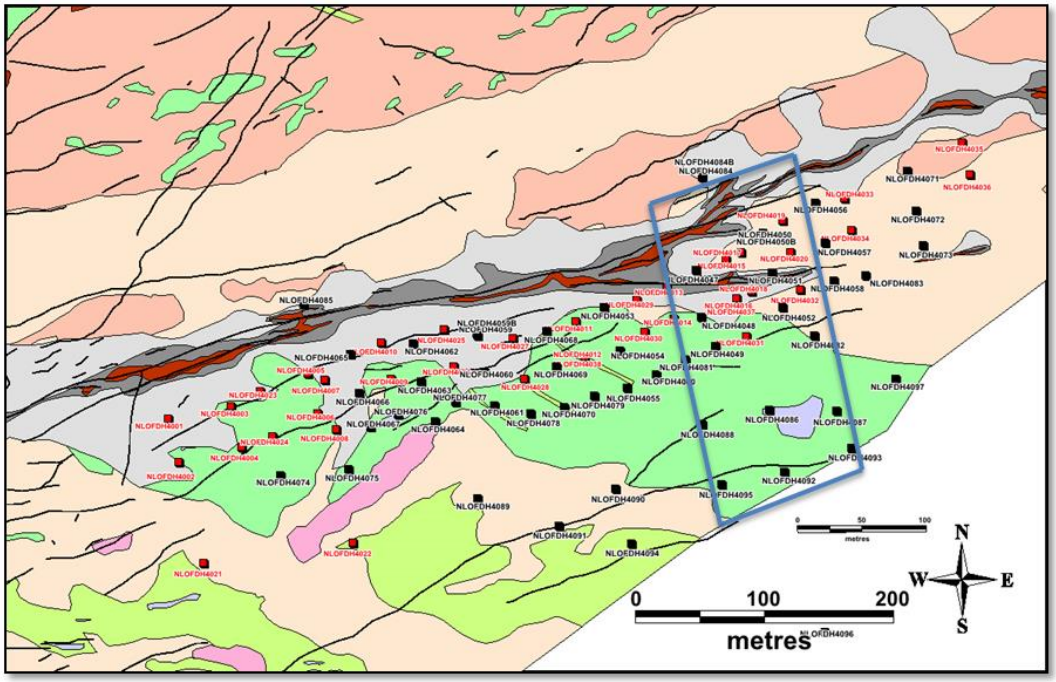

Figure 4.4 Site of diamond drill-core delineation collars, with this report's study area boxed in blue – NRE 2012

A National Instrument CIM 43-101 compliant resource estimate was released by Namibia Rare Earths in November 2012 for Area 4, highlighting the unusual and attractive HREE enrichment of the deposit.

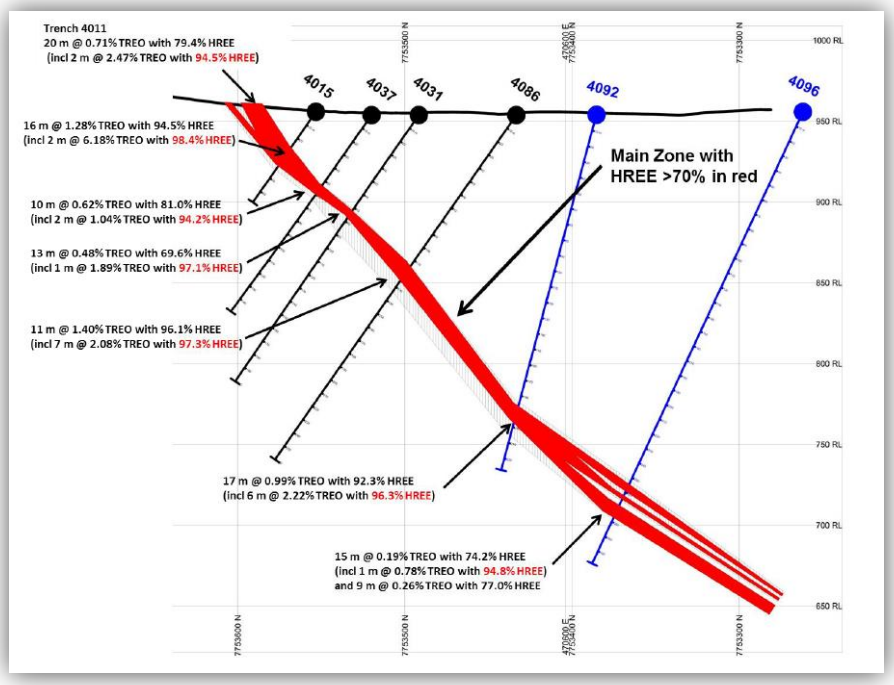

Figure 4.5 - Drill section 563E showing continuity of main mineralised zone to 250 vertical meters – NRE 2012

At a 0.3% TREO cut-off there are Indicated resources of 5,594 tonnes of REO with remarkable 85.6% HREO proportion (see example of high grade HREO continuity in Figure 4.5), and Inferred resources of 4,180 tonnes of REO at 85.1% HREO proportion. This has enabled Lofdal to be listed as one of the highest "basket price" REE deposits currently proven in the world today, courtesy of Technology Metals Research (TMR) - Figure 4.6.

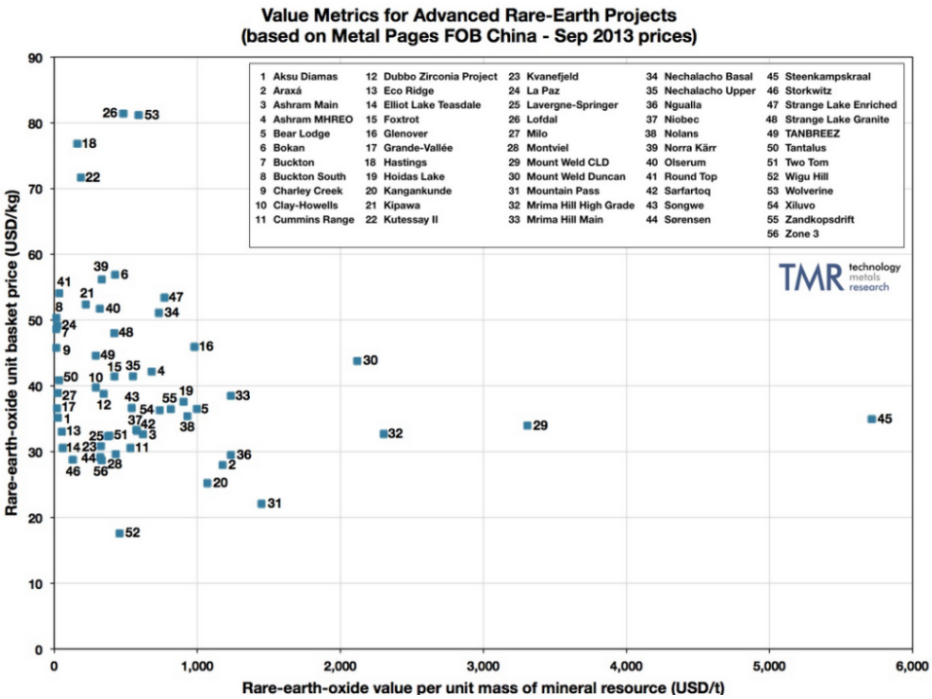

Figure 4.6 - after the release of the NI 43-101 Lofdal entered the Technology Metals Research advanced project list with the highest basket-price (number 26). Courtesy of (TMR, May 2014).

Despite the proven resource at Area 4 questions still surround the origin and nature of the mineralisation. This is just one small corner of the Lofdal property and the possibility of other similarly hosted REE deposits are likely.

Swinden and Siegfried (2012) summarise as follows:

- Exploration has shown that the deposit is not a classic 'carbonatite-hosted' deposit, but in fact a structurally controlled hydrothermal system with diffusive alteration and erratic concentrations of REE
- Continuing exploration shows that in fact there were a number of rare metal settings on the property, that appeared to represent a considerable diversity of timing, geological settings, geological processes and deposit-level characteristics

4.3 General overview of the lithologies of the alteration zone

The alteration zones are visual anomalies that can be identified in outcrop and drill core and are dominantly albitite, consisting principally of albite and quartz, which has been brecciated and re-altered with an overprinting assemblage that includes calcite, dolomite, biotite-phlogopite, chlorite, fluorite and apatite. Swinden and Siegfried (2012) noted that albitisation is uneven, so boundaries between the zones are not always sharp. The albitisation is attributed to sodic metasomatism (Na-fenitisation) perhaps commencing along the structural pathways from the early emplacement of the early nepheline syenite intrusive bodies of the Lofdal Igneous Complex.

Basement lithologies (brief overview):

Gneiss – usually dark brown to black, but can also be green, typically containing muscovitic foliated lamellar textures (Figure 4.7). It always becomes increasingly albititised as the alteration zone is approached. Albitisation can occur in cycles before the main alteration zone is approached. Occasionally it can divide HREE mineralised albitites sequences. Relict lamellar textures can remain in some albitite, assisting the secondary porosity in these altered sequences, or can be totally removed/replaced as albititic alteration tends to remove most features of the original host rock.

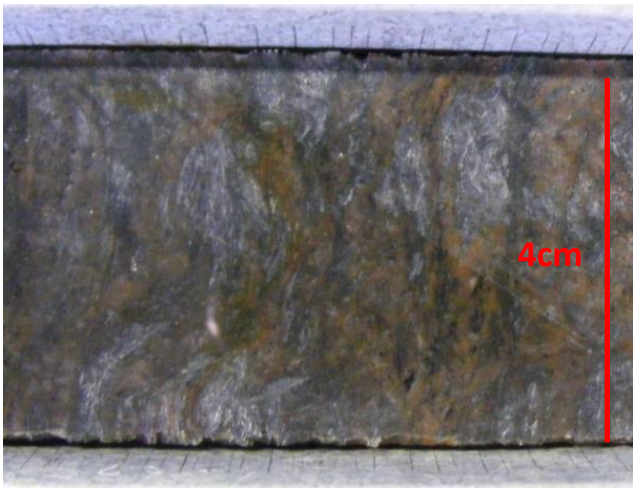

Figure 4.7 an example of the common foliated gneiss which "sandwiches" the alteration zone. Note the foliated books of muscovite, and the pale coloured albitisation. From Hole 4096 249.60m (core 4cm wide). Wholerock analysis from this intercept displays an Eu anomaly.

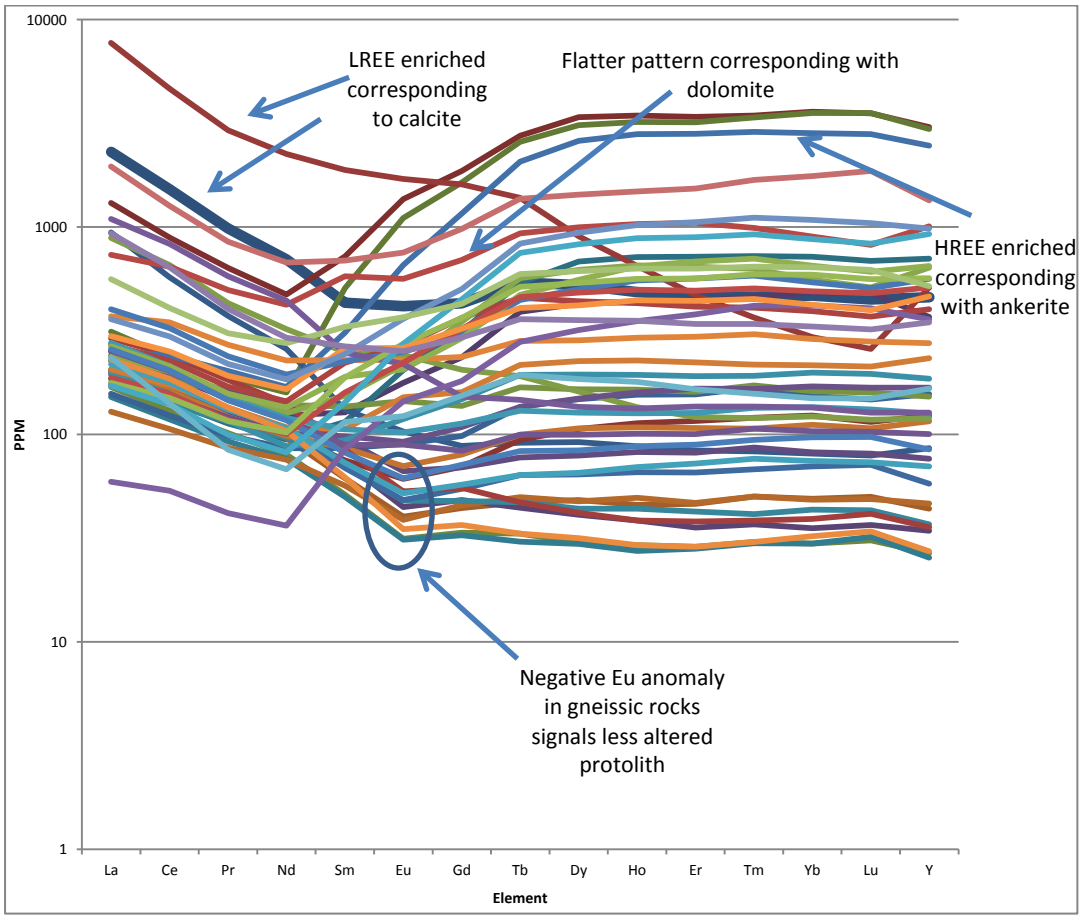

Figure 4.8 Whole-rock chondrite normalised plots per meter through the alteration zone on Hole 4096 Area 4, Lofdal, Eu "dips" or anomalies highlight level of alteration to the protolith – negative Eu anomaly signals less altered protolith. REE normalised to chondrite as of McDonough & Sun (1995).

Generally the protolith either side of the greater alteration displays depletion in REE, and especially an Eu "dip" or anomaly (Figure 4.7 and 4.8). Trace REE contents contained within the HMC, that predate the alkaline and carbonatitic intrusive events, lost Eu to feldspar formation long before. **Therefore, it**

can be inferred that levelling of the Eu anomaly can indicate a visual clue to approaching alteration. Figure 4.8 represents Hole 4096 from 208m (Series 1) through 252m – note the Eu depressions – these are representative of the unaltered, or lesser altered, gneisses of the protolith.

Pegmatite – associated with the basement, and little remains; usually recognised by clots of quartz occasionally incorporating distorted books of muscovitic, and or biotitic micas, and anhedral orthoclase, their presence a possibly reason to Eu depletion in the HMC, as granitoides are well known to be depleted in Eu (Swinden & Siegfried, 2012).

<u>Lofdal Igneous Complex Intrusives in Area 4 (brief overview):</u>

Phonolite: Phonolite dykes predate the carbonatite, but are part of the LIC. They are fine grained and range from a few cms to 10s of cms wide. Very fine grained albitites encountered in Area 4 could represent later fenitisation of these earlier fine grained LIC intrusives, by later metsomatising fluids.

Carbonatite: The carbonatites vary in the composition from "clean" white calcite (sövitic), through dolomitic, ferroan dolomitic and ankeritic, to "dirty" oxidised ferroan calcite. The carbonatites consist of variable amounts of biotite/phlogopite, chlorite-apatite, fluorite, REE minerals, opaque phases (magnetite, rutile, niobian rutile, limonitic iron oxides, and/or pyrite), and clasts of the host albitite that they invariably invade. They are likely to have followed the same structural lines of weakness as the phonolites. Most carbonatites encountered are in the form of dykes varying in width from mms to 10s of cms. No carbonatite plugs as such have been encountered yet in Area 4.

<u>Alteration zone:</u>

Albitite: The albitites are generally fine-grained and contain an assemblage of primarily albite, and variable amounts of biotite/phlogopite, chlorite, calcite, and iron and/or Fe-Ti oxides and discrete quartz. They can exhibit a range of weakly to moderately-developed shear foliation textures. They occur in a range of textures, but are mainly fine grained. The more brecciated, the more likely to host interstitial HREE mineralisation

Dark micas: Consist mostly of biotite-phlogopite group but carry Fe-Ti oxides/hydroxides, and are an important host for REE minerals. Tend to overprint brecciated albitite, usually between fractures, where red or tan alteration overprinting occurs, and also occur as intense shear fabrics orientated parallel to the structural lamellae in shear zones. Importantly they typically occur in areas where high gamma background is present and therefore can be a precipitational environment for thorite. "Dark"

may also refer to the dark-green of chlorite-group which can co-exists with biotite group veins, and HREE minerals.

4.3 Mineralisation within the alteration zone

It has been suggested by Swinden and Siegfried (2012) that hydrothermal fluids have been repeatedly introduced into the structural zone and mineralised structures appear to have been repeatedly altered (early via alkali metasomatism, and later via hydrothermal fluids), producing a wide variety of alteration styles. The introduction of HREE-rich mineralisation appears to have occurred late in the sequence, and is typically related to structural, alteration and mineralogical overprints on earlier alteration. The mineralisation exhibits a great many different appearances reflecting the complexity of the alteration event and the reactions that led to deposition of HREE-rich minerals in different settings. A notable geological characteristic observed in the core before this study is the presence of complex overprinting relationships, and resultant multiple alteration events, the latter of which typically carry the REE mineralisation. This study from Chapter 5 onwards aims to develop a better understanding of these relationships.

5 FIELDWORK

Fieldwork was carried out by the author for 3 week during June 2012 involving detailed analysis of a series of diamond holes intersecting the HREE enriched alteration zone of Area 4. 17 holes over three sections are reviewed here to get a good impression of the styles, and the controls, of the mineralisation within the alteration zone of Area 4, leading to the selection of appropriate samples for later laboratory analysis.

5.1 Core logs overview

Drill core from selected holes was laid out at the NRE core-store near Khorixas. Length of core was selected to show sufficient transition into the hangingwall of the alteration zone, and out of the footwall of the alteration zone. Core was logged to 10cm increments across the alteration zone, as this is the area of interest to NRE and to this study. A problem with fine grained altered rocks, and albite in particular, is that it can assume a wide range of colours (white, grey, pink, brown, tan) due to varying levels of FeO_x (in variable oxidisation states), chlorite and other micas, and carbonate. The heavily overprinted textures of the alteration zone made hand-drawn graphic logs impossible to undertake in the time frame so photography was heavily and appropriately employed, for the task. Selected drillholes, and their collar locations are outlined in Figure 5.1, 5.2, 5.3, and Table 5.1. The mineralised portions of the alteration zones typically have a radiometric response and facilitated the use of a portable dosimeter (Radeye PRD as Figure 5.4) as a guide, however it was found that gamma readings

do not always correspond to the best HREE grades, but rather follow actinide content (Th, U), which doesn't necessarily always correlate with REE content.

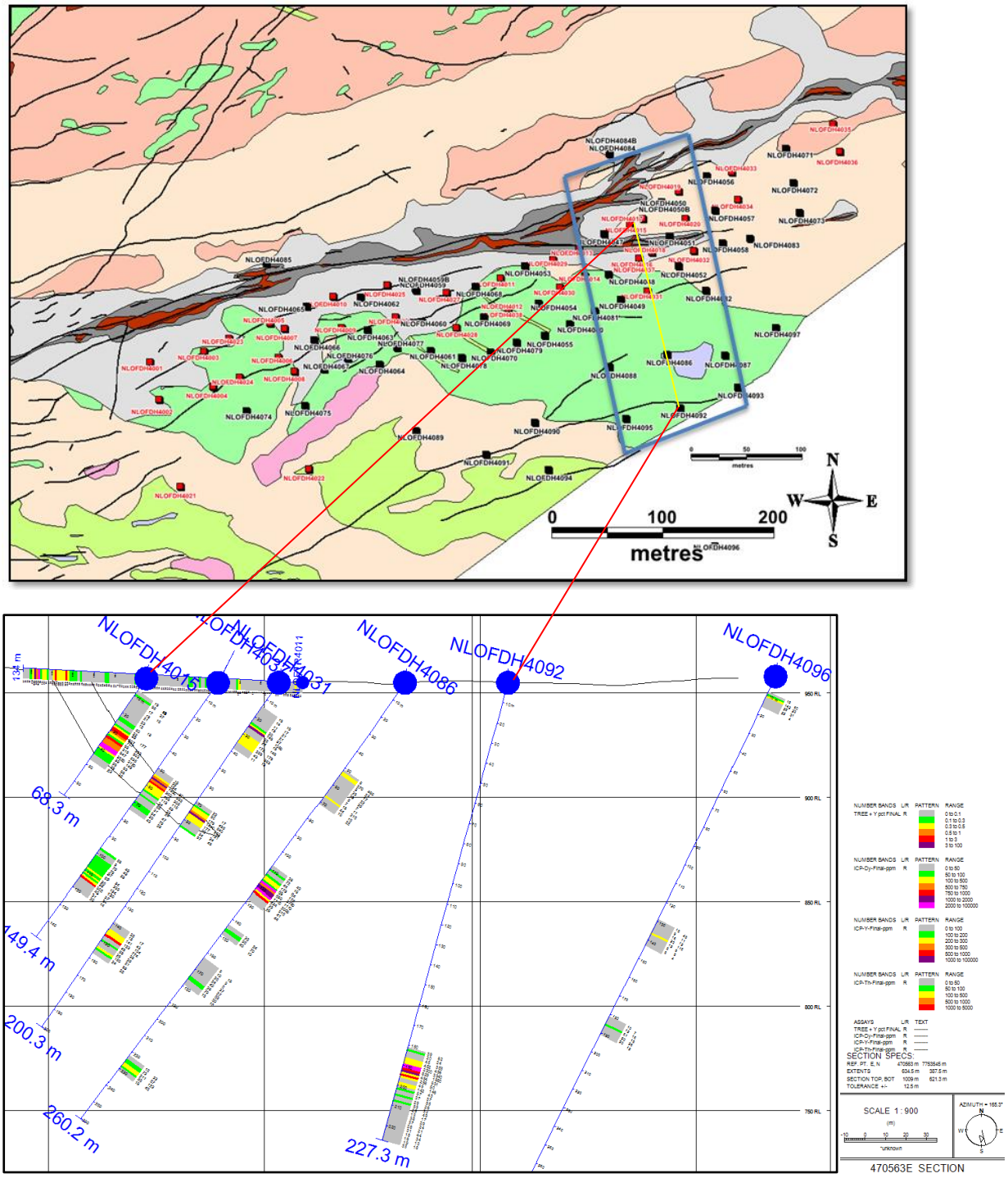

Figure 5.1 & 5.2 Example cross-section through the Lofdal Area 4 alteration zone showing the positions of the numbered drill collars. The section marked in blue is contains the holes that are reviewed in this report. In Figure 5.2 colour bars are for Dy content – NRE 2012

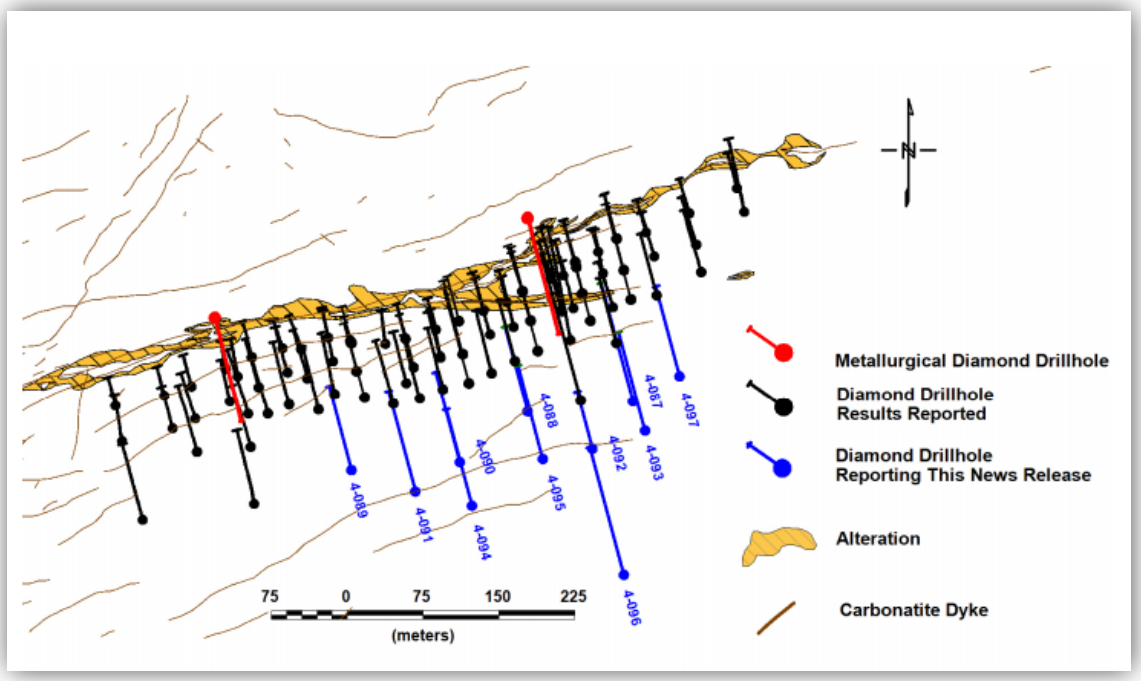

Figure 5.3 Example of drill Plan for Area 4, Lofdal NRE 2012

Section	470 5255E					470 563E						470 613E					
Hole	4013	4014	4081	4088	4095	4015	4037	4031	4086	4092	4096	4019	4020	4032	4082	4087	4093

Table 5.1 Selected holes and from Area 4, Lofdal, Namibia

Figure 5.4 Olympus X-Delta portable XRF for quantitative values of major elements, and importantly Y. Thermo Radeye PRD dosimeter for gamma levels in counts per second (cps)

For selected points within the core a portable XRF was used to gain semi-quantitative values of major elements, and importantly Y in ppm and/or % (Figure 5.4) as a guide to elevated REE content. The rocks being investigated were very fine grained and a Dino-Lite Pro portable microscope proved very useful (Figure 5.5). Observations from the core logging have been included at the end of this section to summarise the lead-ins and lead-outs of the mineralised zones within the greater alteration zones. For

scale purposes core widths are 5cm. Specifications of the handheld microscope, XRF and dosimeter are outlined in Table 5.2.

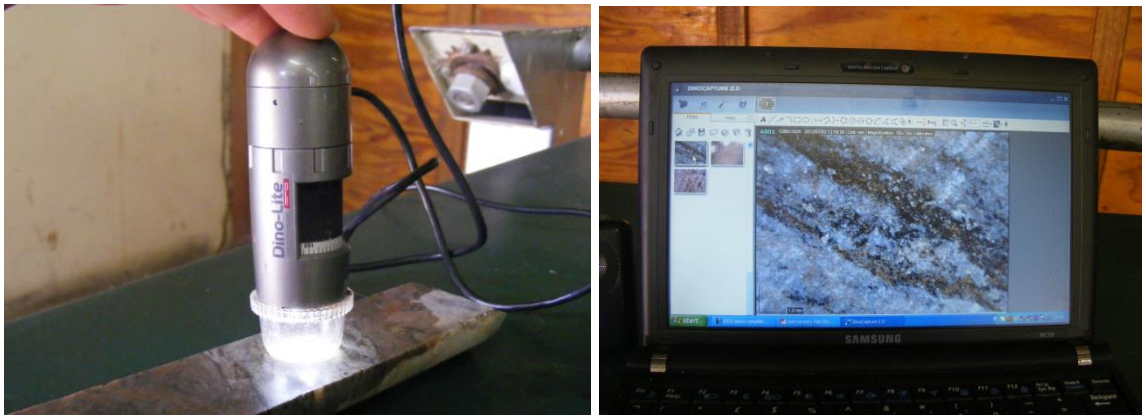

Figure 5.5 Dino-Lite Pro portable microscope – for investigating the fine grained lithologies

Core logging aid	Dinolite Pro ANMo Electronics Corporation Handheld digital microscope	Thermo Scientific Rad-Eye PRD dosimeter High sensitivity gamma radiation detection and dose rate measurement	Olympus X-Delta handheld x-ray fluorescence (XRF) analyser 40kV tube and large area SDD detector
Specification	AM4815ZT • USB 2.0 • 20x ~ 220x • Extended Depth of Field (EDOF) • Extended Dynamic Range (EDR) • Polarizer • High Optical Resolution • Enhanced 1.3 Megapixels	NaI(Tl)-detector with high-quality microphotomultiplier Measurement Ranges: 1µR/h to 25mR/h; 0.01µSv/h to 250µSv/h Certifications/Compliance Designed to meet ANSI™ 42.33/1, 42.32 and IEC 62401 Factory calibrated in exposure rate R/h Over-range Threshold 1000R/h (10Sv/h) -	Excitation Source: 4W Rh, Au, or Ta anode (per application) X-ray tube Detector: Large-Area Silicon Drift Calibrated for Y analysis
Advantages	In fine grained core this portable tool can help identify complex overprinting and some important REE associated phases such as apatite	Indicator of radioactive minerals that largely follow xenotime mineralisation	Qualitative & semi-quantitative analysis of Y content, which is a reliable proxy for HREE content
Limitations	Without geochemical confirmation some observed minerals cannot be distinguished at this scale e.g. apatite or xenotime	Not necessarily an indicator of REE mineralisation, as Th and U can form phases independent of REE	Difficult to calibrate for Ce (proxy for LREE). LREE content determined by ICP-MS analysis of samples (NRE 2014).

Table 5.2 Specifications of equipment used during core analysis

The alteration zones also carry a geochemical anomaly that includes the HREEs and Y, P_2O_5, Th, Zr, Nb. Thankfully a range of elements, including majors and trace elements were measured at 1m intervals from the diamond drill core. Whole-rock ICP data from the 1m sample intervals provide a useful guide to mineralised intervals. However, the reader must be alerted that data from these 1m intervals is not absolute in terms of the distribution of the HREE mineralisation, and won't take into account the "nuggety" nature of the mineralisation – i.e. sub10mm HREE mineralised stringer veins "missed" between sample points. However, the data is useful in the context of graduation of the chemical alteration to the host rocks, and therefore as a pathfinder to the mineralisation.

Samples for whole-rock geochemical analysis were prepared for analysis at the Actlabs laboratory in Windhoek, Namibia. Details of the procedures are outlined in Section 6.

Table 5.3 Summary of alteration zone characteristics for 17 holes over 3 adjoining sections Area 4, Lofdal. HREE enriched interval = +100ppm Dy from whole-rock ICP-MS

Section	Hole	Lead into alteration	Lead into mineralisation	Mineralised zone(s)	Thickness HREE enriched interval(s)	Lead out of mineralisation	Lead out of alteration
525E	**4013**	Albitised gneiss	Reddened carbonatised albitite	Upr: biotite shears Lwr: carbonatised brecciated caramel albitite + black micas	Upper 3m, Lower 4m	Brown mottled albitite into grey albitite	Albitite into muscovitic gneissic rocks
	4014	Albitised gneiss and barren carbonatites	Broken core and gouge	Micaceous sheared caramel albitite, mottled albitite	4m	Quickly into grey albitite	Albitite into gneissic rocks
	4081	Alternating cycles of albitite and gneiss	Dolomite & black mica infusions, fault gouge	Upr: fine grained caramel albitite Lwr: incr. fractured version of upper + foliated dark micaceous shears	10m	Quickly into bounding shear to albitite	Albitite into gneissic rocks
	4088	Albitised gneiss	Increasing number, and thicknesses, of carbonatite x-cutting veins in albitite	Carbonatite and fenitised fractured albitite	5m	Carbonatised footwall continues beneath main zone.	Albitite
	4095	Alternating cycles of albitite & gneiss	Sheared albitite and dark micaceous stringers	Carbonatised fractured albitite, black micas. Heavily brecciate albitite in lower zone	Upr: 4m Lwr: 2m	Abruptly into less brecciated albitite	Albitite into muscovitic gneissic rocks
563E	**4015**	Fragments and gouge	Carbonatite veins	Pink sheeted albitite, mottled tan albitite, black mica infusions	10m	Fine grained cream coloured albitite	Albitite into basement pegmatite & gneiss
	4037	Brown albitite	Carbonatite veins and FeOx stringers	Brecciated carbonatised albitite	9m	10cm thick shear zone into albitite	Albitite into gneiss
	4031	Upr: brecciated foliated albitised gneiss Lwr:fractured albitites w/ carbonatite/ FeOx	Upr: Carbonatite veins, w/ pink overprinting to albitites Lwr: shear zone w/ pink sheeted albitites	Upr: reddened sheeted, pitted fg albitite Lwr: Pink sheeted shear zone & finely brecciated caramel & pink albitite	Upr: 2m Mid: 6m Lwr: 8m	Upr: carbonatite veins in albitite Lwr: less fractured albitite	Upr:into albitites Lwr: albitites into gneiss
	4086	Micaceous stringers in alb/dolomite	Brown sheared albitite	Dolomitic & ankeritic carbonatisation of fractured albitite	15m	Micaceous shear zone and fault gouge	Albitite to gneissic rocks
	4092	Grey albitite into micaceous shear	Increasingly fractured tan albitite	Heavily micaceous veins in dark brown overprinted brecciated albitite & dolomite	10m	Gouge and fragments	Albitite to gneissic rocks
	4096	Albitised gneiss	Cycles of carbonatite veins & sulphides in albitite, sometimes from shear	Cycles of Tan/caramel brecciated albitite w/interstitial black micas, and minor dolomite	Upr: 5m Lwr: 8m	Fracturing in albitite reduces, paler colours to albitite	Albitite to gneissic rocks
613E	**4019**	Fragmented albitite	Sheeted albitite, shear	Tan/caramel brecciated albitite w/ black mica infusion	Upr: 3m Lwr: 3m	Black alteration leaves grey albitite	Albitite to gneissic rocks
	4020	Gouge & fragments	Shear & pinker albitite	Laminated/sheeted albitite, brecciated tan albitite	Upr: 3m Lwr: 2m	Broken core and gouge	Albitite to gneissic rocks
	4032	Magnetite & dolomitic carbonatite	Shear & pinker albitite	Sheared pink and tan albitite	Upr; 2m Lwr: 6m	Gouge and fragments	Albitite to gneissic rocks
	4082	Albitite to carbonatite veins	Tan to orange brecciated albitite	Friable, sandy, fine grained heavily carbonatised albitite	8m	Bounding shear to albitite	Albitite into gneissic rocks
	4087	Fractured grey albitite & micaceous infill	Magnetite & dolomitic carbonatite, + shear	Caramel/tan albitite & micaceous veins	Upr: 3m Lwr: 3m	Shear, gouge and albitite fragments	Albitite into gneissic rocks
	4093	Albitite & carbonatite	Magnetite & dolomitic carbonatite	Caramel/tan albitite & carbonatite	9m	Shear, gouge into sheeted albitite shear	Albitite into gneissic rocks

Table 5.3 gives an outline of the drill core observed in this study, and Figure 5.6 demonstrates textural and mineralogical variability downhole across the alteration zone, here Hole 4081 as an example, showing the HREE bearing dolomitic carbonatite in the hangingwall, and HREE bearing brecciated albitite in the footwall. Detailed petrological study of the drill core can be found in **Appendix 1**. Hole overviews, like Hole 4081 in Figure 5.6, coupled with wholerock data downhole in Figure 5.7, can be found in **Appendix 2.**

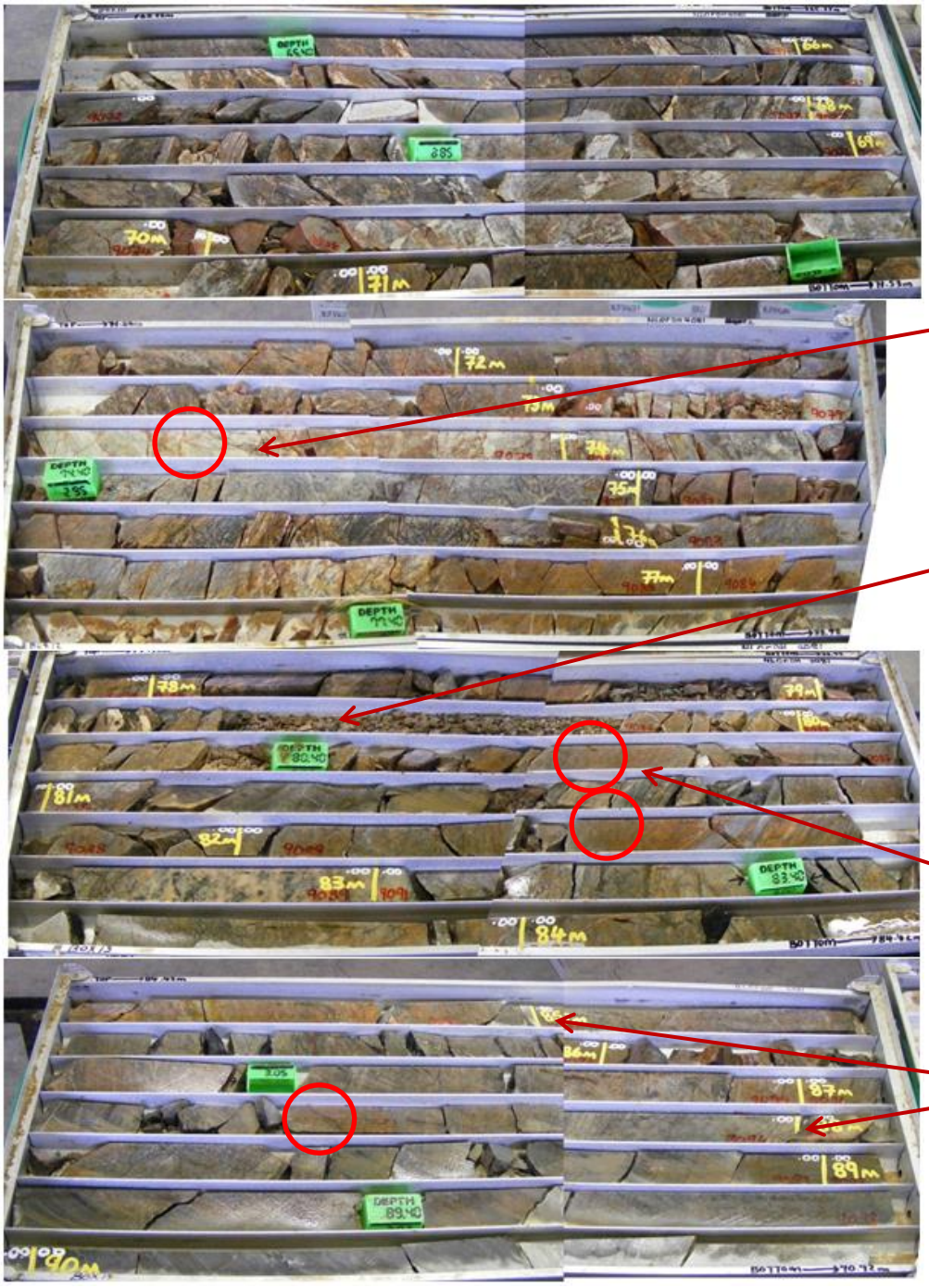

Figure 5.6 layout of Hole 4081 drill core showing an example of the HREE bearing alteration zone downhole – the example here shows HREE bearing dolomitic carbonatite from 73m, and HREE in brecciated albitite in the footwall from 80m.

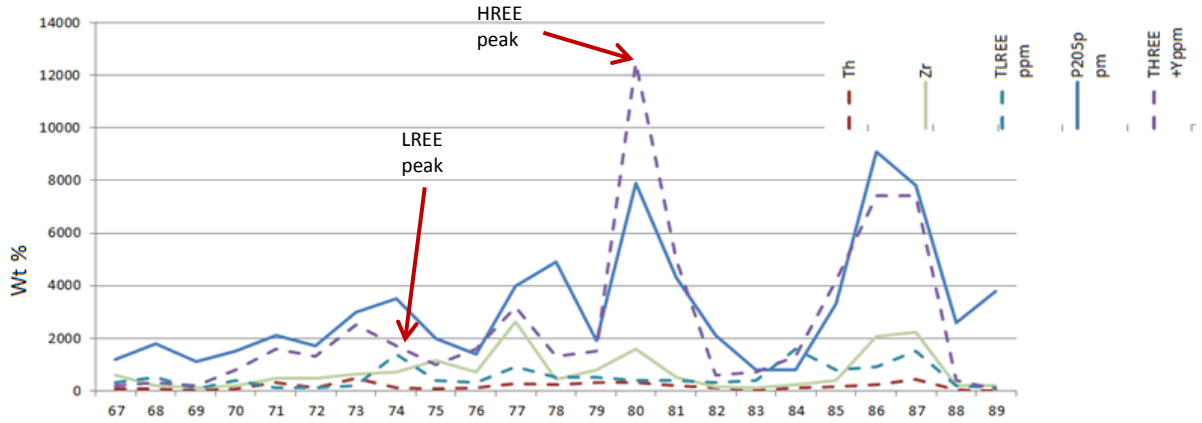

Figure 5.7 Wholerock data downhole on Hole 4081 demonstrating peaks in total light REE and heavy REE and their associated minerals, zircon (Zr as proxy), and thorite (Th as proxy). NB metre depth is on x-axis

6 STUDY OF ALTERATION ZONE IN DETAIL

Outlined below are the techniques deployed in the detailed study of the Area 4 Alteration Zone.

6.1 Methodology whole-rock analysis

Samples for whole-rock geochemical analysis were prepared for analysis at the Actlabs laboratory in Windhoek, Namibia. Samples were first crushed in a jaw crusher to obtain 90% passing 2mm, passed through a riffle splitter to obtain a 250g split for pulverization. Splits were pulverized with a swing mill in hardened steel bowls to 95% passing 105 microns (possible trace Fe and Cr contamination from bowls). Samples were then homogenized in a stainless steel riffle splitter and a 15g sample was drawn from the splitter for analysis. Pulp samples were analysed for major element oxides, REEs and trace elements at the Actlabs analytical laboratory in Ancaster, Ontario, using their code 8 REE Assay Package which involves a lithium metaborate fusion and multi-acid digestion.

Inductively Coupled Plasma Optical Emission Spectroscopy (ICP – OES) was employed for major element oxides, scandium, beryllium, vanadium, strontium, yttrium and zirconium. An ICP-Mass Spectrometry (ICP-MS) was used for other trace elements including the rare earth elements. Nb_2O_5 and ZrO_2 were determined by sample fusion and standard XRF methods for samples with >0.3% P_2O_5.

Actlabs quality assurance and quality control, included the analysis of certified reference materials, blanks and duplicates. These QA/QC procedures were monitored be NRE for all sample batches. Additionally, NRE inserts certified reference materials, blanks and laboratory duplicates each at a frequency of 5% into sample batches prior to submission to Actlabs. NRE also submitted 5% of the total samples to ALS laboratories in North Vancouver as an additional check on data quality (NI 43-101, Swinden and Siegfried, 2012).

6.2 Optical petrography

Polished thin sections were made from 41 samples of drill core. Two ¼ cores were cut on a diamond saw. One ¼ core set aside for polished thin sections, and the other ¼ remaining in the core store at Khorixas. The thin sections were prepared by Stephen Pendray at the Camborne School of Mines. Table 6.1 provides details of the samples.

6.2.1 Methodology microscopy

Thin section analyses were undertaken at Camborne School Mines, Penryn Campus, Penryn, Cornwall, UK on a Nikon Eclipse E600 Pol microscope with instant image capture through a Nikon Digital Sight 5MP camera. Albite, calcites, biotite-phlogopite, chlorite, quartz and opaque phases was identified quite readily in many of the thin sections. Rare earth minerals (xenotime, synchysite and others) are very fine grained and difficult to identify in cross polarised light (XPL). REE minerals, and xenotime associated with zircon especially, can be identified in PPL by their high relief against ubiquitous carbonate phases. Fe and Mn enriched carbonates, notably HREE bearing ankerite, appear browner in PPL against the "cleaner" carbonate phases and can mask much of the finer grained phases.

6.2.2 Methodology cathodoluminescence microscopy (CL)

A useful tool in this study was the use of cathodoluminescence (CL) as many REE bearing minerals, including xenotime can fluoresce clearly. The utilisation of CL upon 19 thin sections proved useful for A) identifying REE bearing mineral phases B) studying variations carbonate phases, and C) ferric iron activation in albite, a gauge of the intensity of alkali-metasomatism (fenitisation, or more aptly re-fenitisation) of the Na-feldspars. Luminescence is produced by activator trace elements, notably REEs, present in minerals (Marshall, 1987). CL also proved useful later in identifying areas for scanning electron microscopy study, and in plotting transects for the later microprobe (EPMA) study.
Equipment: Cathodoluminescence model CCL 8200, running at 15.3 Torr vacuum, running to a maximum 450 µA current, 6.3 kV accelerating voltage.

6.3 Scanning electron microscopy - SEM/EDS

6.3.1 Methodology

The use of scanning electron microscopy (SEM) enabled closer inspection of the textures and minerals associations from areas of interest identified previously via CL. Its use also helped locate high atomic number elements such as the REE minerals, Th bearing phases, and Ti, Nb, Fe bearing phases. Energy dispersive spectroscopy (EDS) enabled qualitative determinations of the minerals in the selected thin sections. EDS spectra for the thin sections studied can be found in the Appendix of this report.
Equipment: SEM model JEOL JSM-5400LV running at 25kV voltage and 69mA current. Polished thin sections were carbon coated to 25nm approx. beforehand to enable conductivity.

Table 6.1 Samples for analysis – codes, location, description, position, and analytical techniques employed. PPL - plain polarised light, Cl - cathodolumiscence, SEM - scanning electron microscopy, EPMA - electron microprobe

Section	Sample (hole & depth)	Description	Position in alteration zone	Analytical method
525E	4013 35.99m	Carbonatite & magnetite	Upper mineralised zone	PPL, CL
	4013 46.93m	Caramel coloured brecciated albitite	Main mineralised zone	PPL, CL, SEM, EPMA
	4014 59.32m	Brecciated albitite	Hangingwall of alteration zone	PPL, CL
	4014 65.95m	Biotitisation oriented to shear carrying HREE grade	Hangingwall in main mineralised zone	PPL, CL, SEM, EPMA
	4014 66.45m	Brecciated micaceous albitite w/tan overprint	Main mineralised zone	PPL, CL, SEM, EPMA
	4081 73.50m	HREE and LREE minerals in dolomitic carbonatite	Hangingwall to main mineralisation	PPL, CL, SEM, EPMA
	4081 80.60m	HREE in fractured albitite	Upper mineralised zone	PPL, CL, SEM, EPMA
	4081 82.40m	Barren caramel fine grained albitite	Splits mineralised zone	PPL, CL
	4081 87.50m	HREE in fractured albitite	Footwall of mineralisation	PPL, CL, SEM, EPMA
	4088 116.16m	Ferruginous carbonatite x-cutting albitite	Hangingwall to mineralised zone	PPL, CL
	4088 123.60m	Pyrite in vein crosscutting albitite	Footwall to mineralised zone	PPL, CL
563E	4015 27.59m	Sheeted albitite carrying opaque Fe-rich phases	Hangingwall of mineralised zone	PPL, CL
	4015 30.40m	HREE occurring in fractures in albitite	Hangingwall of main mineralised zone	PPL, CL
	4015 37.30m	Fluorite bearing carbonatite x-cutting fractured albitite	Centre main mineralised zone	PPL, CL, SEM
	4015 38.40m	Fractured sheeted albitite w/ tan overprint	Footwall of mineralised zone	PPL, CL, SEM, EPMA
	4031 25.25m	Ferruginous carbonatite x-cutting another carbonatite	Hangingwall of mineralised zone	PPL, CL, SEM
	4031 75.20m	HREE occurring in fractures in albitite	Upper mineralised zone	PPL, CL
	4031 77.20m	Fractured albitite	Lower mineralised zone	PPL, CL
	4086 117.14m	Sheeted albitite	Hangingwall of mineralised zone	PPL, CL, SEM, EPMA
	4086 118.80m	Ferruginous carbonatite x-cuts sheeted albitite	Main mineralised zone	PPL, CL, SEM, EPMA
	4092 188.15m	Fractured micaceous albitite	Hangingwall of mineralised zone	PPL, CL, SEM, EPMA
	4092 190.50m	Sheeted albitite	Main mineralised zone	PPL, CL
	4096 208.55m	Albitite x-cutting muscovitic rocks	Hangingwall to mineralised zone	PPL, CL
	4096 209.48m	Fractured albitite w/visibly mineralised fractures	Hangingwall of mineralised zone	PPL, CL
613E	4019 26.74m	Carbonatised albitite	Main mineralised zone	PPL, CL
	4019 31.12m	Fractured albitite	Footwall to mineralised zone	PPL, CL
	4019 32.14m	Albitite x-cutting muscovitic rocks	Footwall to mineralised zone	PPL, CL
	4020 38.90m	Carbonatised fractured albitite	Hangingwall of mineralised zone	PPL, CL, SEM, EPMA
	4020 39.72m	Albitite with shear fabric	Main mineralised zone	PPL, CL
	4032 47.44m	Dolomite, albite w/ magnetite	Hangingwall of alteration zone	PPL, CL
	4032 47.56m	Dolomite and albitite w/ HREE	Upper mineralised zone	PPL, CL
	4032 62.35m	Brecciated albitite w/ carbonatite overprint	Footwall of mineralised zone	PPL, CL
	4082 88.80m	Fine grained caramel albitite	Hangingwall to mineralised interval	PPL, CL
	4082 91.86m	HREE mineralised brecciated albitite	Main mineralised zone	PPL, CL
	4082 92.20m	Heavily HREE mineralised brecciated albitite	Main mineralised zone	PPL, CL, EPMA
	4087 131.50m	Dolomite overprints w/ magnetite	Upper mineralised zone	PPL, CL
	4087 139.88m	Brecciated albitite w/ tan overprint	Footwall of mineralised zone	PPL, CL
	4087 140.26m	Shear fabric in albitite with calcite	Footwall to mineralised zone	PPL, CL
	4093 174.20	Sheared albitite with ankeritic vein and HREE	Hangingwall to mineralised zone	PPL, CL
	4093 176.14m	Carbonatised albitite, or carbonatite	Main mineralised zone	PPL, CL
	4093 176.13	Brecciated albitite with rounded clasts	Footwall of mineralised zone	PPL, CL

6.4 Results from petrological analysis

Full results from the whole-rock data and petrological descriptions of each hole of the study area can be found in **Appendix 1**. As the study is extensive and reveals a wide range of textural styles in the Area 4 alteration zone a summary of the types of REE mineralisation, in paragenetic sequence, from earliest to latest, are displayed here:

6.4.1 Dolomite carbonatite

Dolomite carbonatite hosts the phosphates monazite, apatite and xenotime (although sometime the dolomites can be barren of REE minerals and apatite), examples of which can be found in Hole 4081 at 73.50m as in Figure 6.1 below, with close ups of cathodolumiscence (CL) displayed in Figures 6.2.

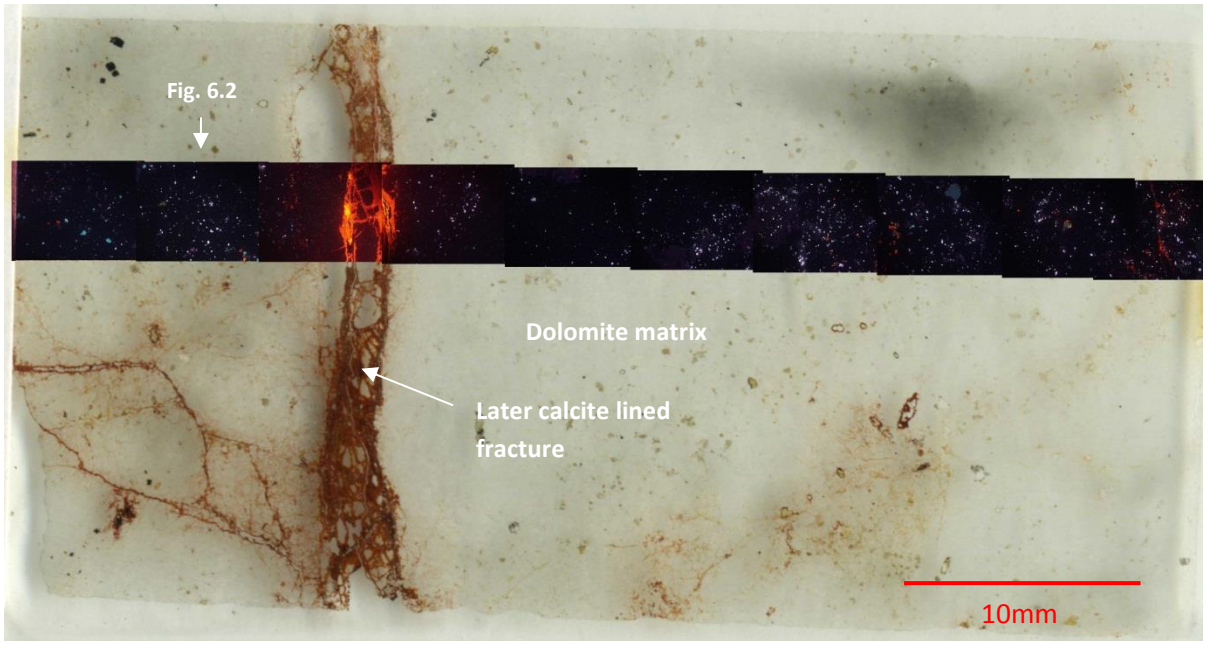

Figure 6.1 4081 73.50m Thin section of dolomite carbonatite

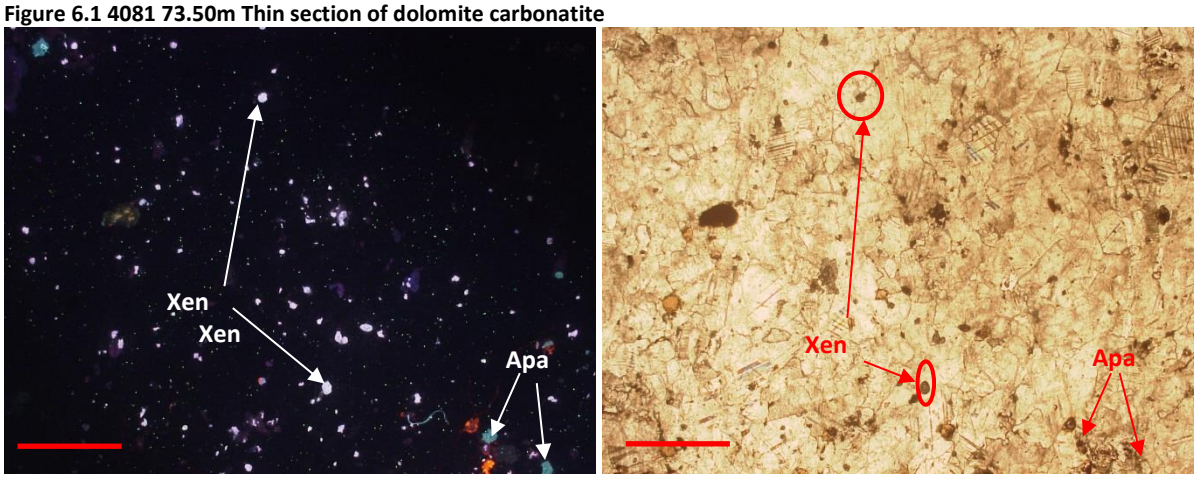

Figure 6.2 4081 73.50m CL image "sky at night" REE minerals in dolomite. Xenotime, monazite (minimal CL reactivity), and apatite. Scale bar 1mm

Further to the above, scanning electron microscope (BSE) images of these areas lit up by xenotime in CL are shown in Figure 6.3, and show that the LREE phosphate mineral monazite is present too.

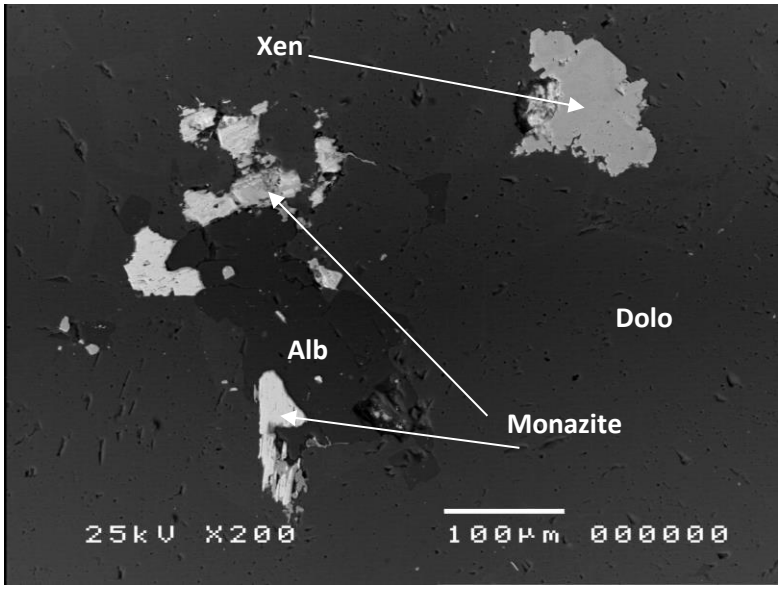

Figure 6.3 BSE image close up of 4081 73.50m. Monazite crystals at base of albite grain. It is worth noting that the LREE minerals are less reactive in CL. Xenotime grain to NE.

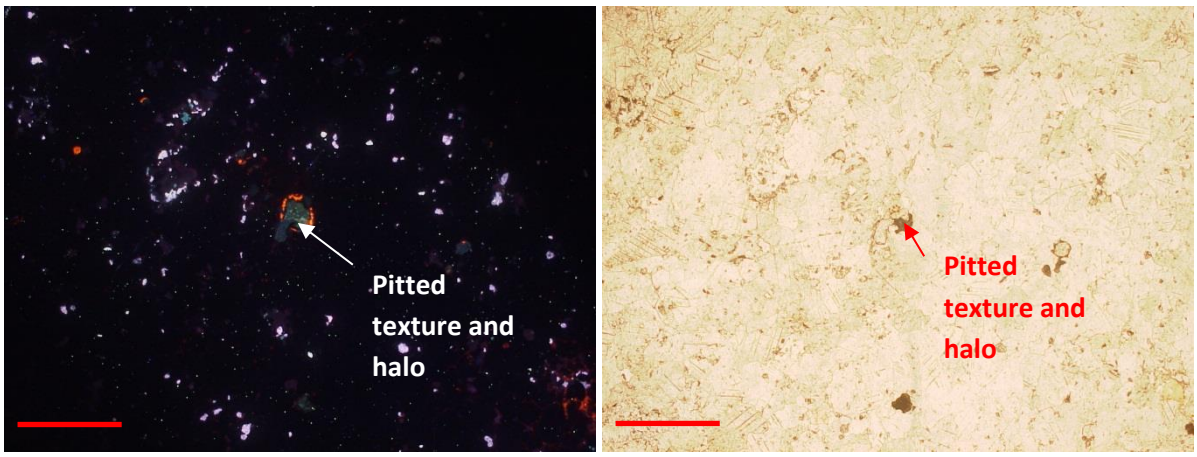

Figure 6.4 4081 73.50m CL images unusual "pits" and halo structures. Scale bar 1mm

An interesting texture seen in the dolomite host are occasional ""halos" as seen in CL (Figures 6.4). Under SEM the pits consist of corroded crystals with a remnant intimate mixture of xenotime and thorite as shown in Figure 6.5.

Similar pits and halos to those in 4081_73m are also present in 4086_118.80m as pits and halos in brecciated albite and dolomite (Figure 6.6). Dolomite is present in high grade intercepts in Hole 4092 between 188-192m. Also in high grade sections in adjacent holes 4086, and 4096. Dolomite clearly has a role either as harbouring REE, or as a favourable depositional site for xenotime, or both.

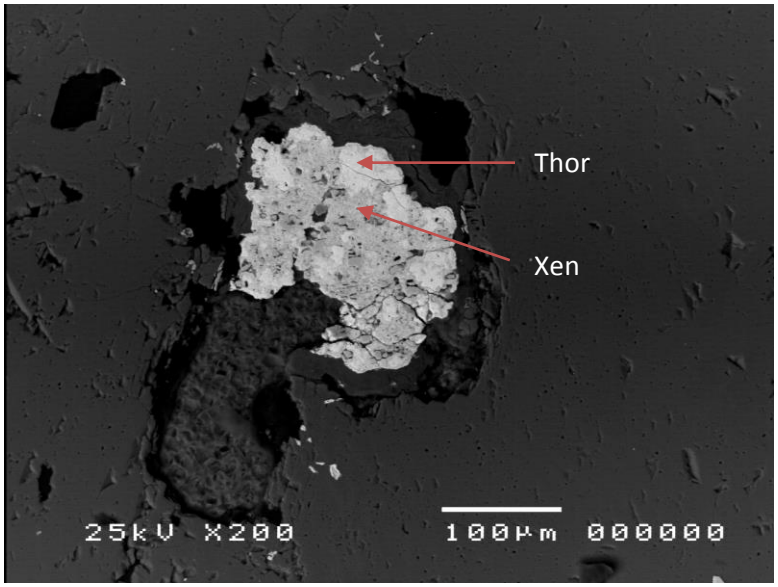

Figure 6.5 4081 73.50m BSE image close up of "halo" in Figure 6.4. Thorite with xenotime and other REE phases in the centre. These sites of thorite may explain higher gamma levels here. They appeared highly altered.

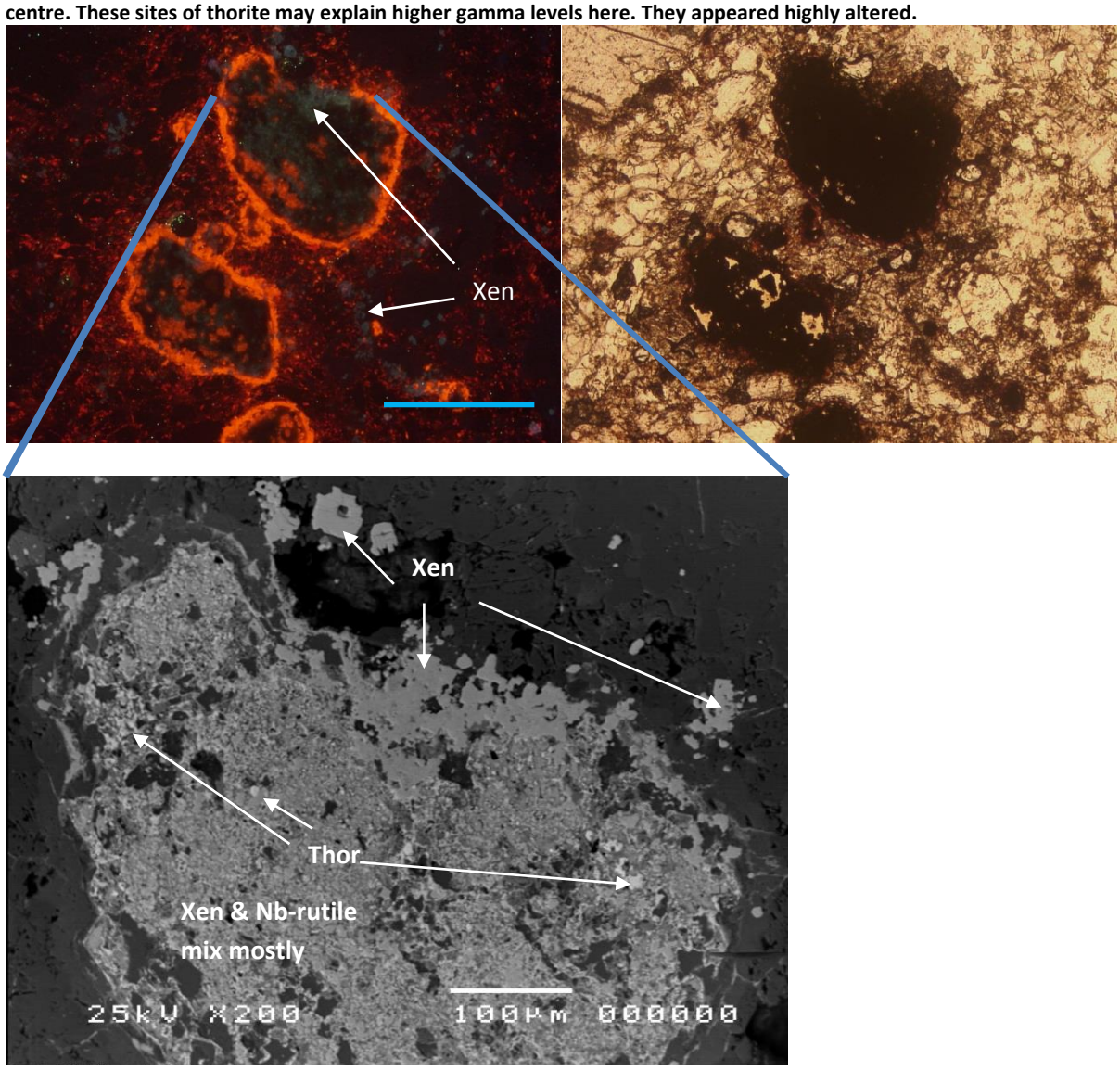

Figure 6.6 4086 118.80m BSE image shows fine grained nature of the minerals contained within partially absorbed clast, and EDS analysis indicates thorite, a fine grained intergration of xenotime, thorite and rutile internally. Note that the peripheral xenotimes are subhedral/euhedral. Scale bar for CL and PPL 0.5mm.

6.4.2 Magnetite bearing dolomitic & calcite carbonatites

Magnetitic bearing carbonatites containing xenotime in association with magnetite, hematite and pyrite, with or without apatite occur in a few holes, and of note usually in the hangingwall to heavily mineralised intercepts such as in holes 4013 (Figures 6.7 & 6.8) and 4087. Carbonate is represented by Fe-calcite and dolomite, but dolomite tends to be the dominant carbonate encountered with magnetite.

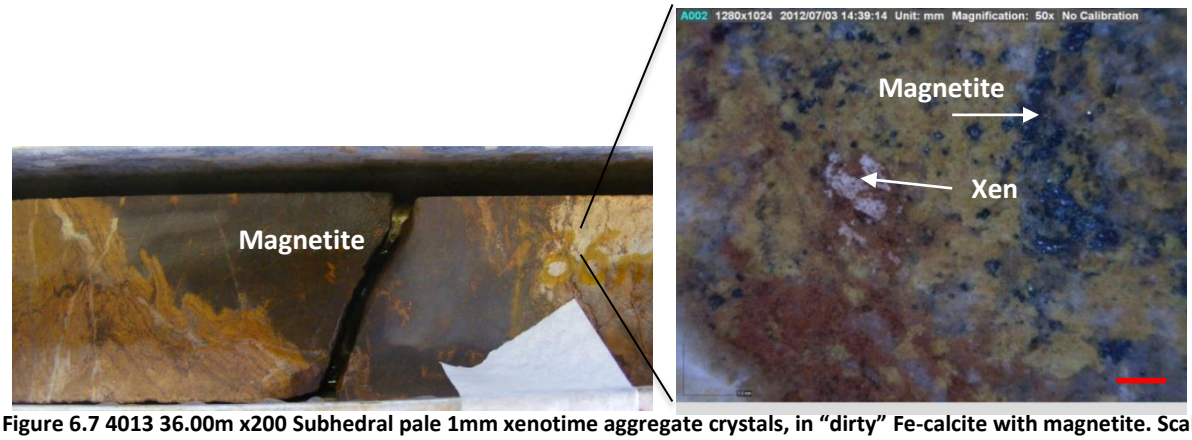

Figure 6.7 4013 36.00m x200 Subhedral pale 1mm xenotime aggregate crystals, in "dirty" Fe-calcite with magnetite. Scale bar 1mm.

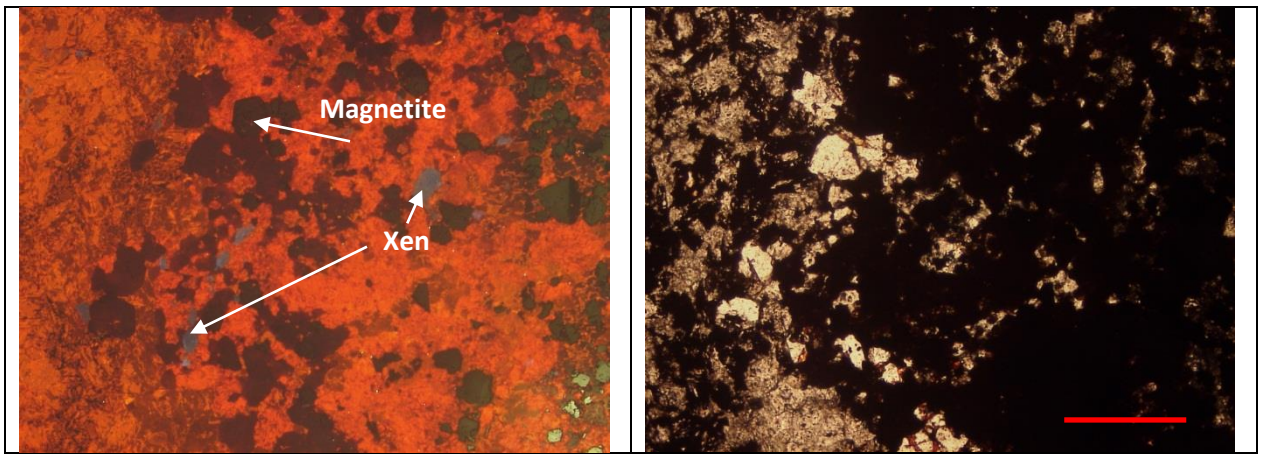

Figure 6.8 4013 35.99m again sporadic subhedral magnetite and xenotime, a texture indicating a co-genetic relationship

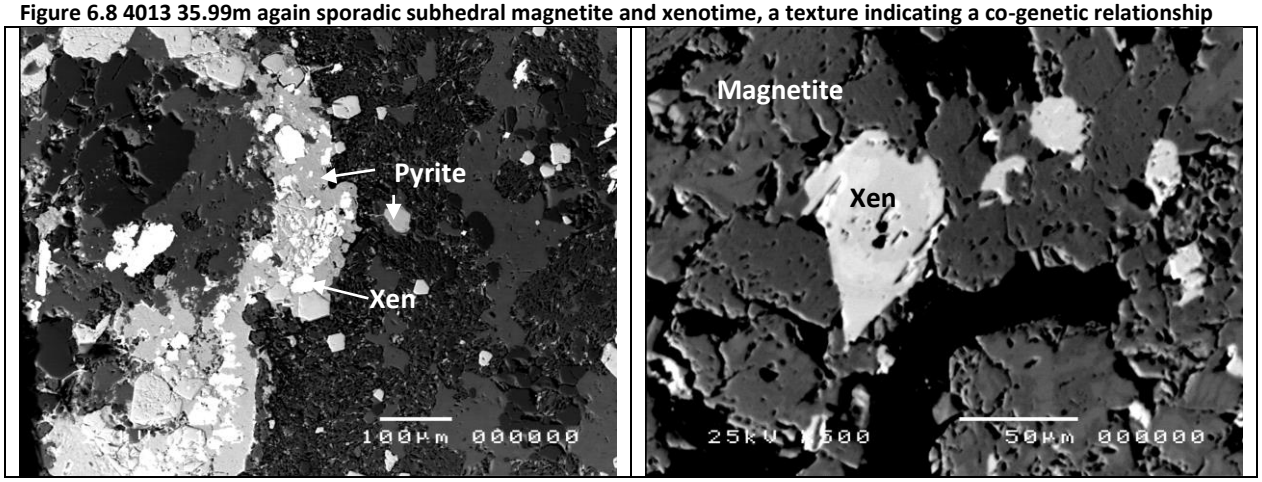

Figure 6.9 4013 35.99m BSE image xenotime, pyrite, and magnetite. Euhedral xenotime with magnetite.

Xenotime tends to be well formed, i.e. subhedral to euhedral crystals (to over 50µm) and some displaying zonation, appearing coeval with magnetite (Figure 6.9). Dolomite host rock in many magnetitic sections such as in 4087 at 131.50m is not reactive in CL (Figure 6.10).

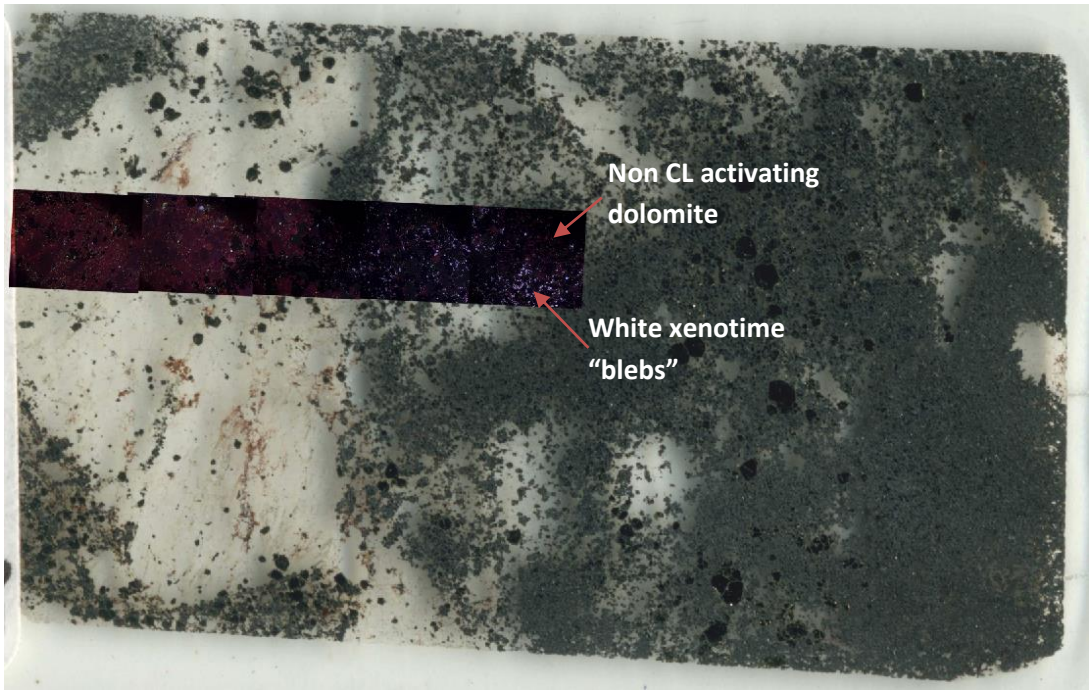

Figure 6.10 4087 131.50m thin section with CL transect. Similar to adjacent hole 4032 (but missing from 4082). FOV 35mm

Magnetitic carbonatite can be seen cross -cutting dolomite carbonatite in Hole 4032 between 47m and 48m showing that the dolomite carbonatite predates the magnetitic carbonatite injection (Figure 6.11a & b). Xenotime is associated more with thorite and apatite, here as displayed in Figure 6.12, but appear to show fresher, uncorroded halos of apatite and the intimate xenotime/thorite association as described above.

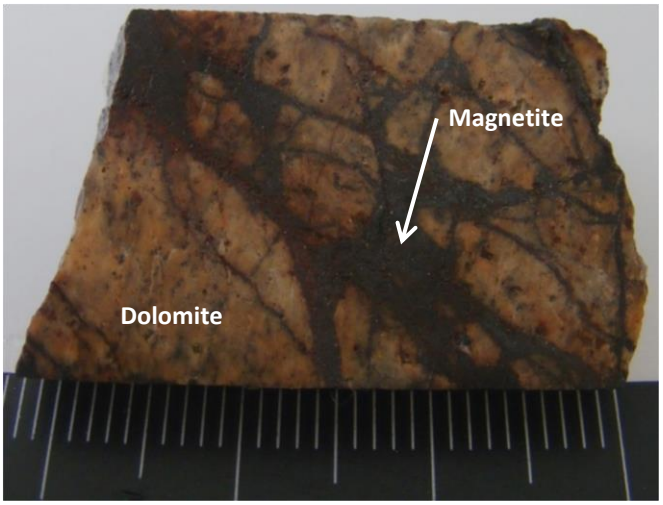

Figure 6.11a 47.44m magnetitic veins cross-cutting dolomitic carbonatite

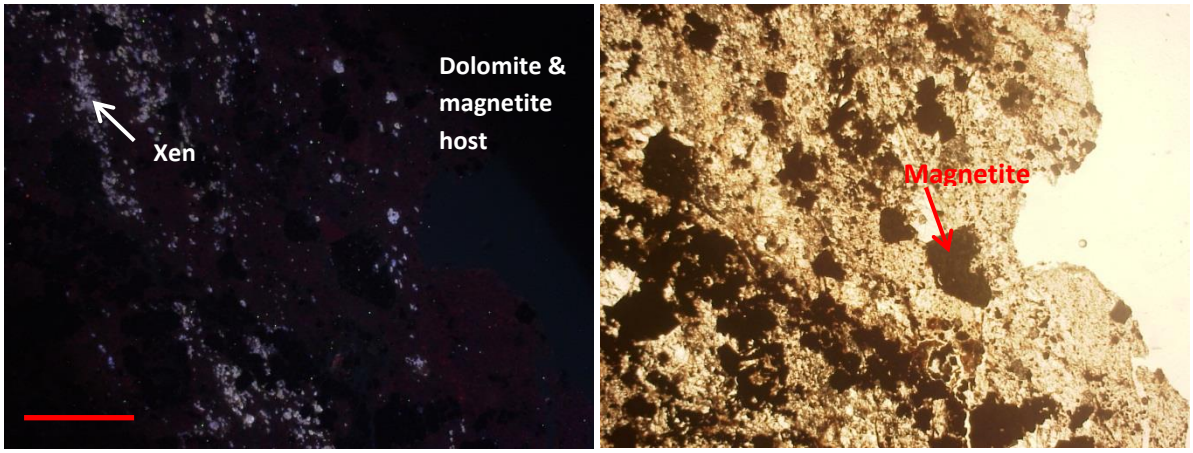

Figure 6.11b 4032 47.56m moving across the section xenotime appears orientated to shear direction in brecciated dolomite and albitite and associated with magnetite/hematite. Scale bar 1mm

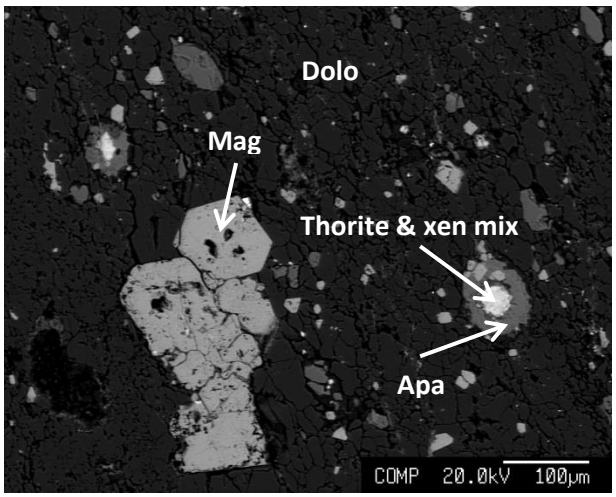

Figure 6.12 4032 47.56m BSE image magnetite with Th-rich xenotime mantled by apatite in dolomitic carbonatite

6.4.3 Stringers in brecciated albitite

Xenotime mineralisation in Area 4 is commonly found as stringers taking advantage of secondary porosity in brecciated albitite (Figure 6.13). With the presence of zircon in many stringers it can be determined that these stringers are associated with ankerite carbonatite emplacement in the Lofdal property. Associated minerals include rutile, hematite and pyrite. However, evidence of overprinting and rounded crystals suggests that there may have been degrees of dissolution, and later xenotime as reprecipitation.

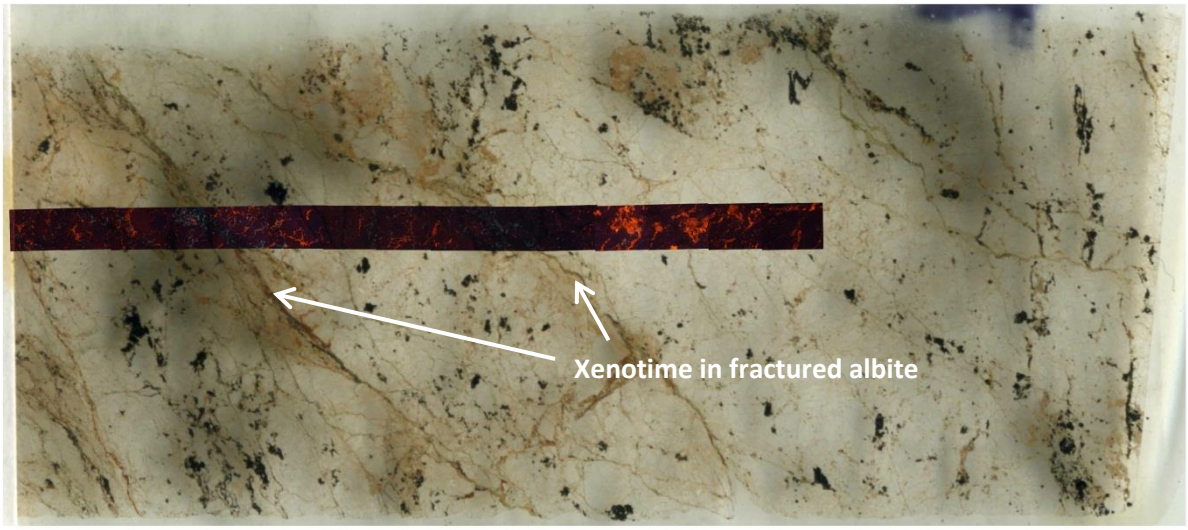

Figure 6.13 4081 80.60m thin section of brecciated albite with mineralised stingers. Scale is approx. 45mm width.

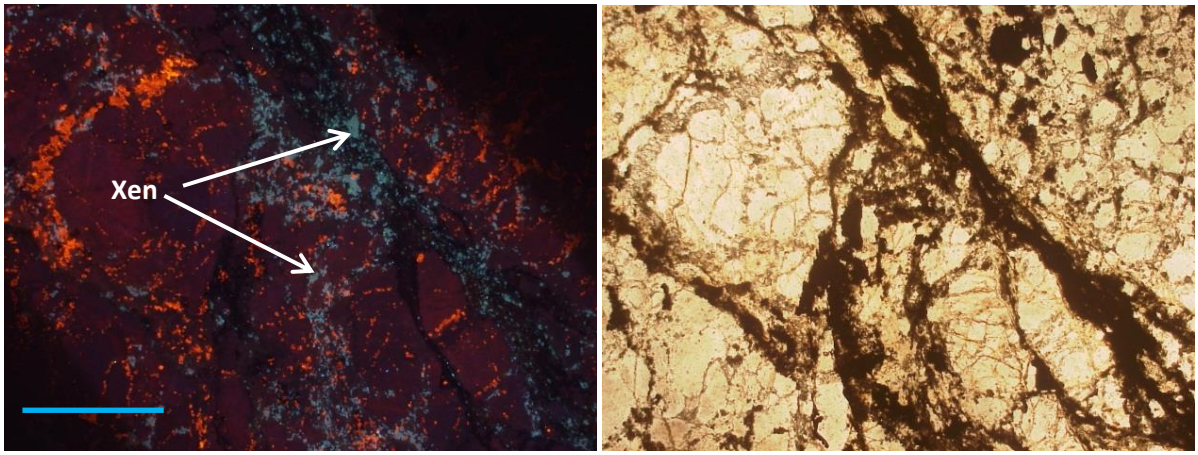

Figure 6.14 4081 80.60m CL image strongly vein orientated xenotime with opaques (both in CL and PPL). Scale bar 0.5mm

Xenotime lines fractures in albite host rock and is accompanied by carbonate and/or biotite (Figures 6.14 & 6.15). This suggests that the albitite pre-dates this episode of xenotime mineralisation. Many of the xenotimes have rounded zircon cores (Figure 6.16), which are different to the sharper xenotime mantled zircon crystals as observed by Wall et al. (2008) from the carbonatite dykes.

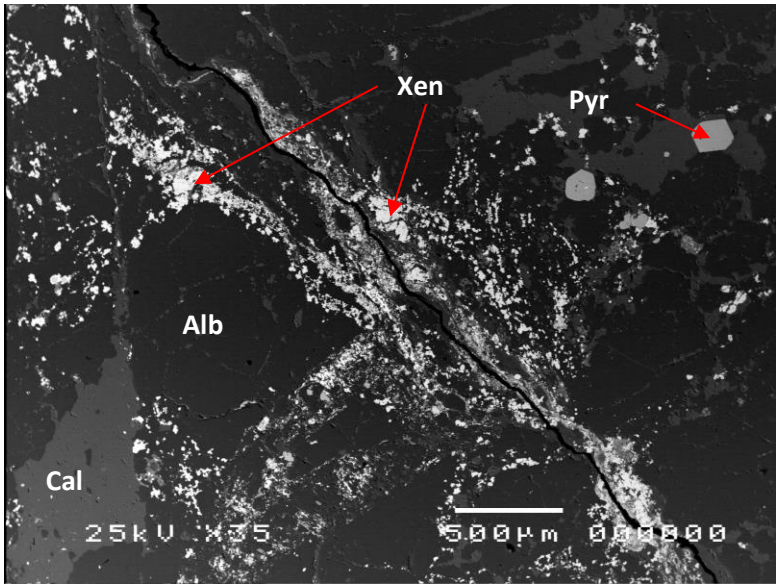

Figure 6.15 4081 80.60m BSE image of Figure 6.14. Xenotime, zircon rutile and pyrite in vein, and infiltrating around brecciated albitite. Dark centre line is fracture, and likely fluid pathway. Subhedral/euhedral crystals to RHS are pyrite.

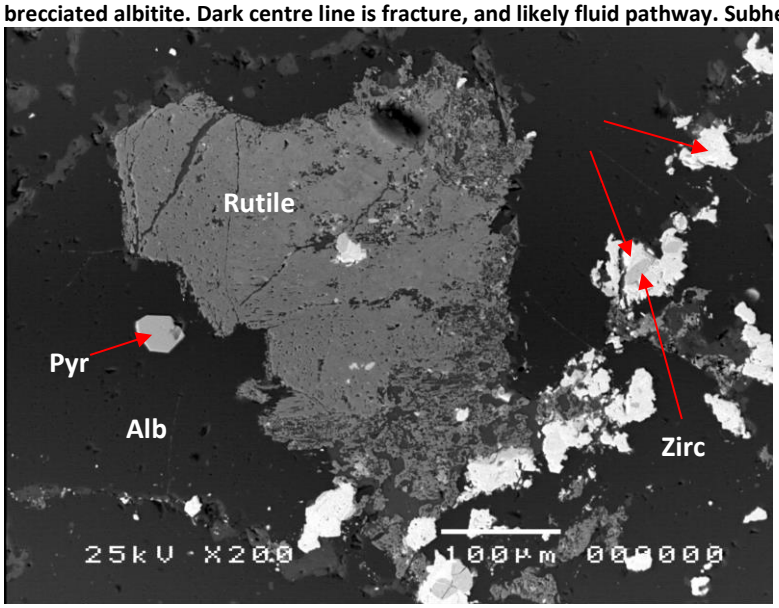

Figure 6.16 4081 80.60m BSE image close up of Figure 6.15. Xenotime with rounded zircon centres, with rutile (large grain)

Similar textures and mineral assemblages to 4081 80.60m are found in 4082 91.8m (Figure 6.17), and at 4020 38.90m.

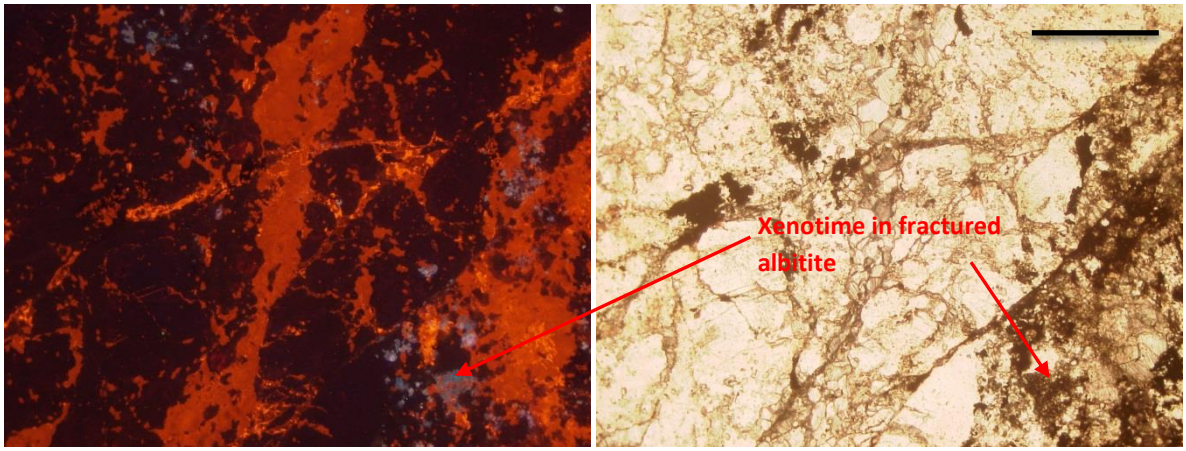

Figure 6.17 4082 91.86m ferruginous channel-way butts up against less impenetrable breccia. Scale bar 1mm.

Some stringers become fractured later and overprinted again, like at 4082 92.20m (Figure 6.18), and it is likely that the processes of their emplacement are similar to those described in Section 6.4.7. Ferric iron activated carbonate is the latest overprint (Figure 6.19), but xenotime seems more abundant in the fractures of earlier brecciated albitite.

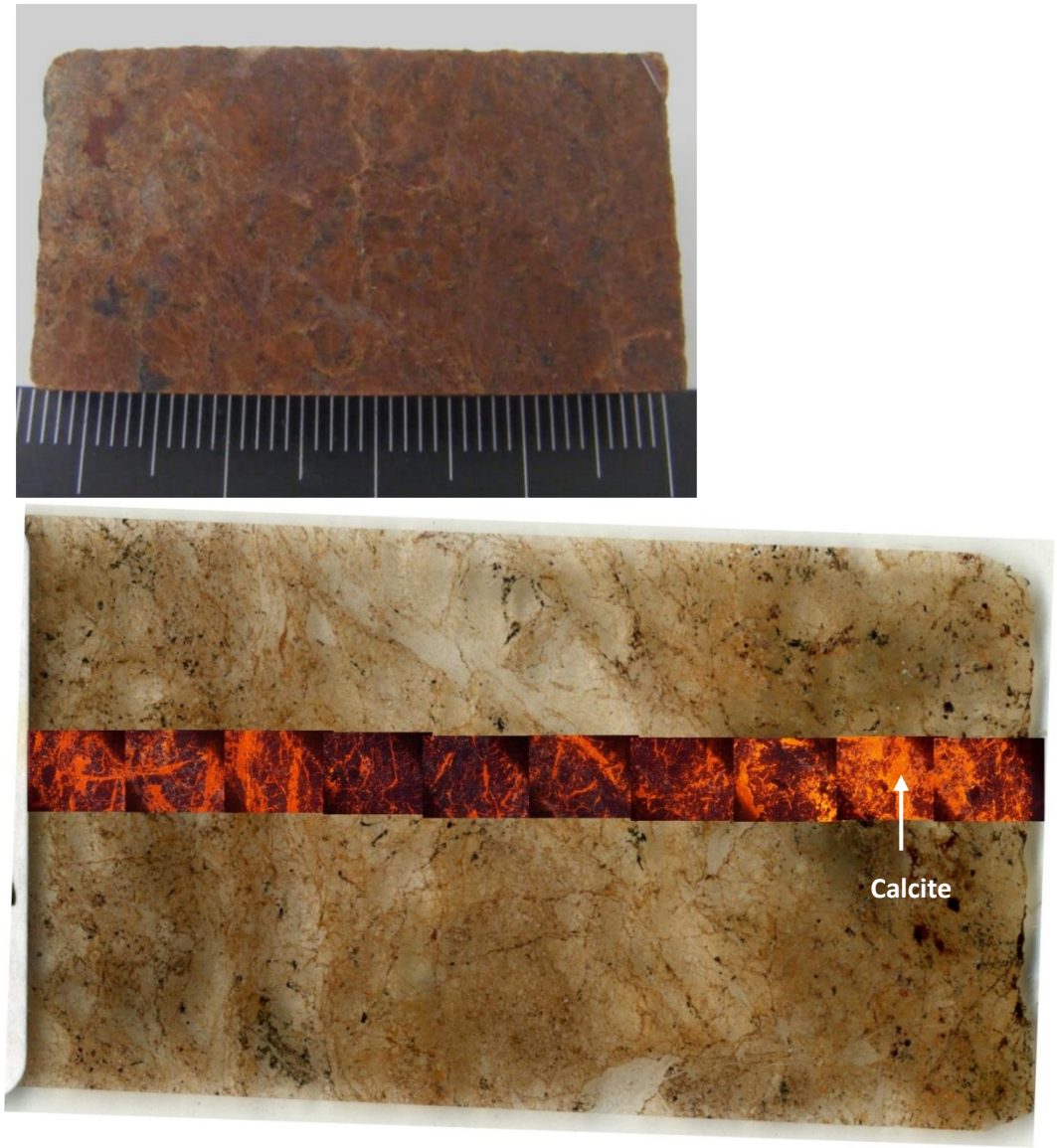

Figure 6.18. 4082 92.20m thin section with CL transect – multiple overprinted texture in brecciated albitite. A few episodes of carbonate infusion, notably ferroan calcite and ankerite. FOV 40mm

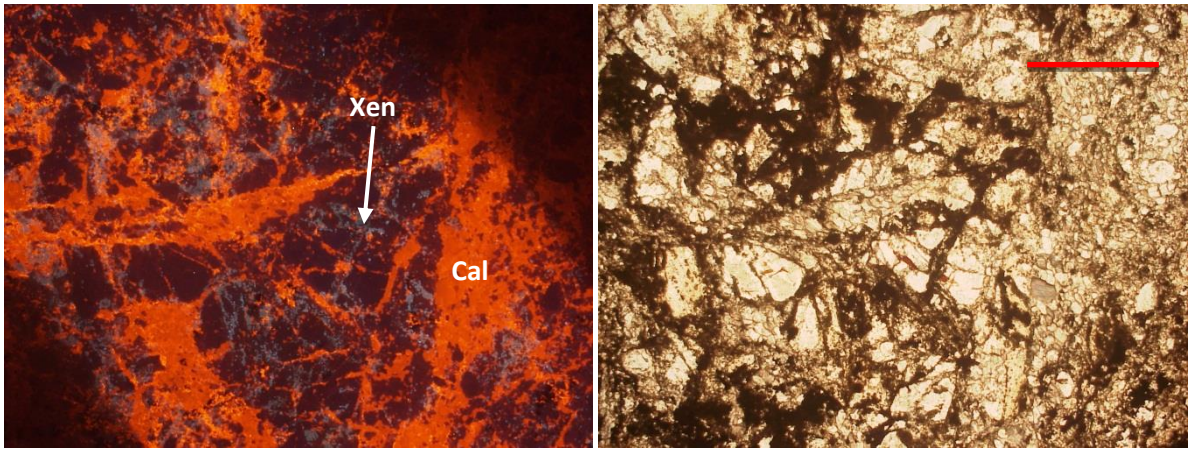

Figure 6.19. 4082 92.20m interstitial ferroan calcite and xenotime in heavily fractured albitite. Appear cross-cut and redistributed xenotime from later fluid infusion. Scale bar 1mm.

6.4.4 Ankerite and apatite reaction fronts

A reoccurring feature is the presence of apatite reaction fronts where an ankeritic ferruginous carbonatite has cross-cut an albitite. Xenotime tends to reside in the "dirty" carbonatite while apatite forms at the junction between the two rock types (Figure 6.20). The pitting could be epimorphs after possibly magnetite/hematite or apatite or REE phosphates, as observed elsewhere in less altered sections.

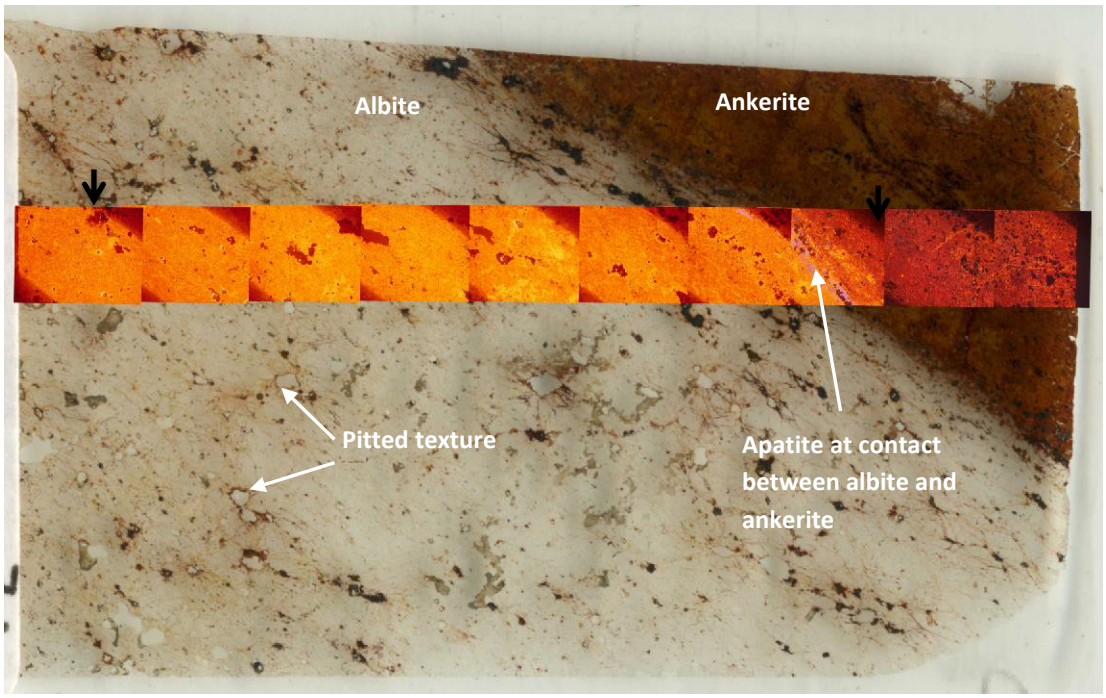

Figure 6.20. 4031 22.25m thin section with CL transect. FOV 35mm. White is albitite, brown is carbonatite. Note the pitting and secondary porosity in the albitite.

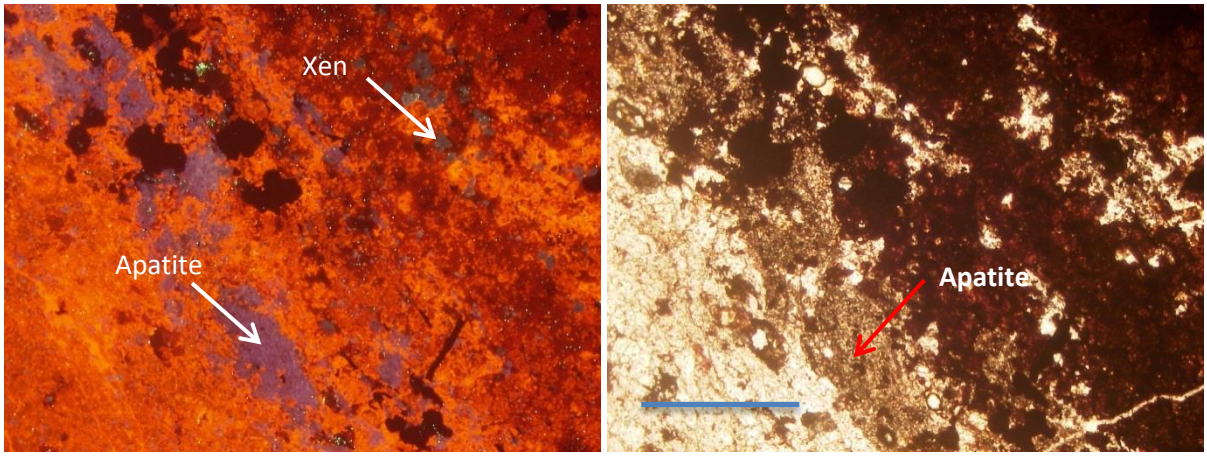

Figure 6.21. 4031-22.25m the ankeritic darker carbonatite hosts xenotime crystals (grey in CL). Scale bar 0.5mm.

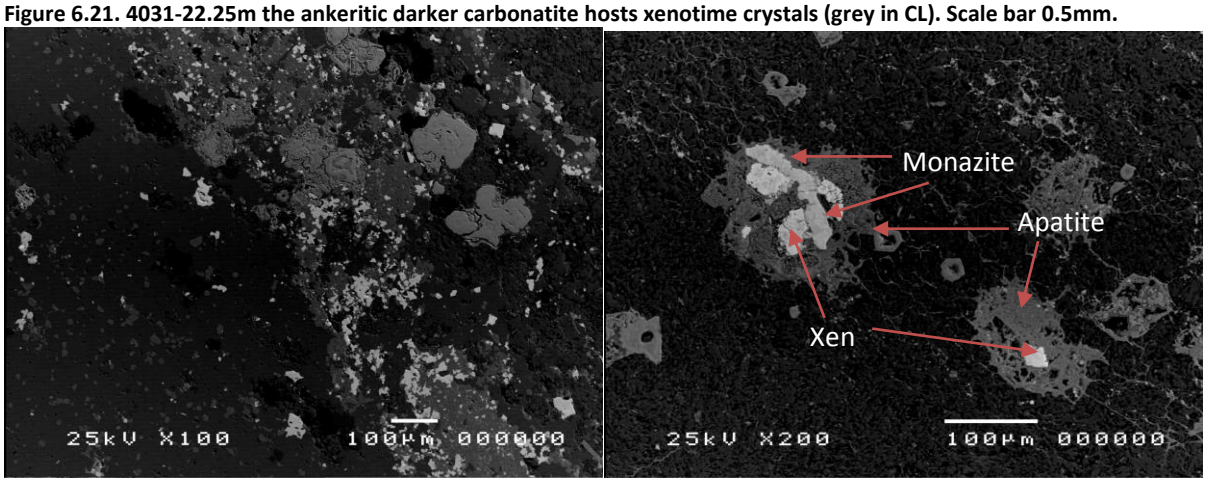

Figure 6.22. 4031 22.25m BSE images of xenotime intergrown with apatite at contact, RHS REE apatite, with monazite and xenotime associated w/ hematite and rutile

Reaction fronts like in Hole 4031 (Figure 6.21) reappear at 4086 117.14m. Of interest is that in shear orientated veins thorite occurs separate to the xenotime (Figure 6.22).

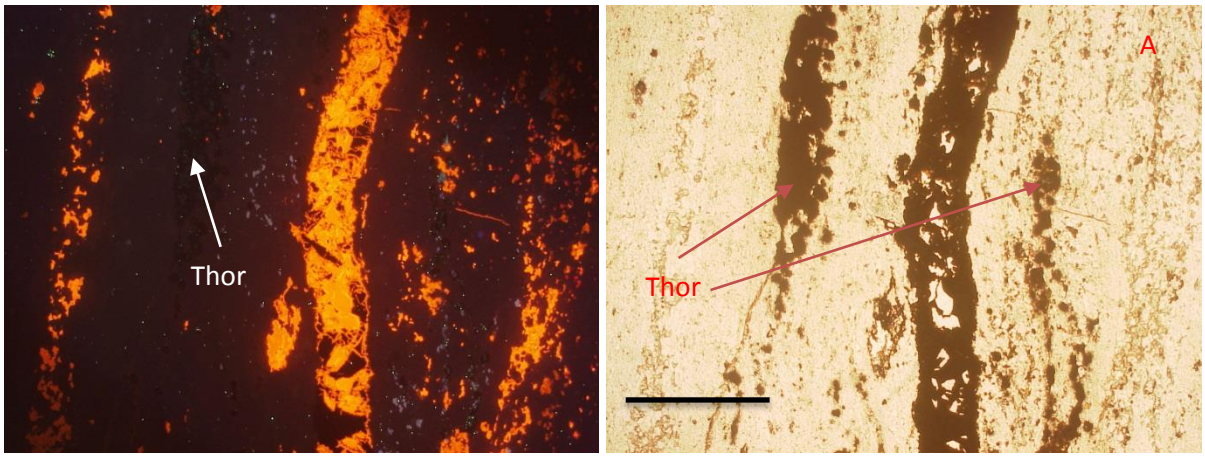

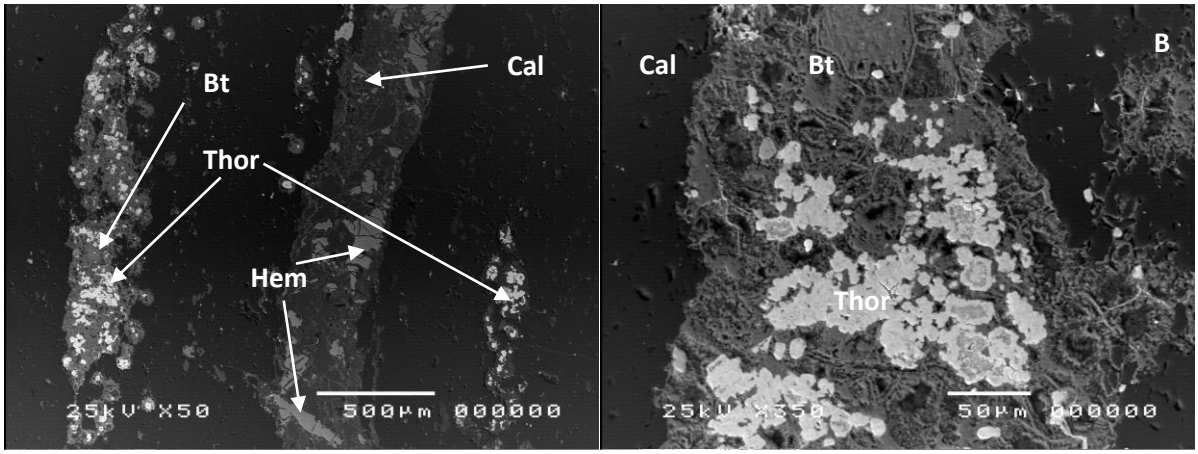

Figure 6.23 a & b. 4086 117.14m CL fails to show thorite mineralisation in an orientated vein. Only under BSE image can the thorite be seen. Thorite appears to be mineralising on its own without noticeable xenotime. Scale bar for CL and PPL measures 1mm.

Another example of the apatite reaction front occurs at 4093 174.20m.

6.4.6 Multi-phase xenotime

Xenotime of different habits and paragenses can exist proximal to each. Xenotime occurs in a range of habits: bands of microcrystalline xenotime associated with apatite, larger xenotime (c. 50µm) in biotite veins, or in chlorite veins associated with fluorite, as demonstrated in Figures 6.24, 6.25 & 6.26.

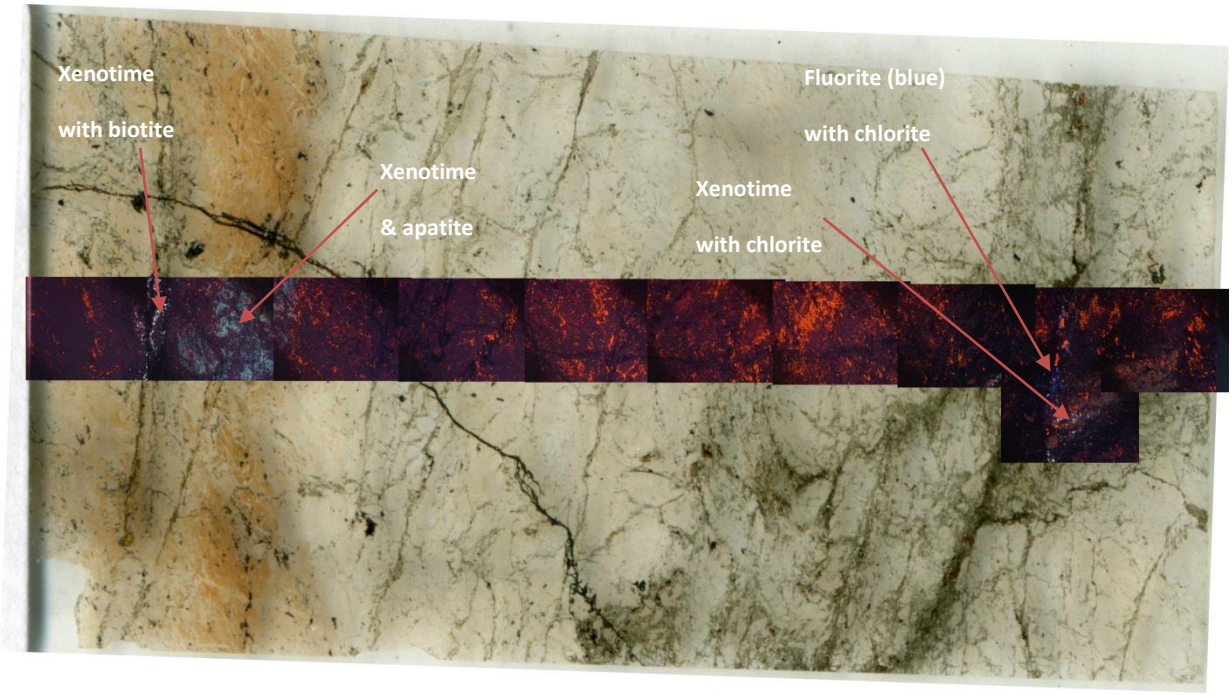

Figure 6.24. 4013 46.93m thin section showing a xenotime mineralised brown smear across the brecciated albitite. Mica lined fractures appear more chloritic to the rhs. FOV 4cm approx.

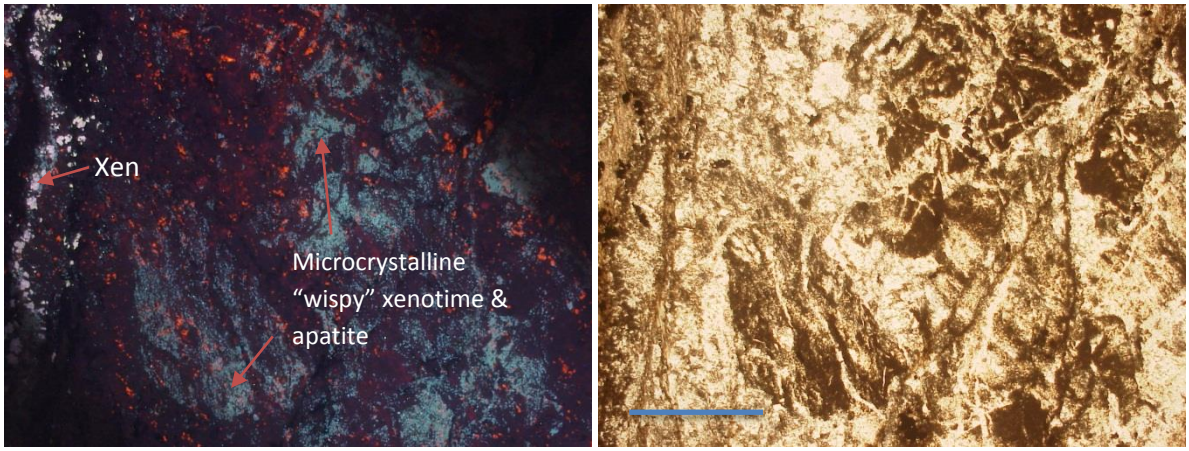

Figure 6.25. 4013 46.93m CL image types of xenotime LHS larger crystals, xenotime w/ apatite, RHS “wispy” fine grained xenotime. The brown “smear” therefore indicates HREE grade. Red scale bar 1mm, blue scale bar 0.5mm.

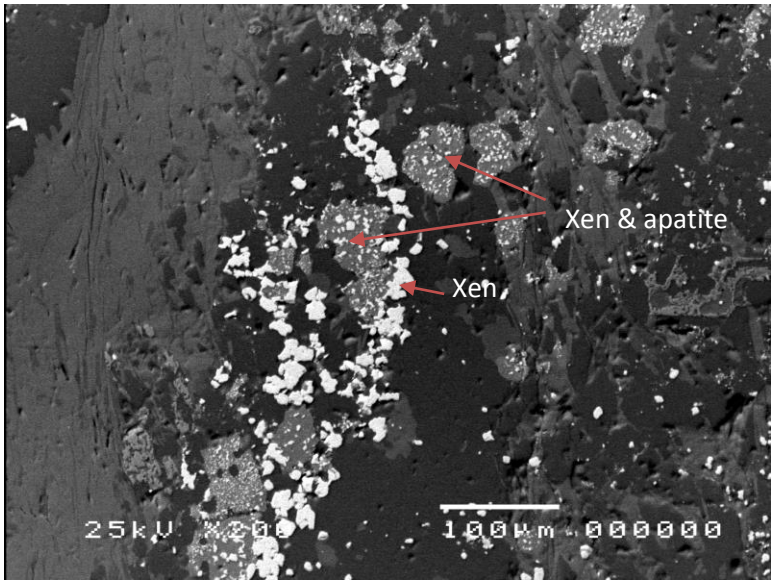

Figure 6.26. 4013 46.93m BSE image close up of Figure 6.25 – Xenotime crystals and apatite with xenotime inclusions or exsolution textures. Xenotime is the bright phase speckles, and the apatite the darker.

6.4.4 Biotite-phlogopite association with xenotime

A common association for xenotime is with biotite-phlogopite mica group minerals, often orientated to shear and reaction fronts as a result of fluid-rock interaction. Sometimes the micas are chloritic pointing to groundwater interaction and/or hydrothermal fluid alteration/transport. Xenotime mineralisation tends to favour these mica hosts and is often found oriented to shear like the micas as demonstrated in Figures 6.27 and 6.28.

Figure 6.27. 4014 65.95m thin section shear orientated micas carry HREE grade (FOV 4cm)

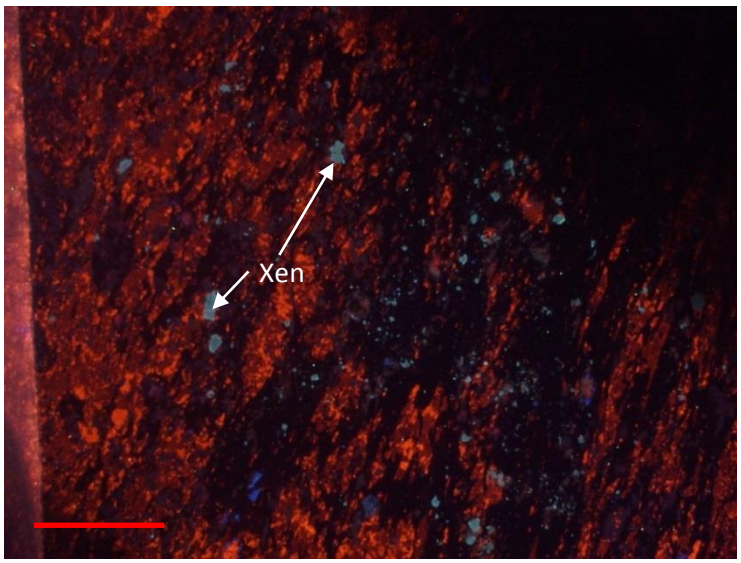

Figure 6.28. 4014 65.95m many subhedral xenotimes, and relatively large (to 50µm), aligned in micaceous shear. Scale bar for CL image 1mm

6.4.7 Heavily overprinted mineralised sections

Intercepts that have undergone a number of overprinting episodes tend to give some of the highest grades. Of course the processes that concentrate the xenotime in this environment are of great interest to this study and to exploration elsewhere on the Lofdal property. Xenotime can be seen to be mineralising at different times in a given overprinted host rock as demonstrated in Figures 6.29 and 6.30. From cross-cutting relationships calcite (with variable Fe content), and not dolomite, appears to be the composition of the later carbonate infusions.

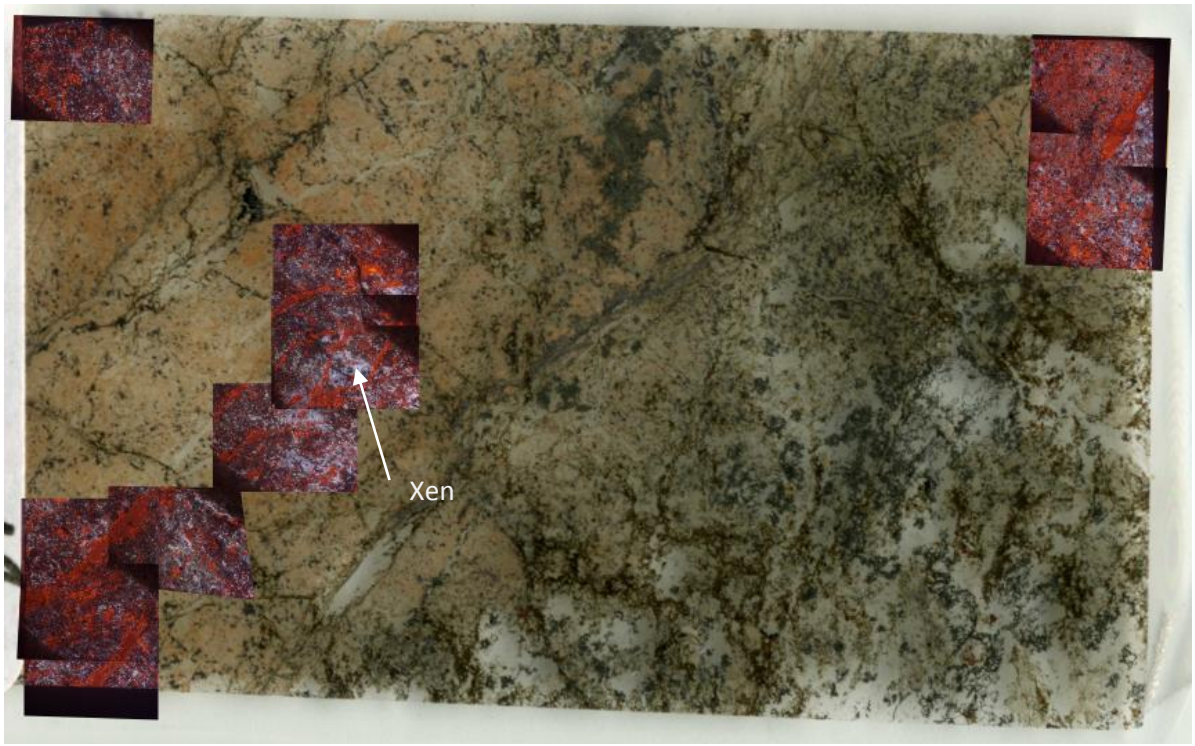

Figure 6.29. 4014-66.45m CL transect slide shear orientation in micas lost and fractures cross-cut and offset– an increasingly fractured and overprinted example compared to 65.95m, also carrying significant HREE grade. Increasingly mineralised in tan section LHS than paler RHS. FOV 35mm.

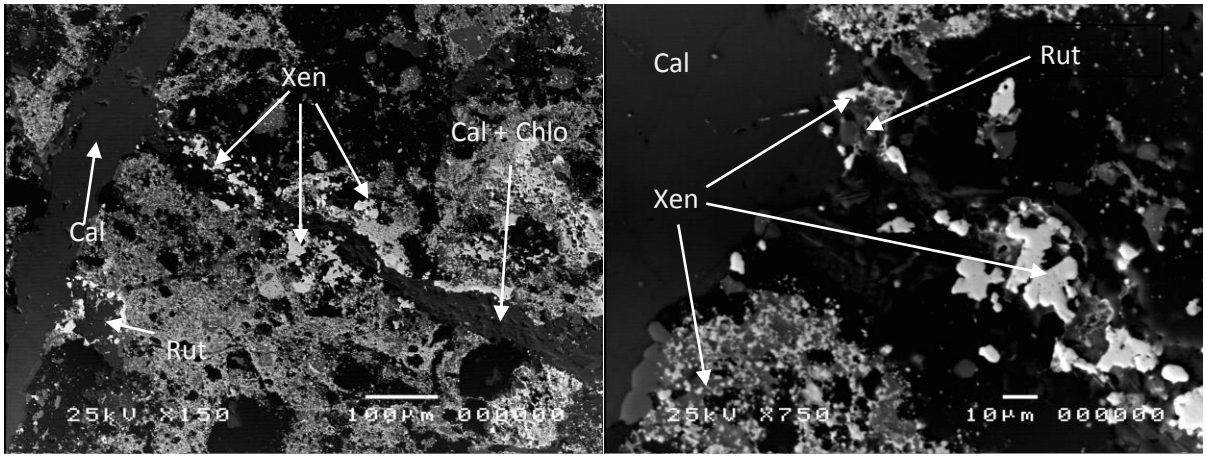

Figure 6.30. 4014-66.45m BSE images calcite cutting xenotime. Xenotime is recrystallizing in later veins, sometimes mantling rutile. RHS close up xenotime at junction to calcite vein

Similar overprints occur in the enriched intercept such as in 4015 38.40m, for example, and again are heavily mineralised as shown in Figure 6.31.

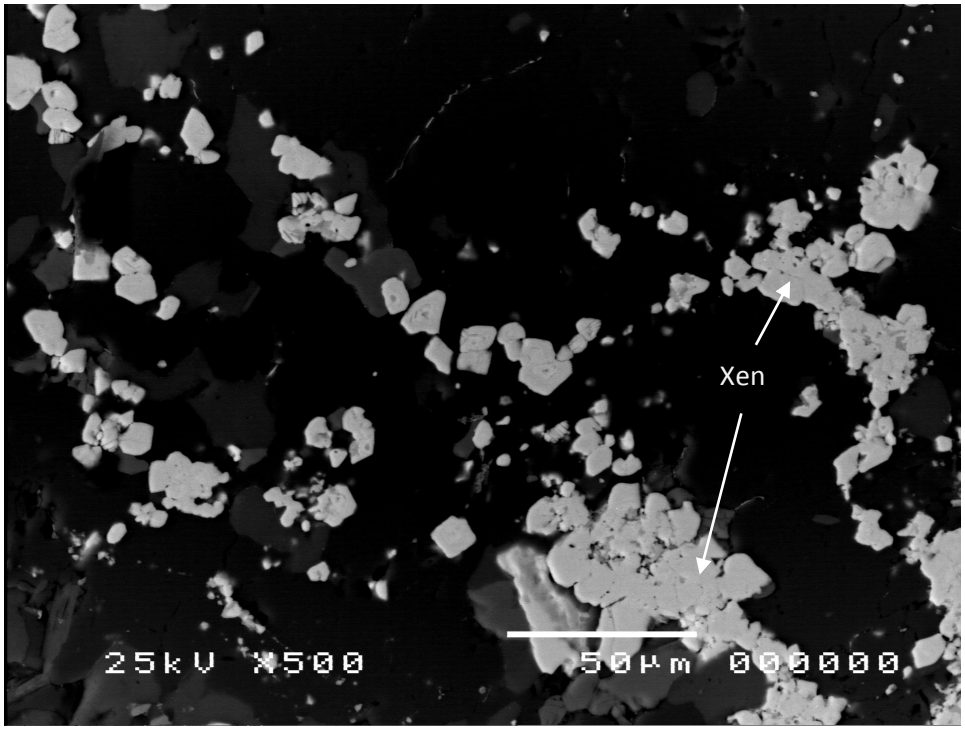

Figure 6.31. 4015-38.40m BSE image of orientated zoned xenotime crystals lining fractures in brecciated albite

The intercept in Hole 4032 at 62.35m is situated below the magnetite associated xenotimes in the hangingwall (on this hole) there is a high grade intercept consisting of fine grained xenotime (Figure 6.32a & b), and older larger grained xenotime with zircon cores, as displayed in Figure 6.33. Thorium appears absent or trace in the fine grained xenotime, and restricted only to thorite, or to older xenotime associated with zircon.

Figure 6.32a. 4032 62.35m core section. Note the mineralisation is concentrated to the RHS where calcite Infusion can be seen. FOV 40mm

Figure 6.32b. 4032 62.35m thin section with CL transect. Note the mineralisation is concentrated to the RHS FOV 40mm

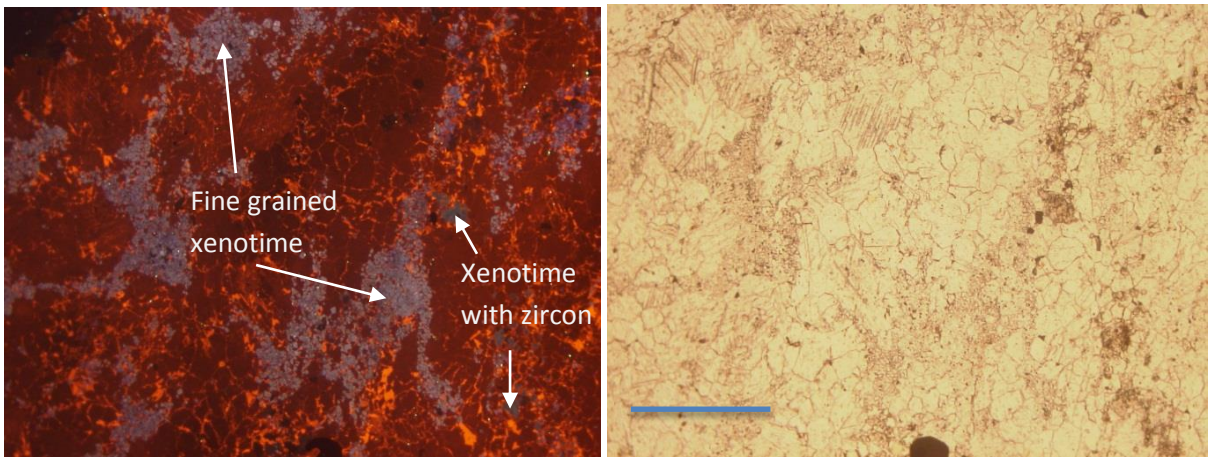

Figure 6.33. 4032 62.35m closer in the albitite appears very finely brecciated and hosting the tiny (<10 µm) xenotimes along grain boundaries, although not along all grain boundaries. A few larger and darker xenotime crystals to RHS in CL of earlier age. CL & PPL. Scale bar 0.5mm

7 MICROPROBE ANALYSIS – EPMA

7.1 Methodology

Electron probe micro-analysis (EPMA) was applied here to discern mineral composition and REE element partitioning in xenotime. It is expected that data recovered may reflect changes and/or differences in the local chemical system of the alteration zone in Area 4, Lofdal.

Mineral compositions were determined by electron microprobe analysis using a JEOL JXA-8200 with 4 wavelength-dispersive spectrometers (WDS), equipped with a range of crystals including individual REE ultra-phosphate standards for the rare earths and a mixture of natural and synthetic, oxide and metal standards were used for other elements (refer to Table 7.1), at Camborne School of Mines (CSM) laboratory. For further standard beam conditions and run beam conditions please refer to Appendix 3. Operating at 15-20Kv and 20-30 nA with a 2 µm to 5 µm spot size, data was corrected using a ZAF matrix correction and empirical corrections for major peak overlaps for Sm on Tb, Tb on Er and Dy on Lu (as used by Williams, 1996).

The small spot size (2 µm to 5 µm) and excitation volume of a focussed electron beam afforded the necessary resolution to study the xenotime crystallisation without ablation or dissolution of the sampled volume. In total 11 polished carbon coated thin sections, representing the different mineralising environments of xenotime in Area 4, were probed across 4 separate runs. Refer to Table 7.2 for sample list.

Points were analysed to confirm mineralogy and identify small xenotime crystals (between 15µm-100 µm). The first step in analysing xenotime was to locate grains in the sample. Coupling the results from CL analysis with SEM/EDS analysis assisted in identifying of probe points of interest.

Xenotime grains were identified from the aforementioned methods and an analytical strategy, or protocol, was devised for gaining useful compositional data.

7.1.1 Considerations

Problems can arise with EPMA analyses of REE phosphates. One must consider the complex REE X-ray spectrum, as well as problems with the choice of standards, variations in the ZAF ratio between standards and samples, inter-element interferences, artefacts from the detector and element detection limits. Defining “true” background can be problematic, in particular with complex spectra such as those from REE- and actinide bearing samples. In addition, viability of certain background locations can vary with electron beam accelerating potentials. (Hetherington, 2008). Inter-element interferences are a major source of difficulty during EPMA analysis of REE minerals. Where the effects of peak overlap are significant a higher resolution detector (e.g. PeTH) was used, at the sacrifice of a lower peak count. Time constraints meant this was not possible for all elements. Automatic peak search during analysis was required to be switched off to stop the software mistaking a nearby high

intensity peak with the peak of interest. This has the unfortunate side effect of removing the ability to compensate for peak drift on long runs (of up to 48 hours) probably caused by stretch in the positioning wire of the detector, leading to smaller concentrations in later analyses than earlier. Some peak overlaps are unavoidable and empirical corrections were applied to elements where major interferences are known, i.e. in xenotime: Sm on Tb, Tb on Er and Dy on Lu (Williams, 1996).

Element	**X-ray**	**Crystal**
Si	Kα	TAP
Na	Kα	TAPH
Dy	Lα	LIF
P	Kα	PETH
Er	Lα	LIF
Y	Lα	PETH
Yb	Lα	LIF
U	Mβ	PETH
Gd	Lα	LIF
Th	Mα	PETH
Ho	Lβ	LIF
Ca	Kα	PETH
Lu	Lβ	LIF
Sm	Lα	LIF
Nd	Lα	LIF
Eu	Lα	LIF
Tb	Lα	LIF
Tm	Lα	LIF

Table 7.1 Standard beam conditions. Crystal acronyms: [a]LiF(H): Lithium Fluoride, [b]TaP(H): Thallium acid phthalate and [c]PetJ(H): Pentaery thritol, H indicates a crystal with a high intensity, lower resolution configuration.

Run	Hole	Depth	Description	Position in the alteration zone

1	4015	38.40m	Xenotime crystals in carbonatised brecciated **albitite**, overprinted by later ankeritic carbonatite	Within main mineralised zone approaching footwall of mineralisation.
1	4086	117.14m	Xenotime crystals in brown ankeritic **carbonatite** overprinting **sheeted albitite**	Within hangingwall of main mineralised zone
1	4086	118.80m	Xenotime crystals in brown ankeritic **carbonatite** crosscutting **brecciated albitite**	Within main mineralised zone
1 & 4	4092	188.15m	Xenotime crystals primarily in **biotite-phlogopite veins**	Within hangingwall to main mineralised zone.
3	4014	65m	Xenotime amongst biotite and chlorite rich host exhibiting shear fabric	Within hanging wall to main mineralised intercept
3	4014	66m	Brecciated and overprinted main albitite	Within main mineralised zone
2	4081	73m	Xenotime in dolomitic carbonatite	Dolomitic veining hangingwall of main mineralised intercept
2	4081	80m	Xenotime in brecciated albitite	Within main mineralised zone
2	4013	48m	Xenotime associated with apatite aka "wispy" type plus larger crystals in vein	Hangingwall of main mineralised intercept
4	4020	38.90	Carbonatised fractured albitite	Hangingwall of mineralised zone
4	4082	92.20	HREE in fractured albitite with rutile	Main mineralised zone

Table 7.2 - Nominated thin sections used for EPMA analysis of xenotime composition

Element detection limits are a major source of analytical error when analysing xenotime. Elements were considered below the detection limit when the counts per second (cps) were below that of the conventional three standard deviations of the background value. Where elements approached this value the error in the background value begins to seriously affect the concentration, it is common to

increase the count time on backgrounds to compensate for this, however this was not carried out to strip down analysis time, and background count times were half those of the peak times for all elements. The designated protocol was set up and the microprobe was left running over 1-3 days for each run to compile the element maps and perform detailed analysis on each of the designated points on all respective samples.

7.1.2 Microprobe Qa/Qc

Results for the nominated elements are given in wt. % oxide. Lu data is unreliable being highly variable, occasionally giving minus values on Run 1, and wasn't relied upon from the additional 4 runs. Some of the low or skewed values could be attributed to "mixed-mineral analyses" with the spot size of 5 µm measuring some xenotimes not much wider than that during Run 1. During runs 2, 3 and 4 the spot size was reduced to 2 µm. Excessive zircon overlap for example will not adversely affect the shape of the REE patterns because zircon is similarly HREE enriched, but most of the element abundances in xenotime will be lowered by dilution with zircon (Hetherington, 2008). However, Zr values are treated with caution from Run 1 because of the close peak positions in WDS analysis of Zr and P.

Analyses were obtained from grains as small as a few µm in diameter. Because of the potential for "mixed-mineral analyses" (i.e., analyses that include a component from sub-5µm inclusions), only those with oxide totals of 98.0 to 102.0 wt. % are accepted as reliable analyses. This results in a high exclusion rate, a consequence of the small grain size and porous, inclusion-rich nature of xenotime. Furthermore, analyses with >1.0 wt. % ZrO_2 have been omitted as xenotime-zircon mixtures.

7.2 Samples for analysis

It is proposed that variance in fractionation of the REE in xenotime, from differing parageneses, can assist in better understanding of the physio/chemical nature of mineralisation, and fluid characteristics of the alteration in Area 4. Choosing samples for EPMA analysis involved probing a range of xenotime mineralised sections with particular host textures and mineral associations. In some cases samples were chosen to see variation downhole, for example across a range of 55cm in Hole 4014. See Table 7.3 for condensed details.

From the studies of the mineralised intercepts, and closer petrological work, it was possible to recognise certain trends in the composition of the xenotimes, between the different host rocks and mineralising styles. Data have been used to generate a range of chondrite normalised REE plots for REE content in the xenotimes (normalised to McDonough & Sun, 1995). As a whole the xenotimes follow a general flat profile into the heavier REEs, with a varying degree of "humpback" in the MREE.

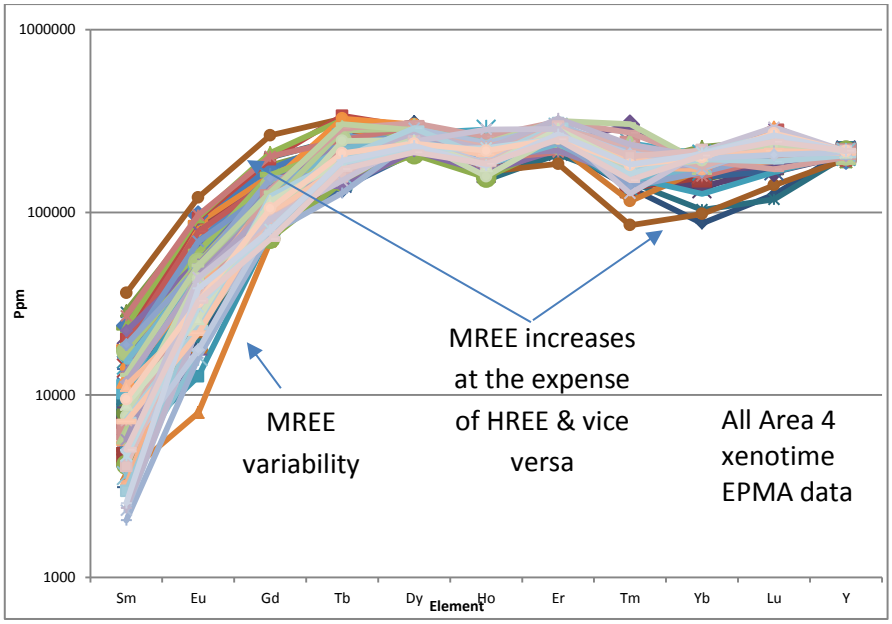

Figure 7.1 Typical normalised chondrite patterns of xenotimes across the alteration zone. Xenotimes show a general HREE enriched trend, and no Eu anomaly. There's variance in most heavy lanthanides, notably in Yb, but especially in the MREEs Sm-Gd. (Normalised against chondrite data from McDonough & Sun, 1995).

7.3 Results from xenotime analysis

All chondrite plots display HREE enrichment (Figure 7.1 as an example), with no negative Eu anomaly as expected from carbonatite-related xenotime, and in this regard, the compositions match the chondrite normalised trends from the alteration zone whole-rocks as displayed in Figure 4.8. Granite related xenotimes invariably display negative Eu anomalies as Eu favours plagioclase during fractionation. Distribution of the HREEs appears relatively evenly distributed. There appears to be variability in Eu and Tm. Generally data shows bias for MREEs in the expense of the heavier HREEs. Dy is one of the more stable REEs in terms of fractionation variance, this being the most important HREE economically today, and showing that the metal is present in appreciable amounts across the xenotime paragenses in the study area.

For **full results from xenotime analysis** please refer to **Appendix 3**. A table of xenotime characteristics across the holes is summarised in Table 7.3. Results from xenotime EPMA analysis are displayed in Table 7.4.

Table 7.3 Xenotime characteristics over REE enriched intercepts in Area 4 Lofdal. EPMA samples highlighted in bold, REE wholerock intercepts in bold

Hole	From	To inclu	Colour anomally	Core condition	EP SAMPLE	Type Xenotime mineralisation	Morphology	Xen grain size	Para	THREE	TLREE	Th	Zr	Nb	P	Associates
4013	34	35.2	Light brown to reddened brecci	Solid, but fault from 36.40m		Magnetite/sulphide (zircon cores sometimes) in ankertic carb	Subh	up to 1mm	1	**2500**	200-1000	250	800	250		Magnetite, py, zirc
4013	37		Light coloured albitite	Solid		LREE in fragmented footwall albitite				**500**	2200	150	150	150		
4013	45	47	Subtle	Solid	**46.93m**	In mica lined fractures, in ankeritic clouds in apatite	Subh, exsol	To 50µm, 5µm in ap	2(3)	**6800**	200-1000	200	2250	350		Apa, fluorite
4014	55	59	Subtle	Some fault fragmentation		n/a				**500**	1800	50	1000	500		
4014	65.5	66.13	Biotite w/ brick red overprint	Solid	**65.95m, 66.50**	Subhedral in black mica veins 66m, fine grain choatic fracturin	Aggr, fg xtals	>5µm - 500 µm agg		**1.42%**	1100	2300	4100	500		Rut
4081	73	74	Cream dolomite	Solid	**73.50m**	n/a				**2700**	1800	460	625	150	3200	Apa, monaz
4081	80	81	Mottled albitite	Solid, footwall of fault goug	**80.60m**	course crystals, quite a few with zircon cores, plus minor synch	Anh	50-100µm	1	**1.29%**	200	300	1500	730	8000	Zirc, synchy
4081	85	87	Caramel fractured albitite	Solid	**87.50m**	As above, more contained to fractures in a finer grained albiti	Anh	50-100µm	1	**7400**	1500	420	2000	600	7800	Zircon
4088	116	120	Ankeritic dolomitic carbonatite	Solid		Eye-visible crystals in carbonatite	Subh	<100µm	?	**1.12%**	800	815	1000	300	7400	
4088	124		Magnetitic carbonatite			n/a				**1000**	1700	300	300	300	3000	
4095	134	137	Black mica to brick red			In black mica veins, fine grained choatic fracturing	?	?	?	**4600**	500	850	400	250	3100	
4015	28	30	Yes, brown	solid between fault breccia		Subhedral crystals with apatite, a few with zircon, 30.40 like 40	Subh	50-100µm	2	**8600**	1400	300	1100	930		Apa, Zirc
4015	33	36		orietated fracture		grade in fractures, akin to sample at 30.40m				**9100**	300	300	950	1270		Apa
4015	37	38	No	micro-fractures+ overprints	**38.40m**	Mass fined grained crystals (akin 4014), aggregates thereof	Subh	5>	2	**7%**	1100	1220	700	400		Rut
4037	54	57	Brown ferruginous	Fragmented		?	?	?	?	**1.40%**	1100	415	1600	1320		
4037	59	62	No	Fragmented		n/a				**1000**	2300	150	500	250		
4031	22	25.9	Ankeritic carbonatite	Solid, occasionally fractured		Subhedral crystals with apatite, a few with zircon, 30.40 like 40	Apa front	50-100µm	2	**1.20%**	700	520	1550	200		Apa, monaz, rut
4031	72	75	Light brown	Solid, occasionally fractured		subhedral crystals in veins assoc zircon		20-100µm		**1.49%**	500	780	7100	1000		Zirc
4031	83					n/a				**300**	4000	150	1100	200		
4086	17	23	Ankeritic/dolomitic carbonatite	Solid	**117.14m, 118.80**	Xenotime ~50micron & exsolution apatite w/xenotime	Subh to euhe	1µm-50µm	2	**4.50%**	1500	2000	1350	450	3.10%	Apa, thorite, minor rut
4092	188	194	Mottled dark brick red & biotite	Solid	**188.15m**	Course euhedral crystals, esp assoc biotite, to 8mm.	Subh to euhe	50µm to 8mm	1 (2)	**3.50%**	1200	6500	1150	620	2.37%	Thorite, py, apa, zir
4096	256		Mottled dark brick red & biotite	Solid		In stringers with black mica (like diluted 4092)				**6100**	250	250	1000	450	5200	
4096	262	264	Mottled dark brick red & biotite	Solid		Again assoc black mica and ractured brick red material				**4300**	750	1220	750	200	4500	
4096	274	276	Shear orientated	Solid		Caramel shear orientated above footwall				**5100**	1700	500	2620	250	9000	
4019	26		Shear orientated	Below fault frag and gouge		Xen associated zircon				**1.29%**	2000	950	1%	950		Zirc
4020	38	40	Reddened	Fragments and gouge	**38.90m**	Xen with rutile, apatite, zircon	Subh to euhe	10-100µm	2(3)	**1.06%**	1600	500	7600	810		Apa, ru, zirc
4020	42	43	Less reddened	Fragments and gouge						**1750**	2400	200	1000	200		
4032	47		Magnetitic carbonatite	solid but fractured		assoc w/ apatite and LREEs	Subh to euhe	10-100µm	1	**1400**	2900	450	2000	500		Apa, thorite, synchy
4032	57	62	None	Below fault gouge and fragments		assoc w/ apatite and LREEs, sporadic zircon cores		1	2	**6400**	3200	1000	2850	750		Apa & monaz, synchy
4082	91	92	slight browning	Solid, overprinted	**92.20m**	assoc w/ apatite & rutile		50-250µm	1	**2.19%**	2500	510	2250	750	1.50%	Apa
4087	131	132	Magnetitic carbonatite	solid but fractured		assoc w/ apatite and LREEs	Subh to euhe	10-100µm	1	**7500**	1900	640	1450	300	6000	Apa & py
4087	139		Brown brecciated albitite		**139.88m**	Large with zircon cores, and fine grained (less apatite)	Subh	1µm-100µm	2	**3.15%**	500	1940	2500	600	1.50%	Zirc cores only
4093	172	177	Pale carbonatised albitite	Solid, reddened fractures		Xen in ankerite, next to apatite front				**1.16%**	2000	550	1500	600	8100	Apa

Table 7.4 Results from electron microprobe analysis of xenotime composition from Lofdal Area 4 Alteration Zone. Results are firstly presented in weight per cent oxide, followed by atoms per formula unit (apfu) based on sixteen atoms of oxygen. * Zr from run 1 can be regarded as eroneous, because of Zr Lα peak overlap with P Kα peak.

ELEMENT			AVERAGE	SD			AVERAGE	SD			AVERAGE	SD			AVERAGE	SD		AVERAGE	SD			AVERAGE	SD			AVERAGE	SD
	4015_5	4015_9	**Av30**	δ	86_117_28	86_117_29	**Av 5**	δ	86_118_02	86_118_09	**Av12**	δ	14_65_32	14_65_41	**Av 20**	δ	14_66_55	**Av 10**	δ	4013v_7	4013v_10	**Av 8**	δ	13_48_22	13_48_32	**Av 7**	δ
SiO2	1.10	0.53	**0.69**	0.40	1.34	0.259	**0.45**	0.51	0.95	0.72	**0.85**	0.83	0.28		**0.21**	0.15	1.15	**0.67**	0.22	0.35	2.09	**0.69**	0.58	0.32	0.06	**0.24**	0.15
P2O5	36.05	36.40	**36.69**	1.63	37.07	39.111	**38.76**	1.04	37.65	37.59	**37.99**	1.46	36.74	37.43	**36.75**	0.76	35.56	**35.69**	0.51	37.12	35.17	**36.20**	0.68	36.24	35.70	**35.78**	0.40
CaO	0.94	0.07	**0.65**	1.45	1.69	0.048	**0.40**	0.72	0.11	0.13	**0.40**	0.85	0.03	0.05	**0.06**	0.04	0.08	**0.10**	0.04	0.05	0.32	**0.14**	0.10	0.17	0.28	**0.15**	0.11
Na2O													0.03	0.04	**0.04**	0.00	0.04	**0.04**	0.00	0.06	0.14	**0.06**	0.03	0.15	0.04	**0.13**	0.11
TiO2	0.02	0.00	**0.03**	0.08	0.02	0.014	**0.01**	0.01	-0.01	0.01	**0.00**	0.01															
* **ZrO2**	6.82	5.72	**6.07**	0.92	5.47	5.401	**5.23**	0.19	6.57	6.12	**6.01**	0.89															
Y2O3	39.24	41.65	**40.95**	1.26	39.08	42.292	**42.17**	1.86	39.01	38.24	**40.52**	2.30	46.58	46.80	**45.14**	0.98	46.60	**43.68**	1.87	45.21	44.33	**44.85**	0.46	43.19	41.76	**42.60**	0.55
Sm2O3	0.11	0.08	**0.10**	0.02	0.30	0.113	**0.23**	0.12	0.43	0.13	**0.19**	0.09	0.09	0.10	**0.09**	0.02	0.08	**0.24**	0.09	0.24	0.21	**0.28**	0.10	0.06	0.17	**0.13**	0.07
Eu2O3	0.18	0.14	**0.15**	0.03	0.23	0.185	**0.23**	0.06	0.42	0.21	**0.21**	0.08	0.17	0.17	**0.14**	0.03	0.16	**0.27**	0.09	0.26	0.22	**0.32**	0.10	0.05	0.27	**0.20**	0.13
Gd2O3	1.59	1.47	**1.55**	0.13	2.72	1.585	**2.35**	0.69	3.00	2.61	**2.09**	0.53	1.19	1.25	**1.04**	0.17	1.22	**1.61**	0.57	1.90	1.92	**2.42**	0.62	1.59	2.95	**2.24**	0.66
Tb2O3	0.56	0.50	**0.52**	0.04	0.52	0.525	**0.58**	0.11	0.65	0.77	**0.56**	0.16	0.42	0.48	**0.43**	0.05	0.48	**0.51**	0.07	0.50	0.53	**0.59**	0.12	0.87	0.96	**0.78**	0.12
Dy2O3	4.78	4.67	**4.64**	0.31	4.42	4.438	**4.59**	0.35	4.69	5.79	**4.49**	0.92	4.83	5.02	**4.67**	0.25	5.30	**5.37**	0.45	4.84	6.11	**5.70**	0.66	6.52	8.66	**6.92**	0.97
Ho2O3	1.02	1.06	**1.07**	0.10	0.78	0.902	**0.94**	0.11	0.92	1.19	**1.06**	0.15	1.11	1.05	**1.10**	0.11	1.11	**1.03**	0.14	1.43	1.37	**1.36**	0.12	1.11	1.16	**1.18**	0.13
Er2O3	3.31	3.43	**3.42**	0.27	2.26	2.959	**2.59**	0.27	2.91	3.17	**2.82**	0.39	4.18	4.25	**4.12**	0.20	3.49	**3.45**	0.27	4.34	3.24	**3.64**	0.40	4.83	4.38	**4.51**	0.20
Tm2O3	0.34	0.39	**0.47**	0.07	0.24	0.519	**0.38**	0.15	0.39	0.40	**0.40**	0.09	0.60	0.60	**0.60**	0.00	0.60	**0.60**	0.00	0.25	0.28	**0.17**	0.12	0.60	0.44	**0.56**	0.07
Yb2O3	3.25	3.22	**3.10**	0.23	1.99	2.683	**2.21**	0.36	2.61	2.65	**2.52**	0.25	3.47	3.42	**3.31**	0.18	2.30	**2.45**	0.35	3.41	2.57	**2.89**	0.35	3.68	2.32	**3.22**	0.47
UO2	0.10	0.00	**0.03**	0.03	0.06	0.028	**0.03**	0.04	0.02	0.04	**0.01**	0.02															
Lu2O3	0.09	0.07	**0.15**	0.07	0.04	0.070	**0.06**	0.09	0.02	-0.03	**0.04**	0.07	0.42	0.32	**0.28**	0.07	0.21	**0.23**	0.03	0.00	0.00	**0.03**	0.05	0.78	0.46	**0.62**	0.10
ThO2	0.68	0.32	**0.38**	0.17	0.38	0.154	**0.28**	0.08	0.50	0.82	**0.42**	0.29	0.42	0.09	**0.20**	0.12	0.19	**0.35**	0.23	0.20	1.17	**0.43**	0.37	0.02	0.04	**0.03**	0.03
PbO	0.17	0.15	**0.17**	0.02	0.16	0.185	**0.15**	0.05	0.15	0.15	**0.16**	0.01															
Total	100.91	100.08	**101.19**		99.06	101.471	**101.89**		101.24	100.99	**101.01**		100.56	101.06	**98.04**	1.36	98.56	**96.19**	1.19	100.17	99.67	**99.77**	0.97	100.19	99.65	**99.31**	1.35
APFU																											
Si	0.15	0.07	**0.09**		0.03	0.13	**0.06**		0.01	0.39	**0.25**		0.01	0.07	**0.02**		0.07	**0.08**		0.05	0.27	0.10		0.04	0.01	**0.03**	
P	4.12	4.15	**4.14**		4.29	4.22	**4.26**		4.37	3.68	**4.02**		4.14	4.07	**4.10**		4.14	**4.05**		4.15	3.82	4.05		4.19	4.03	**4.05**	
Ca	0.14	0.01	**0.09**		0.01	0.02	**0.01**		0.01	0.04	**0.06**		0.00	0.01	**0.01**		0.01	**0.02**		0.01	0.04	0.02		0.02	0.04	**0.02**	
Ti	0.00	0.00	**0.00**		0.00	0.00	**0.00**		0.00	0.00	**0.00**		0.00	0.00	**0.00**		0.00	**0.00**						0.00	0.00	**0.00**	
Y	2.82	2.99	**2.91**		2.99	2.75	**2.90**		3.07	2.43	**2.72**		3.28	3.17	**3.16**		3.16	**3.06**		3.18	3.03	3.12		3.14	2.96	**3.03**	
Sm	0.00	0.00	**0.00**		0.01	0.02	**0.01**		0.00	0.01	**0.01**		0.00	0.00	**0.00**		0.00	**0.01**		0.01	0.01	0.01		0.00	0.01	**0.01**	
Eu	0.01	0.01	**0.01**		0.01	0.02	**0.01**		0.01	0.01	**0.01**		0.01	0.00	**0.00**		0.00	**0.01**		0.01	0.01	0.01		0.00	0.01	**0.01**	
Gd	0.07	0.07	**0.07**		0.07	0.13	**0.09**		0.06	0.09	**0.08**		0.05	0.04	**0.05**		0.04	**0.08**		0.08	0.08	0.08		0.07	0.13	**0.10**	
Tb	0.02	0.02	**0.02**		0.02	0.03	**0.02**		0.02	0.03	**0.02**		0.02	0.02	**0.02**		0.02	**0.02**		0.02	0.02	0.02		0.04	0.04	**0.03**	
Dy	0.21	0.20	**0.20**		0.19	0.20	**0.19**		0.15	0.20	**0.18**		0.20	0.20	**0.20**		0.27	**0.24**		0.21	0.25	0.24		0.29	0.37	**0.30**	
Ho	0.04	0.05	**0.05**		0.04	0.04	**0.04**		0.04	0.04	**0.04**		0.05	0.05	**0.05**		0.05	**0.04**		0.06	0.06	0.05		0.05	0.05	**0.05**	
Er	0.14	0.14	**0.14**		0.12	0.12	**0.11**		0.11	0.12	**0.11**		0.18	0.19	**0.17**		0.17	**0.15**		0.18	0.13	0.15		0.21	0.18	**0.19**	
Tm	0.01	0.02	**0.02**		0.02	0.02	**0.02**		0.02	0.02	**0.01**		0.03	0.02	**0.02**		0.03	**0.03**		0.01	0.01	0.02		0.03	0.02	**0.02**	
Yb	0.13	0.13	**0.13**		0.11	0.11	**0.10**		0.10	0.11	**0.10**		0.14	0.14	**0.13**		0.11	**0.10**		0.14	0.10	0.11		0.15	0.09	**0.13**	
Lu	0.00	0.00	**0.01**		0.00	0.00	**0.00**		0.00	0.00	**0.00**		0.02	0.01	**0.01**		0.01	**0.01**		0.00	0.00	0.00		0.03	0.02	**0.03**	
Th	0.02	0.01	**0.01**		0.00	0.02	**0.01**		0.00	0.04	**0.02**		0.01	0.00	**0.01**		0.01	**0.01**		0.01	0.04	0.01		0.00	0.00	**0.00**	
U	0.00	0.00	**0.00**		0.00	0.00	**0.00**		0.00	0.00	**0.00**		0.00	0.00	**0.00**		0.00	**0.00**						0.00	0.00	**0.00**	
Pb	0.01	0.01	**0.01**		0.01	0.00	**0.00**		0.01	0.00	**0.01**		0.00	0.00	**0.00**		0.00	**0.00**						0.00	0.00	**0.00**	
Zr	0.45	0.38	**0.40**		0.32	0.35	**0.33**		0.42	0.40	**0.42**																
F	0.42	0.17	**0.28**		0.16	0.22	**0.17**		0.19	0.20	**0.20**																
O	8.11	8.09	**8.03**		7.79	7.95	**7.75**		7.96	8.00	**8.11**		8.14	7.74	**7.91**		8.16	**8.06**		7.94	7.71	7.93		8.20	8.01	**8.04**	
P site	4.44	4.25	**4.35**		4.34	4.38	**4.40**		4.40	4.15	**4.36**		4.16	4.15	**4.14**		4.23	**4.16**		4.21	4.17	4.18		4.26	4.08	**4.11**	
Y site	3.47	3.63	**3.55**		3.56	3.43	**3.59**		3.59	3.06	**3.29**		3.98	3.85	**3.82**		3.85	**3.75**		3.90	3.70	3.82		4.01	3.89	**3.90**	

Table 7.4 continued. Results from electron microprobe analysis of xenotime composition from Lofdal Area 4 Alteration Zone. Results are firstly presented in weight per cent oxide, followed by atoms per formula unit (apfu) based on sixteen atoms of oxygen.

ELEMENT			AVERAGE	SD			AVERAGE	SD			AVERAGE	SD			AVERAGE	SD			AVERAGE	SD			AVERAGE	SD
	4092_2	4092_8	**Av 11**	δ	4020_7	4020_12	**Av 18**	δ	4082_6	4082_12	**Av 12**	δ	81_73_05	81_73_10	**Av 18**	δ	81_80_02	81_80_12	**Av 13**	δ	87_03	87_09	**Av 12**	δ
SiO2	0.13	0.28	**0.38**	0.35	0.21	0.13	**0.38**	0.30	0.38	0.21	**0.33**	0.35	0.09	0.02	**0.28**	0.60	0.23	0.82	**0.19**	0.27	0.13	0.00	**0.07**	0.08
P2O5	37.79	36.63	**37.04**	0.80	37.05	36.16	**36.96**	0.70	36.51	35.88	**37.03**	0.67	37.22	37.15	**36.49**	1.28	36.85	35.82	**36.81**	0.70	36.00	37.22	**36.80**	0.58
CaO	0.19	0.06	**0.13**	0.12	0.15	0.16	**0.15**	0.08	0.09	0.07	**0.09**	0.03	0.11	0.08	**0.09**	0.03	0.05	0.06	**0.07**	0.05	0.09	0.03	**0.04**	0.02
Na2O	0.03	0.02	**0.03**	0.01	0.04	0.03	**0.04**	0.01	0.03	0.04	**0.04**	0.01	0.05	0.04	**0.02**	0.02	0.05	0.00	**0.02**	0.03	0.00	0.00	**0.02**	0.02
Y2O3	47.24	46.53	**47.27**	1.09	43.01	43.63	**44.00**	1.78	45.76	41.50	**45.25**	1.48	46.26	45.78	**46.24**	1.48	46.33	42.48	**45.87**	2.23	46.55	45.60	**45.81**	0.81
Sm2O3	0.13	0.22	**0.21**	0.14	0.19	0.25	**0.20**	0.09	0.18	1.49	**0.28**	0.39	0.00	0.12	**0.11**	0.15	0.00	0.18	**0.14**	0.07	0.00	0.12	**0.02**	0.06
Eu2O3	0.16	0.26	**0.26**	0.17	0.30	0.31	**0.30**	0.13	0.23	0.62	**0.25**	0.13	0.09	0.14	**0.16**	0.20	0.19	0.26	**0.20**	0.09	0.11	0.00	**0.07**	0.08
Gd2O3	1.35	1.68	**1.67**	0.55	2.47	2.71	**2.30**	0.66	1.73	4.58	**1.97**	0.85	1.14	2.01	**1.78**	1.39	1.76	2.12	**1.78**	0.43	1.18	1.13	**1.31**	0.24
Tb2O3	0.44	0.40	**0.47**	0.05	0.64	0.72	**0.67**	0.16	0.56	0.56	**0.55**	0.05	0.36	0.48	**0.45**	0.23	0.60	0.57	**0.52**	0.12	0.43	0.45	**0.49**	0.07
Dy2O3	4.59	4.31	**4.60**	0.45	5.97	5.73	**5.71**	0.67	5.36	6.13	**5.34**	0.38	5.04	5.93	**5.02**	0.88	4.98	5.34	**5.17**	0.38	4.88	4.81	**4.88**	0.33
Ho2O3	1.26	1.40	**1.30**	0.11	1.40	1.53	**1.43**	0.14	1.39	1.29	**1.44**	0.10	1.48	1.16	**1.27**	0.13	1.24	1.56	**1.27**	0.18	1.25	1.34	**1.36**	0.10
Er2O3	4.39	4.04	**3.70**	0.43	4.26	4.24	**4.13**	0.31	4.19	3.46	**4.28**	0.31	3.91	2.97	**3.58**	0.45	4.05	4.69	**4.05**	0.56	4.53	4.70	**4.60**	0.18
Tm2O3	0.40	0.40	**0.32**	0.08	0.40	0.36	**0.38**	0.10	0.41	0.19	**0.43**	0.08	0.43	0.11	**0.28**	0.17	0.33	0.28	**0.35**	0.07	0.54	0.40	**0.45**	0.10
Yb2O3	2.65	3.48	**2.58**	0.37	3.18	3.37	**3.20**	0.58	3.14	2.66	**3.28**	0.29	3.43	2.37	**2.98**	0.51	3.40	4.36	**3.49**	0.49	3.86	3.96	**4.00**	0.26
Lu2O3	0.37	0.47	**0.37**	0.07	0.60	0.61	**0.59**	0.09	0.59	0.45	**0.55**	0.07	0.00	0.00	**0.00**	0.01	0.00	0.23	**0.08**	0.12	0.00	0.23	**0.09**	0.10
ThO2	0.17	0.49	**0.59**	0.45	0.88	0.18	**0.40**	0.38	0.15	0.17	**0.18**	0.10	0.10	0.19	**0.21**	0.10	0.11	0.77	**0.17**	0.24	0.25	0.11	**0.14**	
Total	101.19	100.62	**100.85**	0.60	100.68	100.01	**100.76**	1.14	100.59	99.23	**101.18**	1.18	99.71	98.55	**98.96**	1.85	100.17	99.55	**100.17**	1.55	99.81	100.11	**100.16**	0.85
APFU																								
Si	0.02	0.04	**0.05**		0.03	0.02	**0.05**		0.05	0.03	**0.04**		0.02	0.04	**0.04**		0.03	0.11	**0.02**		0.02	0.00	**0.01**	
P	4.25	3.98	**4.06**		4.16	3.92	**4.05**		4.04	3.93	**4.03**		3.97	4.00	**4.05**		4.09	3.93	**4.04**		3.98	4.13	**4.07**	
Ca	0.03	0.01	**0.02**		0.02	0.02	**0.02**		0.01	0.01	**0.01**		0.02	0.01	**0.01**		0.01	0.01	**0.01**		0.01	0.00	**0.01**	
Y	3.34	3.18	**3.26**		3.04	2.97	**3.03**		3.18	2.85	**3.10**		3.19	3.24	**3.22**		3.24	2.93	**3.16**		3.23	3.18	**3.18**	
Sm	0.01	0.01	**0.01**		0.01	0.01	**0.01**		0.01	0.07	**0.01**		0.00	0.00	**0.01**		0.00	0.01	**0.01**		0.00	0.01	**0.00**	
Eu	0.01	0.01	**0.01**		0.01	0.01	**0.01**		0.01	0.03	**0.01**		0.00	0.00	**0.01**		0.01	0.01	**0.01**		0.00	0.00	**0.00**	
Gd	0.06	0.07	**0.07**		0.11	0.11	**0.10**		0.08	0.20	**0.08**		0.05	0.04	**0.08**		0.08	0.09	**0.08**		0.05	0.05	**0.06**	
Tb	0.02	0.02	**0.02**		0.03	0.03	**0.03**		0.02	0.02	**0.02**		0.01	0.01	**0.02**		0.03	0.02	**0.02**		0.02	0.02	**0.02**	
Dy	0.20	0.18	**0.19**		0.26	0.24	**0.24**		0.23	0.26	**0.22**		0.19	0.18	**0.21**		0.21	0.22	**0.22**		0.21	0.20	**0.21**	
Ho	0.05	0.06	**0.05**		0.06	0.06	**0.06**		0.06	0.05	**0.06**		0.05	0.05	**0.05**		0.05	0.06	**0.05**		0.05	0.06	**0.06**	
Er	0.18	0.16	**0.15**		0.18	0.17	**0.17**		0.17	0.14	**0.17**		0.14	0.12	**0.15**		0.17	0.19	**0.16**		0.19	0.19	**0.19**	
Tm	0.02	0.02	**0.01**		0.02	0.01	**0.02**		0.02	0.01	**0.02**		0.02	0.01	**0.01**		0.01	0.01	**0.01**		0.02	0.02	**0.02**	
Yb	0.11	0.14	**0.10**		0.13	0.13	**0.13**		0.13	0.10	**0.13**		0.11	0.11	**0.12**		0.14	0.17	**0.14**		0.15	0.16	**0.16**	
Lu	0.01	0.02	**0.01**		0.02	0.02	**0.02**		0.02	0.02	**0.02**		0.00	0.00	**0.00**		0.00	0.01	**0.00**		0.00	0.01	**0.00**	
Th	0.01	0.02	**0.02**		0.03	0.01	**0.01**		0.00	0.01	**0.01**		0.01	0.01	**0.01**		0.00	0.02	**0.01**		0.01	0.00	**0.00**	
O	7.99	7.72	**7.77**		7.97	7.69	**7.78**		7.85	7.77	**7.72**		7.66	7.82	**7.87**		7.88	7.79	**7.79**		7.84	7.88	**7.85**	
P site	4.30	4.04	**4.14**		4.24	3.96	**4.13**		4.11	3.97	**4.09**		4.01	4.06	**4.11**		4.13	4.07	**4.08**		4.02	4.14	**4.09**	
Y site	4.01	3.86	**3.89**		3.86	3.78	**3.81**		3.92	3.75	**3.85**		3.76	3.78	**3.87**		3.93	3.74	**3.86**		3.93	3.89	**3.90**	

8 DISCUSSION

A main aim of this study is to find out where, and ultimately why, the xenotime sits where it does in the alteration zone of Area 4. Before moving on to the interpretation of the xenotime analysis, there will be a review of the spatial characteristics of the REE mineralisation in the study area of Area 4, and how it compares with the wider Lofdal property.

8.1 Host rocks for mineralisation – whole-rock analysis

Do Cabo (2013) has studied the carbonatite dykes proximal to the carbonatite intrusions, as well as the carbonatite plugs themselves. Outlined here are wholerock comparisons between Do Cabo's dykes and the Area 4 alteration zone mineralised intercepts. Please note that wholerock data used below are from mineralised intercepts (taken every 1m) where TREO was recorded at 2000ppm and above.

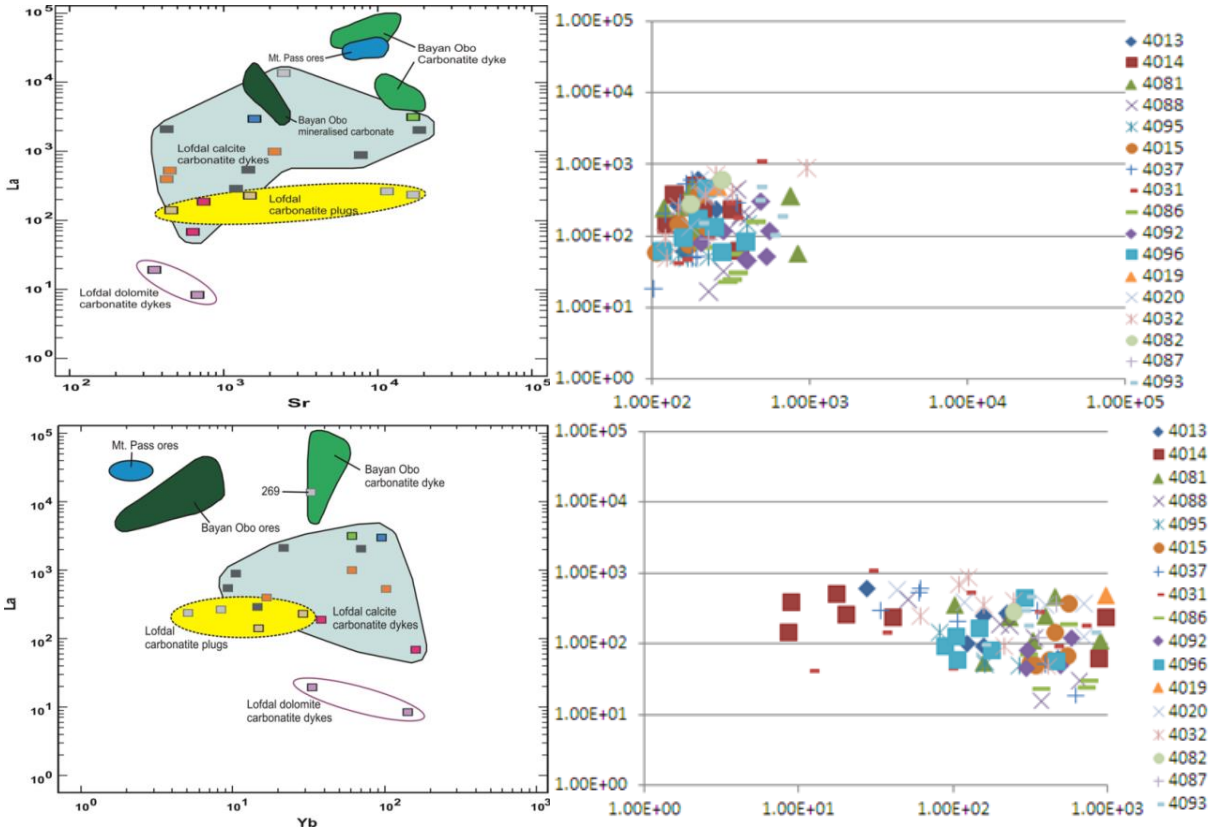

Figure 8.1 – comparison of the REE mineralised intercepts (+0.2% TREE) of alteration zone of Area 4 Lofdal vs Do Cabo's peripheral dykes and carbonatite plugs; and comparisons to other notable worldwide REE deposits. Note lower Sr in Area 4 compared to VDC dykes, NB dolomitic intercepts i.e. 4081, 4092 and 4086 shower higher trace Sr suggesting a link with Sr and Mg; Yb and La are comparable to VDC dykes. Yb lower in magnetitic intercepts and higher LREE & MREE sections e.g. 4013 xenotime in magnetite bearing section 36-37m, 4014 and 4031

Comparing wholerock data from Do Cabo's carbonatite dykes and plugs – Type 2 and 3 dykes particularly against the Area 4 alteration zone, in Figure 8.1, it can be observed that ***both*** show deficiency in the LREE lanthanum (La) compared to the carbonatite deposits of Mountain Pass and Bayan Obo. The calcite carbonatite from the main intrusion (show in Do Cabo's chart in grey) of Lofdal ***is*** however comparable to the aforementioned deposits and within the remit of a typical LREE and Sr enriched carbonatite. Do Cabo's dykes are much lower in La however, and Area 4 is even more

deficient in Sr compared to these dykes, a resultant perhaps of the fact that higher Sr is attributed a more magmatic related genesis of the dykes over the alteration zone, which is perhaps more hydrothermally evolved. Certainly fewer Sr minerals (e.g. strontianite or celestine) have been observed from the petrology of samples from Area 4, compared to the dykes, and rarely have any Sr peaks been noticed from EDS analysis on samples from the study area of Area 4. The dolomitic dykes from the Do Cabo study can be seen to be lower in Sr, which is quite the opposite trend to Bayan Obo dolomite hosted deposit. An interesting difference in Sr content between the dolomitic dykes and the Area 4 dolomitic intercepts is that the latter have higher trace Sr than any other Area 4 intercept (4081, 4092 and 4086 for example). More differentiation between the dykes and the Area 4 intercepts is noticeable from the La vs Yb wholerock dataset. Whilst the La concentrations are low, it is the Yb concentrations that are of interest. Levels can vary considerable across one mineralised intercept on a given hole.

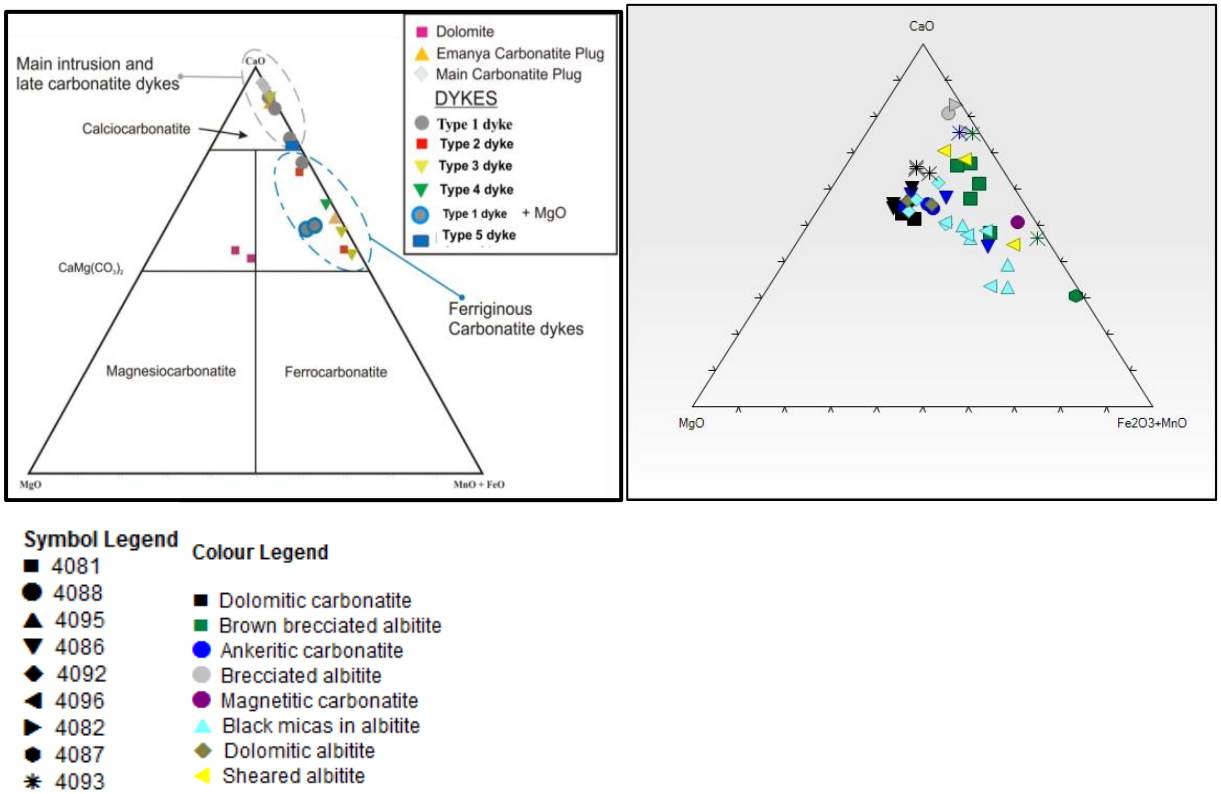

Figure 8.2 Top: ternary plots Top: Do Cabo (2013) whole-rock analysis of carbonatite (adapted from Le Maitre et al., 1989) dykes. Bottom: +2000ppm TREE intercepts in Area 4 whole-rock composition

Taking 4014 for example, this could be interpreted as modification/remobilisation of earlier mineralisation, or multiple mineralising events captured across a single intercept. It could therefore be argued that clustering across some intercepts (such as 4096) could be one, or few mineralising event, or (such as 4015) be a hydrothermal modification and that has left a Yb dominant mineral assemblage. MgO, CaO and FeO+MnO proportions of carbonatite can help differentiate between different carbonatites, as displayed in a ternary diagram in Figure 8.2, as outlined by Le Maitre (1989). A study

of the carbonate contents of RE high-grade intercepts (+2000ppm TREO) from Area 4 alteration zone (Figure 8.2) against those of the dykes shows a comparable trend between calcite carbonatite and ferruginous carbonate, and more dolomite carbonate contents. High CaO contents demonstrated by brecciated albitite reflect higher contents of calcite interstitially between albite fragments in the breccia (Holes 4082 & 4088). Of note is that the holes veering more towards Ca are less enriched intercepts (in terms of TREO) such as holes 4082, 4088, 4093. Holes of greater TREO enrichment across intercepts, such as Holes 4086, 4092, 4081 plot in the more dolomitic field, where, as we see from the core analysis, have a noticeable dolomitic component, sometimes sheared and cross-cut by HREE bearing veins – notably biotitised at contact with dolomite. However, again it is noted that some holes variegate downhole, such as Hole 4081 and 4096. Much of the enriched intercepts on 4092 plots within the dolomite field and suggest perhaps that dolomite is a more favourable REE precipitating environment – i.e. neutraliser of REE bearing acidic fluids resulting in the "dump" of xenotime. Texturally this has been seen from cross-cutting relationships in Appendix 1. Similarities between the dykes and Area 4 in terms of xenotime deposition are outlined in Figure 8.3.

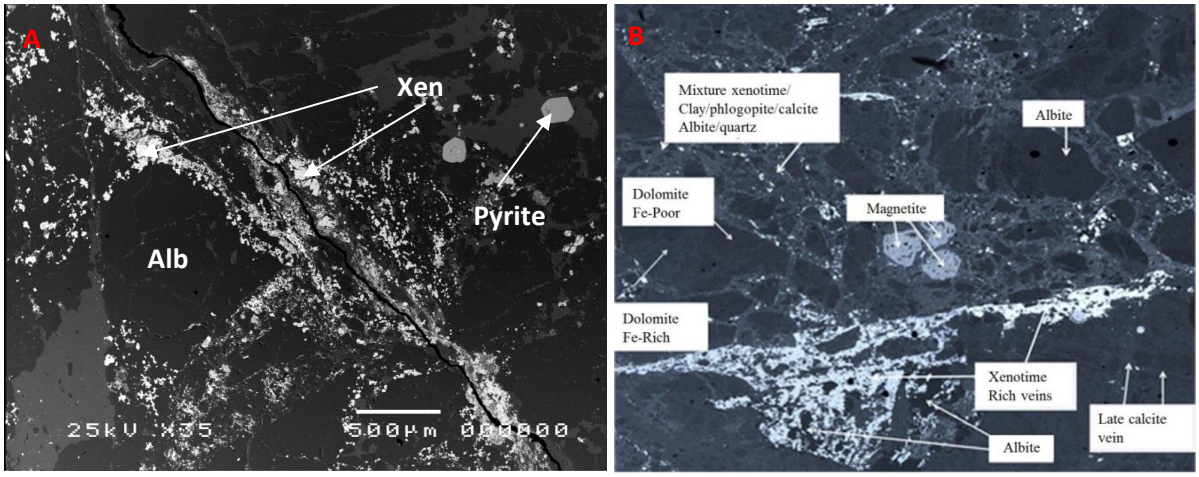

Figure 8.3 A) BSE image of xenotime, zircon, rutile and pyrite in vein, and infiltrating around brecciated albitite from 4081 80.60m. Dark centre is a fracture Subhedral crystals to RHS are magnetite. B) Dolomitic carbonatite Do Cabo (2013)

Previous studies into carbonatite complexes have outlined similar patterns of carbonatite evolution. Kapustin (1986) has recognized several different stages of carbonatite development from calcite to dolomite, to late ankerite-rich carbonatites. Woolley (1982) showed that compilations of whole-rock analyses of carbonatites from different stages in several terranes show calcium depletion accompanied by enrichment in magnesium or iron. Mariano (1989) points out that these Fe-Mg rich carbonatites usually exhibit secondary textures indicative of formation under late stage hydrothermal or carbo-hydrothermal conditions and are normally always REE enriched. This evolution can apply to both the dykes and the Area 4 alteration zone at Lofdal. Similarities between Area 4 whole-rock geochemistry and that of the dykes can be seen in the chondrite normalised plots in Figure 8.4. The

most striking match is between the example of Hole 4081 (80m and 87m intercepts) from Area 4 and Do Cabo's Type 2 dykes. The 4081 74m interval is both LREE and HREE enriched and compares to

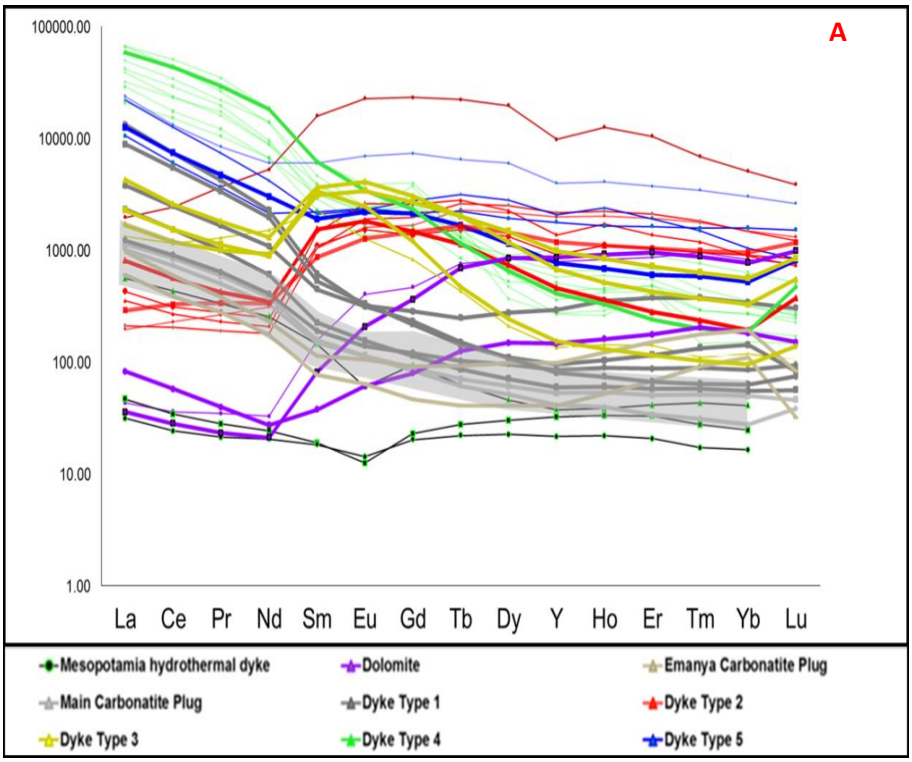

Figure

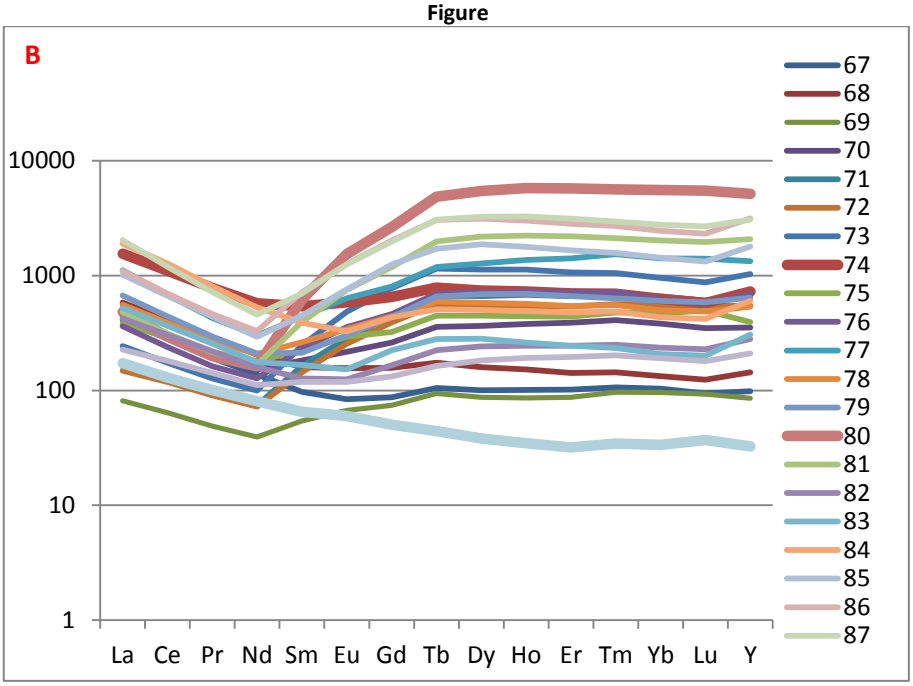

Figure 8.4 A) WR chondrite normalised plots of Hole 4081 Area 4 compared to B) Carbonatite dykes (Do Cabo, 2013). Samples from 80m, 86m and 87m correspond with Do Cabo's Type 2 dykes.

VDC's Type 2 (or Type 3) and VDC's dolomite – which would correspond with observations of modification of the dolomite seen in the hangingwall to the alteration zone in Hole 4081 at 73.50m.

8.2 Ground preparation for REE mineralisation in Area 4

As outlined in the previous sections the REE mineralisation in Area 4 is similar to the dykes, but it is not quite the same. Much of the REE mineralisation in Area 4 is hosted in metasomatised (fenitised) Huab basement rocks associated with established fault structures. That's not to say that there aren't carbonatitic components to the mineralised intercepts, but it appears that their presence may play an important role in controlling, or contributing to, later fluids. The albitites, or Na-fenites, are brittle and their continued brecciation, both tectonically and hydraulically induced, increases secondary porosity and therefore provides ideal ground preparation for REE laden fluids to pass through.

Andersen (1984), from his studies on the Fen Complex in Norway, points out that reactions involving groundwater convecting in hydrothermal cells set up by intrusive themselves may play a significant part in the post-magmatic re-equilibrium of carbonatites. Intense wallrock brecciations commonly extend far from carbonatite bodies, providing permeable zones that permit groundwater convection toward the carbonatite, for example. Zharikov et al. (2007) point out that fault-related alkaline metasomatites are common in Precambrian shields. Albitites related to 'linear' carbonatite bodies in shear zones form rims around carbonatite lenses and veins and separate veins in the upper part of the alkaline-carbonatite rock bodies. Albitites of this type may form by the action of aqueous-CO_2 fluids replacing previously fenitised host rocks (gneisses or amphibolites).

So what is fenitisation? It refers to the process of alkali metasomatism associated with alkaline silicate and carbonatite magmatism (Le Bas, 2008). While carbonatites generally contain very little alkali content, they are believed to inherently contain high concentrations of mantle derived alkalis which are lost as a fluid phase during crystallization There are two recognized types of fenitisation: sodic, and potassic (Le Bas, 2008), and both are observed on the Lofdal property.

Potassic fenitisation of the Main Intrusion:

Potassic fenites are most commonly observed associated with sovite intrusions and this can be seen at the Main Intrusion (carbonatite) at Lofdal, manifest as an irregular, yet persistent, aureole of potassic fenite around the sovite plug. It is believed to have resulted from metasomatism of the nepheline syenite by alkaline fluids released by the carbonatite body during the early intrusive phases, as described by Gaudet (2013). Potassic fenitisation appears to affect both the nepheline syenites and syenitic breccias, indicating that fenitisation post-dated the syenitic brecciation. It has been interpreted that residual magmatic silica and volatile-rich fluids from the carbonatite magma most likely migrated towards the margins of the intrusion during crystallisation. A pseudo-trachyte exists with small fragments of remobilised and parallel orientated recrystallised potassium feldspar interpreted to have formed from melting of high-grade fenite, a result of heat rising from the carbonatite magmatic body; later this melt is emplaced as dikes, sills and plugs within the potassic fenite surrounding the carbonatite body (as recognised from other carbonatite bodies by Le Bas

(2008). Rapid crystallisation of fluorapatite is accompanied by rapid crystallisation of uranpyrochlore in the carbonatite plugs, acting as a sink for Nb and U and perhaps helping to explain the low levels of these elements in the later emplaced, and distal carbonat(it)e dykes and stringers.

Na-fenitisation of the carbonatite dykes and Area 4 alteration zone:

It is reasonable to suggest that potassic fenites were perhaps heterogeneously overprinted by a later calcium and sodium rich alteration event – i.e. albitisation or Na-fenitisation. The sodic fenites of the Silai Patti, North West Frontier Province in Pakistan, for example, contain veins of sovite which cross-cut potassic fenites, containing abundant aegirine and albite; this has been interpreted to indicate that potassium fenitisation pre-dated the release of sodic fluids, which crystallise albite and aegirine in veins developed along fractures (Le Bas, 2008). It can be shown therefore that sodium- and potassium-rich fenites can occur around a single intrusion, and it has been suggested that these distinctions may be related to depth**,** where potassium fenitisation occurs at the upper levels of a carbonatite complex, and sodic fenitisation occurs at greater depths (Le Bas, 1989). Fenitisation manifests by infiltration of alkali-rich fluids from carbonatitic/silicate melts along distinct pathways, producing an assemblage of alteration minerals. In some cases, the presence of disseminated fenitisation products implies diffusive processes, where precursor minerals have been completely replaced, and reflecting pervasive penetration by fenitising fluids (e.g. White-Pinilla, 1996). Variables that control fenitisation by carbonatitic fluids include XCO_2 of the fluid, temperature gradients, oxygen fugacity, FeO/MgO ratio, and activity gradients of SiO_2, Al_2O_3, and CaO (Morogan, 1994). At the Alnö alkaline-carbonatite complex, Sweden, for example, two distinct fluids are thought to have been involved in fenitisation, derived from carbonatitic and ijolitic magmatic sources (Morogan and Woolley 1988). Based on fenitisation products, the carbonatitic-type fluid had $XCO_2 > XH_2O$, high α CaO, possibly high Na_2O or K_2O (or both), very low a SiO_2, and possibly high F and P contents.

Late-stage, selective removal of La and HREE that could be attributed to passage of a late, highly-oxidizing post-magmatic fluid, and changes in fluid composition upon late-stage mixing of fenitising fluids and low-salinity meteoric waters were documented by Williams-Jones and Palmer (2002) based on fluid inclusions in the fenites from the Amba Dongar complex, India. It was shown that at high levels in the crust, continued crystallisation of carbonatite magmas would produce a free fluid phase, which is likely to be containing Cl- complexes and Fe. At Oldoinyo Lengai carbonatite volcanic suite, for example, the natrocarbonatites show that Cl, F, and S are probably constituents of carbonatite fluids, and the mineralogy of the fenites indicates that the fluid must have contained Ca,

Mg, K, Na, and Fe^{3+} (e.g. Morogan and Martin 1983; Gittins 1989). NaCl brine was also considered to be the fenitising fluid at Callander Bay, Ontario, Canada (Currie and Ferguson, 1971).

The sequence of intrusive events at Lofdal, from emplacement of the nepheline syenite through phonolite dyking followed by subsequent ascent of the carbonatite magma and emplacement of two carbonatite plugs would have had resultant alkali metasomatism of intruded basement rocks, as described in the preceding examples. Early magmatic release of potassium rich fluids would explain the K-fenitisation in an aureole of nepheline syenite surrounding the Main Intrusion carbonatite body. The emplacement of carbonatite dykes is spatially very similar to the emplacement of phonolite dykes, yet the extensive fenitisation, observed with these, and especially in Area 4 Alteration Zone, is Na enriched and manifested by the dominance of albite (Swinden and Siegfried, 2012).

Questions surround the role and content of REE during each episodes of fenitisation, i.e. is it the fenitising fluids, or the carbonatite carrying the REE, or do fenitising fluids strip REE from earlier carbonatite episodes? Studies of fenite around carbonatite complexes in Malawi by Dowman (2014) found that HREE enrichment can be found in breccia and in fenite. Breccia around Kangankunde and Chilwa Island, Malawi shows areas with high Y/La ratios within the matrix caused by narrow zones of xenotime enrichment. Fenite around Kangankunde and Chilwa Island has higher HREE:LREE ratios than the carbonatite. Early alkali fenitising fluids are followed by REE-carrying fluids. Dowman (2014) has constructed a model for these fenites, and the evolution of the fluid phases, that resound comparably with observations in the HREE bearing alteration zone in Area 4 Lofdal, and is demonstrated in Figure 8.5.

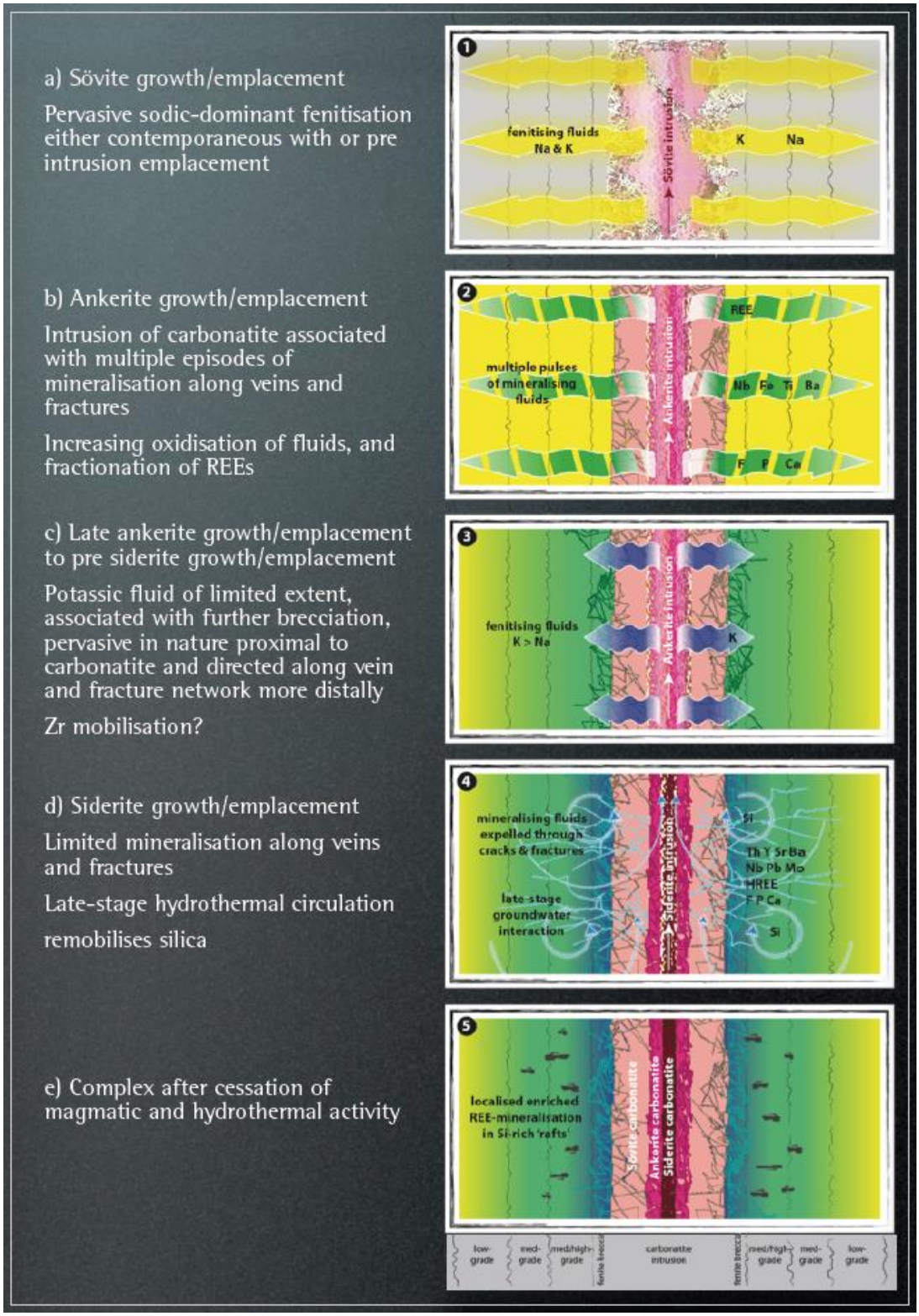

Figure 8.5 sequence of main fluid events in fenite at Chilwa Island, Malawi. Dowman (2014)

8.2 The REE mineralisation in Area 4

There are a range of REE bearing phases in Area 4 (including LREE: monazite, parisite, synchysite HREE: xenotime, aeschynite, for example), but 90% of REEs are hosted in xenotime-(Y), as confirmed from metallurgical work by Mintek (NRE 2013). A common association with xenotime in both the carbonatite dykes and in Area 4 is with subordinate zircon, as described by Wall et al. (2008) but in

Area 4 especially there are also close associations with apatite, rutile (and minor Nb-rutile), thorite, hematite/magnetite, and pyrite.

8.2.1 Summary & discussion of Xenotimes types in Area 4.

1. Xenotime as euhedral to subhedral crystals in association with magnetite, often with high Th or with thorite inclusions, crystal size 20-50 µm

2. Xenotime exsolution or precipitation/dissolution in apatite (<20 µm)

3. Xenotime in the carbonate - subhedral (30-100 µm), notably ankeritic carbonate, as aggregates and disseminations in late stockworks crosscut by FeOx stringers. Assemblages can include calcite, fluorite, chlorite, apatite, aeschynite, (Nb) rutile, synchysite and hematite. Xenotimes often have zircon cores.

4. Xenotime as aggregates and disseminations within, or close to, stringers and veins of biotite-phlogopite, chlorite and/or calcite. Often seen close to, or in, dolomite. Xenotimes can have zircon cores. Accessories include apatite, aeschynite, synchysite, rutile, and/or niobian rutile.

5. Xenotime as granular, very small (<20µm) anhedral to euhedral crystals, sometimes associated with apatite occur in disseminated wisps in heavily ferruginous ankerite infused albitite breccias.

6. Xenotime as stringer veins within fractures in albitites and sometimes thin hairline stingers accompanied by synchysite.

The association with apatite is curious and it is difficult to determine whether the textures seen are evidence of exsolution, or the precipitation of xenotime at contact of pre-existing apatite i.e. interpreted as fluid-wallrock interaction and resultant precipitation. Harrison and Watson (1984) showed that Ca has a transport rate generally 2-orders of magnitude faster than P, data which may help explain the selective removal of Ca from apatite in the presence of RE-rich hydrothermal solutions and their relative immobility of P. For example, complete replacement of apatite by monazite has been observed at Araxa, Brazil in the dolomitic carbonatite, where monazite replaced the original apatite, below the weathering layer and believed to be attributed to hydrothermal replacement (Jones et al., 1996).

Apatite such as this could represent a late-magmatic to hydrothermal phase. Studies of fluid inclusions in apatite from the Fen carbonatite, Norway, identified a magmatic fluid that was rich in CO_2 and NaCl,

which evolved during magmatic differentiation to a CO_2-free, water-dominated system that contained higher salinities and densities as solidification progressed (Andersen 1986).
In contrast, Kapustin (1986) points out that magnetite and apatite are normally associated with earlier carbonatites.

8.2.2 Xenotime REE variability and fractionation

As described earlier, xenotime is characterised by the ideal formula of ATO_4 where A represents Y^{3+} and the T site a tetrahedrally coordinated atom of P. Because of their smaller ionic radii, mid to heavy REE tends to substitute for Y, notably Dy and Ho as closest in size to Y. Studies by Cherniak (2006) measured diffusion behaviour under dry conditions of a range of REEs to explore whether variations in ionic radii markedly affect REE diffusivities**,** as they do in zircon, with which xenotime is isostructural. The REE and Pb distributions in the xenotime were profiled by Rutherford Backscattering Spectrometry (RBS) (Cherniak, 2006), and the results give an insight into the crystal–chemical properties influencing diffusion in minerals.

It is shown that in xenotime, the REE are more closely matched in size to Y, for which they substitute in the xenotime lattice, as they are with Zr, for which they substitute in the zircon lattice. Additionally, in xenotime the trivalent REE can exchange directly with Y^{3+}, with no charge-compensating species necessary as would be the case with Zr^{4+}. These factors may facilitate diffusion, leading to both lower activation energies for diffusion in xenotime, and less variation in the activation energies among the REE. Cherniak points out that although zircon and xenotime are isostructural, there are differences in size and charge of the cations for which the REE substitute in to the respective structures, which appear to influence REE diffusivities and may account for these differences. The ionic radius of Zr^{4+} (0.84 A°) in zircon is considerably smaller than that of Y^{3+} (1.019 A°) in xenotime (both 8-fold coordination; Shannon, 1976). The REEs likely substitute on these respective sites in zircon and xenotime, but given these differences in ionic radii and the ionic radii of the REEs (Yb+3=0.985 A°; Dy+3=1.027 A°; Sm+3=1.079 A°), the REEs provide a closer match in size with Y in xenotime. Calculated differences in ionic radii between the lattice cations Zr and Y and the substituent REE range from 0.145 (for *D*Yb–Zr) to 0.239 A° (for *D*Sm–Zr). In contrast, values ranging from 0.034 (for *D*Yb–Y) to 0.060 A°(for *D*Sm–Y) are obtained for xenotime. These less pronounced differences between the ionic radii of the lattice cation and the substituent cation may lead both to lower activation energies for diffusion, as well as a less pronounced dependence of activation energy on ionic radius due to lower lattice strain (e.g., Van Orman et al., 2001). As well as this the trivalent REE can exchange directly with Y^{3+}, with no charge-compensating species necessary as is the case with Zr^{4+}. These factors may

facilitate diffusion, leading to lower activation energies required for diffusion in xenotime. Because diffusivities of the REE in xenotime are much faster than in zircon, **intra-crystalline compositional variations in the REE will be lost more readily in xenotime**. Dy, for example, is extremely resistant to diffusional alteration in zircon, but much less so in xenotime; for example, at 800 °C, 1 A° scale zoning will be retained in zircon for times on order of a billion years, but in xenotime will be lost in a little over 1000 years, demonstrated in Figure 8.6. Heavier REE of smaller ionic radius diffusing faster (and with lower activation energies for diffusion) than the lighter, larger REE. In xenotime the REE diffuse at similar rates, and with less disparate activation energies for diffusion, as displayed in Figure 8.7. These differences may reflect the variations in size and charge among the cations for which the REEs substitute in the respective mineral structures

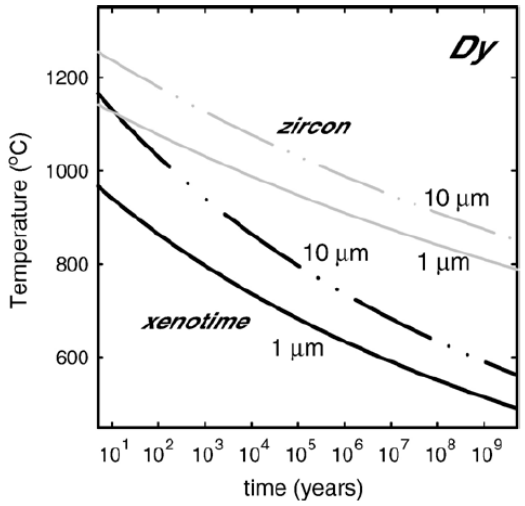

Figure 8.6 preservation of Dy zoning in xenotime and zircon. Curves represent maximum time–temperature conditions under which 1 and 10 A° zoning in Dy composition will be preserved in xenotime. For conditions above the upper curve, well-defined zoning on the 10 A° scale will be lost; zoning on the finer 1 A° scale will be lost for conditions above the lower curve. Also plotted for comparison are curves for Dy zoning in zircon, which indicate that REE zoning in zircon is far more resistant to diffusional alteration than is zoning in xenotime – Cherniak 2006

So it has been shown that the heavier REEs of smaller ionic radius diffuser faster (and with lower activation energies for diffusion) than the lighter, and larger REEs. Although this example is measuring REE variability in a closed system, it is a good place to start when looking at REE partitioning behaviour before contemplating the added variables of an open system of a hydrothermal environment.

Studies by Heinrich (1997) suggest that values of *D*REE (TREO content) in xenotime also depend strongly on ionic radii of the REEs, and on temperature. Solid solutions of the REE orthophosphates monazite and xenotime were synthesized hydrothermally between 300°C and 800°C at 2 and 5 kbar using REE+Y-oxides and H_3PO_4 as starting materials. What was discovered was that at temperatures below 600°C, the natural HREE content in monazite is about 3 mol% lower than the experimental value. **It was assumed that Th may saturate the monazite structure with small ions and thus suppress further incorporation of HREE into natural monazite.**

Similarly for the xenotime structure 1 mol% Th + Si in natural samples may lower the concentrations of LREE Sm-Nd from about 2 to about 1 mol%. This simple explanation obviously does not hold at 650°C. If interpretation is correct, this would imply that U and Th were progressively **partitioned into xenotime or into other phases with increasing temperature.**

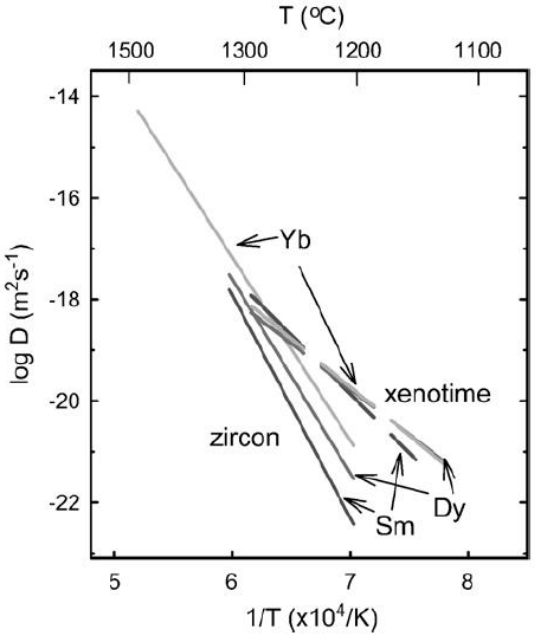

Figure 8.7: Comparison of REE diffusion between xenotime and zircon (from Cherniak et al., 1997). For zircon (solid lines) there is a systematic variation in REE diffusivities, with the heavier REE of smaller ionic radius diffusing faster (and with lower activation energies for diffusion) than the lighter, larger REE. In xenotime (dashed lines), the REE diffuse at similar rates, and with less disparate activation energies for diffusion. These differences may reflect the variations in size and charge among the cations for which the REEs substitute in the respective mineral structures.

Heinrich also found that **synthetic xenotimes have only about half of the Gd contents ~2 wt.% Gd_2O_3 compared to natural xenotimes at 4 wt.% Gd_2O_3**. It is suggested that this is attributed to the special position of $GdPO_4$ within the pure $REEPO_4$ series. **At 258°C and 1 kbar, pure $GdPO_4$ crystallises into the monazite structure and under these conditions** the transition between the monazite and xenotime structure, along the pure $REEPO_4$ end-member series, occurs between $GdPO_4$ and $TbPO_4$ (Ni et al.,1995). Interestingly synthesis experiments by Gratz and Heinrich (1997) at different *P–T* conditions always yielded a two-phase product, i.e. a $GdPO_4$ polymorph with both the monazite and xenotime structure. It is not clear which $GdPO_4$ polymorph is stable under metamorphic conditions and where the possible transition curve in *P–T* space is located. It is therefore suggested that **the additional incorporation of U, Th, and Si into xenotime may shift *D*Gd strongly towards higher values in naturally occurring xenotime.** Irber (1999) also notes that Gd is in a unique position as it marks the change from unpaired to paired electrons in the filling stages of 4*f* orbitals, and Gd is shared between the second and the third tetrad. How Gd relates across the miscibility gap between MREE and HREE in

the Area 4 xenotimes is demonstrated in Figure 8.8 where Gd correlates with lighter REs, but Dy does not correlate well with lighter REs – interpreted to mean that Gd appears to follow MREEs rather than HREEs.

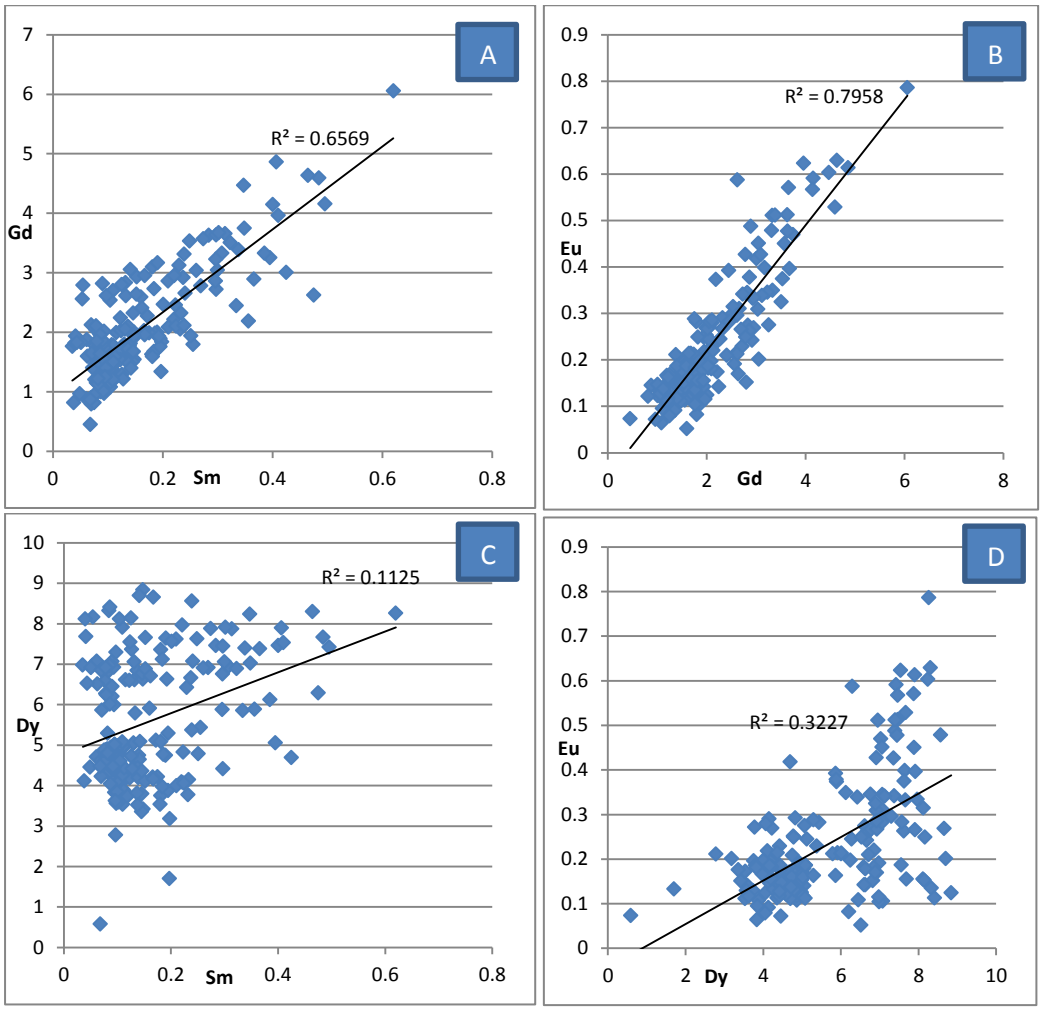

Figure 8.8 Gd correlates better with lighter REE such as Sm & Eu (A & B), whereas Dy correlates poorly with Sm & Eu (C & B). Units are wt. % oxide.

In Figure 8.9 Dy is used because of its general stability across the samples, and to gauge Gd variability against the HREE between samples. General results appear to suggest that Gd is more weakly associated with Dy in xenotimes in more overprinted environments samples. Gd dissociates from Dy and is more closely related to MREE, perhaps as LREE are stripped by modifying fluids. Differences in atomic radius of the occupant of the tetrahedral site were also discussed in Ni et al. (1995), and can cause the shortening of the a and c parameters in the xenotime structure, and modified to different extents i.e. the parameters are affected by a factor other than the replacement of Y by REE – for example replacement of O by F in the T site. A smaller volume to xenotime's unit cell has been proven to increase the HREE content in elements that are heavier than Y, such as Yb (Pereira et al., 2012). It has been found that Ca, Ti, Zr are able to substitute for Y and REE because of their similar ionic radii.

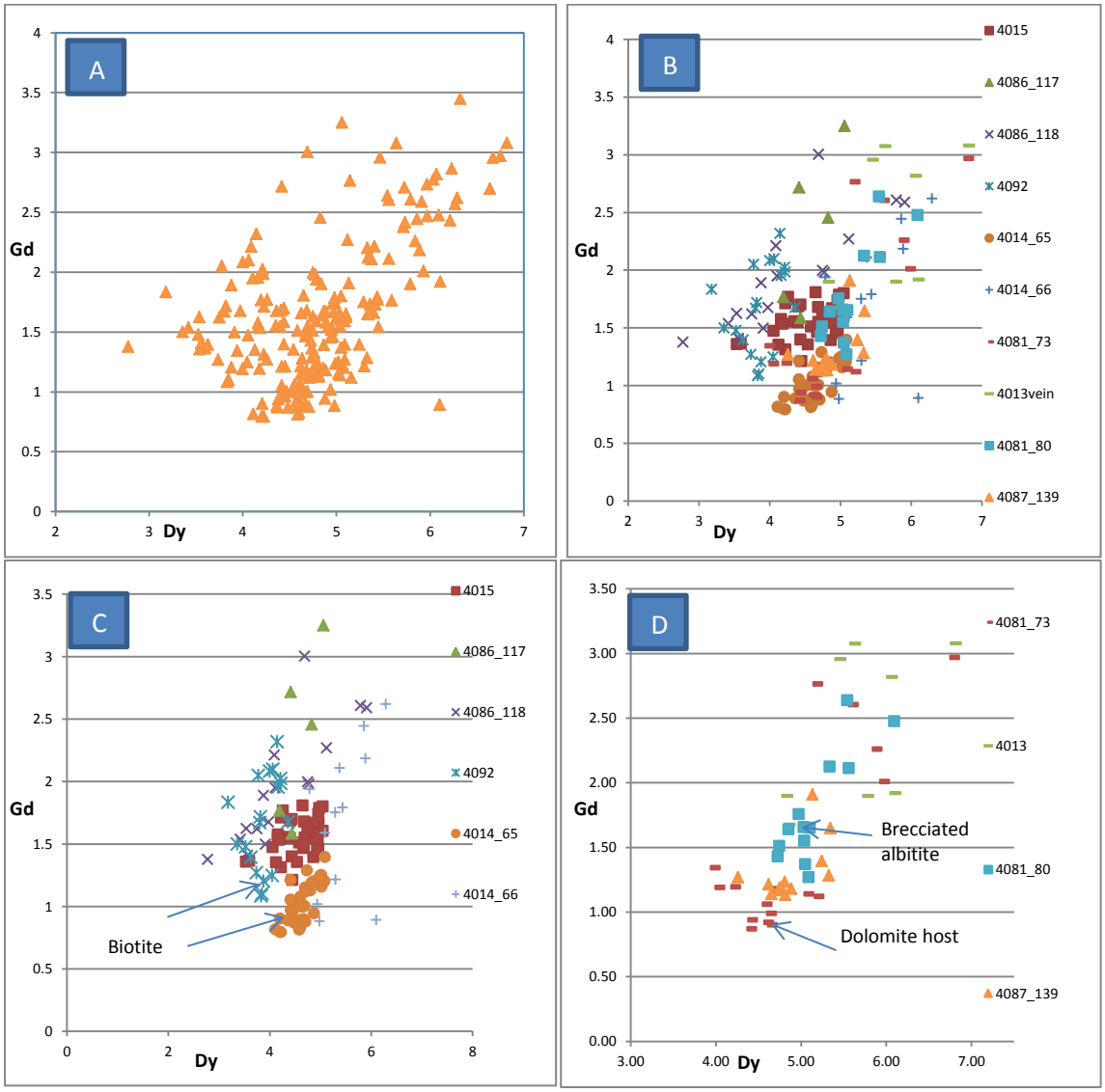

Figure 8.9 Gd vs Dy all points (units are wt. % oxide) Gd generally correlates with heavier REE like Dy, but dependant on type of xenotime. A) All points B) All points split C) Run1 and 3 D) Run 2 Strong correlations (strongest to weakest): 4081_73 r^2 0.65, 4013wisp r^2 0.76, 4081_80m r^2 0.68, 4086_118m r^2 0.66, 4086_117m r^2 0.59, 4014_65 r^2 0.53 **Weak correlations** (strongest to weakest): 4087_139 r^2 0.31, 4013 r^2 0.29, 4014_66 0.2, 4015 r^2 0.15, 4092 r^2 0.11.

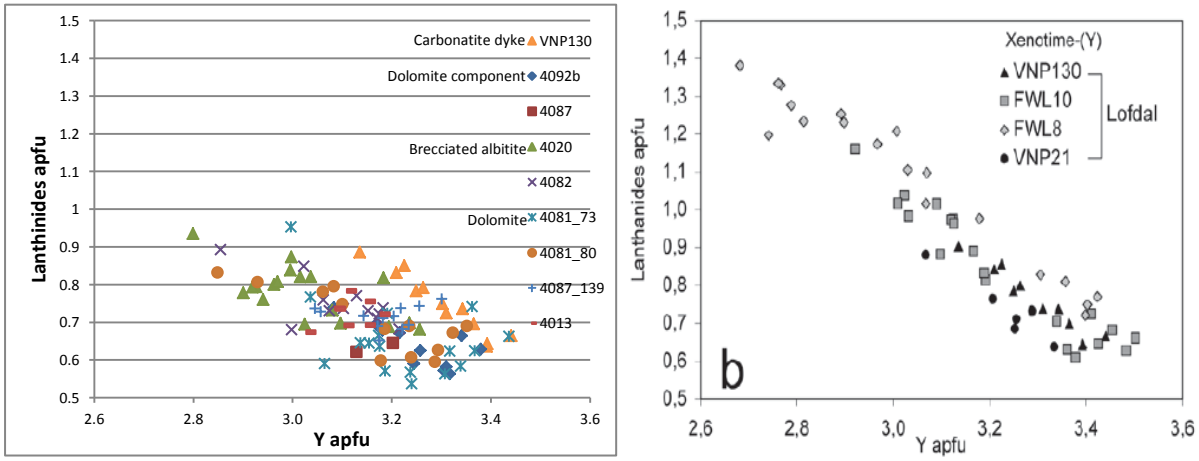

Figure 8.10 THREE vs Y apfu 16 oxygens comparison of Area 4 xenotimes to Wall 2008 dyke xenotimes

The Area 4 xenotimes analyses display a marked variability in Y and TREE contents, even locally by sub-mm scale, as shown by the spread of the results in Figure 8.10. Although variability could be partly explained by zonation differences in crystals, and possible timing of crystallisation (e.g. dissolution/re-precipitation), and analytical errors/differences between runs, there are definitely differences dependant on position in the alteration zone and host lithologies/associations. In Figure 8.10: **Higher Y values** = 4014_65m (biotitised hangingwall of HREE enriched intercept), 4081_73m (dolomite hangingwall to main HREE enriched intercept), 4013"wisp" (xenotime intergrown with apatite). **Spread values** = 4087_139m – reflecting overprinting and different xenotime parageneses here perhaps. **Higher TREE values** = 4014_66m (main mineralised zone), 4081_80m (main mineralised zone), 4013"vein" (biotitised vein cutting xenotime intergrown with apatite). The hanging walls of the main mineralised intercepts appear more enriched in Y, and the main mineralised zones and footwalls are in turn more enriched in TREE.

To help interpret what the REE variability in Lofdal xenotimes it is important to compare REE variability from other xenotimes in the world. Kositcin et al. (2003) undertook geochemical experiments on xenotimes from variety of geological terranes in the Witswatersrand Basin of South Africa. They discovered that chemical composition of xenotimes, determined by in-situ electron microprobe analysis, can be correlated with their origin, with the main chemical discriminators being the proportions of MREE-HREE abundance. These experiments helped to distinguish igneous-detrital xenotime from diagenetic and hydrothermal xenotime by having higher Yb and lower Eu, Dy, and Gd concentrations, and therefore a distinctively lower Gd/Yb ratio. They showed that Dy vs Eu can be used to discriminate between xenotime derived from a melt (igneous-detrital and igneous) in that Eu would be lost to feldspars in the igneous environment, and xenotime derived from a hydrous fluid (diagenetic and hydrothermal xenotime).

Comparing the EPMA data from the xenotimes from Area 4 to the xenotimes of the Witswatersrand basin by Kositicin et al. (2003), provides some interesting parallels, as can be seen in the chondrite normalised REE distributions displayed in Figure 8.11. It must be considered that Kositcin's model while being suitable for that deposit may not fit to a carbonatite related deposit like Lofdal, where Eu variability may not be attributed to a granite-related environment and divalent Eu lost to plagioclase fractionation for example, but certainly there is also marked **Gd and Yb variability** in the Lofdal xenotimes.

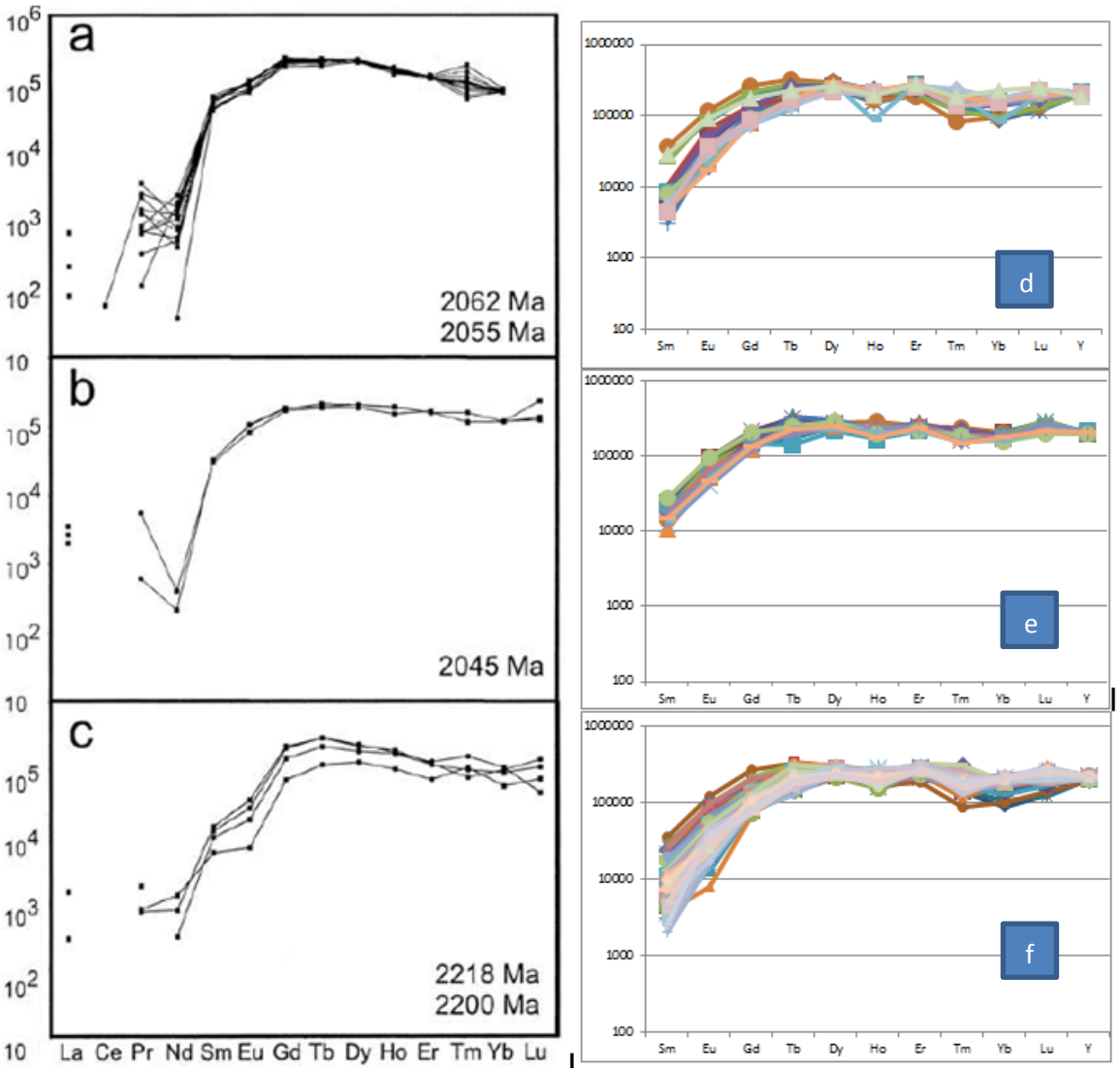

Figure 8.11. Comparison of chondrite-normalised REE patterns for xenotime crystals of hydrothermal origin from Witwatersrand SA (Kositcin, 2003) vs Lofdal, ppm vs element. (a) Hydrothermal crystal from the Parktown Formation, Witwatersrand SA (b) Hydrothermal xenotime grain from the Krugersdorp Formation, Witwatersrand SA. (c) Hydrothermal overgrowth on a detrital zircon grain from Denny's Reef, Elsburg Formation, Witwatersrand SA Kositicin 2003 d) xenotime in dolomite Area 4, Lofdal 4081_73m, e) xenotime in brecciated albitite 4081_80m, f) general pattern for Area 4 xenotime. B and C comparable to Lofdal xenotimes with a generally flat pattern across the heavier lanthanides; note the Gd "hump" in C.

It is worth considering again Gd's unique position in REE fractionation sequence as outlined above. Kositcin suggested Gd/Yb against Gd could be used to discriminate between igneous/detrital and hydrothermal xenotime (Figure 8.12). It can be seen that the xenotimes of Area 4 do vary in their REE abundances depending on their site of precipitation, and that some xenotimes of different chemistries and timings co-exist in the same area depending on abruptness of fluid-rock interaction, and/or dissolution/re-precipitation, and can be argued as evidence of transition between magmatic (carbonatite) to and hydrothermal environments.

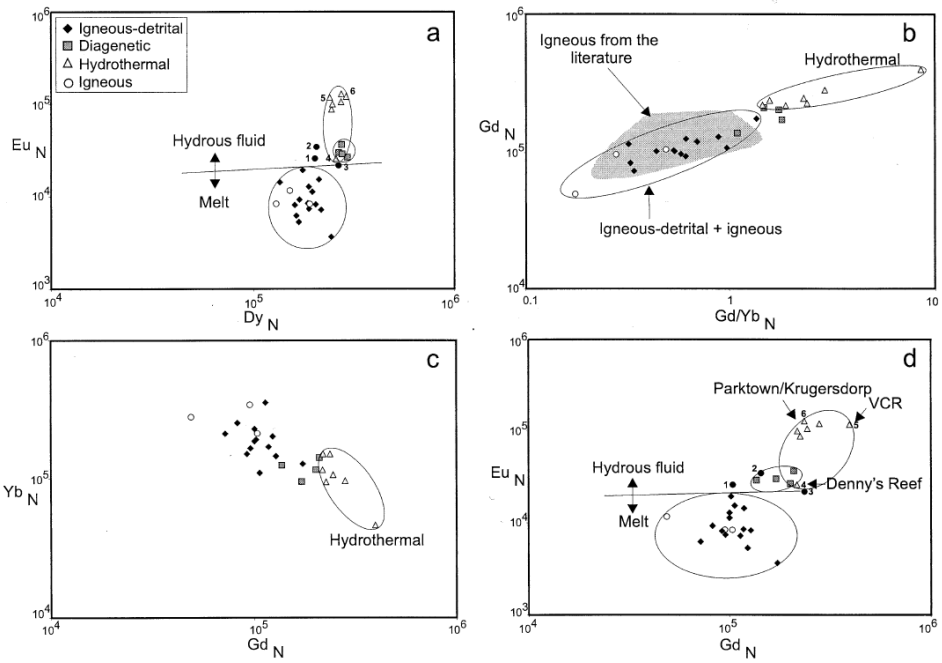

Figure 8.12 Kositcin's model. Log scale binary plots of xenotimes from the Witwatersrand, South Africa - a) Plot of Dy vs Eu b) Plot of Gd/Yb vs Gd (xenotime of known igneous origin from worldwide studies is the grey shaded area) c) Plot of Gd vs Yb d) Plot of Gd vs Eu. Adapted from Kositcin et al. 2003.

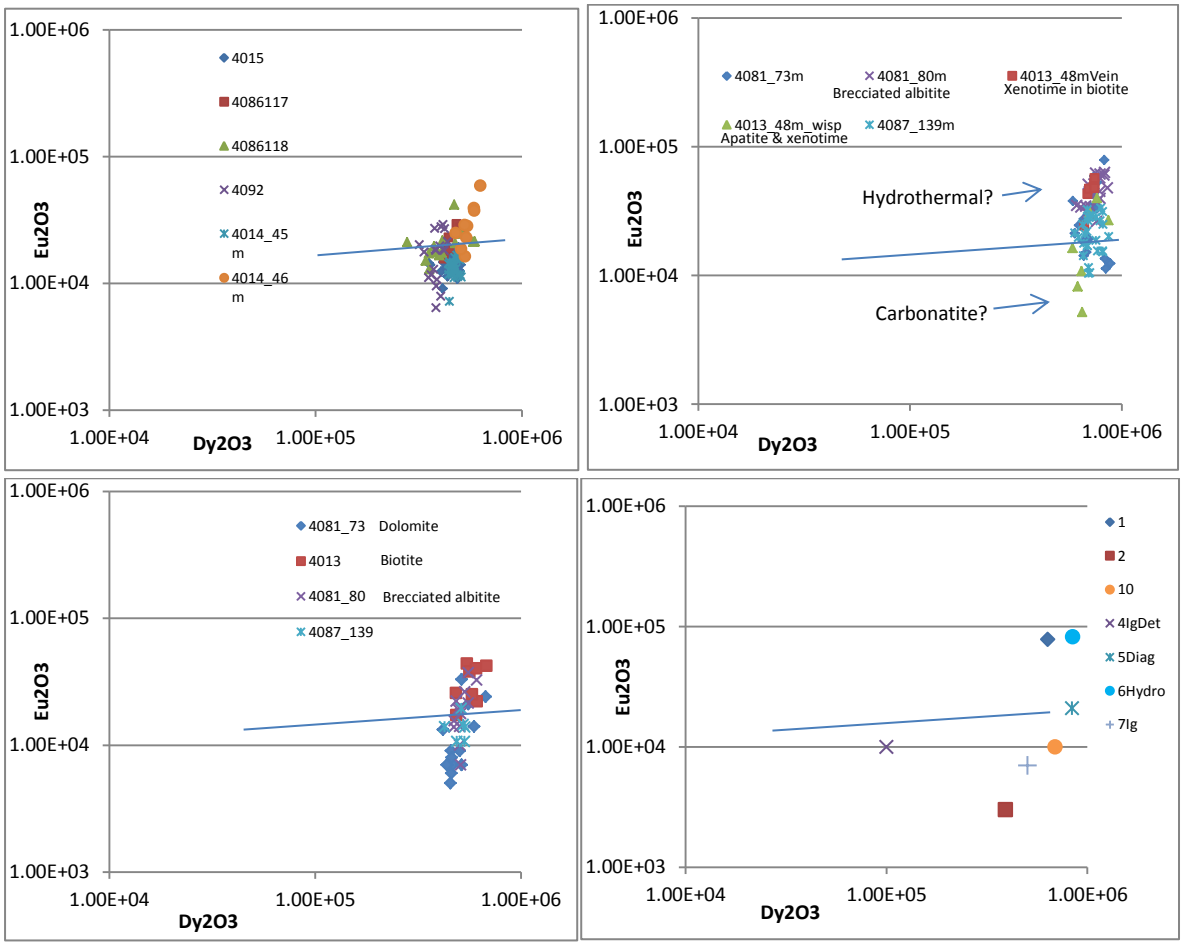

Figure 8.13 Eu vs Dy xenotime from 1. Rhyolite (Ondrejka et al., 2007). 2: Xenotime from pegmatite (Hetherington et al., 2008). 4-7: Xenotime from Wits, SA (Kositcin, 2003). 8: Xenotime from granite (Wang et al., 2003). 10: Xenotime from alpine vein (Demartin et al., 1991). NB other samples have marked Eu anomaly and plot at "2" or below. Values are wt. %.

The results in Figure 8.13 could be significant as there are parallels between the geochemical data and the textural and optical observations. Certainly 4013_vein has textural characteristics of hydrothermally re-deposited xenotime, and 4013 wisp drifts into igneous/carbonatite field suggesting that the apatite association is indeed an earlier paragenesis. Also that it can be construed that 4014_66m is a more overprinted version of 4014_65m, for example.

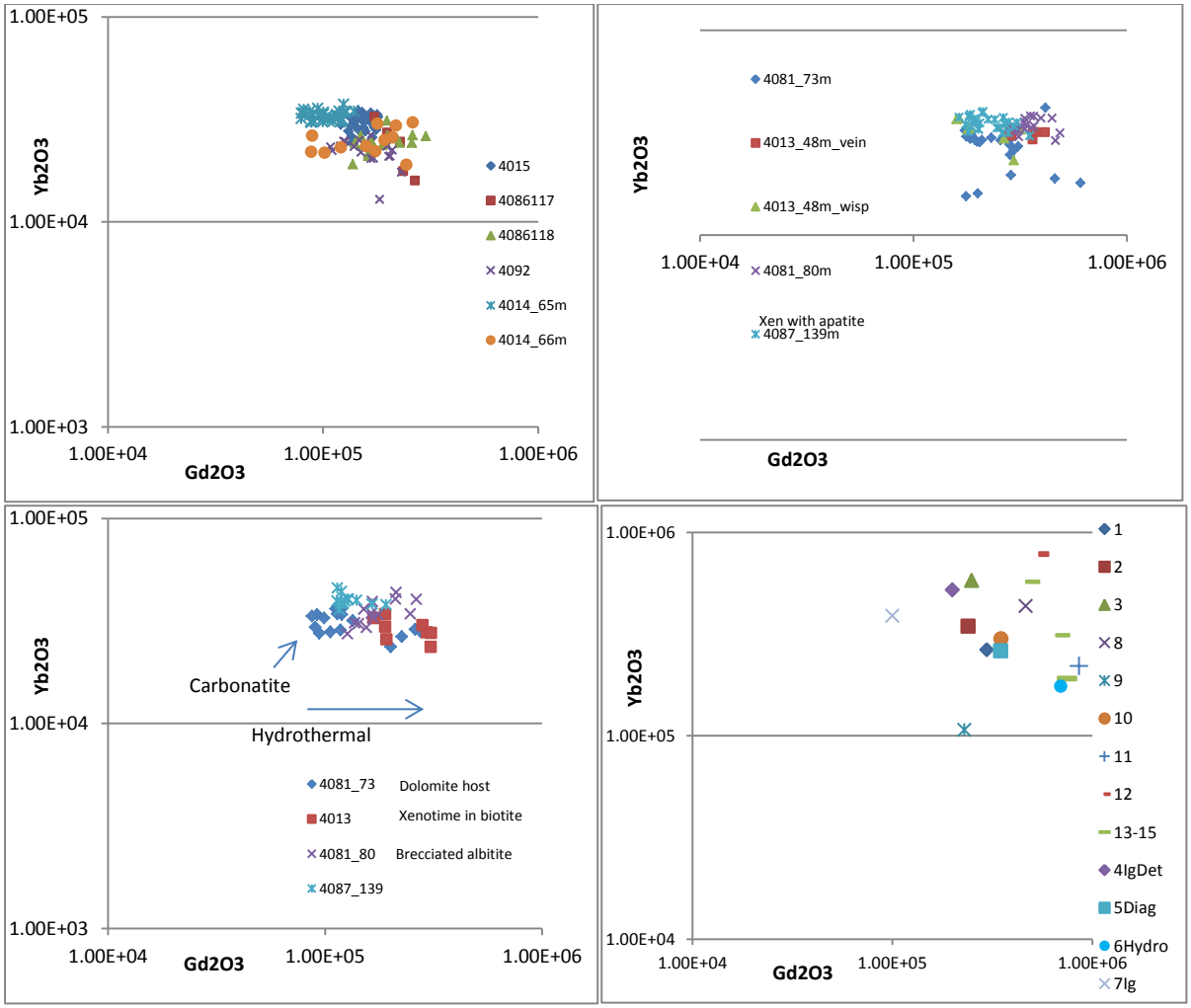

Figure 8.14 Yb vs Gd xenotime from 1. Rhyolite (Ondrejka et al., 2007). 2: Xenotime from pegmatite (Hetherington et al., 2008). 3: Xenotime from BIF (Bowins & Crocket, 2011). 4-7: Xenotime from Wits (SA Kositcin, 2003). 8: Xenotime from granite (Wang et al., 2003). 9: Xenotime from pegmatite (Masau et al., 2000). 10: Xenotime from alpine vein (Demartin et al., 1991). 11: Xenotime from metasediments (Franz et al., 1996). 12: Xenotime from granite (Forster, 1998). 13-15: Xenotimes from Browns Ranges (Cook et al., 2013). Adapted from Cook et al. (2013), and Kositcin (2003). Values are wt. %.

Results from Area 4 xenotimes in Figure 8.14 follow Kositcin's model. The more hydrothermal xenotimes seem more enriched in Gd. The clustering represents less variability in the distribution of REE in a given sample and perhaps one parageneses. More scatter relates to multiple parageneses i.e. xenotimes of different chemistries, and/or the presences of other REE phases e.g. in 4081 73m.

Figure 8.15 is interesting in that there are again some parallels. Not strictly applicable to Kositcin's model but certainly data that plots in the SW corner ties in with a more magmatic textures and associations observed in the samples. Data with a wider spread (i.e. shows greater variance) can be interpreted as having components of original, and re-deposited mineralisation (like in 4081_73m). But it is not only the distribution that's interesting – the relationship between Eu and Gd (how they correlate) is again of interest. It could be interpreted that when their relationship falls apart (i.e. they don't correlate so well) is indicative of modification e.g. xenotime crystals in 4015 are well rounded, crystals from 4081 73m occupy weathered pits in dolomite, for example.

From Figures 8.13, 8.14, and 8.15, of note are the similarities of the Area 4 xenotimes to those of the Browns Range REE deposit in Northern Territories, Australia. The mineralisation there is attributed to percolation of a volatile-rich, acidic fluid, possibly granite-derived, through porous arkose units. Late hematite may suggest mixing with meteoric water and subsequent oxidation. Like in Area 4 at Lofdal

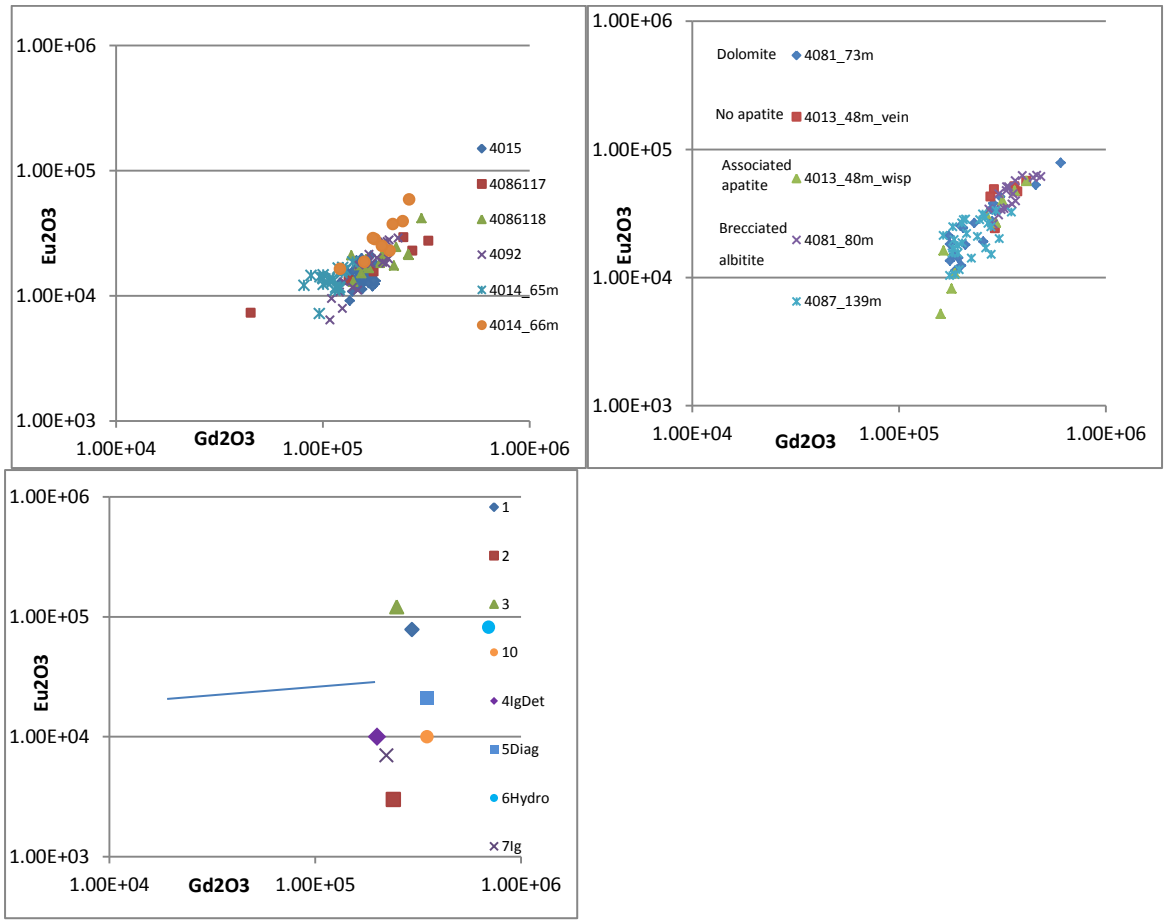

Figure 8.15 Eu vs Gd xenotime from 1. Rhyolite, Ondrejka et al. (2007). 2: Xenotime from pegmatite, Hetherington et al. 2008. 3: Xenotime from BIF Bowins & Crocket 2011. 4-7: Xenotime from Wits, SA Kositcin 2003. 8: Xenotime from granite Wang et al 2003. 9: Xenotime from pegmatite Masau et al 2000. 10: Xenotime from alpine vein Demartin et al. 1991. 11: Xenotime from metasediments Franz et al 1996. 12: Xenotime from granite Forster 1998. 13-15: Xenotimes from Browns Ranges Cook et al. 2013. Adapted from Cook et al 2013, and Kositcin 2001. Area 4: Strong correlation (strongest to weakest): 4013wisp r^2 0.948 (like Dy), 4086_117 r^2 0.85 (like Dy), 4092 r^2 0.817 (opposite to Dy), 4014_66 r^2 0.746 (opposite to Dy), 4081_80 r^2 0.668 (opposite to Dy), 4086_118 r^2 0.538. **Weak correlation:** 4013 vein 0.418 (like Dy), 4087_139 0.265 (like Dy), 4014_65 r^2 0.205, 4015 r^2 0.026, 4081_73 r^2 0.02 (like Dy). **Values are wt. %.**

field observations at Browns suggest that faults acted as fluid conduits and that brecciation, possibly associated with release of volatiles from the fluid, occurred along these faults.

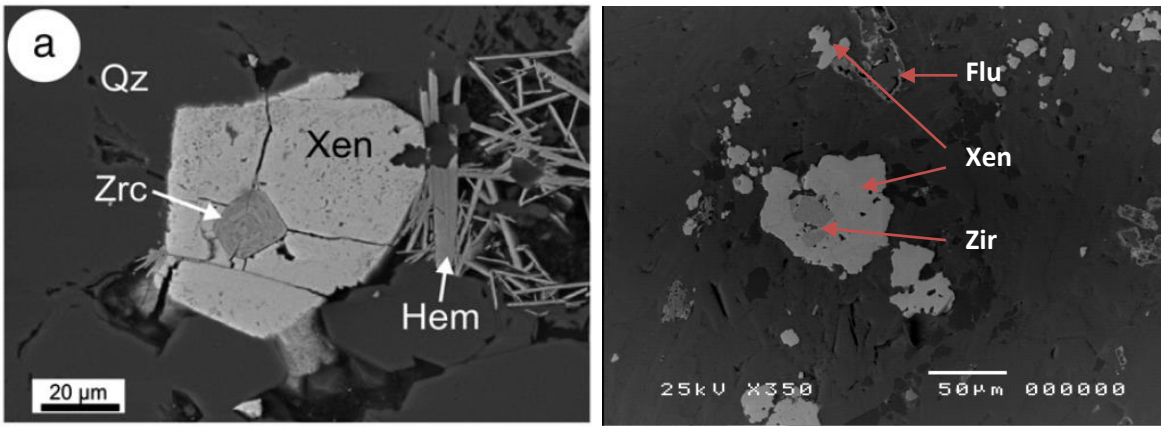

Figure 8.16 – Left image is an EPMA image of a coarse euhedral xenotime crystal surrounding a zoned zircon grain from Brown's Range (Cook et al., 2013) and it compares to an SEM BSE image (on the right) of Area 4 xenotime mantled zircons of Lofdal e.g. BSE image of 4092 188.15m on RHS

The six prospects at Browns Range are generally comparable to Area 4 xenotimes in terms of mineralogy, host rocks and macroscopic features. Xenotimes are seen as overgrowths on zircon (Figure 8.16), and in the form of euhedral disseminations (5–20 µm in size), akin to xenotime in Hole 4015 38.40m in Area 4. A main difference to the xenotime associations is the presence of later florencite at Browns deposit.

MREE and HREE values and proportions of the Brown's Range xenotimes are comparable to the Area 4 xenotimes. Yttrium concentrations range from 39.06 to 43.39 wt. % - see Table 8.1. U and Th are typically below 0.8 wt.%, and BDL respectively, at Browns Range and these are broadly similar to the Lofdal xenotimes. One difference is that the xenotime at Brown's Range is more uraniferous than the Lofdal xenotimes which have much lower U >0.2 wt. %.

Studies by Cook et al. (2013) of Browns Range point out differences in the REE chemistry of xenotime that are of considerable interest to understand the partitioning of REE-mineral systems. EPMA data for xenotime from Brown's Range (Table 8.1) show that the composition is relatively constant across all samples and prospects, despite the different morphologies and possible generations observed, as well as the lack of marked zonation. Again, like at Lofdal Area 4 the 2 elements that display significant variance across the xenotime dataset from Browns Range are Yb and Gd. Yb in xenotime varies from as low as 1.46 wt.% to as much as 4.01 wt.%. At Lofdal Yb ranges from 1.4-4%.

As demonstrated above, it is possible for the slightly larger REE to enter the 'A' site in xenotime such as Sm and Eu. The 'A' site in xenotime can also be substituted via complex isomorphic substitutions involving Ca^{2+}, Fe and Mn (Förster, 2006; Ondrejka et al., 2007). Although these cations are similar in size to Y they are **less likely** to fill the 'A' site in large concentrations (typically >10%; Ondrejka et al., 2007; Hetherington et al., 2008).

Electron probe microanalytical data for xenotime.

Sample no.	A5a		A5b		A5Nb		A5Na		GP1		Gpa		WP2		WP1		Wpa		WPb		MPb		Mpa		BPb	
no. of SPOTS	n = 12		n = 7		n = 5		n = 16		n = 12		n = 8		n = 11		n = 19		n = 7		n = 17		n = 8		n = 7		n = 10	
(Wt.%)	Mean	SD	Mean	SD	Mean	SD	Mean	SD	Mean	SD	Mean	SD	Mean	SD	Mean	SD	Mean	SD	Mean	SD	Mean	SD	Mean	SD	Mean	SD
CaO	0.00	0.00	0.21	0.14	0.15	0.06	0.17	0.04	0.19	0.06	0.23	0.08	0.25	0.10	0.27	0.20	0.16	0.07	0.26	0.05	0.42	0.11	0.43	0.11	0.19	0.06
Y_2O_3	42.42	0.92	41.47	0.50	43.05	1.57	42.79	0.90	41.02	1.58	43.39	0.95	39.73	0.82	39.06	1.74	42.50	0.47	41.83	0.96	41.56	1.16	40.86	1.18	43.34	0.70
Ce_2O_3	0.05	<mdl	<mdl	<mdl	<mdl	<mdl	0.11	0.05	0.08	0.07	0.14	0.10	0.08	0.06	0.06	0.05	0.05	0.03	0.14	0.06	0.05	0.10	0.12	0.03	0.10	0.06
Nd_2O_3	0.47	0.17	0.37	0.37	0.40	0.12	0.14	0.09	0.83	0.48	1.14	0.82	0.74	0.42	0.76	0.41	0.44	0.25	0.80	0.36	0.24	0.10	0.25	0.08	0.77	0.40
Sm_2O_3	1.12	0.24	1.04	0.09	1.19	0.15	1.36	0.30	1.43	0.34	1.63	0.45	1.15	0.33	1.39	0.34	1.11	0.46	1.50	0.23	0.69	0.21	0.68	0.12	1.97	0.52
Gd_2O_3	5.61	0.46	5.02	0.42	5.66	0.31	6.00	0.33	6.14	0.53	6.53	0.68	5.53	0.90	5.57	0.74	6.88	0.79	5.51	0.84	4.97	0.28	4.54	0.45	7.56	0.40
Dy_2O_3	0.38	0.25	0.39	0.25	<mdl	<mdl	0.51	0.26	0.80	0.10	0.72	0.24	0.55	0.36	0.42	0.41	0.87	0.19	0.73	0.16	<mdl	<mdl	0.43	0.20	0.57	0.21
Ho_2O_3	6.50	0.17	6.27	0.14	6.05	0.23	6.04	0.18	6.48	0.32	6.52	0.23	6.53	0.40	6.37	0.37	6.80	0.44	6.13	0.34	6.02	0.25	5.88	0.13	6.04	0.27
Er_2O_3	4.35	0.52	4.04	0.16	3.58	0.09	3.35	0.18	3.45	0.46	3.32	0.21	4.18	0.26	3.83	0.34	4.12	0.25	3.64	0.32	4.58	0.37	4.16	0.11	2.83	0.14
Yb_2O_3	4.24	0.86	3.60	0.16	2.64	0.18	2.46	0.31	2.19	0.65	2.09	0.42	3.81	0.48	3.02	0.47	3.48	0.49	3.05	0.62	4.65	0.56	4.03	0.26	1.46	0.17
Lu_2O_3	0.75	0.12	0.61	0.05	0.56	0.05	0.48	0.05	0.44	0.10	0.47	0.08	0.66	0.09	0.55	0.12	0.72	0.06	0.54	0.09	0.83	0.07	0.64	0.07	0.36	0.04
Sc_2O_3	0.03	0.01	0.03	0.01	0.02	0.01	0.03	0.01	0.03	0.03	0.01	0.02	0.06	0.03	0.04	0.02	0.04	0.03	0.05	0.02	0.12	0.03	0.09	0.02	0.01	0.01
PbO	0.07	0.04	0.13	0.07	0.08	0.04	0.09	0.04	0.06	0.05	<mdl	<mdl	<mdl	<mdl	<mdl	<mdl	<mdl	<mdl	<mdl	<mdl	0.10	0.08	0.17	0.09	0.06	0.02
K_2O	<mdl	<mdl	<mdl	<mdl	<mdl	<mdl	<mdl	<mdl	0.01	0.02	<mdl	<mdl	0.01	0.01	0.01	0.01	<mdl	<mdl	<mdl	<mdl	<mdl	<mdl	<mdl	<mdl	<mdl	<mdl
ThO_2	0.02	0.03	0.11	0.08	0.00	0.00	0.00	0.00	0.00	0.00	0.00	0.00	0.00	0.00	0.00	0.00	0.03	0.05	0.00	0.00	0.00	0.00	0.94	0.46	0.00	<mdl
UO_2	0.57	0.22	0.80	0.19	0.42	0.11	0.55	0.14	0.35	0.21	0.22	0.16	0.36	0.15	0.41	0.20	0.38	0.24	0.28	0.16	0.62	0.15	0.61	0.18	0.43	0.14
PrO	0.68	0.92	1.02	1.19	3.12	3.71	0.93	1.20	0.00	0.01	0.46	0.87	0.53	0.70	1.72	2.41	0.00	0.00	0.03	0.08	0.82	0.74	0.66	0.51	0.71	0.40
TiO_2	0.01	0.01	<mdl	<mdl	<mdl	<mdl	0.01	0.01	0.01	0.01	<mdl	<mdl	0.01	0.02	0.01	0.01	<mdl	<mdl	0.01	0.01	<mdl	<mdl	0.01	0.02	0.01	0.01
SiO_2	0.09	0.07	0.16	0.04	1.45	2.71	0.30	0.59	0.12	0.26	0.04	0.05	0.08	0.16	0.20	0.26	0.01	0.01	0.59	0.44	0.71	0.45	2.23	1.62	0.41	1.05
Al_2O_3	<mdl	<mdl	<mdl	<mdl	<mdl	<mdl	<mdl	<mdl	0.01	0.04	<mdl	<mdl	<mdl	<mdl	<mdl	<mdl	<mdl	<mdl	0.01	0.03	0.01	0.02	0.37	0.79	<mdl	<mdl
P_2O_5	34.08	0.59	32.13	0.43	33.43	1.01	32.37	0.48	33.67	0.55	33.81	0.64	33.00	0.77	32.93	1.07	34.31	0.33	32.31	0.74	32.80	0.59	30.98	1.59	33.98	0.38
F (wt.%)	<mdl	<mdl	0.13	0.04	<mdl	<mdl	0.14	0.04	0.10	0.04	<mdl	<mdl	0.13	0.04	0.22	0.44	<mdl	<mdl	0.14	0.03	<mdl	<mdl	0.19	0.07	<mdl	<mdl
Cl (wt.%)	0.01	0.01	0.01	0.01	<mdl	<mdl	0.02	0.02	0.02	0.02	0.03	0.03	0.02	0.02	0.02	0.02	<mdl	<mdl	0.03	0.02	0.02	0.01	0.03	0.02	0.02	0.01
Total	101.54		97.68		102.14		97.98		97.66		101.13		97.54		97.13		102.06		97.66		99.52		98.22		101.10	
Formulae on basis of 6 a.p.f.u.																										
Ca	0.00	0.00	0.01	0.01	0.01	0.00	0.01	0.00	0.01	0.00	0.01	0.00	0.01	0.00	0.01	0.01	0.01	0.00	0.01	0.00	0.02	0.00	0.02	0.00	0.01	0.00
Y	0.76	0.01	0.78	0.01	0.76	0.04	0.79	0.02	0.76	0.03	0.78	0.02	0.74	0.01	0.73	0.03	0.76	0.01	0.78	0.01	0.76	0.02	0.75	0.02	0.77	0.02
Ce	0.00	0.00	0.00	0.00	0.00	0.00	0.00	0.00	0.00	0.00	0.00	0.00	0.00	0.00	0.00	0.00	0.00	0.00	0.00	0.00	0.00	0.00	0.00	0.00	0.00	0.00
Nd	0.01	0.00	0.00	0.00	0.00	0.00	0.00	0.00	0.01	0.01	0.01	0.01	0.01	0.01	0.01	0.01	0.01	0.00	0.01	0.00	0.00	0.00	0.00	0.00	0.01	0.00
Sm	0.01	0.00	0.01	0.00	0.01	0.00	0.02	0.00	0.02	0.00	0.02	0.01	0.01	0.00	0.02	0.00	0.01	0.01	0.02	0.00	0.01	0.00	0.01	0.00	0.02	0.01
Gd	0.06	0.00	0.06	0.01	0.06	0.00	0.07	0.00	0.07	0.01	0.07	0.01	0.06	0.01	0.06	0.01	0.08	0.01	0.06	0.01	0.06	0.00	0.05	0.01	0.08	0.00
Tb	0.00	0.00	0.00	0.00	0.00	0.00	0.01	0.00	0.01	0.00	0.01	0.00	0.01	0.00	0.00	0.00	0.01	0.00	0.01	0.00	0.00	0.00	0.00	0.00	0.01	0.00
Dy	0.07	0.00	0.07	0.00	0.06	0.00	0.07	0.00	0.07	0.00	0.07	0.00	0.07	0.00	0.07	0.00	0.07	0.00	0.07	0.00	0.07	0.00	0.07	0.00	0.07	0.00
Er	0.05	0.01	0.04	0.00	0.04	0.00	0.04	0.00	0.04	0.00	0.04	0.00	0.05	0.00	0.04	0.00	0.04	0.00	0.04	0.00	0.05	0.00	0.05	0.00	0.03	0.00
Yb	0.04	0.01	0.04	0.00	0.03	0.00	0.03	0.00	0.02	0.01	0.02	0.00	0.04	0.01	0.03	0.00	0.04	0.01	0.03	0.01	0.05	0.01	0.04	0.00	0.02	0.00
Lu	0.01	0.00	0.01	0.00	0.01	0.00	0.01	0.00	0.00	0.00	0.00	0.00	0.01	0.00	0.01	0.00	0.01	0.00	0.01	0.00	0.01	0.00	0.01	0.00	0.00	0.00
Sc	0.00	0.00	0.00	0.00	0.00	0.00	0.00	0.00	0.00	0.00	0.00	0.00	0.00	0.00	0.00	0.00	0.00	0.00	0.00	0.00	0.00	0.00	0.00	0.00	0.00	0.00
Pb	0.00	0.00	0.00	0.00	0.00	0.00	0.00	0.00	0.00	0.00	0.00	0.00	0.00	0.00	0.00	0.00	0.00	0.00	0.00	0.00	0.00	0.00	0.00	0.00	0.00	0.00
Nb	0.00	0.00	0.00	0.00	0.00	0.00	0.00	0.00	0.00	0.00	0.00	0.00	0.00	0.00	0.00	0.00	0.00	0.00	0.00	0.00	0.00	0.00	0.00	0.00	0.00	0.00
Fe	0.02	0.03	0.03	0.04	0.09	0.11	0.03	0.04	0.00	0.00	0.01	0.02	0.02	0.02	0.05	0.07	0.00	0.00	0.00	0.00	0.02	0.02	0.02	0.01	0.02	0.01
Th	0.00	0.00	0.00	0.00	0.00	0.00	0.00	0.00	0.00	0.00	0.00	0.00	0.00	0.00	0.00	0.00	0.00	0.00	0.00	0.00	0.00	0.00	0.01	0.00	0.00	0.00
U	0.00	0.00	0.01	0.00	0.00	0.00	0.00	0.00	0.00	0.00	0.00	0.00	0.00	0.00	0.00	0.00	0.00	0.00	0.00	0.00	0.00	0.00	0.00	0.00	0.00	0.00
Total	1.04		1.07		1.07		1.07		1.02		1.06		1.04		1.05		1.04		1.05		1.05		1.04		1.05	
P	0.97	0.01	0.96	0.01	0.94	0.03	0.96	0.01	0.99	0.01	0.97	0.01	0.98	0.01	0.98	0.02	0.98	0.01	0.96	0.01	0.95	0.01	0.91	0.04	0.97	0.02
Si	0.00	0.00	0.01	0.00	0.05	0.08	0.01	0.02	0.00	0.01	0.00	0.00	0.00	0.01	0.01	0.01	0.00	0.00	0.02	0.01	0.02	0.02	0.08	0.06	0.01	0.03
Total	0.98		0.96		0.98		0.97		0.99		0.97		0.98		0.98		0.98		0.98		0.98		0.99		0.98	
F	0.00	0.00	0.02	0.00	0.00	0.00	0.02	0.00	0.01	0.00	0.00	0.00	0.01	0.00	0.02	0.05	0.00	0.00	0.02	0.00	0.00	0.00	0.02	0.01	0.00	0.00
Cl	0.00	0.00	0.00	0.00	0.00	0.00	0.00	0.00	0.00	0.00	0.00	0.00	0.00	0.00	0.00	0.00	0.00	0.00	0.00	0.00	0.00	0.00	0.00	0.00	0.00	0.00
Total	0.00		0.02		0.00		0.02		0.01		0.00		0.02		0.03		0.00		0.02		0.00		0.02		0.00	
mol.% end-members																										
Xenotime-(Y)	73.0	1.8	72.7	2.0	71.1	6.2	74.5	2.4	74.3	1.4	73.9	2.2	71.5	1.9	69.7	4.8	73.3	0.7	74.5	1.1	72.1	1.7	72.7	0.9	74.1	1.2
Xenotime-(Gd)	6.0	0.5	5.5	0.4	5.8	0.7	6.5	0.4	6.9	0.6	6.9	0.8	6.2	1.0	6.2	0.9	7.4	0.8	6.1	0.9	5.4	0.3	5.0	0.5	8.0	0.4
Xenotime-(Dy)	6.8	0.2	6.7	0.2	6.0	0.6	6.4	0.2	7.1	0.4	6.7	0.3	7.1	0.5	6.9	0.6	7.1	0.4	6.6	0.4	6.3	0.3	6.3	0.3	6.2	0.3
Xenotime-(Yb)	4.3	0.9	3.7	0.2	2.6	0.3	2.5	0.3	2.3	0.7	2.1	0.5	4.0	0.5	3.2	0.5	3.5	0.5	3.2	0.7	4.7	0.6	4.2	0.3	1.5	0.2
Pretulite-(Sc)	0.1	0.0	0.1	0.0	0.0	0.0	0.1	0.0	0.1	0.1	0.0	0.0	0.2	0.1	0.1	0.1	0.1	0.1	0.1	0.1	0.3	0.1	0.3	0.1	0.0	0.0

Table 8.1 Xenotime EPMA analysis data from Browns Range, Australia. Data shows the marked enrichment in HREE relative to LREE, with notable Gd (5.02–6.88 wt.%), Tb (up to 0.87 wt.%), Dy (5.88–6.52 wt.%), Er (3.32–4.58 wt.%), Yb (2.09– 4.65 wt.%) and Lu (0.36–0.83 wt.%); Ho is below mdl in all analyses. REE distributions are similar to Lofdal (Table from Cook et al., 2013).

Element maps from Cook et al. (2013), reveal a subtle yet systematic zoning in some Browns xenotimes. Importantly, LREE (La–Pr) are either concentrated in the grain cores, or, alternatively, closest to the initial point of growth. The heaviest REE, notably Tm, Yb and Lu, are highest along the outer margins of the grains. It is suggested that such variance is likely controlled by the initial abundance of certain REE from the source fluid or from interaction with wallrock during flow to the site of deposition.

8.2.3 The actinides issue - Th and U

Generally xenotime, like zircon, incorporates more U than Th into its structure. It has been shown in variety of deposits that hydrothermal xenotime possesses distinctively lower U and Th concentrations (0.12–0.02 wt.% U; 0.59–0.0 wt.% Th) compared to magmatic derived xenotime.

The main mechanisms for the replacement of Y & REE by U or Th are charge balancing coupled substitutions involving Si and Ca (van Emden et al., 1997):

Substitution 1: $(REE, Y)^{3+} + P^{5+} <> (Th, U)^{4+} + Si^{4+}$

Substitution 2: $2(REE, Y)^{3+} <> (U, Th)^{4+} + Ca^{2+}$

The incorporation of U and Th in to xenotime is dominantly by substitution 1, mainly because of the size constraints imposed by the xenotime structure (Emden et al., 1997). This structure accommodates Si_4 in the P_5 site, but precludes significant amounts of other charge-balancing cations, such as Ca_2 for example, due to their larger size compared to the HREE (Emden et al., 1997; Forster, 1998). From EPMA analysis Ca content in Area 4 xenotime is low (generally below 0.05 wt. % as in Figure 8.18) and do not correlate as well as Si does with Th. When considering substitution of elements into the Y-site, there is commonly an overabundance of ions when Y, REE, Si, Ca, Fe, Zr, U, Th, and Pb are combined. Removing Si, which substitutes in the P-site (substitution 1), removes most of the excess ions in the Y-site. However, xenotimes can have excess ions, which can probably be attributed to “mixed” analyses with zircon, because removal of both Si and Zr reduces all analyses to within error of, or below, 1.00 cations in the Y-site for four oxygens. The positive correlation of Si and Th indicates the occurrence of a thorite substitution (Figure 8.17).

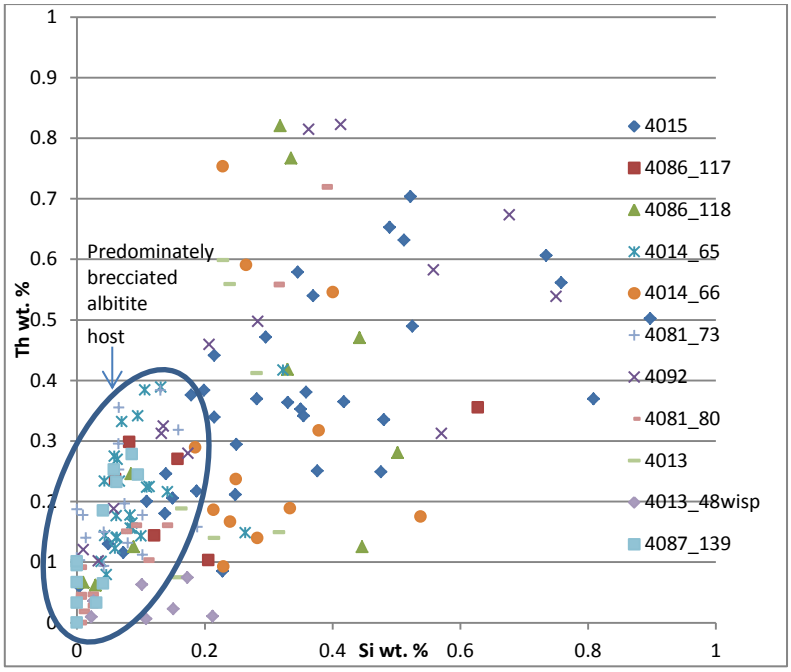

Figure 8.17. Th (y) vs Si (x)(element) for a range of Lofdal xenotimes – correlation suggests substitution 1
R2: 4081_80=0.95, 4015=0.42 (affecting Eu/Gd?), 4086_117=0.23, 4086_118=0.31, 4014_65=0.18, 4014_66=0.0018, 4092=0.04, 4081_73=0.03

From Figure 8.17 it appears that sample 4081_80m and 4015 has undergone a degree of substitution 1 with a strong correlation of Th vs Si. Other samples from highly radiogenic sections such as 4092 _188m do not display the correlation and it is suggested that Th must reside in another phase such as thorite, akin to what is seen via SEM at 4086_117m.

Förster (1998) states that xenotime that has formed from the breakdown of zircon or thorite, or both, can explain higher than average HREE contents. Monazite's structure has been show to better accommodate Th whereas xenotime better accommodates U due to differences in ionic radii and the cell parameters of the respective minerals (Förster, 1998). Suppressed amounts of U in Area 4 xenotimes (see Figure 8.19) could be attributed to the fact that U could be locked-up in uranpyrochlore of the sovites intrusive bodies of the Lofdal Igneous Complex as described by Gaudet (2012). Indeed, the crystallisation of pyrochlore in the CAG of the Madeira deposit, Amazonia, Brazil began prior to xenotime crystallisation. The pyrochlore here contains significant amounts of U and Th (Minuzzi et al, 2006) and it is thought that the paucity of U especially, and Th, in the xenotime is partly due to this. The uraniferous pyrochlore found in the sövites of the main intrusion could explain the low U found in the xenotimes as the rapid crystallization of fluorapatite in the main intrusion would reduce the activities of P and F, which would decrease the solubility of Nb, Ta, and notably U (Hogarth et al., 2000), i.e. via the formation of fluorine and phosphate complexes, P and F are consumed through the crystallisation of fluorapatite, and as a result the solubility of Nb, Ta and U decreases rapidly (Hogarth et al., 2000).

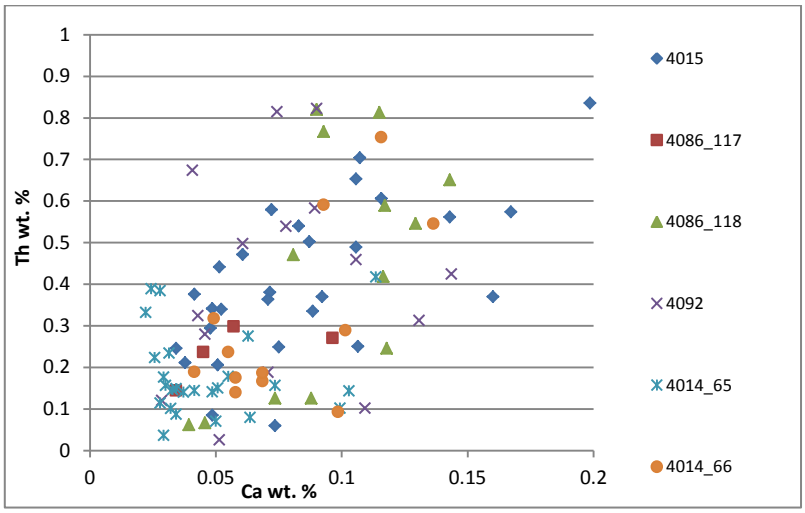

Figure 8.18 Th vs Ca (element) – correlations could suggest substitution 2 – but only in minor amounts comparatively to substitution 1. R^2: 4015=0.04, 4014_65=0.001, 4014_66=0.41, 4086_117=0.48, 4086_118=0.01, 4092=0.19

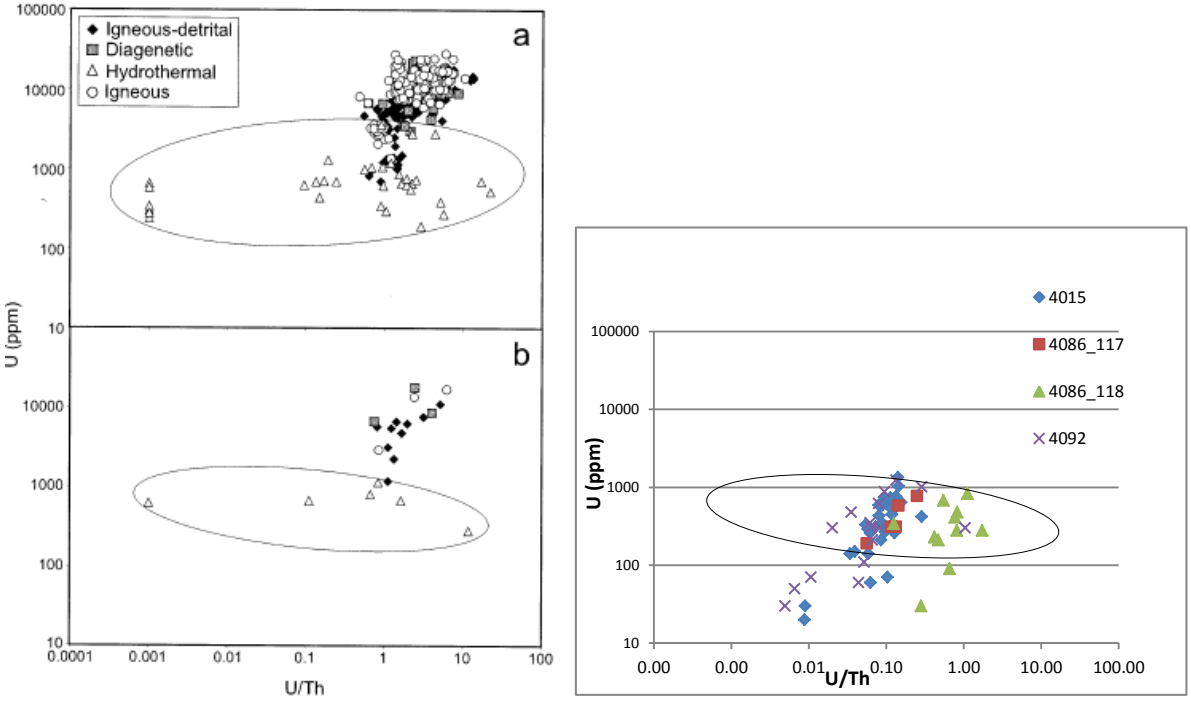

Figure 8.19 plot of U/Th against U ppm Kositcin 2003 Witwatersrand xenotime LHS vs Area 4 Lofdal xenotimes RHS.

Xenotime from the Area 4 alteration zone appears to have an association with thorite, whether as a separate phase or as a component within xenotime. Th may reside in other minor phases such as aeschynite. Why other parts of the Lofdal Igneous Complex are highly radiogenic in comparison such Area 5 is not known. In the dykes Wall (2008) reported Th as existing interstitially between zonations in xenotime and rimming the zircon cores of mantled crystals. Figure 8.20 displays a BSE image of magnetite-rich dolomitic carbonatite with a xenotime intergrown with thorite with a halo of apatite.

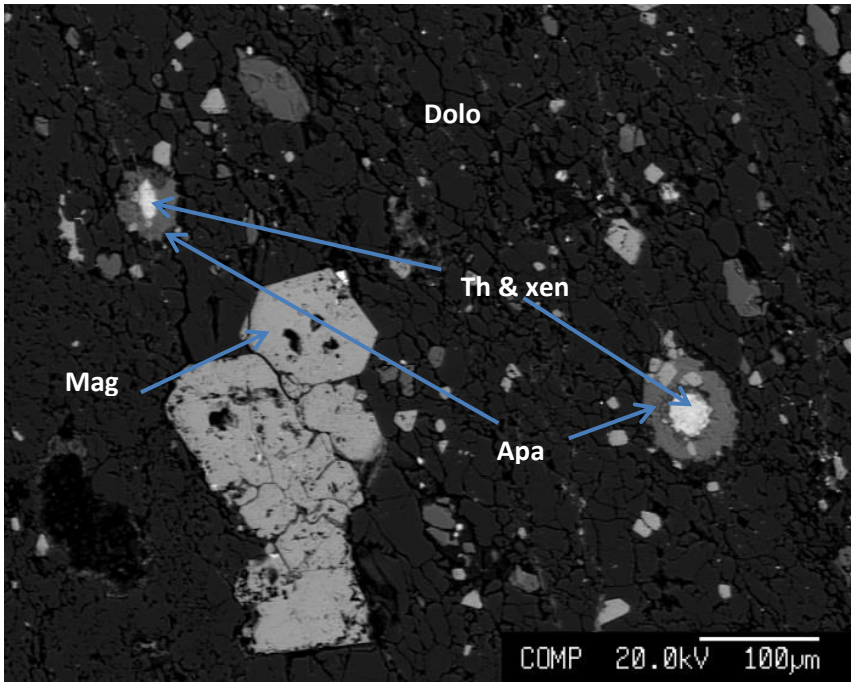

Figure 8.20 4032 47.56m BSE image magnetite with Th-rich xenotime mantled by apatite in dolomitic carbonatite

Förster & Wirth (2006) point out that compositional exchange between the two end members of xenotime and thorite are continuous, **and** the minerals are iso-structural. The distinction therefore between structural association (iso-structural seeding, like zircon), and chemical (Th uptake into the xenotime lattice) therefore must have important implications from a processing point of view, as well as for ore genesis.

Harlov & Wirth (2012) conducted experiments that involved heating and pressurising huttonite (thorite group mineral) with xenotime to metamorphic grades and introducing in sodic silicate and water, creating perhaps a sodic metasomatic environment similar to what Area 4 may have experienced. At 600° and 500MPa, amphibolite-facies grade, huttonite is incorporated into xenotime (Table 8.2). It is probable that these conditions that could have occurred in the Lofdal Igneous Complex that could explain the association of thorite and xenotime. However, temperature determinations by Wall (2008) claim a temperature of formation of xenotimes in the dykes at circa 400°C indicating perhaps that any Th incorporated may be testament to an earlier xenotime associated with higher temperatures of carbonatite origin. Importantly with decreasing temperature Th is less preferentially incorporated into xenotime and is more likely to form in its own phase as a thorite group mineral.

Table 8.2 Experimental results of heating and pressurising huttonite with xenotime to metamorphic grades and introducing alkali fluids. Harlov & Wirth 2012

Experiment	*P* (MPa)	*T* (°C)	Time	Xn	SiO_2	Al_2O_3	$ThSiO_4$*	NaF	$Na_2Si_2O_5$	H_2O	2 *N* NaOH	2 *N* KOH	Comments
MX-89	500	600	548 h	21.28	5.67	5.59	5.27					28.16	no obvious $ThSiO_4$-enriched textures
MX-88	500	600	548 h	20.27	5.31	5.54	6.19				26.92		no obvious $ThSiO_4$-enriched textures
MX-90	500	600	548 h	22.69	5.31	5.73	6.13		21.84	19.98			$ThSiO_4$-enriched textures along Xn grain rims
MX-76	1000	900	596 h	20.32	9.87	5.62	5.62					31.31	$ThSiO_4$-enriched texture on one grain
MX-75	1000	900	24 d	20.26	10.02	5.44	5.1				29.5		no $ThSiO_4$-enriched textures
MX-74	1000	900	596 h	19.68	4.80	5.36	7.75		15.15	27.62			$ThSiO_4$-enriched textures along a few Xn grains
MX-94	1000	900	8d	20.08			5.12	5.35		24.32			$ThSiO_4$-enriched textures along Xn grain rims

Note: Solids and fluid in milligrams.
* Actually $ThSiO_4 + ThO_2 + SiO_2$.

Structural lattice parameters, AND temperature are important factors in dictating both the REE budget in xenotime, as well as the incorporation of Ca and Si into the P site, and for the incorporation of deleterious elements such as Th into the Y site (Figures 8.21 and 8.22). The REE content of the original source fluid must be taken into consideration in dictating a given minerals REE budget, and this will be discussed in the following section i.e. to what extent is REE fractionation dependant on fluid dynamics.

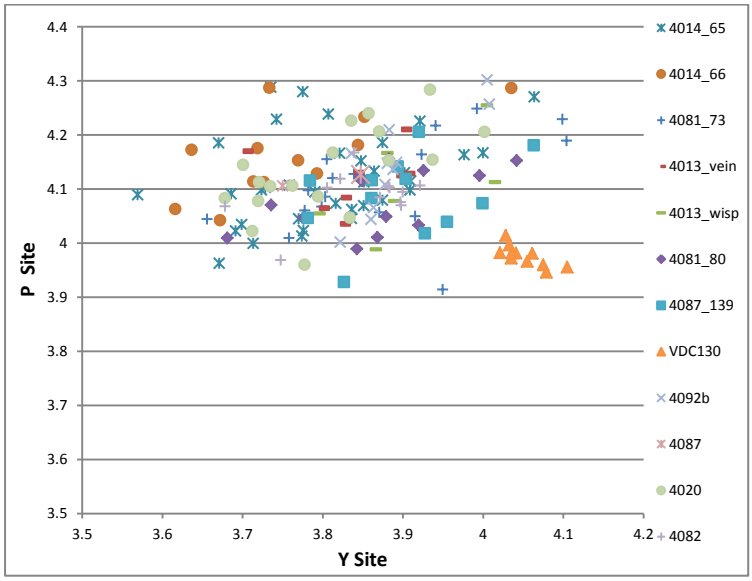

Figure 8.21 P site vs Y site apfu 16 oxygens

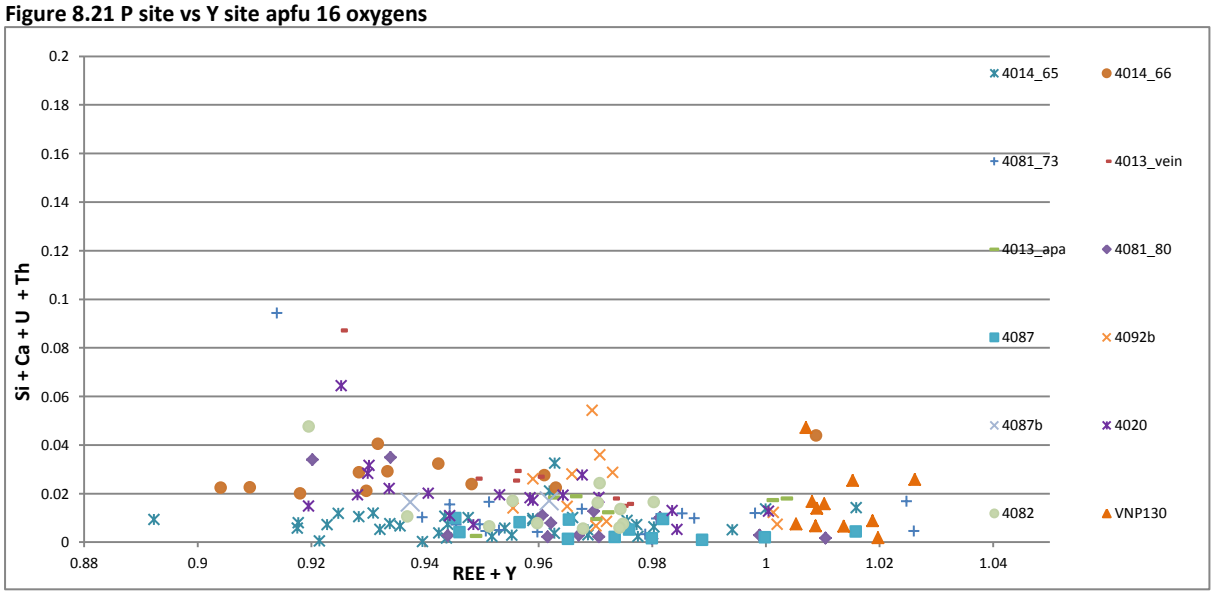

Figure 8.22 Si+Ca+U+Th vs REE+Y apfu 4 oxygens

8.4 Hydrothermal system and mineralising fluids

To accept that the xenotime in the alteration zone of Area 4 was transported and deposited here by hydrothermal solutions then questions remain about the chemistry of the HREE bearing fluids that passed through the protolith and deposited, and/or re-deposited the xenotime and associated phases i.e. what were the nature of fluids?

It is generally agreed that the presence and concentration of REE in hydrothermal fluids are mainly controlled by temperature, pressure and the composition of the fluid phase – these variables combined with crystallochemical factors and reaction kinetics, also control the REE partitioning between the minerals and the solution as well as between the solution and the melt from which the fluids may have been derived (Gieré, 1986).

The role of biotite-phlogopite is an important associate of the HREE bearing phases in Area 4. Biotite and phlogopite form part of the observed flow texture in areas that are rich in albite. This observation suggests that biotite and phlogopite are part of the albitisation, which preceded the HREE enrichment process. Contrary, to this observation is the association of biotite with dolomite and perhaps dolomite is crucial in offering Mg to these micas in fluid-rock interaction, thus leading to addition of OH and the development of chloritisation. Do Cabo (2013) obtained K/Ar dates on the biotite from HREE bearing dykes giving an age of 500-600Ma an age consistent with deformation phases of the Pan African Orogeny, but yes, is quite a bit earlier than the Lofdal zircon dating of the carbonatites at c.760Ma. This suggests that the biotite developed via metamorphic processes during the Pan African Orogeny. However, reliability of K/Ar dating of micas is notoriously untrustworthy, but is worth considering as a possibility, and could certainly reinforce the notion of activities of later fluids and REE mobility.

While on the subject of dating, Heinrich et al. (1997) demonstrated that REE partitioning between monazite and xenotime is appropriate for geothermometry, notably in metapelitic rocks. Solid solutions of rare earth phosphates were synthesized hydrothermally between 300°C and 1000°Cmat pressures of 2, 5, 10, and 15 kbar. As well as noting that variations of the unit-cell dimensions are directly correlated with variations in composition, as described previously, the boundaries of the asymmetric miscibility gap between monazite and xenotime are strongly dependent on temperature. At 2 kbar and from 300–1000 °C, maximum Y concentrations in monazite, coexisting with xenotime, are shown to increase from 3 to 16 mol%. With increasing pressure, this limb is shifted to higher Y contents so that at 15 kbar it ranges from 6 to about 25 mol% for the same temperature range. The essential point is that incorporation of the HREE (Gd to Yb) into monazite and of LREE (La to Sm) into xenotime for metapelitic bulk compositions tends to be temperature dependent, see Figure 8.23 (Heinrich et al., 1997).

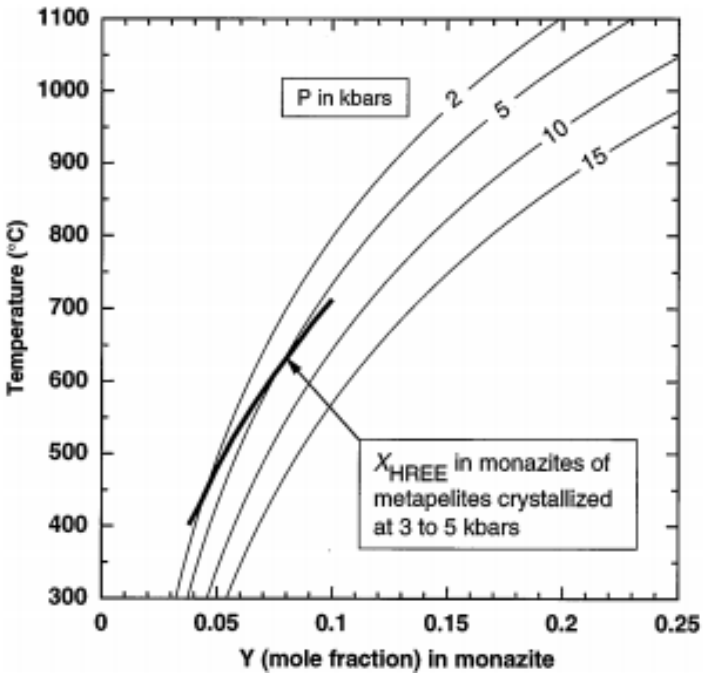

Figure 8.23. *X* monazite/Y temperature plot showing the monazite Y limb of the miscibility gap at various pressures, calculated using Equation 1. Thick curve indicates the mole fraction of Y 1 HREE (Gd-Lu) of natural monazites from a metapelite suite that crystallized together with xenotime at about 400–700°C and about 3 to 5 kbar (Heinrich et al., 1997)

How relevant these studies are to Lofdal REE phosphate minerals is up for debate considering the fact that the metapelitic host in Heinrich's study is different from Lofdal's host rocks. Heinrich's geothermometrical principal was applied by Wall (2008) to a sample of coexisting monazite and xenotime (sample VNP21 2km southwest of Area 4, and 1km south of the main intrusion). With a molar proportion of HREE [(Gd-Lu + Y)/total REE] of 0.051 for the Lofdal monazite-(Ce), a temperature has been interpolated of 450-500°C at 5-2 kbar when plotted on the monazite limb of the (Ce-Y)PO_4 binary after Heinrich's model. Mole fractions of LREE in xenotime are much less sensitive, and with a value of 0.008, the Lofdal xenotime corresponds to a higher temperature of 600°C, but as Wall (2008) points out that may be a little high for a carbonate dominated domain and formational temperature for xenotime in VNP21.

Early sodic metasomatic fluid infusion, and subsequent fenitisation of the gneissic protolith along structural weaknesses and faults, has been influential for the suitable ground-preparation for HREE depositional processes, and for the evolution of the hydrothermal system in Area 4. Hetherington & Harlov (2010) experimentally metasomatised xenotime from Zagi Mountain pegmatite in northern Pakistan were in a series of common metamorphic and igneous fluids at 600°C/500 MPa and 900°C/1000 MPa. Among the results was that successful partial replacement of monazite grain rims by Th-enriched monazite occurred only in the alkaline fluids, i.e. small compositional changes and partial replacement of the monazite grain rim by Th-enriched monazite in NaOH and ($Na_2Si_2O_5$+H_2O) fluid. Applying this principal to a HREE phosphate, i.e. xenotime, could be an explanation of the association

of Th with xenotime, as a coeval component, and later replacement or removal, and reinforce the notion that sodic metasomatism could have been present throughout the Area 4 system's evolution, and into the meteoric hydrothermal phase. It could also explain the process of "re-albitisation" of pre-existing albite. But these temperatures are high (600°C), and although could have been experienced in the early emplacement of carbonatite can't explain the transport of REE at the lower temperatures of later hydrothermal activity.

A lower temperature system, and/or hydrothermal reworking, can be evidenced from oxygen isotope analysis (Figure 8.24). Do Cabo's "carbonatite" dykes give a wide range of $\delta^{18}O$ reinforcing interpretation of intensive hydrothermal overprinting, and early Na-fenitisation, observed in both the distal dykes and the albitisation in Area 4. The carbon and oxygen isotopes of highest variation are in Do Cabo's Type 2 dykes exhibiting a noticeable spread away from the primary field, low-temperature hydrothermal towards the field for meteoric water. Type 2 dykes are most akin to geochemistry of a majority of the Area 4 REE mineralisation.

Although fractional crystallisation and liquid immiscibility may affect the oxygen and carbon isotopic composition of the main intrusion carbonatite, it is mainly the hydrothermal alteration that affects the oxygen and carbon isotopic composition highlighting the shift from the magmatic to the hydrothermal meteoric field in the proximal dykes, or fault zones (as displayed in Figure 8.24).

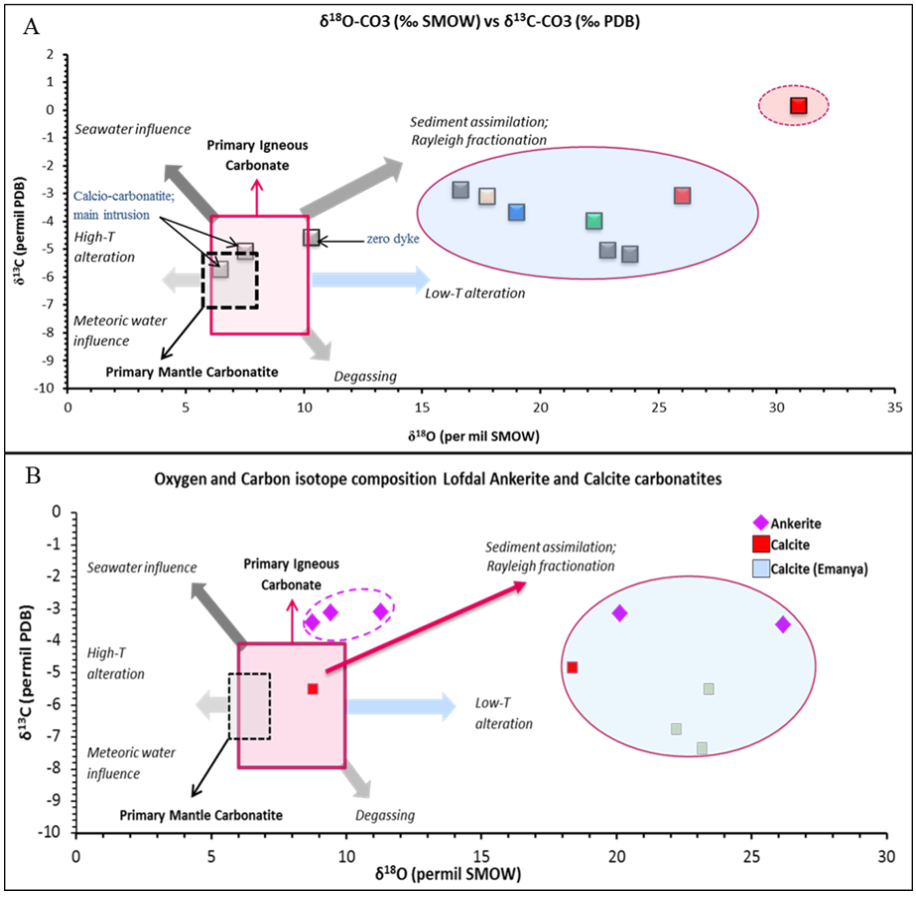

Figure 8.24 O and C isotope data from Lofdal dykes and plugs, from Do Cabo 2013

Intense interaction with the cooler country rocks evidence Sr isotopes and large variations in $\delta^{18}O$ and $\delta^{13}C$ in those complexes in which the REE-rich carbonatite dykes and the host country rocks of the carbonatites are extensively hydrothermally altered. Of interest here, as they have a similar REE fractionation trend to Area 4, calcite in Type 2 dykes show $^{87}Sr/^{86}Sr$ of 0.70804 and thus much higher than in samples of the Main Intrusion calciocarbonatite ($^{87}Sr/^{86}Sr$ 0.70274). This suggests a slightly enriched ^{87}Sr source pointing to assimilation of crustal materials during shearing and brecciation of gneissic country rocks in similar fashion as those described (Bell & Blenkinsopp, 1989).

The distinct trace element behaviour and the common features of magmatic-hydrothermal alteration around a carbonatite complex like Lofdal suggest the increasing importance of an aqueous-like fluid system during the final stages of carbonatite intrusion. Chakhmouradian & Wall (2012) put forward that Y and Ho show different partitioning behaviour in aqueous solutions, which has been attributed to the involvement of *f* or *s* electrons in metal– ligand bonding (Choppin, 2002), or to stereochemical changes during the transition from a solute to a solid (Tanaka et al, 2008). Chakhmouradian & Wall (2012) interpret that these differences in radius, oxidation state, and bonding drive fractionation of REEs in natural systems, can be used to determine hydrothermal systems.

The tetrad effect (as described for Gd earlier), and the highly fractionated trace element ratios of Y/Ho, and Zr/Hf as well ,indicate a trace element behaviour that is similar to that in aqueous systems in which chemical complexation is of significant influence, as championed by Bau (1996). Bau proposes that a geochemical system is characterized by *CHA*rge-and-*RA*dius-*C*ontrolled (*CHARAC*) trace element behaviour, elements of similar charge and radius, akin to Goldschmidt's Rule in that isovalent trace elements of equal or very similar ionic radii should remain tightly coupled in geological processes. Y-Ho and Zr-Hf twin pairs, for example, should display extremely coherent behaviour, and retain their respective chondritic ratio. One should expect normalized patterns of REE to be smooth functions of ionic radius and atomic number. **However, aqueous solutions and their precipitates normally show non-chondritic Y/Ho and Zr/Hf ratios** (Figure 8.25).

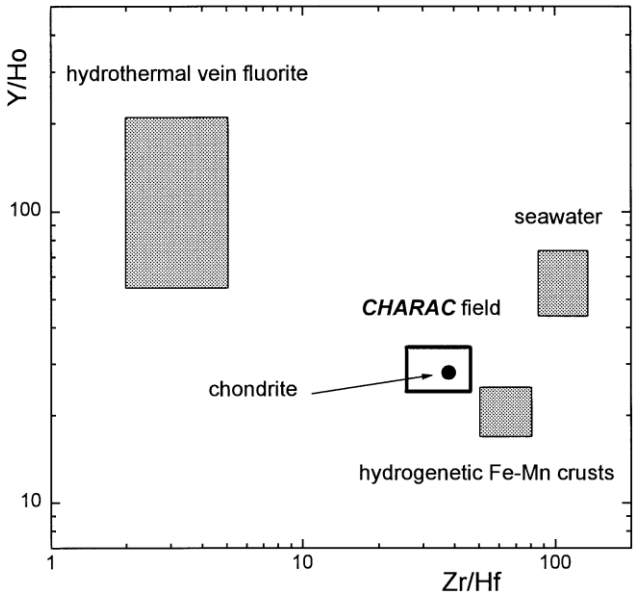

Figure 8.25 the geochemical twin pairs Y-Ho and Zr-Hf are highly fractionated in aqueous media. Non-CHARAC behaviour of Y, REEs, Zr, and Hf in aqueous fluids results from chemical complexation, and electron structure must be considered as an additional parameter - Bau 1996.

An important process that causes trace element fractionation in aqueous media is chemical complexation. **The complexation behaviour of a trace element, however, does not only depend on its ionic charge and radius, but is additionally controlled by its electron configuration and by the type of complexing ligand**, and these determine the character of the chemical bonding (i.e. covalent *vs* electrostatic) for various complexes. It can therefore be assumed that aqueous systems are characterized by non-CHARAC trace element behaviour, and electron structure must be considered as an important additional parameter.

Figure 8.26 displays the Zr/Hf versus Y/Ho from whole-rock analysis of high grade intercepts (+2000ppm TREE) for Area 4. The blue-lined box represents the rocks that adhere to CHARAC behaviour. Of interest is that intercepts include magnetitic carbonatite intercepts from Hole 4032, 4082, dolomitic sections of 4092 and 4081, 4095.

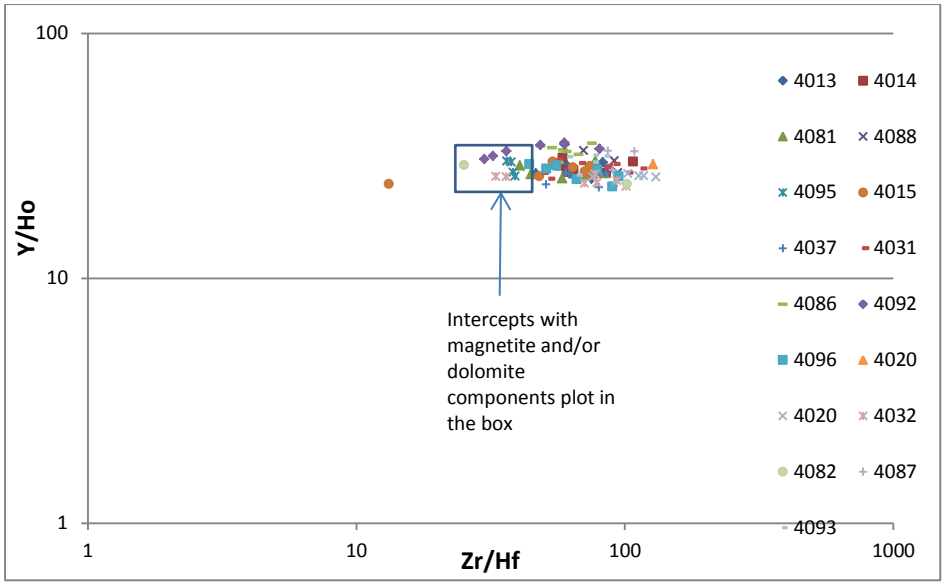

Figure 8.26 Y/Ho versus Zr/Hf for Area 4 wholerock data from +2000ppm TREE intercepts on all holes. Blue-lined box represents the CHARAC range of Zr/Hf (CHARAC = CHArge and RAdius Controlled cation behaviour) as displayed in Figure 8.25.

If REE is mobilised by complexing ligands in a hydrothermal environment, what complexing ligands are the most likely candidates? Williamson-Jones (2012) points out that REE have been regarded by many workers to be immobile in hydrothermal fluids (even though it has been known since the late 19th C that REEs are soluble in aqueous solutions). The occurrence of REE deposits of indisputable hydrothermal origin, however, including the giant Bayan Obo REE deposit, proves that the **REEs are highly mobile**. Briefly, Na-fenites (albititic), similar to Lofdal, occur adjacent to sövitic carbonatite dykes at Bayan Obo, Inner Mongolia, China, at the contact with the massive H8 dolomite carbonatite intrusion bordering the north–south-striking Wu sövitic carbonatite dyke a kilometre to the north. A strong enrichment of REE in the fenite alongside the fractured and sheared western margin of the carbonatite dyke is unique among all the other carbonatites dykes nearby and is interpreted as being a later REE-rich hydrothermal event, most probably related to the formation of the massive REE–Nb–Fe orebodies for which Bayan Obo is famous (Le Bas, 2008). It is of interest that dolomite could also be an effective neutraliser of HREE bearing fluids in Area 4, as we see highly enriched precipitation of xenotime at in brecciated dolomite in holes such as in 4092, as well as REE mineralised dolomites in Hole 4081 for example. Reaction of potential ore fluids with dolomite, for example, would provide a very effective mechanism for xenotime deposition because of the reaction:

$$2H^+ + CaMg(CO_3)_2 = Ca^{2+} + Mg^{2+} + 2HCO_3^-$$

Questions surround the type, or types, of ligands that could transport REE in solution in a system like in Area 4. During the past 15 years, a research group at McGill University, Montreal, Canada lead by Migdisov and Williams-Jones, has systematically investigated the speciation of the REE experimentally in fluoride- and chloride-bearing aqueous solutions (Migdisov et al, 2009). The scarcity of fluorite in

Area 4 could be explained by Buhn (2008), who reports that HREE and Y fractionates from the carbonatite melt into hydrothermal, HREE and Y-rich fluorites proximate to other, younger, carbonatite complexes in NW Namibia, notably Kalkfeld and Ondurakorume, and that this reflects the composition of the expelled fluid. The high strength of fluoride complexes suggests that fluoride complexing in the carbonatitic fluid is the process responsible for extracting HREE and Y from the carbonatite magma, leaving fractionated carbonatite rocks depleted in these elements. Perhaps F is not important to the REE distribution in Area 4 though. Studies by Williams-Jones and Migdisov suggest stability of REE complexes involving halogens like F is opposite to that predicted by Pearson's rules because of a very large decrease in the dielectric constant of water with temperature. Under ambient conditions, the high dielectric constant and resulting hydrogen bonding lead to strong shielding of aqueous ions and inhibition of electron transfer. At higher temperature, however, the decrease in the dielectric constant reduces resistance to electron transfer, promoting "softening" of ions. $LREEF^{2+}$ species are more stable than $HREEF^{2+}$ species at elevated temperature (Migdisov et al. 2009). This change in the relative stability of $LREEF^{2+}$ and $HREEF^{2+}$, from that at ambient temperature, occurs at approximately 150°C. Although fluorite does occur at Lofdal, as well as a minor accessory F bearing bastnasite group REE minerals such as synchysite (Ce), it's not very common as one would expect from an alkali-carbonatite complex. Significant amounts of fluorine have either travelled far from original source, as fluorite can be very mobile, or was deficient in fluorine in the first place. If there was F moving through the system it would form fluorite as soon as it met any calcite. Minor fluorite can be seen in high grade HREE sections of drill core notably in Holes 4015 and 4092, but it is not clear if it is coeval with HREE bearing carbo-hydrothermal phase, or an earlier Mg-carbonatite, or later infill hydrothermal. In Hole 4092 fluorite is associated with dolomite and perhaps earlier than the ankeritic carbonates that carries, or redistributes, most of the REE as xenotime (Figure 8.27).

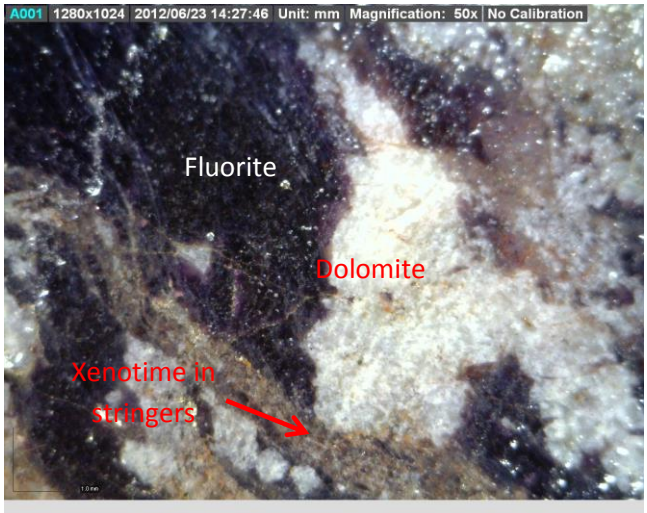

Figure 8.27. Hole 4092 189.59m fluorite in high grade intercept. Fluorite is associated with white dolomite, cut by later HREE bearing stringers (tan coloured).

EDS spectra for fluorite from Hole 4015 (Figure 8.28), however shows peak for Y suggesting that the fluorite is REE bearing whether associated with source, or inherited along fluid pathway.

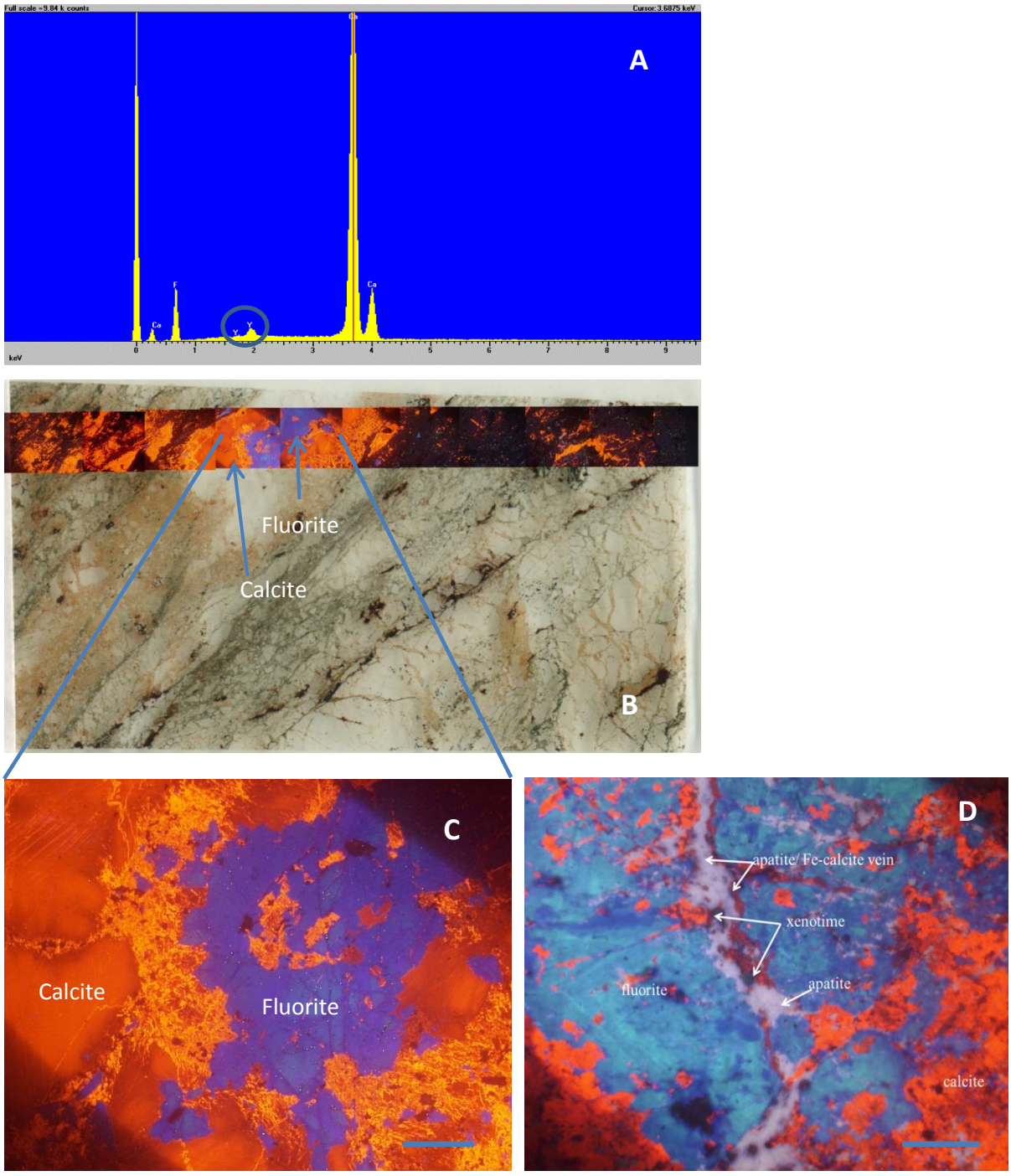

Figure 8.28. Fluorite in Hole 4015 37.30m gives Y peak on EDS (A) . B is a thin section with CL information hoighlighted , approx.. 45mm width. C is the corresponding CL, and D is the RHS Do Cabo 2013 Type 5 dyke associated with apatite and xenotime and similar CL reactive calcite. Scale bar 1mm.

CL spectra studies of the fluorite from VDCs Type-5 dykes show a blue emission range and an emission band of Dy^{3+} at 470 nm. Dy^{3+} is also responsible for the strong bands, which appear at 565, 650-660 (Figure 8.29).

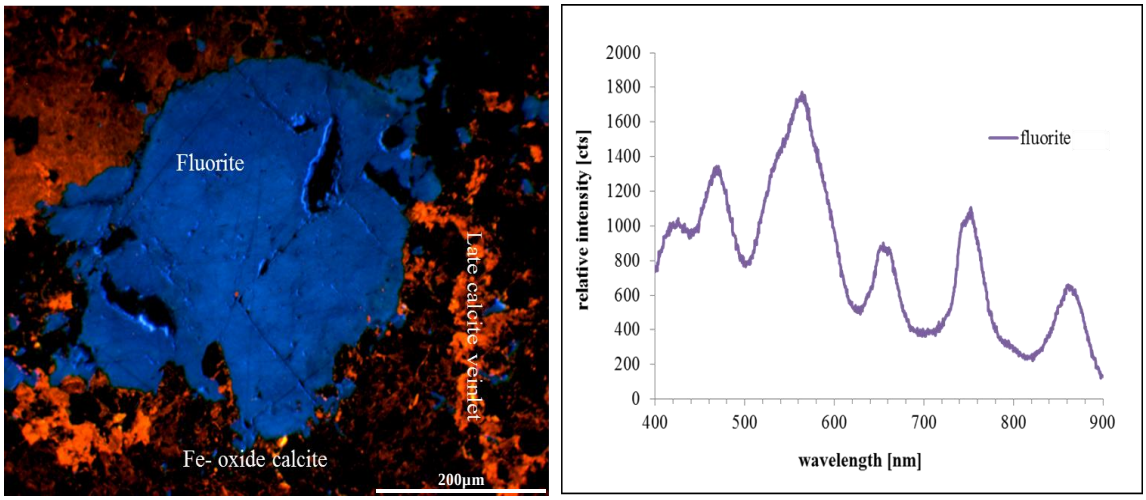

Figure 8.29 Cathodoluminescence spectrum of fluorite from VDC type 5 dyke (Do Cabo, 2013).

and 745-755 nm in the CL spectra. The fact that the fluorite is REE bearing is of great interest, and perhaps coeval with one, or some, REE mineralising process, and not just regarded as late infill. Ongoing fluid inclusion studies at University of McGill of fluorite from 4092 189.59m (Figure 8.27) aim to deduce more about the mineralising fluids.

Chloride complexing:

Tropper et al. (2011) undertook weight-loss experiments on synthetic single crystals of xenotime and monazite using hydrothermal piston-cylinder methods at 800 °C and 1 GPa, in H_2O and H_2O–NaCl fluids. Solubility of xenotime in pure H_2O is very low. The solubility of YPO_4 is greater than that of $CePO_4$ at NaCl mole fractions (X_{NaCl}) of 0.00–0.27. The solubility enhancement behaviour implies that Ce dissolves as anhydrous chloride complexes, whereas Y forms mixed Cl–OH solutes. The results provide a simple mechanism for redistributing REE and Y in environments like the shear zone of Area 4. The experiments indicate that neutral-pH H_2O–NaCl fluids can transport substantial REE and Y, infer that xenotime doesn't need highly acid solutions in environments where they are unlikely. Gieré (1993) however suggests that fluid that transports REE more than likely is acidic, and from paragenetic relationships suggests REE transports by in sulphur complexes (H_2S, HS^-, S^{2-} ligands) in certain fluids containing large amounts of reduced sulphur (acidic), and perhaps these should be considered as a possible addition to the suite of possible REE transporting ligands (Figure 8.30).

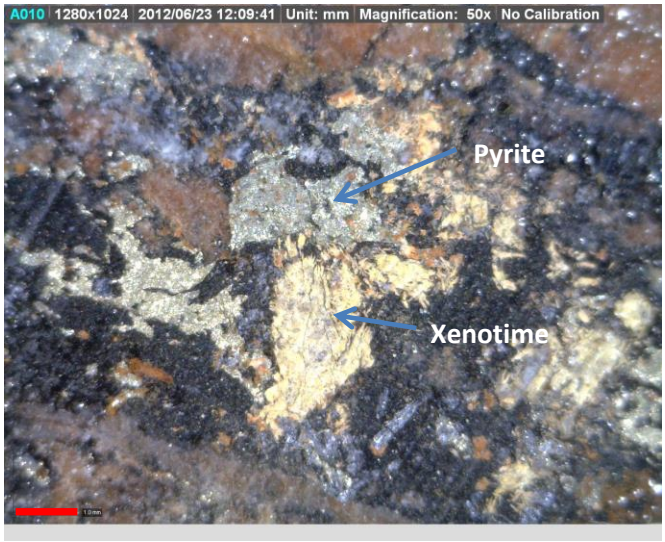

Figure 8.30. Dinolite-pro image at 4092 189.80m: Xenotime associated with pyrite in HREE enriched section – sulphide appears coeval with large grained xenotime (>1mm). NB Fe minerals are less oxidised at depth. Scale bar 1mm

However, if other potentially strong complexing ligands are present, then they would be preferred because of their strong affinity to the hard REE ions for hard ligands such as OH^-, Cl^- and PO_4^{3-}, especially at elevated temperatures, as proposed by Williams-Jones et al. 2012. The Browns Range in Western Australia hosts multiple generations of granites and these have been proposed as potential sources of REE contained in the mineralisation. Granites are well-known sources of REE and these are readily released from a granitic magma into a hydrothermal fluid (Lottermoser, 1992; Migdisov et al., 2009; Monecke et al., 2003), possibly via unmixing during the final stages of granite crystallisation (Bottrell and Yardley, 1988). These granite-derived fluids can also be rich in volatiles, notably P, F and Cl. Elevated F and Cl are measured in sericite and clay minerals. Although crystal-structural constraints still apply, modification of REE distributions in a given mineral can be related to REE mobility which increases with increased fluid/rock ratios. Naturally this is dependent on the reactivity (ground preparation: porosity, permeability) of the host rocks, and changes in physical–chemical parameters (Eh, pH, temperature, REE fluid activities, REE complexation etc.). Also to bear in mind is the co-existence of other REE-bearing species will also influence REE distributions i.e. apatite may keep, or scavenge LREE & MREE. Cook (2013) suggests that the first generation of xenotime at Browns Range, characterised by coarse grain size and generally euhedral morphology, would have removed Y + HREE from a hydrothermal fluid. A second stage of auto-brecciation contributes to the fragmentation of the early xenotime, which could be related to boiling of the hydrothermal fluids, and in turn have increased fluid salinity and acidity as outline by Burt (1981).

The above is describing granite derived fluids, hydrothermal REE deposits that are genetically associated with carbonatites and peralkaline silicate rocks include Bayan Obo, Inner Mongolia, China, which is responsible for 45% of global REE production, and has reserves of 135 million tons grading 6

wt.% REO. The REE mineralisation is hosted by a dolomitic sedimentary unit that is LREE-enriched. Early monazite-(Ce) stringer facies containing 3 to 6 wt.% REO; and an inner layered facies of dolomite replaced by monazite-(Ce), bastnäsite-(Ce) plus accessories minerals similar to those of Area 4. Other examples of REE deposits, which are of indisputable hydrothermal origin, are the Gallinas Mountains deposit, New Mexico, in which a fluorite-bastnäsite-(Ce) assemblage cemented quartz-syenite and sandstone breccias and the Karonge deposits in Burundi, which occur as cm- to dm-thick bastnäsite-(Ce) veins and stockworks in granitic gneiss. Both deposits have been interpreted to have formed between 300 and 400°C from brines containing between 7 to 25 wt.% NaCl equivalent. Although the deposits mentioned here show hydrothermal features similar to Area 4, they are predominately LREE-enriched, and the proposed fluid temperatures likely lower than the granite derived fluids of Browns Range.

Economically important HREE deposits with a combination of magmatic and hydrothermal processes include the Nechalacho deposit, Northwest Territories, Canada and the Strange Lake deposit in Québec, Canada and are both characterised by high proportions of HREE. At Nechalacho there is evidence that hydrothermal fluids dissolved HREE bearing zirconium silicates (eudialyte and zircon) and re-precipitated the REE with the HREE minerals deposited proximal to the precursor minerals, and LREE mobilised to 10s of meters away. At Strange Lake fluid inclusion analyses indicate that remobilisation took place at temperatures ranging from 350°C to 150°C, and involved interaction of sodic magmatic brines along with lower temperature calcic brines. It seems that the LREE are more mobile hydrothermally than the HREE, and that HREE mobilisation if it does occur, occurs close its source i.e. perhaps explaining why the Area 4 hydrothermal systems is positioned relatively close to its parental carbonatite, or close to fluid-wallrock interface. It can be proposed therefore that REEs form stable complexes with chloride ions at high temperature and chloride complexes can mobilise the REE in appreciable quantities. Concentrations of REEs occur mainly when fluids containing these complexes interact with cooler pH neutralizing rocks, or mix with cooler, pH neutralizing fluids. In Area 4's case this could be inferred as interaction and deposition in contact with albitite, and especially pre-existing carbonate e.g. dolomite. Fluid/rock interaction is important to precipitation of xenotime as hydrogen ion metasomatism of wall rocks tends to reduce the stability of the Cl complexes and leads to sulphide mineral precipitation.

The most common kinds of hydrogen ion-consuming reactions are a) solution of carbonates b) hydrolysis of feldspars and mafic minerals to form micas and clays. Therefore, fluid/rock interaction is a key factor to the precipitation and accumulations of xenotime in Area 4. It is important to not discount the influence of pressure. Much of the xenotime mineralisation in Area 4 occupies site s within faults and in the rock flour in breccia. Decrease in pressure can be sudden when hydrothermal

fluids enter open pore space such as fractures, fissures, cavities or brecciated rocks. Solubility of certain REE minerals decreases as confining pressure is decreased. This has been confirmed for monazite Ayres and Watson (1991). By contrast apatite's solubility *increases* with decreasing pressure in the same study. At the same time loss of pressure can lead to loss of volatiles and therefore resultant rise in pH and breakdown of REE complexes. Loss of CO_2 would displace the equilibrium. Volatiles are also lost through boiling and induce the precipitation of RE minerals.

8.5 Blending core studies with analytical observations

On the basis of field mineralogical and textural observations, whole rock geochemistry, and quantitative and qualitative mineral composition data, the REE mineralisation in Area 4 can be followed from source to sink as follows:

- On the basis of REE mantle signatures, the nepheline syenite and carbonatite bodies of the Lofdal Igneous Complex are likely to be genetically related, sharing a common HREE, Nb and U-enriched metasomatised mantle source. HREE enrichment was here early on.
- Alkali-rich fluids were released into the country rock from the crystallising nepheline-syenite converting the host rocks into fenite, predominantly the Huab basements gneiss in Area 4, to an assemblage predominately of albite. Fenitisation is notably potassic close to the Main Intrusion. Sodic distally – as halos around carbonatite plugs, but also linear in shape utilising pre-existing structural weaknesses/pathways.
- Brecciation occurs within these albitised gneisses within active sinistral basement faults, exacerbated by episodes of carbonatite/carbonate dominated intrusion/ingress; from early calcite dominant (sövitic), through dolomite dominant, to an evolved Fe-ankeritic carbonatite. Fluid pathways can be repeatedly overprinted.
- The carbonatites are pervasive and at times show evidence of facilitating hydraulic fracturing within the structures they have infiltrated, and incorporate sharp clasts of the albitite wall rock. Sometimes the albitite can be texturally diffuse, appearing "ghosted-out".
- Fluids of varying composition (depending on timing) permeate through the breccia in an irregular way utilising combinations of open spaces and rock flour as the major channelways. Albititised gneisses tend to produce courser grained sodic alteration products whereas fine grained rocks such phonolites change to finer grained alteration products, and although both of these can be sheared, the "harder" structural integrity of altered phonolites may act as impermeable barriers to facilitate and/or contain the HREE bearing fluid pathways, and ultimately HREE precipitation in more permeable hosts.
- Albititic alteration removes most features of the original host gneissic rocks but preferred shear orientation, and mineralisation takes advantage of this relict foliation lamellae.

- The degree of alteration increases as main channel way (main mineralised zone) is approached. The amount of change is more intense closest to the main channel way of the highest REE mineralised intercepts i.e. increased secondary porosity within reactivated faults/breccia zones. Pressure decrease could also facilitate mineralisation.
- There is much mineralogical and structural superimposition. Structures that acted as conduits for hydrothermal fluid are very prone to reactivation i.e. keep breaking, and in the same place. Each influx of fluid results in an additional infill assemblage, coupled with alteration of pre-existing alteration.
- Xenotime at Lofdal forms from magma AND from hydrothermal fluids. Associated phases are more LREE in the earlier stages. The graduation of LREE to HREE has been observed in the Khibina carbonatite, Kola Peninsula, Russia, is an example of where early LREE carbonatites become increasingly HREE-enriched as magmas evolve to carbo-hydrothermal fluids as observed by Zaitsev et al. (1998).
- Magmatic calcite and dolomite accompanied by oxides such as magnetite from earlier stage carbonatites bearing LREE and HREE minerals tend to react with fluids at lower temperatures to form the ankeritic assemblages of the later stage as outlined above (as also observed by Kapustin, 1986).
- Overprints are evident from the expanding front of a particular fluid, particularly late HREE bearing ankeritic carbonate, dependent upon rate of diffusion, particular grain boundary controls and degree of micro-fracturing. Potential variables in aiding precipitation of HREE minerals within favoured sites are temperature, pressure, pH, Eh, fluid composition, rate of flow and periodicity of flow.
- The preferred orientation of shear foliation structures defines the alignment of biotite/phlogopite stringers (with alteration to chlorite – usually interpreted as evidence for hydrous (OH) ingress). These minerals are major interstitial components, and hosts for xenotime in brecciated albitites, and at the contact with dolomite (Mg from dolomite perhaps exchanged into the biotite). There is an important close relationship between these micas and xenotime.
- Textural and compositional data indicate replacement and breakdown of magmatic-hydrothermal REE bearing phases. Suggested REE transporting ligands are perhaps a combination and evolution through HCO_3, PO_4 and HS >300°C, to Cl complexing ligands at to lower temperature <300°C.

- Dolomitic carbonatite hosting xenotime associated with LREE phosphate monazite, and other phases pre-dates the later Fe-rich fluid. The dolomite can be seen to have been overprinted, and perhaps a source of reworked REE.
- Paragenetic boundaries are gradational, and can be heavily overprinted – different parageneses can co-exist proximal to each other
- LREE located in faulted structures distal (to 10s of meters) from main HREE mineralised zones could be attributed to their greater mobility over HREE in a Cl rich system, as proposed by Williams-Jones et al. (2012). It is not unusual to see LREE peaks from whole-rock data in the hangingwall and/or footwall to the main HREE "channel" in Area 4.
- The Area 4 fault system/alteration zone could have initially been a pathway for alkali-rich metasomatism as well as for episodes of carbonatite with an initial LREE enrichment, through to the later Fe-enriched HREE bearing fluid phase, as the carbonatite moved from magmatic to hydrothermal regime, and subsequent hydrothermal evolution and reworking of all aforementioned episodes to varying degrees.

9 PARAGENETIC SEQUENCE

Textural observations and geochemical data have indicated a sequence of events that led to the accumulation of REE mineralisation in the alteration zone of Area 4, Lofdal, Namibia, as outlinedin the suggested model in Figures 9.1 a &9.1b below:

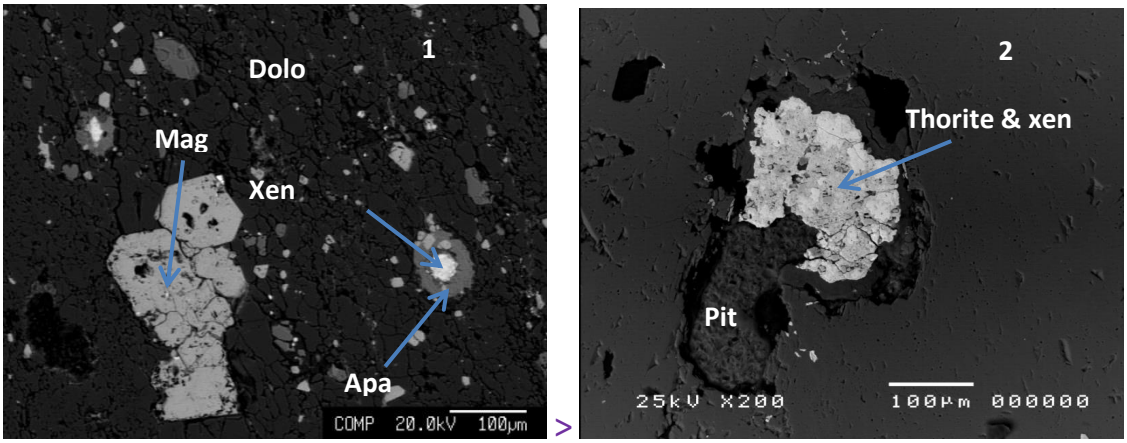

1.LREE & HREE bearing dolomite carbonatite, including xenotime (BSE image 4032 47.56m) & minor thorite, with or without magnetite, becomes > 2. Hydrothermally altered removing apatite and/or monazite leaving pit with only thorite and minor xenotime remaining (BSE image 4081 73.50m).

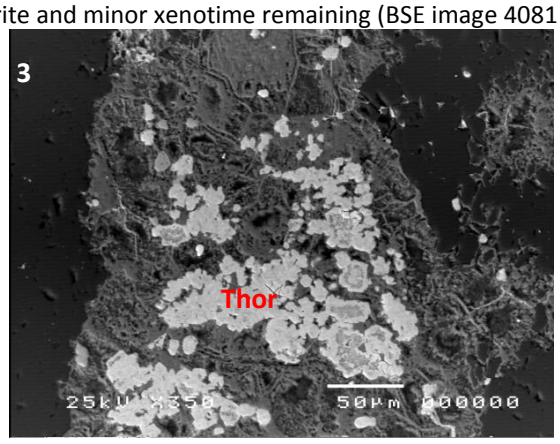

3. Any Th removed will re-deposit as soon as is it can but in its own phase, normally as thorite, but sometimes within aeschynite (BSE image 4086 117.14m), at higher temperatures there is a possibility of incorporation into xenotime lattice.

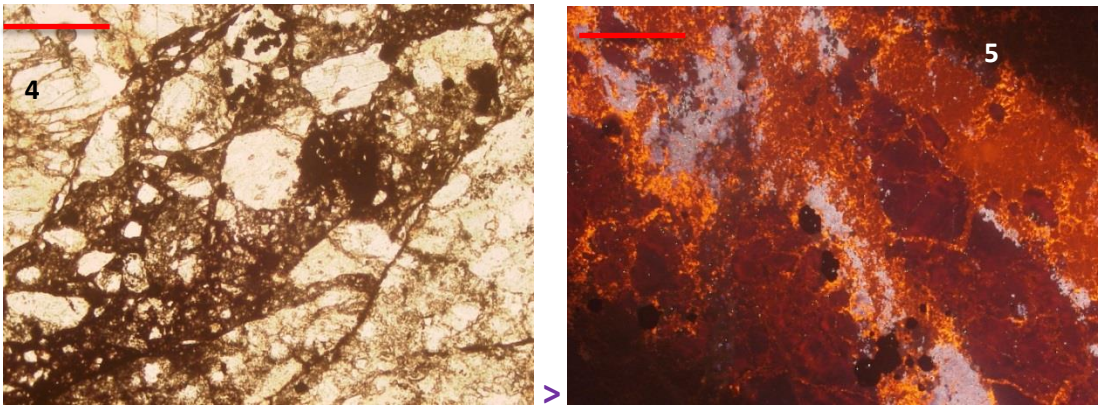

4. REE bearing fluids pass through rock flour of the brecciated albitite (PPL image 4082 91.86m) 5. Xenotime depositing as pressure drops in more open space, or because of fluid/rock interaction (CL image 4032 62.35m) Scale bar 1mm.

Figure 9.1a. Model of sequence of REE mineralisation in Area 4

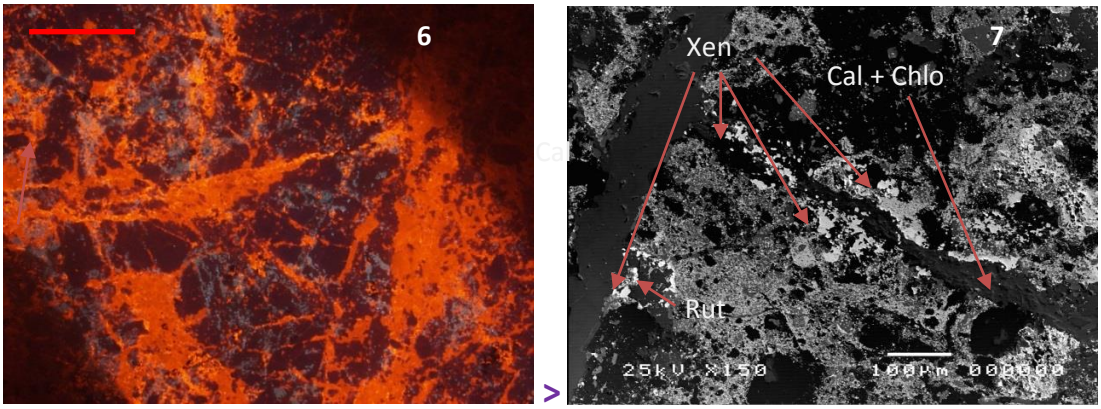

6. Fine grained re-deposited xenotime can be remobilised again. Each time the fluids become cooler & the complexing ligand proportions change to predominantly Cl complexes, the less thorium is contained in xenotime. (CL image 4082 92.20 & 7. BSE image 4014 66.45m).

Figure 9.1b. Model of sequence of REE mineralisation in Area 4

A paragentic sequence of mineralisation is presented below in Figure 9.2 and shows how predominately carbonatite related mineral phases (dolomite, magnetite, apatite) are superseeded by less magnesian carbonates (ankerite, calcite) and iron oxides. Importantly xsenotime spanns across the sequence, but as indicated becomes less associated with thorium and more MREE enriched to the expense of the heavier REE.

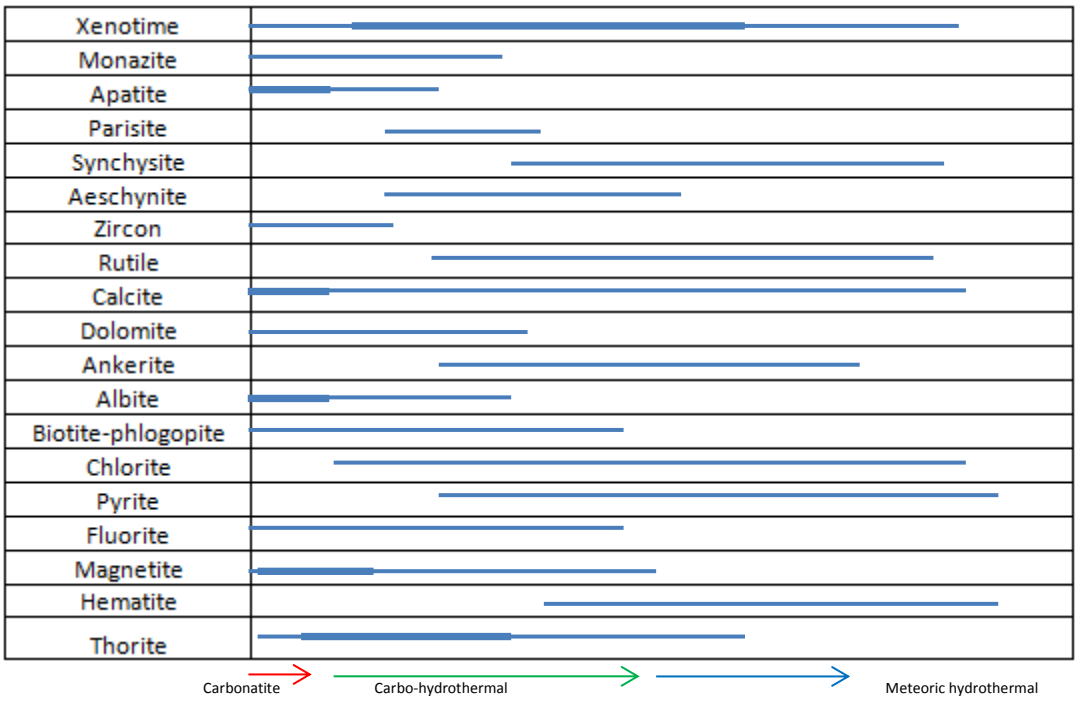

Figure 9.2 Paragenetic sequence for Area 4 Lofdal, Namibia

10 CONCLUSIONS

The Lofdal Igneous Complex is relatively enriched in HREE compared to other carbonatites indicating a fertile mantle source enriched in HREE, as well as Th, LREE, U and Nb. The LREE, U and Nb mineralising within the earlier sövitic carbonatites, the former (more incompatible HREE and Th) travelling out with later dolomitic, and subsequent magnetitic, ankeritic to ferruginous carbonatite as it moved from the magmatic regime into the hydrothermal regime.

- Na-fenitisation of the Huab basement rocks (the albitites), associated with emplacement of earliest carbonatite episodes, along pre-existing faults, has been subsequently brecciated tectonically and hydraulically to provide ideal ground preparation for episodes HREE bearing fluids.
- Dolomite carbonatite carries LREE and HREE minerals and their textures and geochemical data suggest a magmatic regime for their emplacement. This early carbonate can also act as a buffer to later REE bearing fluids resulting in overprinted generations of xenotime.
- Pressure conditions may play an important role where REE hydrothermal fluids enter open pore space such as fractures, fissures, cavities or brecciated rocks, and the pressure drop results in the dump of xenotime, and could explain the preferred precipitation of xenotime interstially in brecciated albitite.
- As for transporting ligands: S complexes can be discounted as hard REE ions have preferred affinity for hard ligands such as OH-, F-, and PO_4^{3-} especially at elevated temperatures.
  At lower temperatures Cl is favoured as the probable transporting ligand, but in the real world it is likely that there was a combination of ligands, albeit Cl being most dominant.
- Textural and geochemical evidence suggests that xenotime has a range of morphologies, and infer at least four parageneses:
- **1.** An early euhedral type associated with magnetite and thorite, and commonly associated with dolomitic carbonatite 20-50 µm
- **2.** Xenotime exsolution or precipitation/dissolution in apatite also deemed early
- **3.** Relatively large, subhedral to euhedral, singular crystals (30-100 µm), many mantling zircon, or larger aggregates associated with rutile. Assocatated with biotite-phlogopite veins.
- **4.** A granular, very small (<20 µm) anhedral crystals as “wispy” disseminations associated with ankeritic overprints, and these can be further remobilised and recrystallized locally, by lower temperature fluids.
- Fractionation and partitioning in REE in xenotime is controlled by crystallochemical factors and reaction kinetics, temperature, pressure and the composition of the fluid phase.

Experiments here have shown early xenotime is more HREE enriched than latter xenotime, which are more MREE enriched.

- Later xenotime, that is transported and deposited in a more hydrothermal regime, tends to have a higher MREE content, yet a lower Th content

11 LIMITATIONS & RECOMMENDATIONS

Additional EPMA work could investigate the compositional variations in the apatite to analyses the REE deportment in this phase, and to see if it is a sink of LREE and/or HREE. Findings would add to the genetic model of the Area 4 deposit, as well as being economically pertinent.

The REE content of the early fenitising fluids is also of interest, to determine whether the REE deportment in Area 4 is indeed only introduced by carbonatite dykes and later fluids. Fluid inclusion, work similar to that undertaken on the fenites at Chilwa Island, Malawi by Emma Dowman, is recommended.

Additional fluid inclusion work on fluorite is also recommended. Fluorite is sparse in Area 4 but does turn up occasionally, and of interest, in the high HREE grade section of Hole 4 at 189.59m.

A better understanding of the compositions biotite/phlogopite and chlorite would aid the paragenetic sequence of crystallisation i.e. is it carbonatite related, or related to metamorphism linked to the later Pan African Orogeny.

Iron isotope compositions of carbonatites record melt generation, crystallisation, and late-stage volatile-transport processes. Iron isotope variations in carbonatites can be used as a tracer of fluid interactions and cooling history as outline by Johnson (2010). Many minerals in the carbonatites studied are out of Fe isotope equilibrium at igneous temperatures, and, considering the large contrasts in Fe contents among carbonate, silicate, oxide, and sulphide minerals, isotopic disequilibrium likely reflects the effects of cooling and fluid/rock interaction.

12 REFERENCES

Andersen, T (1984): Secondary processes in carbonatites: petrology of “rodberg” (hematite-calcite-dolomite carbonatite) in the Fen Central Complex, Telemark, Norway. Lithos 17, 227-45.

Argus Metal Pages (2014) - https://www.argusmedia.com/Metals/Metal-Pages

Ayers, J. C. & Watson, E.B. (1991): Solubility of apatite, monazite, zircon and rutile in supercritical aqueous fluids with implications for subduction zone geochemistry. Phil. Trans. Roy. Soc. Lond. A 335: 365-375

Barker, D.S. (2001): Calculated silica activities in carbonatite liquids. Contrib. Mineral. Petrol. 141, 704-709.

Bau, M. (1996): Controls on the fractionation of insolvent trace elements in magmatic and aqueous systems: evidence from Y/Ho, Zr/Hf, and lanthanide tetrad effect. Contributions Mineralogical Petrology 123: 323-333.

BBC – Lynas learns fate of rare earth refinery - http://www.bbc.co.uk/news/business-19880168

Bell, K. (1989): Carbonatites Genesis and Evolution. London, England: Unwin Hyman Ltd.

Bell, K. and Blenkinsop, J. (1989) Neodymium and strontium isotope geochemistry of carbonatites. In: Bell, K. (ed.) Carbonatites: genesis and evolution. 278-300, Unwin Hyman, London.

Bodeving S. (2013): Geochemistry of the nepheline syenites at Lofdal. Lofdal Conference, Chaired by A. E Williams-Jones, McGill University, Montreal, Canada, October 2013.

Bowens and Crocket (2011): Monazite, xenotime and REE minerals in Archean banded iron formation from the Sherman and Adama Mines, Ontario, Canada. Canadian Mineralogist 49, 749–763.

British Geological Survey (2012): Rare earth elements profile
www.bgs.ac.uk/downloads/start.cfm?id=1638

Broom-Fendley S, Wall F, Gunn A.G (2012): Targeting heavy rare earth elements in carbonatite complexes Geophysical Research Abstracts Vol. 14, EGU2012-8541.

Buck et al., (1999): Xenotime-(Yb), $YbPO_4$, a new mineral species from the Shatford Lake pegmatite group, South-eastern Manitoba, Canada. Canadian Mineralogist, v. 37, p.1303-1306.

Buhn B. (2008): The role of the volatile phase for REE and Y fractionation in low-silica carbonate magmas: implications from natural carbonatites, Namibia. Mineral Petrol 92: 453–470.

Burger et al., (1976): Through U/Pb dating methods the FGS was imprecisely dated with two discordia, giving ages of 1871±30Ma and 1730±30Ma, Precambrian Research, 3, 405-431.

Burt, D.M. (1981): Acidity–salinity diagrams; application to greisen and porphyry deposits. Economic Geology 76, 832–843.

Chakhmouradian A. R & Wall F. (2012): Rare Earth Elements: Minerals, Mines, Magnets (and More) Elements Magazine Oct 2012 8.5, 335-342.

Cherniak, D.J., Hanchar, J.M., and Watson, E.B. (1997): Diffusion of tetravalent cations in zircon. Contributions to Mineralogy and Petrology, 127, 383–390.

Cherniak D. J. (2006): Pb and rare earth element diffusion in xenotime Lithos 88, 1 – 14.

Choppin, G.R. (2002): Covalency in f-element bonds. Journal of Alloys and Compounds 344: 55-59.

Cook et al. (2013): Mineral chemistry of Rare Earth Element (REE) mineralization, Browns Ranges, Western Australia. Lithos 172-17, 3 192-213.

Demartin et al. (1991): The chemical composition of xenotime from fissures and pegmatites in the Alps. Canadian Mineralogist 29, 69–75.

Do Cabo, V. (2013): PhD thesis Geology of REE bearing carbonatites of the Lofdal Carbonatite Complex, Khorixas, Namibia.

Dowman, Emma (2014): Mineralisation and fluid processes in the alternation zone around the Chilwa Island and Kangankunde carbonatite complexes, Malawi. (PhD thesis), Kingston University.

Emden et al. (1997): THE INCORPORATION OF ACTINIDES IN MONAZITE AND XENOTIME FROM PLACER DEPOSITS IN WESTERN AUSTRALIA. Canadian Mineralogist Vo1. 35, pp. 95-104

Ferguson, J. and K. L. Currie (1971): Evidence of liquid immiscibility in alkaline ultrabasic dikes at Callendar Bay, Ontario. J. Petrol., 12, 561-58.

Förster H.J. (1998): The chemical composition of REE-Y-Th-U-rich accessory minerals in peraluminous granites of the Erzgebirge-Fichtelgebirge region, Germany. Part II: Xenotime. *Am. Mineral.* **83,** 1302–1315.

Förster, H.-J., (2006): Composition and origin of intermediate solid solutions in the system thorite–xenotime–zircon–coffinite. Lithos 88, 35–55.

Franz et al. (1996): Crystal chemistry of monazite and xenotime from Saxothuringian-Moldanubian metapelites, NE Bavaria, Germany. European Journal of Mineralogy 8, 1097–1108.

Frets, D. C. (1969): Geology and structure of the Huab-Welwitchia area. South West Africa, Chamber of Mines, Precambrian Research Unit: University of Cape Town Libraries. 235 pp.

Gaudet, M.A. (2013): MINERALOGICAL STUDY OF URANIUM AND NIOBIUM MINERALIZATION AT THE MAIN INTRUSION OF THE LOFDAL CARBONATITE COMPLEX, NAMIBIA, AFRICA. BSc thesis, Dalhousie University, Halifax, Canada.

Geological Society of Namibia (2002) - http://www.mme.gov.na/gsn/

Gieré, R., 1996. Formation of rare earth minerals in hydrothermal systems. In: Jones AP, Wall F, Williams T. Rare Earth Minerals: Chemistry, Origin and Ore Deposits. Mineralogical Society, Series 7. pp: 105-150.

Gittins J. (1989): The origin and evolution of carbonatite magmas. In: Bell K., editor. Carbonatites: Genesis and Evolution. London: Unwin Hyman; p. 580-600.

Grantz & Heinrich (1997): Monazite-xenotime thermobarometry: Experimental calibration of the miscibility gap in the binary system CePO4-YPO4 American Mineralogist, Volume 82, pages 772–780.

Great Western Minerals Group (GWMG) (2013): - http://www.gwmg.ca/index.cfm

Harlov D.E., Wirth R. (2012): Experimental incorporation of Th into xenotime at middle to lower crustal P-T utilizing alkali-bearing fluids. American Mineralogist, Volume 97, pages 641–652.

Harrison, T.M. and Watson, E.B. (1984): The behavior of apatite during crustal anatexis: Equilibrium and kinetic considerations. Geochimica et Cosmochimica Acta, 48, 1467–1477.

Heinrich, W., Andrehs, G. & Franz, G. (1997): Monazite–xenotime miscibility gap thermometry. I. An empirical calibration. J. Metam. Geol. 15, 3-16.

Hetherington C.J. (2008): Understanding geologic processes with xenotime: Composition, chronology, and a protocol for electron probe microanalysis. Chemical Geology 254 133–147.

Hetherington C. J, Harlov D.E, (2010): Experimental metasomatism of monazite and xenotime: mineral stability, REE mobility and fluid composition.

Hoffman, P.F., Hawkins, D.P., Isachsen, C.E. and Bowring, S.A. (1996): Precise U-Pb zircon ages for early Damaran magmatism in the Summas Mountains and Welwitschia Inlier, northern Damara belt. Communs geol. Surv. Namibia, 11, 47–52.

Hogarth, D.D., Williams, C.T., Jones, P. (2000): Primary zoning in pyrochlore group minerals from carbonatites. Mineralogical Magazine, Vol. 64(4), pp. 683-697.

Industrial Minerals Company of Australia (IMCOA) 2012. Rare earth oxide (REO) supply and demand. Technology Metals Summit, Toronto, February 2012.

Irber, W. (1999): The lanthanide tetrad effect and its correlation with K/Rb, Eu/Eu*, Sr/Eu, Y/Ho and Zr/Hf of evolving peraluminous granite suits. Geochim. Cosmochim. Acta 63, 489–508 .

Johnson, C.M., Bell, K., Beard, B.L., Shultis, A.I. (2010): Iron isotope compositions of carbonatites record melt generation, crystallization, and late-stage volatile-transport processesMineralogy and Petrology, Volume 98, Issue 1-4, pp 91-110.

Jones A. P., Wall F., & Williams C. T. (1996): Rare Earth Minerals: chemistry, origin and ore deposits. Bodmin, Cornwall, Great Britain: The Mineralogical Society.

Jung et al. (2007): Neo-Proterozoic rift-related syenites (Northern Damara Belt, Namibia): Geochemical and Nd-Sr-Pb-O isotope constraints for mantle sources and petrogenesis. Lithos 96, 415-435.

Kapustin, Y.L. (1986): The origin of early calcitic carbonatites. International Geology Review Vol. 28, Issue 9.

Kaul, A. (2010): A petrological study of REE-Rich carbonatite intrusions from the Lofdal Farm area, Namibia, Africa. Wolfville, Nova Scotia, Canada: Acadia University.

Kositcin N, McNaughton N. J. (2003): Textural and geochemical discrimination between xenotime of different origin in the Archean Witwatersrand Basin, South Africa Geochimica et Cosmochimica Acta, Vol. 67, No. 4, pp. 709–731.

Le Bas, M.J. (2008): Fenites associated with carbonatites. Canadian Mineralogist Vol. 46, pp. 915-932.

Le Maitre, R. W. et al. (1989): A Classification of Igneous Rocks and Glossary of Terms. Oxford: Blackwell Scientific, 193 pp.

Lee W, & Wyllie P. J. (1998): Processes of Crustal Carbonatite Formation by Liquid Immiscibility and Differentiation, Elucidated by Model Systems. Journal of Petrology, 39, 2005-2013.

Lottermoser, B.G. (1992): Rare earth elements and hydrothermal ore formation processes.
Ore Geology Reviews (Impact Factor: 3.38). 04/1992; 7(1):25-41.

Lynas Corporation 2014 - https://www.lynascorp.com/Pages/home.aspx

Mann V. (2013): University of Birmingham. BGS Meeting 24th October NERC project GEMCRE Workshop 1.

Masau, M., Černý, P., Chapman, R. (2000): Dysprosian xenotime-(Y) from the Annie Claim #3 granitic pegmatite, South Eastern Manitoba, Canada: evidence of the tetrad effect? The Canadian Mineralogist 38, 899–905.

Mariano A. N. (1989): Nature of economic mineralisation in carbonatites and related rocks, in Rare Earth Minerals: Chemistry, Origin and Ore Deposits By Jones A. P, Wall F, Williams C. T. 149-176.

Marshall D.J. (1987): Cathodoluminescence of Geological Materials. Kluwer Academic Publishers, 172 pp.

McDonough W.F., Sun S. (1995): The composition of the Earth. Chemical Geology 120: 223-253.

Migdisov A.A, Williams-Jones A.E, Wagner T. (2009): An experimental study of the solubility and speciation of the REEs (III) in fluoride- and chloride- bearing aqueous solutions at temperatures up to 300°C. Geochemica et Cosmochimica Acta 73 7087-7109.

Miller R.M. (2008): Neoproterozoic and early Palaeozoic rocks of the Damara Orogen - The Geology of Namibia. Geological Survey of Namibia.

Mindat mineralogical database (2014) – www.mindat.org

Mintek (2013) - http://www.mintek.co.za/technical-divisions/hydrometallurgy-hmd/services/extraction-group/

Minuzzi et al. (2006): Pyrochlore columbitization in the albite-enriched granite from Pitinga Mine: The relationship with the cryolite mineralization. Revista Brasileira de Geociencias 36, 124-137.

Mitchell, R. H., & Jambor, J. L (Eds.) (1996): Minerological Association of Canada Short Course Series. Undersaturated Alakaline Rocks: Mineralogy, Petrogenesis, and Economic Potential (Vol.24).Winnipeg, Manitoba, Canada.

Molycorp (2014) - http://www.molycorp.com/

Monecke, T., Kempe, U., Monecke, J., (2003): Comment on the paper ‘‘Wand M-type tetrad effects in REE patterns for water-rock systems in the Tono uranium deposit, central Japan’’ by Takahasi, Y., Yoshida, 352 T. Monecke et al. 71 (2007) 335–353 H., Sato, N., Hama, K., Yusa, Y., Shimizu, H. Chem. Geol. 202, 183–184.

Morogan, V. (1994): Ijolite vs. carbonatite as sources of fenitization. Terra Nova 6, 166–176.

Morogan V, Martin RF (1983): Mineralogy and partial melting of fenitized crustal xenoliths in the Oldoinyo Lengai carbonatitic volcano, Tanzania. Am Mineral 70:1114–1126.

Morogan, V. and Woolley, A.R. (1988): Contrib. Mineral. Petrol., 100, 169-82.

Namibia Rare Earths (2011, 2012, 2013, 2014) – Internal reports, and press releases from www.namibiarareearths.com

Ndalulilwa, K. D. (2009): The semi-quantitative petrographic, mineralogical and geochemical characterization of mineralisation of carbonatites from the Lofdal area in Namibia. Windhoek, Namibia: University of Free State (UFS).

Ni Y., Hughes J. M., and Mariano A. M. (1995): Crystal chemistry of the monazite and xenotime structures. Am. Mineral. **80,** 21–26.

O’Connor D. E. (2011): Petrogenesis of the nepheline syenites and phonolites from the Lofdal intrusive complex, Namibia. BSc thesis, Dalhousie University, Halifax, Canada.

Oakdene Hollins (2013): BGS Meeting 24th October NERC project GEMCRE Workshop 1

Ondrejka M., Uher, P., Pršek, J., Ozdín, D., (2007): Arsenian monazite-(Ce) and xenotime- (Y), REE arsenates and carbonates from the Tisovec-Rejkovo rhyolite, Western Carpathians, Slovakia: composition and substitutions in the (REE, Y)XO4 system (X = P, As, Si, Nb, S). Lithos 95, 116–129.

Pereira et al. (2012): Fluorine-rich xenotime from world-class Madeira Nb-Ta-Sn deposit associated with the albite-enriched granite at Pitinga, Amazonia, Brazil. Canadian Mineralogist, Vol. 50, 1453-1466.

Pyle, J.M., Spear, F.S., and Wark, D.A. (2002): Electron microprobe analysis of REE in apatite, monazite, and xenotime: Protocols and pitfalls. In M.J. Kohn, J. Rakovan, and J.M. Hughes, Eds. Phosphates: Geochemical, Geobiological, and Materials Importance, 48, p. 337-362. Reviews in Mineralogy and Geochemistry, Mineralogical Society of America.

Rubin et al. (1989): Hydrothermal zircons and zircon overgrowths, Sierra Blanca Peaks, Texas. American Mineralogist, Volume 74, 865-869.

Schneider, G. (2008): The Roadside Geology of Namibia, 2nd Edition, Gebruder Borntaeger Stuttgart, Germany. 294pp.

Shannon, R.D. (1976): Revised effective ionic radii and systematic studies of interatomic distances in halides and chalcogenides. Acta Crystallogr., A 32, 751–767.

Swinden, H.S., Siegfried, P. (2012): 43-101 Technical Report on the Rare Earth Element Occurrences in the Lofdal Carbonatite Complex, Kunene Region, Khorixas District, Namibia. Published report for Namibia Rare Earths Ltd., Halifax, Canada.

Tanaka K, Takahashi Y, Shimizu H. (2008): Local structure of Y and Ho in calcite and its relevance to Y fractionation from Ho in partitioning between calcite and aqueous solution. Chemical Geology 248, 104-113.

Tasman Metals Ltd 2014 – www.tasmanmetals.com

Technology Metals Research 2014 - http://www.techmetalsresearch.com/

Tropper P, Manning C.E, Harlov D.E. (2011): Solubility of $CePO_4$ monazite and YPO_4 xenotime in H_2O and H_2O–NaCl at 800 °C and 1 GPa: Implications for REE and Y transport during high-grade metamorphism. Chemical Geology 282 58-66.

Ucore Rare Metals Inc. 2014 – www.ucore.com

US Department of Energy Critical Materials Strategy (2010): Technology Metals Research 2014

USGS - United States Geological Survey (2014) - http://minerals.usgs.gov/minerals/pubs/commodity/rare_earths/

Van Orman, J. A., Grove, T. L., Shimizu, N., and Graham, D. L. (2001): Rare earth element diffusion in diopside: influence of temperature, pressure and ionic radius, and an elastic model for diffusion in silicates. Contrib. Mineral. Petrol. 141, 687-703.

Verwoerd W.J.(1993): Update on carbonatites of South Africa and Namibia. S. Afr. J. Geol. 96, 75–95.

Wall F, & Mariano A. N. (1996): Rare earth minerals in carbonatites: a discussion centred on the Kangankunde Carbonatite, Malawi. (A. P. Jones, F. Wall, & C. T. Williams, Eds.) London, UK: Chapman & Hall.

Wall F, Niku-Paavola V. N, Storey C, Muller A., & Jeffries T. (2008): Xenotime-(Y) from carbonatite dykes at Lofdal, Namibia: unusually low LREE:HREE ratio in carbonatite, and the first dating of xenotime overgrowths on zircon. The Canadian Mineralogist, 861-877.

Walters, A., Lusty, P., Chetwyn, C. and Hill, A. (2010): Rare Earth elements: Commodity profile. British Geological Survey.

Wang et al. (2003): Accessory minerals in the Xihuashan Y-enriched granitic complex, Southern China: a record of magmatic and hydrothermal stages of evolution. The Canadian Mineralogist 41, 727–748.

Webmineral mineralogical database 2014: – www.webmineral.com

White-Pinilla, K.C. (1996): Characterization of fenitizing fluids and processes involved in fenitization at the Iron Hill carbonatite complex, Gunnison County, Colorado: Golden, Colorado School of Mines, Master's thesis, 170 pp.

Williams, C.T. (1996): Analysis of rare earth minerals. In Rare Earth Minerals: Chemistry, Origin and Ore Deposits (A.P. Jones, F. Wall & C.T. Williams, eds.). Mineralogical Society, Ser. **7**, 327-348.

Williams-Jones A.E., Migdisov A.A., Samson I.M. (2012): Hydrothermal Mobilisation of the Rare Earths – a tale of “Ceria” and “Yttria”. Rare Earth Elements: Minerals, Mines, Magnets (and More) Elements Magazine Oct 2012 8.5. 355-360.

Williams-Jones, A. E. & Palmer, D. A. S. (2002): Fluid evolution of the Amba Dongar carbonatite complex, India. Chemical Geology 185, 283–301.

Winter (2001): An introduction to igneous & metamorphic petrology: New Jersey, Prentice Hall, 697 pp.

Woolley A.R. (1982): A discussion of carbonatite evolution and nomenclature, and the generation of sodic and potassic fenites. Mineralogical Magazine, Vol. 46, 13-17.

Woolley A.R. & Kempe D.R.C. (1989): Carbonatites: nomenclature, average chemical compositions, and element distribution. *In* Carbonatites: Genesis and Evolution (K. Bell, ed.). Unwin Hyman, Ltd., London, U.K. (1–14).

Woolley A. R., & Kjarsgaard B. A. (2008): Paragenetic types of carbonatite as indicated by the diversity and relative abundance of associated silicate rocks: evidence from a global database. The Canadian Mineralogist, 46, 741-752.

Zaitsev, A.N., Wall , F. & Le Bas, M.J. (1998): REE–Sr–Ba minerals from the Khibina carbonatites, Kola Peninsula, Russia: their mineralogy, paragenesis and evolution. Mineral. Mag. **62**, 225-250.

Zharikov V. A, Pertsev, N. N, Rusinov V. L, Callegari E, & Fettes A. (2007): Systematic nomenclature for metamorphic rocks: 9. Metasomatic rocks. Recommendations by the IUGS Sub-commission on the Systematics of Metamorphic Rocks. British Geological Survey recommendations, www.bgs.ac.uk - web version of 01.02.2007.